Characterising and Modelling Calvarial Growth and Bone Formation in Wild Type and Craniosynostotic Type Mice

A thesis submitted in partial fulfilment

of the requirements for the degree of

Doctor of Philosophy

By

Arsalan Marghoub

Department of Mechanical Engineering

University College London

2019

Declaration

I, Arsalan Marghoub, confirm that work presented in this thesis is my own. Where information has been derived from other sources, I confirm that this has been indicated.

Signature:

Date:

This work is wholeheartedly dedicated to my wife *Azade*, and my son *Araz*. They gave me the extra energy that I needed to complete this PhD. My heartfelt regard, and deepest gratitude is extended to my mother *Sorayya*, my father *Abdollah*, mother in law, *Tayyebeh*, and my father in law, *Yadollah* for their love and moral support. My most sincere thanks to my sister and brother, *Farideh* and *Mehran*, and all my family in Tabriz and Bojnourd, I deeply miss them.

Abstract

The newborn mammalian cranial vault consists of five flat bones that are joined together along their edges by soft tissues called sutures. The sutures give flexibility for birth, and accommodate the growth of the brain. They also act as shock absorber in childhood. Early fusion of the cranial sutures is a medical condition called craniosynostosis, and may affect only one suture (non-syndromic) or multiple sutures (syndromic). Correction of this condition is complex and usually involves multiple surgical interventions during infancy.

The aim of this study was to characterise the skull growth in normal and craniosynostotic mice and to use this data to develop a validated computational model of skull growth. Two oncogenic series of normal and craniosynostosis (Crouzon) mice were microCT scanned and various morphological features of their skulls was characterised at postnatal days (P) 3, 7 and 10. Finite element model of a normal mouse at P3 was developed and used to predict the radial expansion of the skull and the pattern of bone formation at the sutures at P7 and P10. A series of sensitivity tests were carried out. Note the specific ages used in this study correspond to the age that this condition is diagnosed and treated in human.

Results highlighted a good agreement between the finite element results and the *ex vivo* data both in terms of the radial expansion of the skull and the pattern of bone formation at the sutures. Nonetheless, the FE results were sensitive to the choice of input parameters. The modelling approach and the platform that was developed and validated here has huge potentials to be applied to human skull and to optimise the management of various forms of this condition.

Impact Statement

In this work, a new approach was introduced to simulate the calvarial growth. This approach was tested and validated in wild type and craniosynostotic mice. The same modelling approach can be applied to model human skull growth and optimise management of various craniofacial abnormalities.

The modelling work presented here was presented in several international meetings e.g. the 8th world congress of biomechanics, the 17th congress of international society of craniofacial surgery, and the 11th International Congress of Vertebrate Morphology. It was very well received and apprised by other colleagues. For example, this work was runner up for the European Society of Biomechanics Student Award at the 8th World Congress of Biomechanics. Chapter 4 and 5 of this work were published in two well respected journals i.e. Journal of Anatomy (featured front cover) and Physical Review Letters.

This work has led to another PhD studentship (funded by the Rosetree Trust) in the group that I have been working (Moazen Lab). The new PhD student is applying the methodologies that I developed to optimise the management of sagittal craniosynostosis. This in long term can improve the quality of life of children affected by this condition and improve the quality of the care provided by National Health Services.

Acknowledgments

List of Abbreviations

MRI	Magnetic Resonance Imaging
CT	Computer Tomography
microCT	Micro Computer Tomography
WT	Wild Type
MT	Mutant Type
FE	Finite Element
FEA	Finite Element Analysis
ICV	Intracranial Volume
P	Postnatal Day
E	Embryonic Day
3D	Three Dimensional
CS	Craniosynostosis
FGF	Fibroblast Growth Factor
CSF	Cerebrospinal Fluid
RMS	Root Mean Square
LM	Landmark
L	Left
R	Right

Contents

Chapter 1: Introduction

1-1 Overview

Vertebrate cranium consists of many bones. Major cranial bones in human are two frontals that shape the forehead, two parietals that form a large portion of the skull roof, lambdoid bone that form the posterior part of the skull and temporal bones that form the lateral sides of the skull (Fig. 1.1). These bones are joined together at their edges by soft and deformable fibrous tissue called sutures (Opperman, 2000; Morriss-Kay and Wilkie, 2005; Herring, 2008; Robert, 2014). Each suture connects a different part of the skull (Fig. 1.1). Frontal bones are connected together via the metopic suture. Sagittal suture connects the two parietal bones. The frontal and parietal bones are connected via the coronal sutures. The parietal and lambdoid bones are joined via the lambdoid suture, and the temporal and parietal bones are connected via the temporal sutures.

Sutures have several functions. They allow the brain to grow, give the skull flexibility for birth and work as shock absorber (Rasmussen *et al.*, 2008). During the development, the intracranial volume gradually increases and bone forms at the cranial sutures. Finally, the complex of the bones and sutures turns into a relatively rigid solid structure to protect the brain. The timing of the suture closure varies between different sutures. While some sutures close early in infancy, some fuse during the adulthood. For example, in human, the sagittal, coronal, and lambdoid sutures are usually fused by the third decade of life (Badve *et al.*, 2013). On the other hand, the metopic suture is closed at about 8 months after birth (Melott, 1999; Weinzweig *et al.*, 2003) however, it may remain patent until adulthood in about 10% of people (Rasmussen *et al.*, 2008). The morphologies of the sutures also vary greatly, e.g. the coronal and temporal sutures are overlapping sutures while the sagittal suture is an interdigitated suture (Morriss-Kay and Wilkie, 2005).
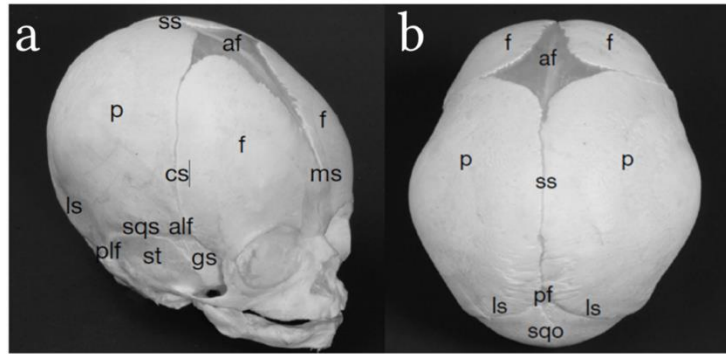
Fig. 1.1: Skull bones and sutures. ***af:*** anterior fontanelle; ***alf:*** anterior lateral fontanelle (sphenoidal); ***cs:*** coronal suture; ***f:*** frontal bone; ***gs:*** greater wing of sphenoid bone; ***ls:*** lambdoidal suture; ***ms:*** metopic suture (interfrontal); ***p:*** parietal bone; ***pf:*** posterior fontanelle; ***plf:*** posterolateral fontanelle (mastoid); ***sqo:*** squamous part of occipital bone; ***sqs:*** squamosal suture; ***ss:*** sagittal suture; ***st:*** squamous part of temporal bone (from Rice, 2008).

Premature fusion of the sutures is a medical condition called craniosynostosis (CS). CS is a relatively common anomaly occurring in 1 in 2000 birth (Kimonis *et al.*, 2007; Bannink *et al.*, 2010). A vast majority of craniosynostosis cases (90%) are non-syndromic synostosis, in which a single suture is affected. The remaining instances are syndromic CS like Crouzon and Apert syndromes, in which more than one suture is affected. The most common types of CS are sagittal, metopic, and coronal synostoses. Fig. 1.2 shows a schematic of the most common types of this condition. It highlights different skull shapes caused by different forms of craniosynostosis.

Molecular biologists have been working to understand causes of syndromic and nonsyndromic CS, investigating various signalling pathways and genetic mutations. Various genetically modified animal models have been developed to understand the genetic bases of craniosynostosis (Holmes, 2012).

Mouse is a good mammalian model to study the craniofacial system. With different shape, size and orientation, it has the same bones and sutures as of human skull (see Fig 1.3 - Rice, 2008). Our knowledge of mouse genetics and biology has made mouse a key animal model to understand the genetic causes of CS (Holmes, 2012). A variety of mutant mice have been developed to understand the genetic causes of different types of CS. A summary of some of these models is presented in the Chapter 2. These models provided an invaluable source of data to investigate the biomechanics of craniosynostosis.
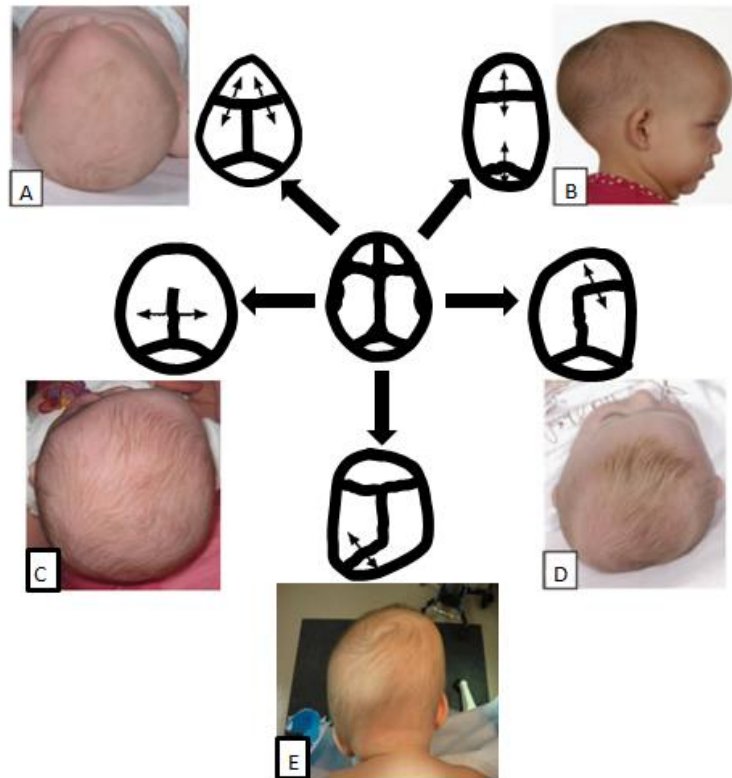
Fig. 1.2: Craniosynostosis: (A) metopic; (B) sagittal; (C) bicoronal; (D) unicoronal; (E) lambdoid premature suture fusion (from Johnson and Wilkie, 2011).
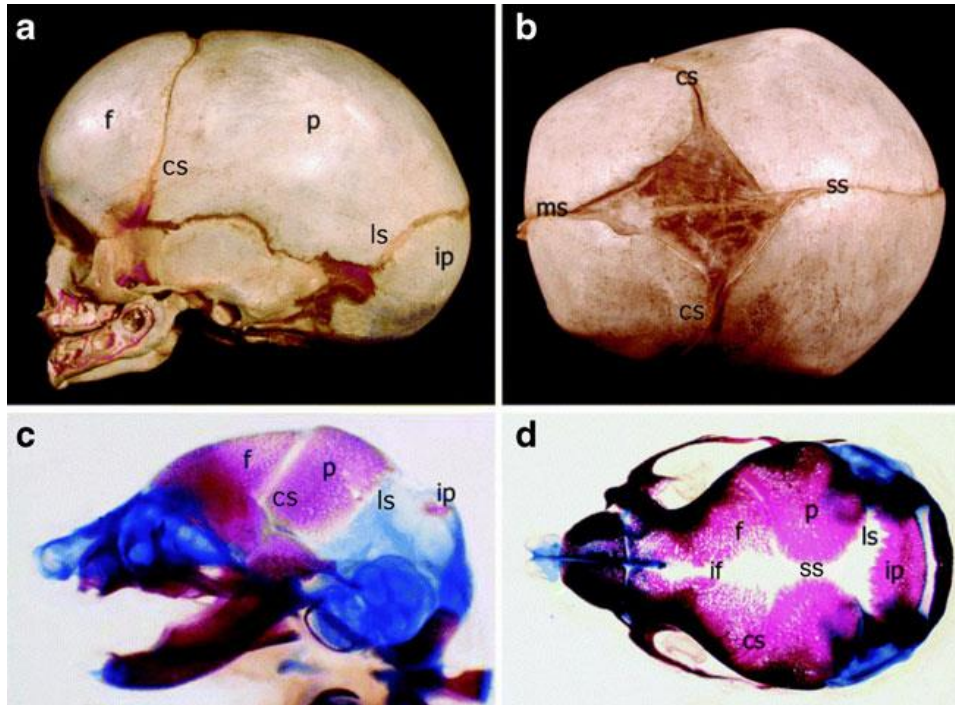
Fig. 1.3: The similarities between human and mouse skull. Lateral (a, c) and superior (b, d) views of a newborn human (a, b) and mouse at embryonic days (E) 17.5 (c) or E18.5 (d). The mouse skulls show the common organization of frontal (f), parietal (p), and interparietal (ip) bones and metopic (ms), interfrontal (if), sagittal (ss), coronal (cs), and lambdoid (ls) sutures. The mouse skulls are stained for bone (red) and cartilage (blue) from Morriss-Kay and Wilkie (2005).

1-2 Aims of the project

This project is part of a larger project investigating the biomechanics of the normal and craniosynostotic skull growth. Internal and external loads applied on the cranium, such as loads from various muscles, brain, or daily exposures to external impacts, trigger the growth factors. However, the contribution percentage of each one in not clearly known. It is also unclear how these loads interact with each other. For example, while the brain plays a major role in the dynamics of cranial growth at the early stages of life, the biomechanics of this relation has not been investigated before.

The overall aim of the project is to understand how the biomechanical forces, especially from the growing brain, interact with the soft tissue structures and individual bone plates, to shape the skull. This can enable us to investigate the biomechanical differences between different reconstruction approaches for craniosynostotic patients to optimise the treatment of this condition. The long term goal of the work is to provide advice to surgeons on when to operate and how to manage the condition from a biomechanical point of view, to ensure the best possible outcome for the child.

The specific aims of the current project were: (1) to characterise the skull growth in wild type (WT) and mutant type (MT- Crouzon) mice during the development; (2) to develop a computational approach based on the finite element (FE) method, to predict the calvarial growth in normal and craniosynostotic mice; (3) to develop an algorithm to simulate the bone formation at the cranial sutures. Validation of the computational models is crucial to build confidence in their outcome. Hence the results were compared to *ex vivo* data throughout the project. In brief:

1) The anatomical dimensions of the mouse calvaria and its sutures were obtained for WT and MT mice using the microCT imaging at postnatal days (P)3, 7 and 10,

2) A 3D FE model of a wild type mouse skull was developed based on microCT data at P3,

3) The developed FE model was used to predict the calvarial growth and bone formation at the cranial sutures at different ages from P3 to P10,

4) FE predictions were compared with the *ex vivo* data at P10

5) The same modelling approach was repeated to model the MT mouse calvarial growth.

1-3 Methodology

Fig. 1.4 shows an overview of the methodology used to address the aims and objectives of this research. MicroCT data of an *ex vivo* WT mouse skull at P3 was imported into an image processing software and it was segmented to develop a 3D meshed model. Intracranial volume (ICV) was modelled as one structure. This model was imported into a finite element analysis (FEA) program. Material properties were obtained from the literature for the calvarial bones, sutures, and the brain. Thermal expansion analogy was used to model the growth of the brain or here ICV changes from P3 to P10. Obtained results were validated using the *ex vivo* microCT data at P10, in terms of calvarial length, width and height. Finally, the bone formation at the sutures was simulated by changing the material properties of the sutures based on the mechanical strain they undergo as brain expands. Resultant suture dimensions were also compared versus the *ex vivo* measurements.
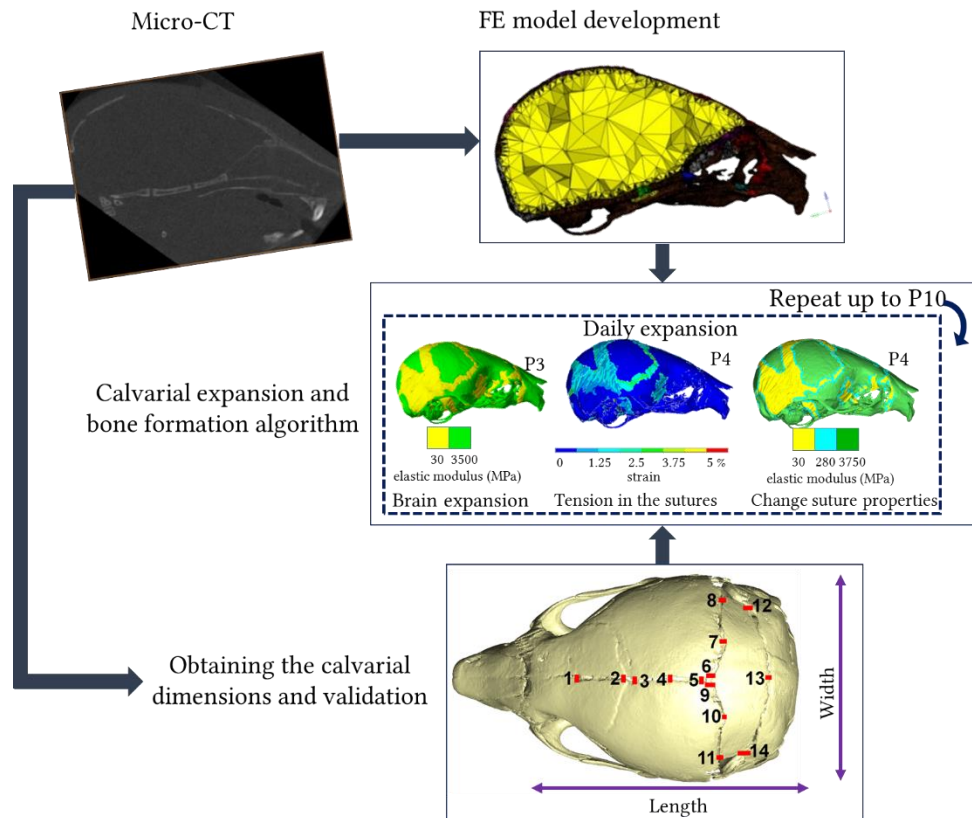
Fig. 1.4: Thesis methodology overview. MicroCT data is used to develop the FE model at P3, and also to obtain the calvarial dimensions that were used for validations. At the FEA stage, brain was expanded daily to the next age (P3 to P10) and based on the strain values, sutures were changed into bone. Results were validated by *ex vivo* values at P7 and P10.

1-4 Chapter organisation

The thesis organisation is as follows:

Chapter 2: provides a brief review of previous works related to various aspects of this project. These include e.g. basic anatomy of the mouse skull, various mouse models for CS, mechanical properties of the cranial bone, sutures and brain, finite element models of skulls in general, finite element models of skull growth and some of the existing bone remodelling theories.

Chapter3: describes the morphological study of the mouse skull during the development from P3 to P10, including the overall shape (length, width, and height) and cranial suture sizes. This data is used to validate the results in Chapter 4 and 5.

Chapter 4: describes the finite element models that were developed to predict the radial expansion of the skull from P3 to P10. Several sensitivity tests were performed that are summarised here. This chapter is divided to two sections describing the wild type mouse skull prediction and mutant type mouse skull predictions. The baseline model developed in this chapter was then used in Chapter 5. The results of Chapter 4 are compared to the average skulls obtained in the Chapter 3.

Chapter 5: describes the modelling approach developed to model the bone formation at the cranial sutures. Several sensitivity tests were performed based on the wild type model. The results for both the WT and MT mouse models were compared with the overall shapes and suture sizes obtained from the Chapter 3.

Chapter 6: summarises the main finding of this thesis.

Chapter 7: outlines the future work that can be carried out to expand the modelling approach presented here.

Chapter 2: Literature review

2-1 Introduction

This chapter reviews the key literature associated with different aspects of the present research. Considering the biological aspects of this study a brief overview of the animal models used to investigate craniosynostosis and craniofacial development is provided. Then key anatomical features of the mouse skull is described. This is followed by summarising the key literature that has quantified the mouse skull development. Then, some of the existing genetically modified mouse models of craniosynostosis is described with more details on the specific mouse model that is used in this study i.e. Crouzon *Fgfr2* $^{C342Y/+}$.

Considering the biomechanical aspects of this project, mechanical properties of the cranial bones and sutures, and the brain are studied. Then, previous studies of the skull development and its biomechanics are briefly reviewed. Then, a detailed review of the craniofacial studies that have investigated the cranial bone formation and suture ossification, with particular attention to those that have used finite element method is presented. Finally, some of the existing theories on tissue differentiation and bone formation are discussed in the last section.

2-2 Animal models of craniosynostosis

Genetic mutations that cause syndromic and nonsyndromic craniosynostosis have been investigated by molecular biologists for many years (Rice, 2003; Ishii *et al.*, 2015; Fish, 2016; Flaherty, Singh and Richtsmeier, 2016; Katsianou *et al.*, 2016; Lee, Stanier and Pauws, 2019). Several genetically modified animal models have been introduced to investigate and understand the genetic bases of premature suture fusion in craniosynostosis. These models are also used to study the growth pattern of the skull

and brain (Grova *et al.*, 2012; Holmes, 2012). The most commonly used type of mammals in experimental studies are rodents. Many studies have been performed using rats, mice, gerbils, guinea pigs, and hamsters (Simmons, 2008). In this section, some of the animal models used in craniofacial studies are introduced.

Animal studies can be categorised into two groups of large and small animals. Each group has some advantages and disadvantages, and based on the nature of that research and its aims, it could be decided which animal model would be best for that study. Animals such as mice, rat, and rabbits (small size animals) have the advantage of their maintenance being relatively low cost with rapid development over a short period of time. However, operating detailed surgeries on them is challenging. On the other hand, larger animals such as sheep and goats can provide even prenatal surgical studies, but the operation and husbandry costs are relatively high (Miller and Chinzei, 2002). Table 2.1 summarises some advantages and disadvantages of each group. Fig. 2.1 presents a schematic comparison of the cranial bones and sutures, and their orientation in human and several animal models. It can be seen how main calvarial bones and sutures are present in most of the models.

Table 2.1: Advantages and disadvantages of using small and large animals in studies (from Miller and Chinzei, 2002).

	Advantages	Disadvantages
Small size, short gestation	Large sample number; low cost; sophisticated biomolecular analysis	Late gestational manipulation; adult phenotype wound healing; limited clinical application
Large size, long-gestation	Longer postoperative intrauterine period; multiple and complex intrauterine procedures	Expensive husbandry; limited spontaneous Craniosynostosis
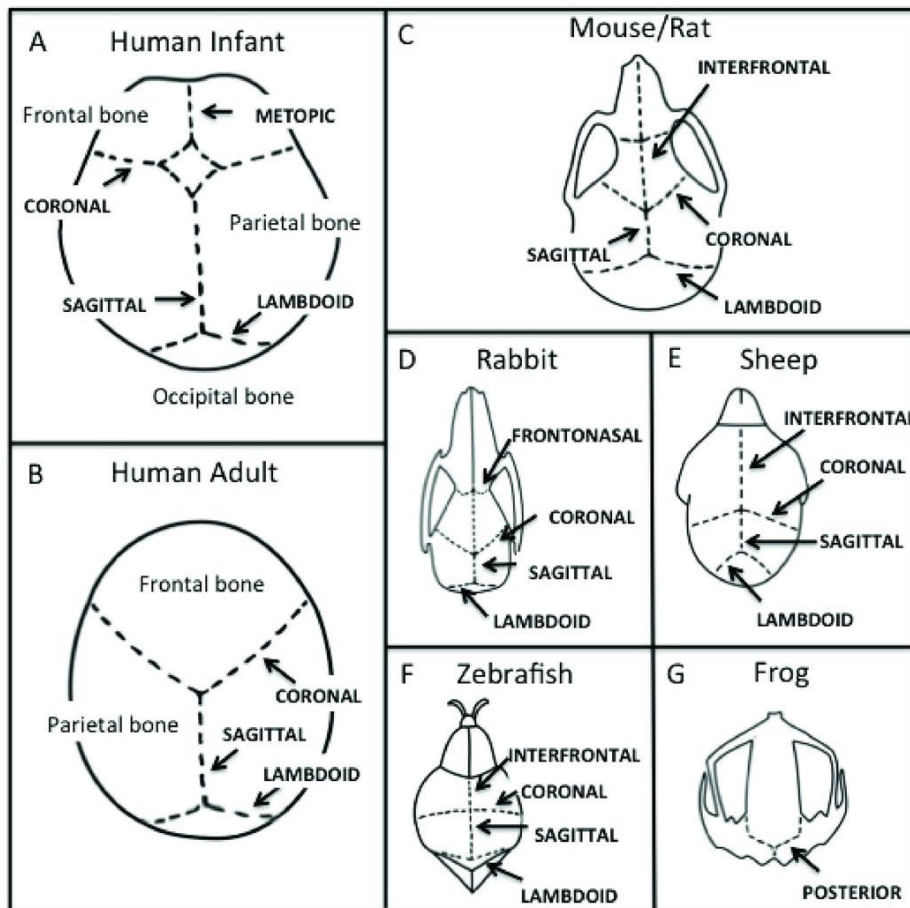
Fig. 2.1: Schematic cranial bones and sutures orientation in human and some other animal models. Human Infant (A), human adult (B), mouse/rat (C), rabbit (D), sheep (E), zebrafish (F), and frog (G). Note the similarities of cranial bones and sutures between human infant and adult, and different animals (from Grova *et al.*, 2012).

Animal studies of human diseases are usually performed on rodents and among rodents, the majority of the studies use mouse models. The key reason is the similarity between the human and mouse genome as well as the similarities in the craniofacial development and molecular pathways between the two. Further, mice are widely available, easy to be handled, have high reproductive rates. Also, historically, genetic modification and the production of gene 'knockout' animals was pioneered in the mouse (Simmons, 2008; Grova *et al.*, 2012).

Mouse skull, like all other vertebrates, is composed of several bony parts enclosing and protecting the brain, olfactory organ, inner and middle ears and also to some extent eyes, from impacts. It also supports feeding and breathing functions and forms the overall shape of the head (Hunt, 1924; Morriss-Kay and Wilkie, 2005). Fig. 2.2 illustrates how human skull is adapted for the large brain, while mouse skull shows

the importance of olfaction and tooth (Jerome and Hoch, 2012). In the next section, a brief overview of the anatomy of the wild type mouse (WT) cranium is described.
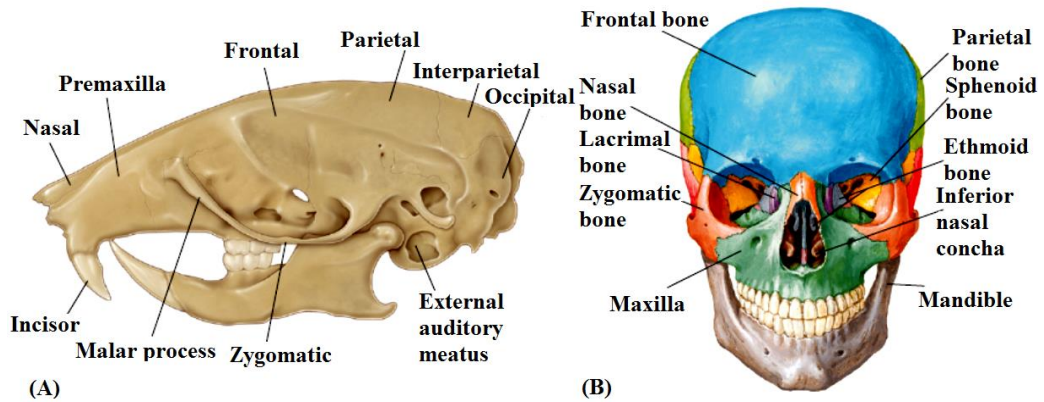
Fig. 2.2: (A) The mouse skull: designed for large olfaction and teeth. (B) The human skull: designed for large brain size (from Jerome and Hoch, 2012).

2-3 Wild type mouse anatomy

Mouse skulls can be divided into two parts, the calvaria, and the visceral skeleton[1], and the calvaria surrounding the brain. The visceral includes some bones of the face, lower and upper jaws, some of the bones in the ear region and on the lateral surface of the head, and small bones of the middle ear that transmit sound (Hunt, 1924).

Mouse has a long and narrow skull. Its width decreases gradually from the posterior to the anterior part of the skull. The long axis of the mouse body and the extreme posterior surface of the skull are almost perpendicular. This surface joins the dorsal surface at a nearly right angle. The region that these two surfaces unify is the lambdoidal ridge. It has a semi-circular form. There is a second ridge extending ventrally to the region of the ear and anterior to the lambdoidal ridge. This ridge joins the temporal line at right angles dorsally. Then it has a lateral and forward extension on the dorsal surface of the cranium to the orbit disappearing while it turns medially (Hunt, 1924).

The ventral part of the mouse skull is modified to form the upper and lower jaws which are used in grasping, killing, and chewing the food (Hunt, 1924). Fig. 2.3 and

---

[1] The skeleton that forms part of an organ such as ear.

2.4 show diagrams of the adult mouse cranium in the lateral, ventral, and dorsal views. These figures highlight main cranial bones and sutures such as the frontal, parietal, interparietal (this bone is unique to mouse/rodent and does not exist in the human skull), occipital, and temporal bones, coronal, sagittal, interparietal, and lambdoid sutures. Fig. 2.5 illustrates the dorsal view of the cranium base. It is highlighting the isolated bones, mainly to illuminate the position of the presphenoid bone. This bone is not visible from outside of the skull (Carretero *et al.*, 2017). The next section summarises some of the key studies that have investigated the skull and brain development in WT mouse.

Occipital — Interparietal — Parietal — Temporal — Frontal
Nasal — Basisphenoid — Pterygoid — Zygomatic — Maxilla
Incisive — Lacrimal — Palatine — Vomeronasal
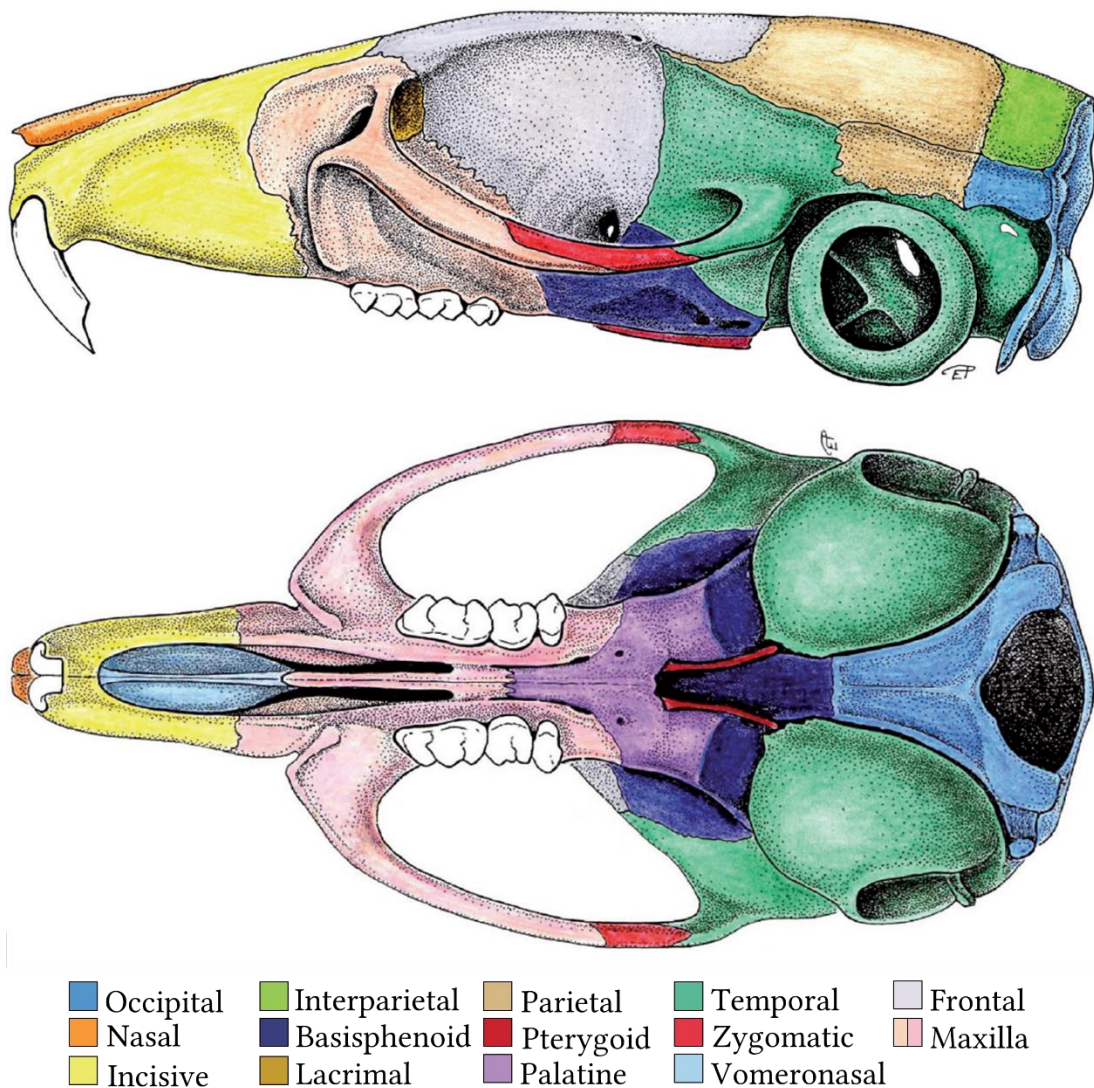
Fig. 2.3: Mouse cranium diagrams highlighting calvarial bones, lateral and ventral views (from Cook, 1965, and Carretero *et al.*, 2017).
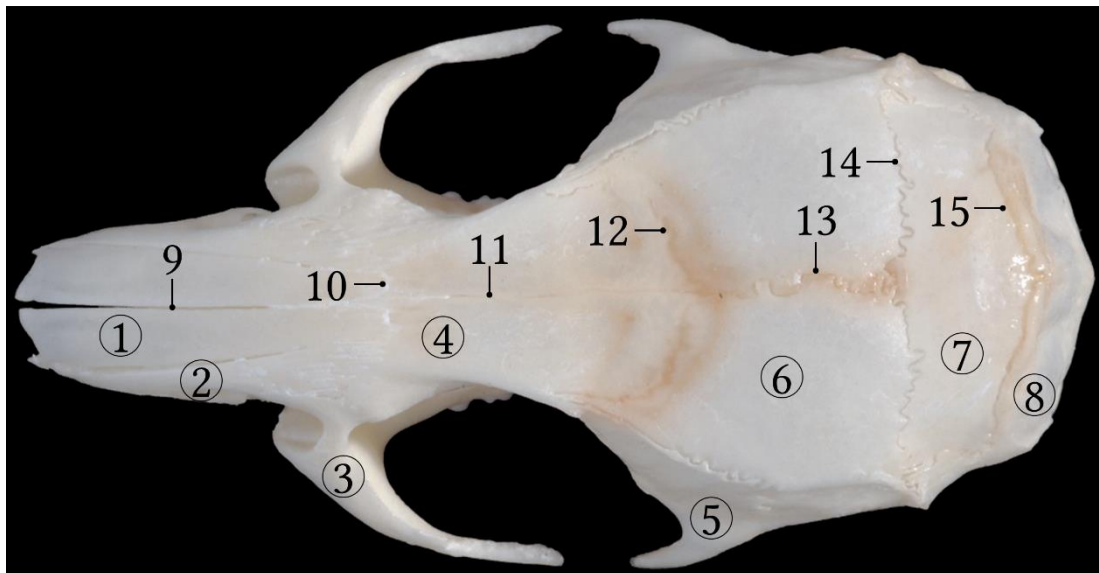
Fig. 2.4: Dorsal view of mouse cranium highlighting calvarial bones and sutures, a schematic diagram and an *ex vivo* skull. 1: Nasal bone; 2: Incisive bone; 3: Maxilla; 4: Frontal bone; 5: Temporal bone; 6: Parietal bone; 7: Interparietal bone; 8: Occipital bone; 9: Internasal suture; 10: Frontonasal suture; 11: Frontal suture (anterior and posterior); 12: Coronal suture; 13: Sagittal suture; 14: Interparietal suture; 15: Lambdoid suture (from Cook, 1965, and Carretero *et al.*, 2017)
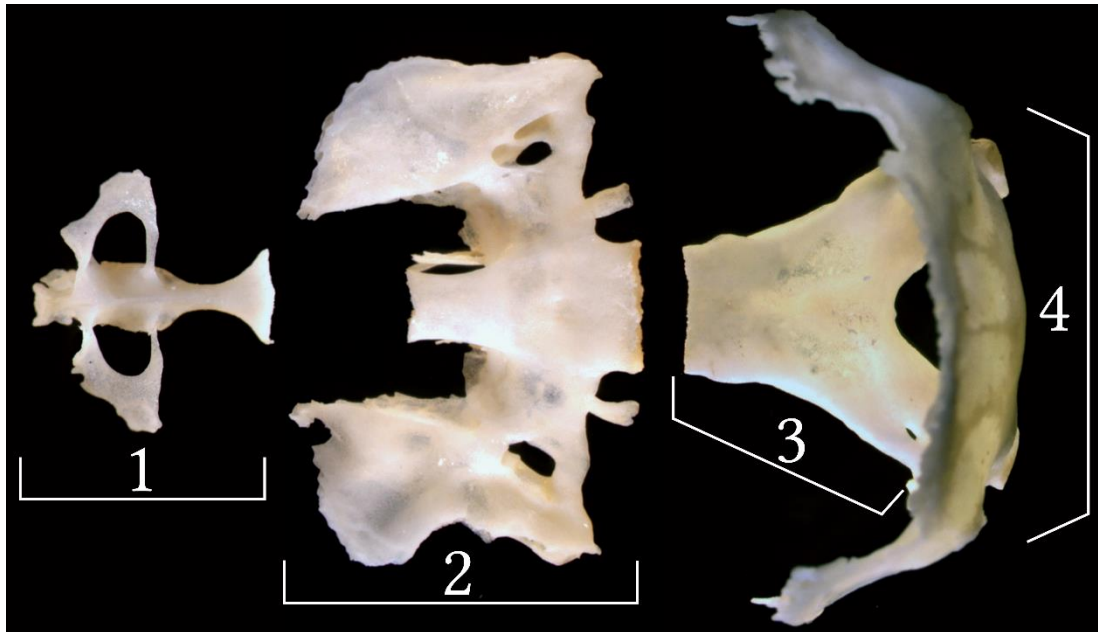
Fig. 2.5: Dorsal view of base of the cranium, 1: Presphenoid bone (this bone is not visible from outside of the skull); 2: Basisphenoid bone; 3: Basioccipital bone; 4: Occipital bone (from Carretero *et al.*, 2017).

2-4 Wild type mouse skull and brain growth patterns

Cyclic loads induced by blood vessels pulsation, locomotion, feeding, or sudden forces like sudden impacts, and quasi static loads due to tensile strains caused by intracranial pressure are sensed by the cranial sutures. These sutures are complexes with two ontogenetic bone fronts: the suture mesenchyme, and underlying dura mater. When the mesenchyme is at rest, it consists of collagen fibres and undifferentiated cells. Being under load, the mesenchymal cells differentiate into various cell types (osteoblasts, osteoclasts, osteocytes), and the collagen fibres adopt different orientations. The cranium expands as bone forms at the sutures through intramembranous or endochondral ossifications (Katsianou *et al.* 2016).

Various anatomical landmarks and key morphological features such as intracranial volume have been widely used to characterise and quantify the mouse skull and brain development (Zhang *et al.*, 2005; Perlyn, DeLeon, *et al.*, 2006; Kawakami and Yamamura, 2008; Aggarwal *et al.*, 2009; Baloch *et al.*, 2009; Laurita *et al.*, 2011; Jin, Shahbazi, *et al.*, 2014; Weisbecker *et al.*, 2019). In this section some of the key studies that have studied the growth pattern of mouse cranium and brain will be reviewed.

Nakata (1981) investigated the relationship between the development of the cranial bones and the masticatory muscles. Various diagrams of development pattern were derived by superimposing the mean values of coordinate measurements at various postnatal days. Cephalometric analysis was performed using various landmark measurements. The results indicated different growth patterns for individual muscles, and showed that muscle development was not essentially in parallel with the changes in bones. However, different loading patterns from the masticatory muscles can affect the craniofacial morphology (Engström, Kiliaridis and Thilander, 1986).

Fig. 2.6 shows the position of the landmarks that were used to perform the measurements (top), and the bone growth pattern from 11 days to 135 days. The profile-diagrams were registered by point **Or** (the lowest margin of anterior opening of infraorbital fissure) and **Or-S** plane (**S** is the lowest point of the interesphenoidal synchondrosis). Fig. 2.7, highlights that the mouse skull reaches its maximum size at about thirty days after birth, while muscles' growth plateaus at about postnatal day 70.

Aggarwal *et al.* (2009) developed an atlas of mouse skull development, combining magnetic resonance imaging (MRI) and micro-computed tomography (microCT) of developing mice. They developed three-dimensional atlases of mouse brains and skulls at five postnatal ages (P7, P14, P21, P28, and P63) and two adult ages (P140 and P160). They co-registered these two datasets using a landmark-based approach. Landmarks were also used to measure cranial dimensions. Fig. 2.8 and 2.9, highlight the growth of the soft and hard tissues occur hand in hand during the development. The gradual growth of the mouse skull was from a length of about 12mm, width of about 7.5mm, and height of about 6mm at the age of P7, to about 17mm, 9mm and 7.3mm respectively, at the age of P140. The landmarks shown in Fig. 2.8 were used to investigate the skull growth.

In a more recent study, Vora *et al.* (2016) measured various calvarial dimensions including length, width and height of a male mouse using landmarks as presented in the Fig. 2.10. Their results showed that the skull width and height increase up to P21 and then decreases slightly, and finally plateaued after P28. However, the skull length increased up to P112. Their results also showed that the bones in the skull

base (Presphenoid, Basisphenoid, and Basioccipital bones) had the lowest development rate, and did not change much in size after P7. They also showed that in the cranial region, almost 80% of the growth took place up to P14. The results indicated a different growth pattern for the facial region with most of it completing by P21. As a result, the studies which are aiming to analyse the calvarial development patterns, may focus on the earlier stages of growth (up to P14).
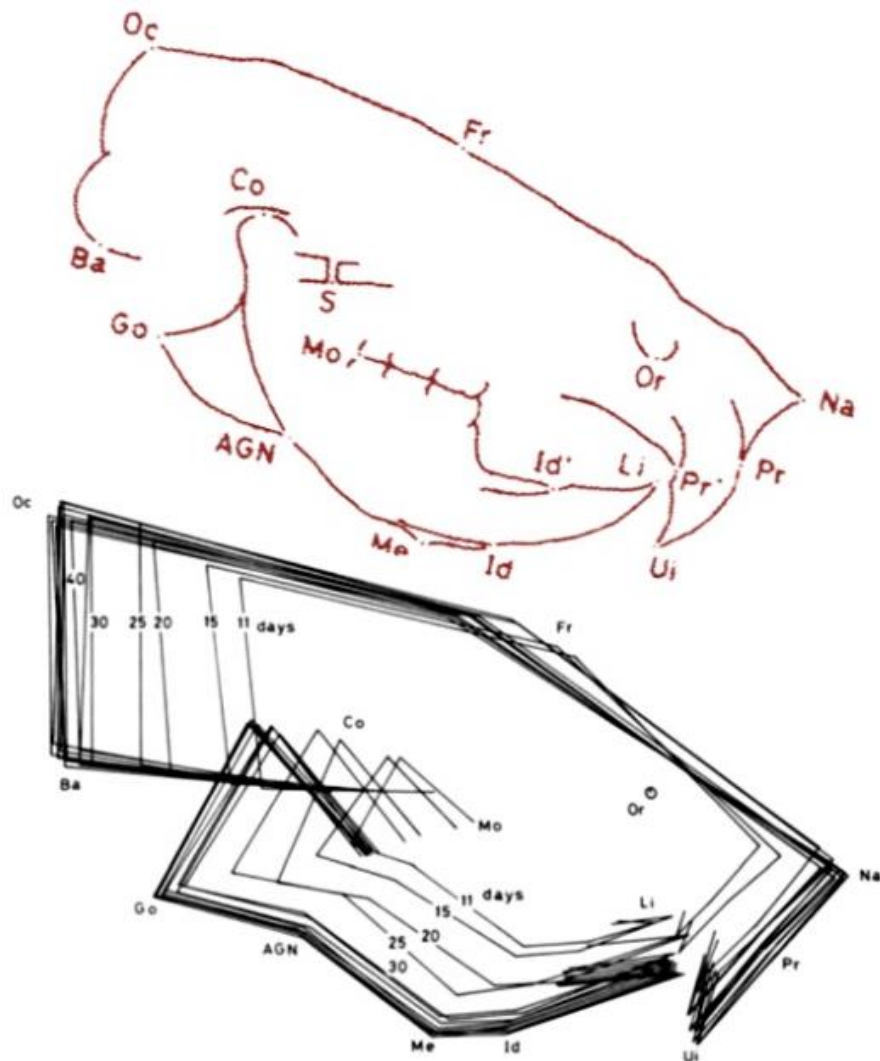
Fig. 2.6: Profile diagrams drawn by superimposing the mean values of coordinate measurements at various postnatal days. A cephalometric analysis was performed using the landmark measurements. **AGN**: ante gonial notch, the lowest point intersected between the angular process and the mandibular body; **Ba**: basion; **Co**: top of mandibular condyle; **Fr**: center of frontal sinus homologue; **Go:** gonion, the most posterior point of the bony contour of gonial angle; **Id:** infradentale, tip of lower labial alveolar crest on the midsagittal plane; **Id':** tip of lower lingual alveolar crest on the midsagittal plane; **Li:** tip of lower incisor tooth; **Me:** menton, top of mental protuberance; **Mo:** intersecting point between distal surfaces of upper and lower third molars; **Na:** tip of nasal bone; **Oc:** tip of external occipital crest; **Or:** the lowest margin of anterior opening of infraorbital fissure; **Pr:** prosthion, tip of upper labial alveolar crest on the midsagittal plane; **Pr':** tip of upper palatal alveolar crest on the midsagittal plane; **S:** the lowest point of the intersphenoidal synchondrosis; **Ui:** tip of upper incisor tooth (from Nakata, 1981).
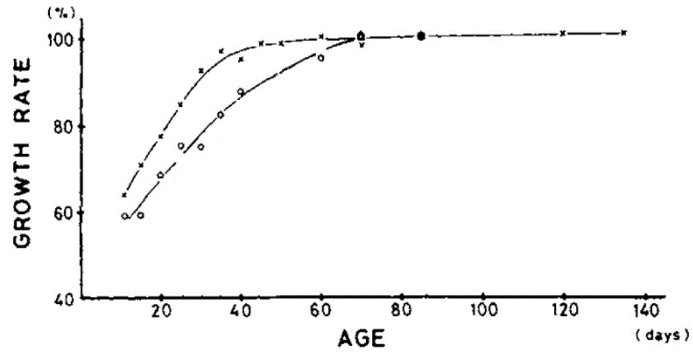
Fig. 2.7: Growth diagrams for the length of Me-Go, and masseter muscle fibres on various postnatal days. x and o represent bone and muscle fibres data points respectively (from Nakata, 1981).

Fig. 2.8: Overall growth pattern of mouse skull with landmarks used to define the cranial dimensions shown on P140 (from Aggarwal *et al.*, 2009).
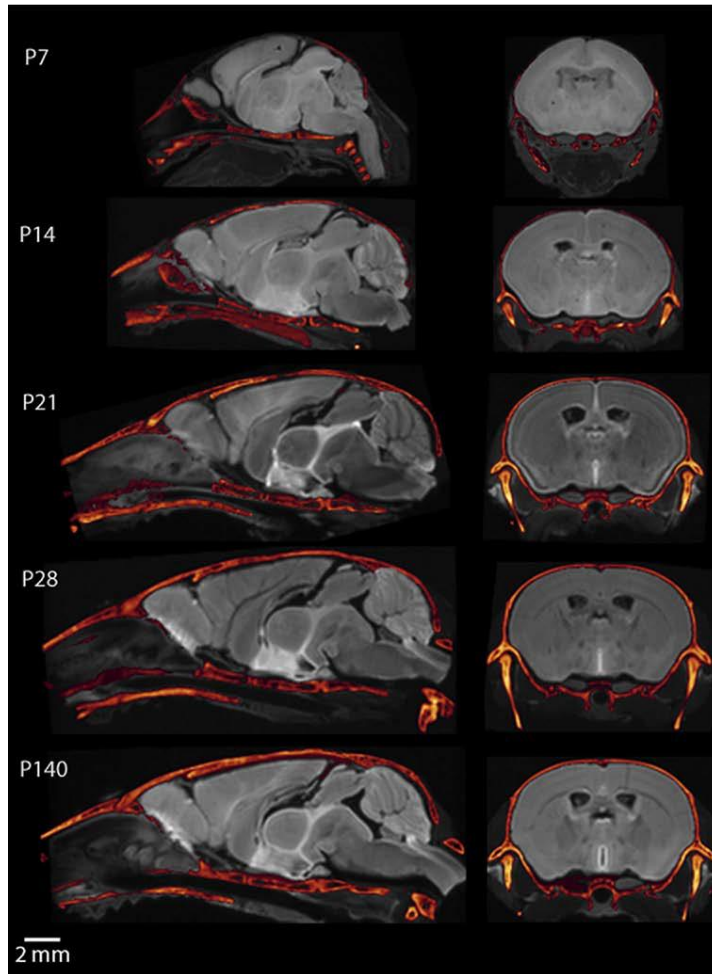
Fig. 2.9: Co-registered mouse brain CT and MRI sections from P7 to adult. Average diffusion-weighted MR images of the brain (grey-scale) are overlaid on CT skull images (in metallic colour), from Aggarwal *et al.*, (2009).
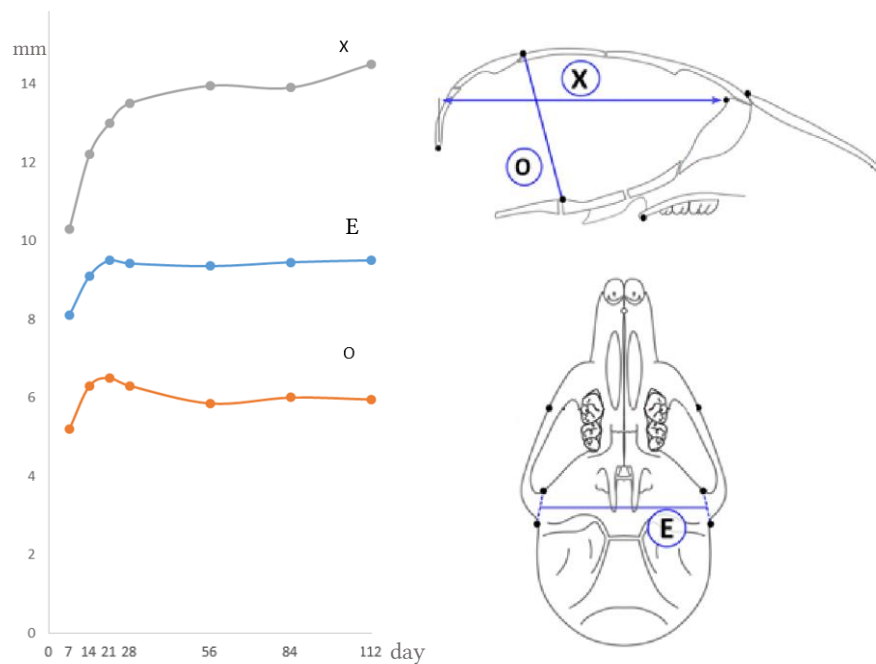
Fig. 2.10: Skull length (X), width (E) and height (O) changes from P7 to P122 (from Vora *et al.*, 2016).

In order to have a good understanding of the craniosynostotic cranial development, it is also essential to understand the pattern of cranial suture closure. Bradley *et al.* (1996) studied the pattern of sutures closure in different cranial sutures in mice. Their results showed that the anterior frontal, coronal, sagittal, interparietal, and lambdoid sutures did not fully fuse up to P50. While the midpoint of the posterior frontal suture started to close at about P35 day and completely fused at P40 in mice.

At P25, the anterior portion of the posterior frontal suture started to close and was fully closed by P29. Closure started at P31 at the midpoint of the posterior frontal suture, and was fully closed at P37. The posterior portion of the posterior frontal suture stared to close at P39 and was fully closed by at P45 (Bradley *et al.*, 1996).

It is also critical to understand the rate of bone formation in the cranium during the development. It's widely believed that the mechanical loads that the calvarial sutures are exposed to trigger the suture ossification. One of the main forces experienced by the cranial sutures during the postnatal skull development arises from the expanding brain (Sun *et al.*, 2004). Several authors have characterised the relation between the strain levels and the bone deposition rate in various models.

Henderson *et al.* (2004), measured the bone deposition rates and strain levels in human and rat skulls. Their results highlighted an average sutural bone deposition rate of about 0.1 mm/day at the first month after birth for human with an almost exponential reduction pattern up to four years of age. Strain levels experienced by the sutures were estimated to be in the range of 20 to 400 microstrains in the first month. For the rat cranial sutures, the bone deposition rate was measured to be about 0.12 mm/day from birth to 10 days of age.

The other important developmental parameter to investigate is the pattern of brain growth. Early studies of the brain development were based on histological sectioning and were mostly focused on only one region of the brain at a time during (Jacobs, 2001). With later advancements of imaging techniques, researchers such as Badea *et al.* (2007), Aggarwal *et al.* (2009), and Baloch *et al.* (2009), investigated detailed and region specific morphological changes during the brain development in mouse.

Variations in the brain's regional densities can have a direct effect on its mechanical properties. It is essential to develop a method to measure the brain's spatial density

quantitatively. Huang *et al.* (2008) investigated the brain growth in rats. They used landmarks to map different cortical surfaces of the brain (Fig. 2.11). They investigated the growth in different regions of the brain at five postnatal ages of P0, P3, P7, P11, and P19. Fractional anisotropies were mapped for the cortical surface.
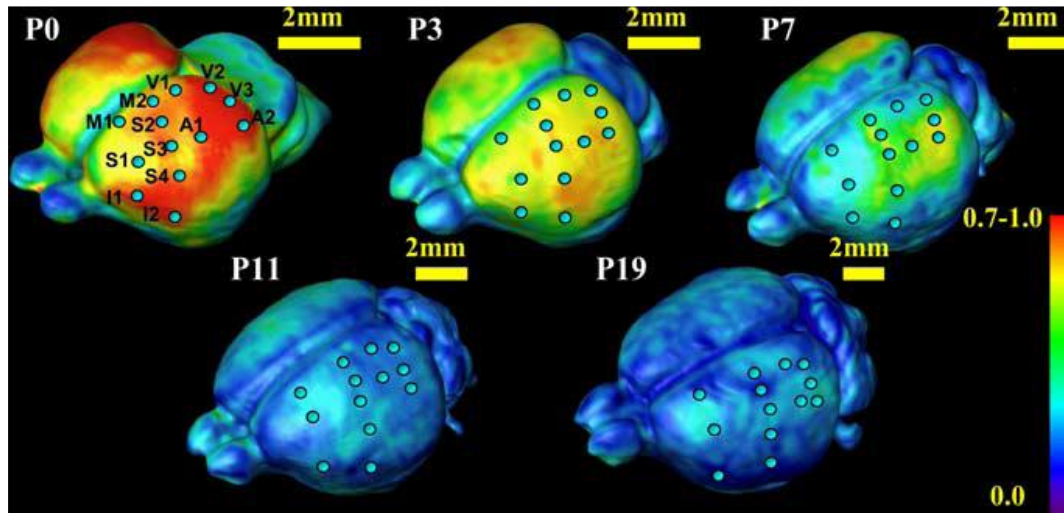
Fig. 2.11: Mapping of the cortical surfaces of rat brains from P0 to P19. The bar shows the colour representations of Fractional Anisotropy during the brain development. A, I, M, S and V represent auditory, insula, motor, somatosensory and visual cortices respectively (from Huang *et al.*, 2008).

Another important characteristic of the brain during its development is its volume. Chuang *et al.* (2011), investigated the changes in the brain volume of the mouse during its development. Anatomical variation in the brain was characterised without segmentation. Instead, using the anatomical information combined with the imaging data, they generated measurements of the anatomical variation for each pixel. Fig. 2.12-A highlights that brain volume grows rapidly in the first twenty days after birth and there seems to be minimal growth in its volume after P20. For instance, brain volume increased from about 200mm^3 at the age of P3 to about 400mm^3 at the age of P10.

In a more recent study, Hammelrath *et al.* (2016), investigated the regional and total volume changes in the mouse brain by combining *in vivo* MRI and histology. Their study started from an age that it is known to be when mouse brain development plateaus (three weeks), and included next three stages of eight, twelve, and twenty four weeks. Their results showed an increase of about 10% from 345 mm^3 at 3 weeks to 380 mm^3 at 8 weeks. The brain volume was almost the same for the other ages.

Regional volume changes were reported to be very similar same in all investigated ages (Fig. 2.12-B). In the next section, some of the genetically modified, craniosynostotic mouse models are reviewed.
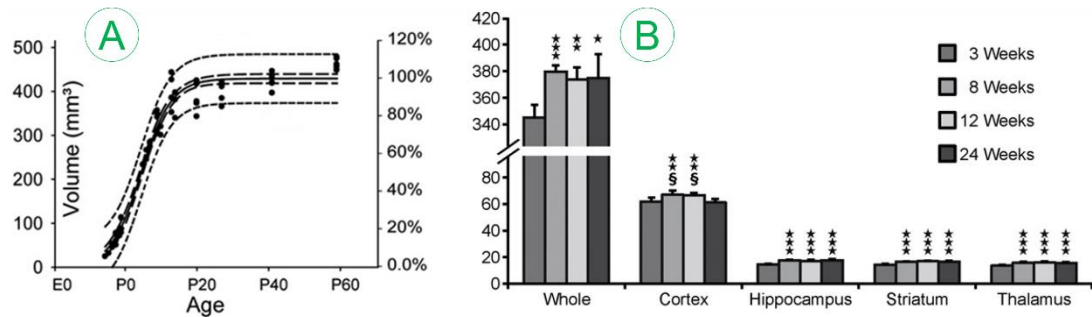
Fig. 2.12: A: Total brain volume changes (left vertical axis) and its percentage of adult volume (right vertical axis) according to the estimated values, reported by Chuang *et al.* (2011). B: Total and regional brain volume changes from three to twenty four weeks, reported by Hammelrath *et al.* (2016).

2-5 Genetically modified craniosynostotic mouse models

During the past decades, there has been a significant progress in understanding the genetic causes of craniosynostosis. In several forms of craniosynostosis fibroblast growth factor (FGF) signalling pathway seems to play a crucial role (Kimonis *et al.*, 2007). This section provides a brief review on the previous studies on craniosynostotic mouse models with a particular focus on the Crouzon $Fgfr2^{C342Y/+}$ mouse.

The main advantage of using mice to study craniosynostosis is because of the ability to study transgenic animals with mutations analogous to those observed in syndromic patients. The identification of some of the genes associated with various forms of craniosynostosis, such as FGFR-1, FGFR-2, FGFR-3, TWIST1, EFNB1, and MSX2, has sparked the development of numerous transgenic mice with similar gain- or loss-of-function mutations mimicking each condition. These mice have offered a wealth of information on the etiopathogenesis of syndromic craniosynostosis. Importantly, they also serve as a potential platform to study future genetic strategies aimed at preventing premature pathologic suture fusion and all the secondary associated dysmorphologies (Grova *et al.*, 2012).

Cellular proliferation and differentiation need FGF signalling. While FGFR2c gene is one of the main regulatory factors of the craniofacial development, premature differentiation and abnormal proliferation of sutural mesenchyme seem to be the main factors leading to various CS types such as Crouzon (Lee *et al.,* 2018; Doro *et al.,* 2019).

Some of the active genes in the development of the cranial sutures in mice are presented in Fig. 2.13. Some genes such as Fgf2 are active in all three regions of the dura, sutural mesenchyme, and osteogenic front of bone. However, some genes may be active only in one region, such as Twist, which is active only in the sutural mesenchyme.

Mouse models can also be modified to fit a specific type of CS. For instance, Fgfr1$^{P220R/+}$, Fgfr2 $^{P253R/+}$, Fgfr2 $^{C342Y/+}$, and Fgf3/4 mouse models are showing CS types of Pfeiffer, Apert, Crouzon, and Syndromic multiple craniosynostoses. Table 2.2 provides an overview of the key features of the human and mouse Craniosynostosis syndromes and their affected genes. Crouzon type syndromic craniosynostosis which affects coronal, sagittal, and lambdoid sutures in mice, and coronal sutures in human, can be caused by mutations in the FGFR2 gene (Wilkie, 2005; Holmes, 2012).

Mutations in FGF3 and FGF4 can cause syndromic multiple craniosynostosis. FREM1 may affect only posterior frontal suture and cause trigonocephaly, and FGFR3 can cause the Muenke syndrome by affecting the coronal suture (Holmes, 2012). Fig. 2.14 shows two mutants, Crouzon and Muenke, mouse models and how their sutures are affected. Crouzon syndrome is one of the most common syndromes, where patients are characterised by coronal craniosynostosis (Peskett *et al.,* 2017). This mouse model has been studied throughout this project due to its similarities with the human Crouzon patients and being a well establish mouse model of craniosynostosis.
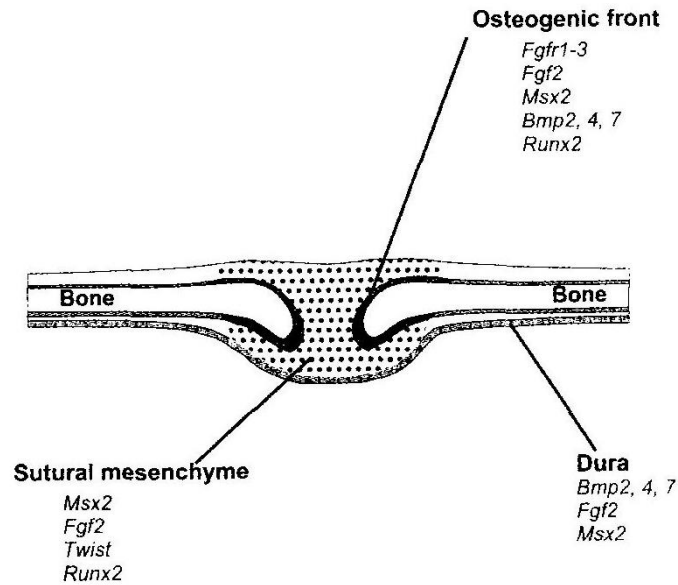
Fig. 2.13: Schematic diagram showing some of the active genes in mouse skull sutures development (from Rice, 2003).

Table 2.2: Mouse models of defined human syndromic and nonsyndromic Craniosynostosis (from Holmes, 2012).

Mouse mutant	Calvarial sutures affected	Human syndrome or condition	Affected human gene
Fgfr1 $^{P220R/+}$	Coronal, interfrontal, sagittal	Pfeiffer	*FGFR1*
Fgfr2IIIc $^{+/\Delta}$	Coronal	Apert	*FGFR2*
Fgfr2 $^{S252W/+}$	Coronal, sagittal, lambdoid	Apert	*FGFR2*
Fgfr2 $^{P253R/+}$	Coronal	Apert	*FGFR2*
Fgfr2 $^{C342Y/+}$	Coronal, lambdoid, sagittal	Crouzon	*FGFR2*
Fgfr2 $^{W290R/+}$	Coronal, sagittal	Crouzon	*FGFR2*
Fgfr2 $^{Y394C/+}$	Coronal	Beare-Stevensin	*FGFR2*
Fgfr2 $^{P244R/+}$	Coronal	Muenke	*FGFR3*
Twist1 $^{+/-}$	Coronal, occipito-interparietal	Saethre-Chotzen	*TWIST1*
Twist1 $^{S192P/+}$ (Charlie Chaplin; CC)	Sagittal, coronal, lambdoid	Isolated sagittal synostosis	*TWIST1*
TIMP1-Msx2 ^{P7H}, CMVMsx2 ^{P7H}, CMV-Msx2	Sagittal, coronal, lambdoid	Boston-type CS	*MSX2*
Frem1^{bat}; Frem1^{Qbrick}	Posterior frontal	Trigonocephaly	*FREM1*
Mesp1Cre; Jagged1$^{cko/cko}$; Jagged1 $^{+/-}$	(Enhances Twist$^{+/-}$ phenotype)	Alagille	*JAGGED1*
EphA4 $^{-/-}$	Coronal	Nonsyndromic coronal CS	*EFNA4*
Xt-J (Extra toes ^{J})	Lambdoid	Greig cephalopolysyndactyly	*GLI3c*
Fgf3/4 (Bulgy-eye; Bey)	Pan-synostosis	Syndromic multiple craniosynostoses	*FGF3/FGF4*
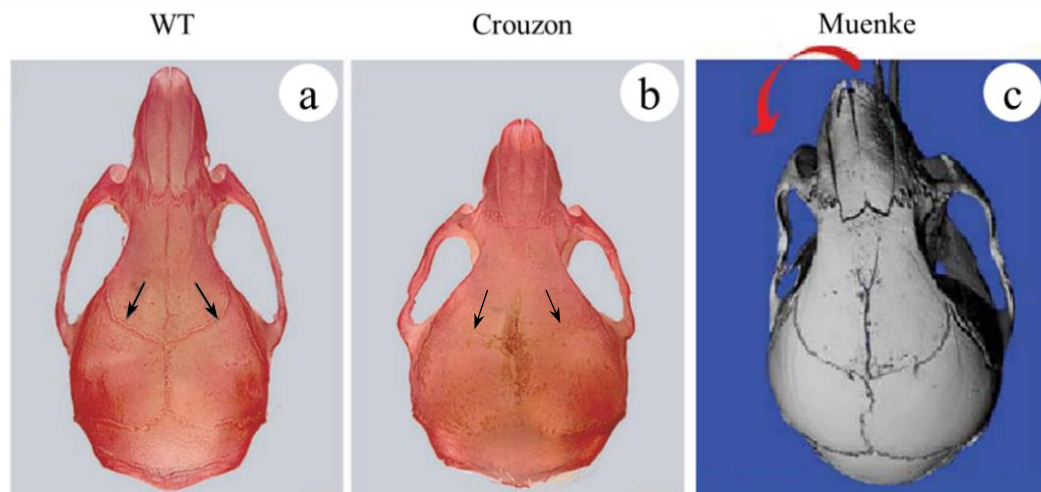
Fig. 2.14: Syndromic Craniosynostotic mouse models. **a:** wild type, **b:** Crouzon (*Fgfr2* $^{C342Y/+}$) and **c:** Muenke syndrome (*Fgfr3^{P244R}*) mouse models. Coronal sutures (arrow) and distorted facial bones caused by facial sutural fusion are shown in the μ-CT (from Eswarakumar *et al.*, 2006; Laurita *et al.*, 2011; Holmes, 2012).

One of the main characteristics of the Crouzon syndrome is premature fusion of the coronal sutures in human. This leads to abnormal skull shape development observed as brachiocephaly and flattened forehead, restricting the brain growth, and increasing the intracranial pressure (Perlyn, Morriss-Kay, *et al.*, 2006; Flaherty, Singh and Richtsmeier, 2016). Similarly, Crouzon mouse typically shows early fusion of the coronal, frontal and lambdoid sutures which lead to a shorter and wider cranium with extended height compared to the wild type mouse (Perlyn, Morriss-Kay, *et al.*, 2006; Liu *et al.*, 2013; Martínez-Abadías *et al.*, 2013).

A closer look at the Crouzon mouse

Fig. 2.15 provides a more quantitative comparison of the wild type and Crouzon type mice skull dimensions. Fig. 2.16 shows normal and Crouzon infant skulls and compares their skull morphologies with the Crouzon mouse model. It can be seen how sutures are patent or fused in different skulls and how normal and Crouzon skulls are different. Observing the infant skull, it can be seen how premature fusion of the coronal sutures affect the morphology of the skull. The skull on the right (B) is shorter with extended height (and width), because the fusion restricts the skull

development towards its length, and since the sagittal suture is still patent, the pressure from the growing brain will make the skull to become wider.

Liu *et al.*, (2013) carried out a detailed morphological analysis on the Crouzon mouse and compared it to the WT mouse. For example, they reported that the sagittal suture and spheno-occipital synchondrosis were not fused significantly at 4 weeks, while the lambdoid and coronal sutures, and intersphenoidal synchondrosis were fused to a significant extent in the Crouzon mice compared to wild type littermates. The zygomatic, palatomaxillary, and the nasofrontal suture were also fused to a significant extent. Various observations that they reported were also observed in Chapter 3 and were used as a validation point for the computational models that are described in Chapter 4 and 5. The next section, provides an overview on the mechanical properties of cranial sutures, calvarial bones, and the brain.
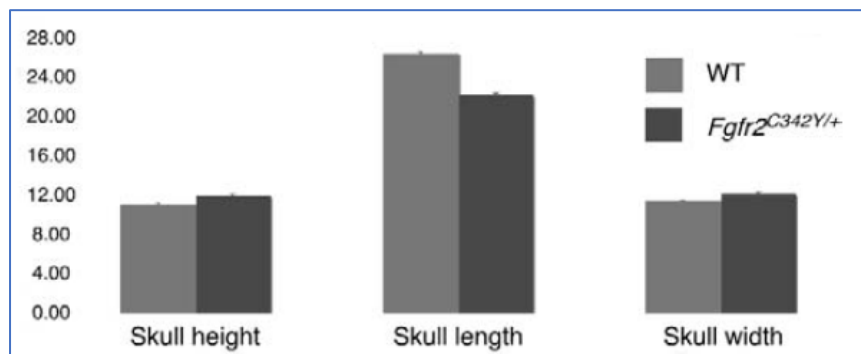
Fig. 2.15: Cranial measurements of 6-week-old wild-type and *Fgfr2$^{C342Y/+}$* mutant type mice indicating an increase in skull width and height while the length is decreased (from Perlyn *et al.*, 2006).

.
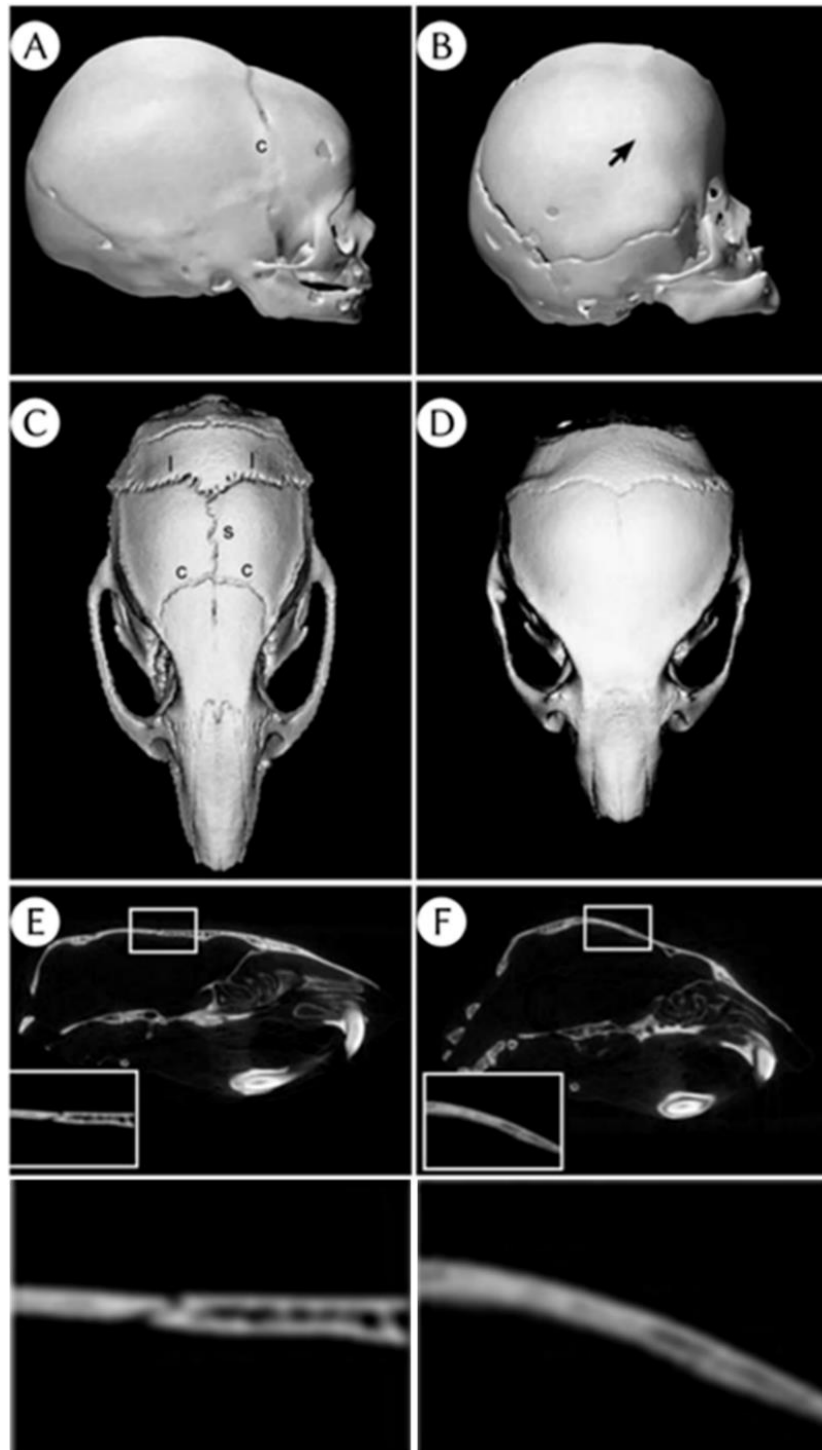
Fig. 2.16: 3D CT scan of a normal infant (A) and an infant with Crouzon syndrome (B) showing unfused and fused coronal sutures that has led to ridging and abnormal head shape (brachycephaly). 3D CT scan of a 6-week-old wild-type (C) and a 6-week-old $Fgfr2^{C342Y/+}$ mouse (D), illustrating unfused and fused coronal and sagittal sutures. The sagittal section of 2D CT shows patency of the coronal suture in WT mouse (E). Similar view of $Fgfr2^{C342Y/+}$ mouse illustrates fusion of coronal suture (F), (from Perlyn, Morriss-Kay, *et al.,* 2006).

2-6 Mechanical properties of the cranial sutures, bones, and brain

Material properties of the cranial sutures, calvarial bones, and brain are among the key input parameters for the finite element models (described in Chapter 4 and 5). Several methods have been used to estimate these properties experimentally. These methods include three-point bending, tensile or compression tests, as well as indentation. The main advantage of the latter is that it does not require large samples and specimen smaller than 0.1mm in size can be used. This method can also be used to estimate the material properties at different regions of the specimen, while other methods provide the overall properties of the tissue under investigation. Following sections summarise previous studies on the material properties of cranial sutures, calvarial bones, and brain.

2-6-1: Cranial sutures

Mechanical properties of the sutures have been measured in various animals and across different sutures. Some of the key studies that have investigated the mechanical properties of the cranial sutures are summarised in Table 2.3. One of the recent studies (and most relevant to this project) that has characterised the mechanical properties of sutures in a mouse model is the study of Moazen *et al.* (2015). They carried out nanoindentation on various sutures across the wild type mouse skull. They reported an average elastic modulus of 32±32 MPa for the sagittal, coronal, and posterior frontal sutures at P10 and P20 (for wild type mouse). This data is used in Chapter 4 to model calvarial sutures in wild type mouse.

Haigh variability exist in the range of elastic modulus measured for the sutures. For example, Jaslow (1990) reported a value of 120 to 240 MPa for the elastic modulus of frontal-parietal suture in goat. Henderson *et al.* (2005), estimated the elastic modulus of the sagittal suture in rats in the range of 4.7 to 13 MPa. This variability could be due to the high viscoelasticity nature of the sutures or the fact that their size, morphology and level of mineralisation within them can vary considerably (Moazen *et al.*, 2015; Rahmoun *et al.*, 2014; Jaslow, 1990).

Although most of the reported values are in the ranges of 10 to 100 MPa, Rahmoun *et al.*, 2014 reported relatively high values of 2038.39 ± 923.61 MPa for the coronal suture. This high value could be related to the very high age of their specimen (88 years) and the way they have taken the sample. Among these, values reported by Moazen *et al.*, (2015) are closely relevant to this project, due to being on mouse and an age which is early postnatal days.

2-6-2: Cranial bones

Similar to the suture studies, calvarial bones properties have been measured in a large number of species. Table 2.4 summarises the studies that have investigated the mechanical properties of the cranial bones. Study of McElhaney *et al.* (1970), is one of the early studies that characterised the mechanical properties of calvarial bones. They reported an elastic modulus of 2.4 ± 1.4 GPa for human at the age of 56 to 73 years using compression testing.

Reported values for the elastic moduli by Jaslow (1990), Gefen *et al.* (2003), and Maloul *et al.* (2013) were relatively low compared to other works (259 ± 43 MPa – goat – 2 to 4 years; 4 MPa to 11 MPa – rat – 13 to 43 days; and 243 ± 63 MPa – human – 81 ± 15 years respectively). The main reason for this is the position of the taken samples which included sutures as well. Other low values are mainly due to lower age of studied samples (Margulies *et al.* (2000) – pig – 2 to 3 days; Coats *et al.*, (2006) – human – less than one month; and, Li *et al.* (2011) – human – six months).

Moazen *et al.* (2015) investigated the material properties of WT and MT mice at P10 to P20. They reported elastic modulus of the calvarial bones to be in the range of 4 to 7 GPa depending on the anatomical position and age. They reported that the elastic modulus of the frontal bones differs significantly between the wild type and mutant type models. However, parietal bones showed similar properties between the two models. There is a large variability across the studies in terms of mechanical properties of calvarial bones. A range of parameters can explain this variability. Perhaps two key factors could be age and sample preparation protocols (Wolfinbarger *et al.*, 1994).

2-6-3: Brain

Brain is a viscoelastic material with nonlinear properties. Many studies have focused on characterising the brain mechanical properties. Given that in this study brain geometry was used to drive the morphology of the skull during the development, detail modelling of the brain as a viscoelastic material was not the focus of this study. Here, the brain was considered as an elastic material. A few studies have characterised the elastic properties of the brain and are summarised in Table 2.5. The reported values were found to be in a relatively wide range, from as low as 60 Pa reported by Koser *et al.* (2018) for mouse with an age range of 4 to 7 weeks, to as high as 16 MPa for human at 6 months of age (Coats and Margulies, 2006).

Comparing the material properties of white matter and grey matter shows that grey matter is significantly stiffer than the white matter in mouse and rat (Christ *et al.*, 2010; Koser *et al.*, 2018), while this seems to be inversed for pigs and cows (Kaster *et al.*, 2011; Budday *et al.*, 2015). Another interesting point to note shown by Gefen *et al.* (2003), is that the material properties of the brain decreases as it ages. Generally, it can be said that there are several parameters that can affect the material properties of the brain. For instance, brain tissue stiffens as the strain increases, or it is stiffer in compression than in tension (Miller and Chinzei, 2002; Budday *et al.*, 2017). Similarly, it is stiffer during loading than unloading. Brain tissue also stiffens with increasing the strain rate. Stiffness of the brain is region-dependant and interestingly it can recover from preconditioning (Budday *et al.*, 2019).

In summary, there seems to be a large variability in the mechanical properties of the cranial sutures, bones, and brain. This is perhaps the case for all biological tissues. Testing protocols, tissue preparation, the age of the specimen, the region that the sample is taken from, and the testing parameters all could be various factors that can impact the experimental measurement of mechanical properties of such tissues (Hrapko *et al.*, 2008; Budday *et al.*, 2019). This highlights the importance and value of sensitivity tests when using computational methods to investigate the biomechanics of skull development. In the next section some of the developmental and biomechanical studies of the skull are briefly reviewed.

Table 2.3: Some of the studies that have worked om the material properties of calvarial suture, including elastic modulus (E), Poisson's ratio (ν), studied animal and the age, and their testing method.

Author	Suture	E (MPa)	ν	Animal	Age	Testing Method
Jaslow,1990	internasal	10 to 35	-	Goat	2-4years	three-point bending
Jaslow,1990	frontoparietal	120 to 240	-	Goat	2-4years	three-point bending
Margulies *et al.*, 2000	NA*	194.2 ± 42.5	-	Pig	2-3 days	three-point bending
McLaughlin *et al.*, 2000	sagittal, coronal and posterior frontal	13, 14 and 2.3	-	Rat	7 days	tensile test
Henderson *et al.*, 2005	sagittal	4.72 to 13.0	0.28	Rat	20-60 days	three-point bending
Coats *et al.*, 2006	coronal	8	-	Human	<1 month	three-point bending
Grau *et al.*, 2006	synostosed metopic	0.5 ± 0.1	-	Human	9.1±2.8 months	nano-indentation
Grau *et al.*, 2006	synostosed sagittal	0.7 ± 0.2	-	Human	9.1±2.8 months	nano-indentation
Popowics *et al.*, 2007	nasofrontal	68±32 (C); 43±16 (T)	-	Pig	3-6 weeks	Compression (C) and Tensile (T)
Popowics *et al.*, 2007	nasofrontal	3.4±1.4 (C); 0.9±0.5 (T)	-	Pig	5-6 months	Compression (C) and Tensile (T)
Li *et al.*, 2011	NA*	8	0.49	Human	6 months	FE + optimisation techniques
Maloul *et al.*, 2013	bone containing sagittal and coronal	213±93	-	Human	81±15 years	three-point bending
Chen *et al.*, 2014	coronal	354.83 ± 44.86	-	Human	1.5±0.5 years	three-point bending
Chen *et al.*, 2014	sagittal	408.12 ± 59.08	-	Human	1.5±0.5 years	three-point bending
Rahmoun *et al.*, 2014	coronal	2038.39 ± 923.61	-	Human	88 years	three-point bending
Moazen *et al.*, 2015	sagittal, coronal and posterior frontal	32 ± 32	-	Mouse	10-20 days	Nano-indentation

*NA: not available

Table 2.4: Some of the studies that have worked om the material properties of calvarial bones, including elastic modulus (E), Poisson's ratio (v), studied animal and the age, and their testing method.

Author	Bone (strain/load rate)	E (GPa)	v	Animal	Age	Method
McElhaney *et al.,* 1970	NA*	2.4 ± 1.4	0.19±0.8	Human	56-73 years	compression
McPherson *et al.,* 1980	parietal and frontal	1.3 ± 0.6 to 4.2 ± 0.7; 7.4± 0.8	-	Human	25 to 40 gestation weeks; 6 years	three-point bending
Jaslow,1990	NA*	0.259 ± 0.043	-	Goat	2-4years	three-point bending
Claessens *et al.,* 1997	NA*	6.5	0.2	Human	infant	FE + transient response to impact
Margulies *et al.,* 2000	NA*	0.615 ± 0.096	-	Pig	2-3 days	three-point bending
Margulies *et al.,* 2000	left parietal (2.54 and 2540 10^{-3}m min^{-1})	2.1 and 2.7	-	Human	6 months	three-point bending
Margulies *et al.,* 2000	right parietal (2.54 and 2540 10^{-3}m min^{-1})	2.2 and 3.6	-	Human	6 months	three-point bending
Gefen *et al.,* 2003	braincase (skull/suture composite)	0.004 to 0.011	0.4	Rat	13 to 43 days	indentation and FE
Coats *et al.,* 2006	parietal	0.260	-	Human	<1 month	three-point bending
Motherway *et al.,* 2009	R Parietal (0.5 to 2.5 m s^{-1})	10.33 ± 7.04 to 12.80 ± 5.50	-	Human	81±11 years	three-point bending
Motherway *et al.,* 2009	L Parietal (0.5 to 2.5 m s^{-1})	5.70 ± 1.73 to 18.12 ± 14.36	-	Human	81±11 years	three-point bending
Motherway *et al.,* 2009	Frontal (0.5 to 2.5 m s^{-1})	4.35 ± 1.71 to 16.34 ± 10.18	-	Human	81±11 years	three-point bending
Mao *et al.,* 2010	NA* (0.02 to 200 mm s^{-1})	5.9 ± 0.8 to 9.5 ± 1.9	0.22	Rat	43 days	three-point bending
Li *et al.,* 2011	NA*	0.171	0.22	Human	6 months	FE + optimisation techniques
Maloul *et al.,* 2013	NA*	0.243 ± 0.063	-	Human	81±15 years	three-point bending
Chen *et al.,* 2014	frontal	1.266 ± 0.121	-	Human	1.5±0.5 years	three-point bending
Chen *et al.,* 2014	parietal	1.103 ± 0.113	-	Human	1.5±0.5 years	three-point bending
Rahmoun *et al.,* 2014	frontal	3.3 ± 2.0	-	Human	88 years	three-point bending
Rahmoun *et al.,* 2014	left and right parietal	4.5 ± 4.8 and 3.7 ± 2.9	-	Human	88 years	three-point bending
Rahmoun *et al.,* 2014	left and right temporal	6.0 ± 2.2 and 5.2 ± 3.0	-	Human	88 years	three-point bending
Moazen *et al.,* 2015	frontal	5.32 ± 0.68 to 7.14 ± 0.79	-	Mouse	10 to 20 days	nano-indentation
Moazen *et al.,* 2015	parietal	4.33 ± 0.18 to 6.3 ± 0.47	-	Mouse	10 to 20 days	nano-indentation
Li *et al.,* 2019	Frontal/parietal (10^{-3}s^{-1} to 10s^{-1})	0.4 to 0.8	-	Pig	8 weeks	tensile
Li *et al.,* 2019	Occipital (10^{-3}s^{-1} to 10s^{-1})	0.1 to 0.2	-	Pig	8 weeks	tensile

*NA: not available

Table 2.5: Some of the studies that have worked om the material properties of brain tissue, including elastic modulus (E), Poisson's ratio (ν), studied animal and the age, and their testing method.

Author	E	ν	Animal	Age	Method
McElhaney *et al.*, 1970	4.7 kPa	-	Human	56-73 years	compression
Claessens *et al.*, 1997	1 MPa	0.48	Human	infant	FE validated by transient response to impact
Miller *et al.*, 2000	3.240 kPa	0.499	Pig	100 days	*In-vivo* indentation
Gefen *et al.*, 2003	2 to 1.3 kPa	0.5	rat	13 to 43 days	indentation
Coats *et al.*, 2006	16.2 MPa	-	Human	6 months	three-point bending
Christ *et al.*, 2010	340.5 ± 39.8 Pa (Grey matter)	-	Rat	2 to 3 months	scanning force microscopy
Christ *et al.*, 2010	220.5 ± 55.5 Pa (White matter)	-	Rat	3 to 3 months	scanning force microscopy
Kaster *et al.*, 2011	1.2 ± 0.2 kPa (Grey matter)	-	Pig	-	indentation
Kaster *et al.*, 2011	1.8 ± 0.2kPa (White matter)	-	Pig	-	indentation
Budday *et al.*, 2015	1.9 ± 0.6 kPa (White matter)	-	Cow	16 months	indentation
Budday *et al.*, 2015	1.4 ± 0.3 kPa (Grey matter)	-	Cow	16 months	indentation
Bouchonville *et al.*, 2016	10.2 to 15 kPa	0.45	Human	NA*	atomic force microscopy
Koser *et al.* 2018	159 ± 26 Pa (Grey matter)	-	Mouse	4-7 weeks	immunohistochemistry
Koser *et al.* 2018	60 ± 7 Pa (White matter)	-	Mouse	4-7 weeks	immunohistochemistry

2-7 Biomechanical studies of the skull

There is a relatively large body of literature on biomechanical studies of the skulls. These studies can be categorised into three groups based on the question that they have been asking with either: evolutionary, trauma or developmental focus (Fig. 2.17). In this section an overview of a few of the studies related to the first two categories are provided. Section 2.8 of this thesis is focused on a more detailed review of the studies with developmental focus.
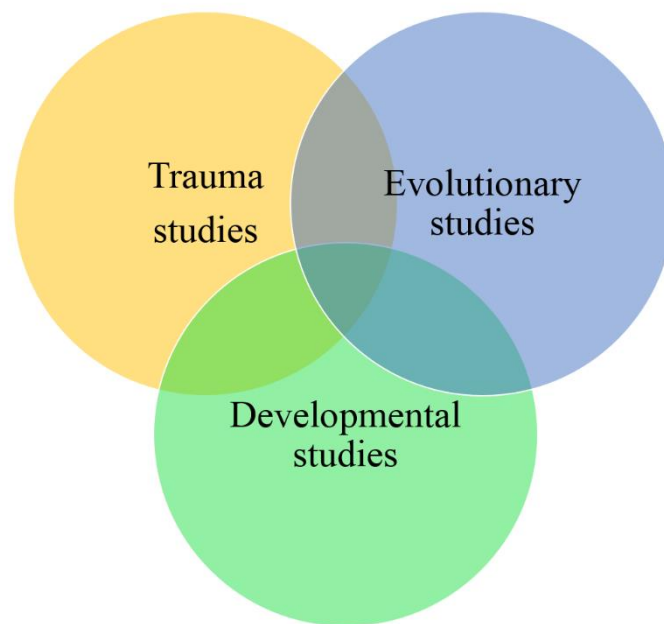
Fig. 2.17: Three main categories of studies investigating the biomechanics of the skull.

2-7-1 Evolution

Evolution of the cranium and how various biomechanical parameters might have affected its evolution has been investigated by a number of authors on a wide range of groups e.g. reptiles, birds and mammals (see e.g. Rayfield, 2007; Sakamoto, 2010; Brusatte *et al.*, 2012; Button, Barrett *et al.*, 2016). For example, Moazen *et al.* (2008, 2009) and Curtis *et al.*, (2011, 2013) investigated the biomechanics of lizard skulls. They investigated the role of biomechanical forces in morphological changes during the evolution of lizard (Moazen *et al.*, 2009; Moazen, Costantini and Bruner, 2013).

Wang *et al.* (2012), investigated the role of cranial sutures in the evolution of the craniofacial system in macaques.

Ballell *et al.* (2019), investigated the form and function of the skull in some crocodiles from Mesozoic era (the thalattosuchian Pelagosaurus and Gavialis). They digitally reconstructed the musculoskeletal system of the skull, and used the finite element modelling. They showed that there was a difference in their arrangements of the jaw muscle and biomechanical behaviour.

Rayfield (2007), and Bright (2014), reviewed the studies that had investigated the evolution of vertebrate morphology and applications of FE models in paleontological studies. They concluded that the FEA has great potential in investigating the vertebrate function, morphology, and evolution in both extant and extinct animals. Also, a detail characterisation of the material properties of various tissues within the models as well as detail understanding of the loading applied to the models can build more confidence in the outcome of FE studies.

2-7-2 Trauma

Head injuries can occur in a great variety of accidents from daily life occasions to professional sports. Fernandes and Sousa (2015), reviewed studies that had investigated impact biomechanics and head injuries in different sports such as motorsports, cycling, skiing, horse riding, mountaineering and most contact sports such as football, ice and field hockey, soccer, and lacrosse. The outcome of head impacts in these sports can be very severe. Many of them are associated with neurological injuries, affecting the central nervous system, with the possibilities of worst-case scenarios of permanent disability or even death.

Magnitude of the loads that can cause skull fractures, depend on the shape of the impactor and the thickness of the skull where the impact occurs (Fernandes and Sousa, 2015). Skull may fracture e.g. at the temporal area, if the pressure exceeds 4 MPa and the area of impacted is less than 5 cm^2 (Hume and Mills, 1995). Table 2.5 summarises some of the existing values in the literature for the forces that can lead to fracture at different parts of human skull during impact injuries. Occipital bone

can withstand highest loads, while temporal region, with a fracture load of 2 kN, reported by Schneider and Nahum (1972), is perhaps the weakest part of the skull.

Finite element method has been used extensively to investigate and predict the behaviour and response of the head under impact conditions. These models can be validated by relating their results to the medical investigations on autopsies of corpses involved in real accidents (Kang *et al.*, 1997). With the huge development of computational powers in recent years, more accurate models have been developed. For instance, Tuchtan *et al.* (2015) developed their model to investigate the force transmission to the skull during mandibular impacts. They validated their model based on the previous data available from cadaveric tests by Schneider and Nahum (1972) and Viano *et al.* (2005). Their model included different parts of the cranium such as brain, scalp, compact and spongy bone, maxilla, and mandible. Fig. 2.18 shows a more detailed view of their finite element model.

Dixit and Liu (2017) reviewed recent developments of finite element models for head injury simulations. They categorised the traumatic brain injuries based on their occurrence, location, and severity. Their study indicated that linear elastic models had been used in a few of the earlier studies, while the recent ones use viscoelastic properties for the brain as is in nature. Also, many of the earlier researches had not modelled the cerebrospinal fluid (CSF) as a fluid, while recent studies such as Wu *et al.* (2017), considered it as a fluid in their simulations.

In summary, it can be said that finite element method has a great potential in investigating the biomechanics of cranial development. The next section will provide a detailed review of different computational models of cranial development, and calvarial bone formation.

Table 2.5: Peak force for fracture at different regions of the skull.

Impact area	Force (kN)	Reference	Av
Frontal	4	(Schneider and Nahum, 1972)	6.53
	4.2	(Nahum *et al.*, 1968)	
	4.45	(Yoganandan *et al.*, 1995)	
	4.7	(Allsop *et al.*, 1988)	
	6.2	(Advani *et al.*, 1975)	
	15.6	(Voo *et al.*, 1994)	
Temporal	2	(Schneider and Nahum, 1972)	4.18
	3.9	(Yoganandan *et al.*, 1995)	
	3.6	(Nahum *et al.*, 1968)	
	5.2	(Allsop, Perl and Warner, 1991)	
	6.2	(Voo *et al.*, 1994)	
Occipital	11.8	(Yoganandan *et al.*, 1995)	12.15
	12.5	(Advani *et al.*, 1982)	
Parietal	3.5	(Hume and Mills, 1995)	3.5
Vertex	3.5	(Yoganandan *et al.*, 1995)	3.5
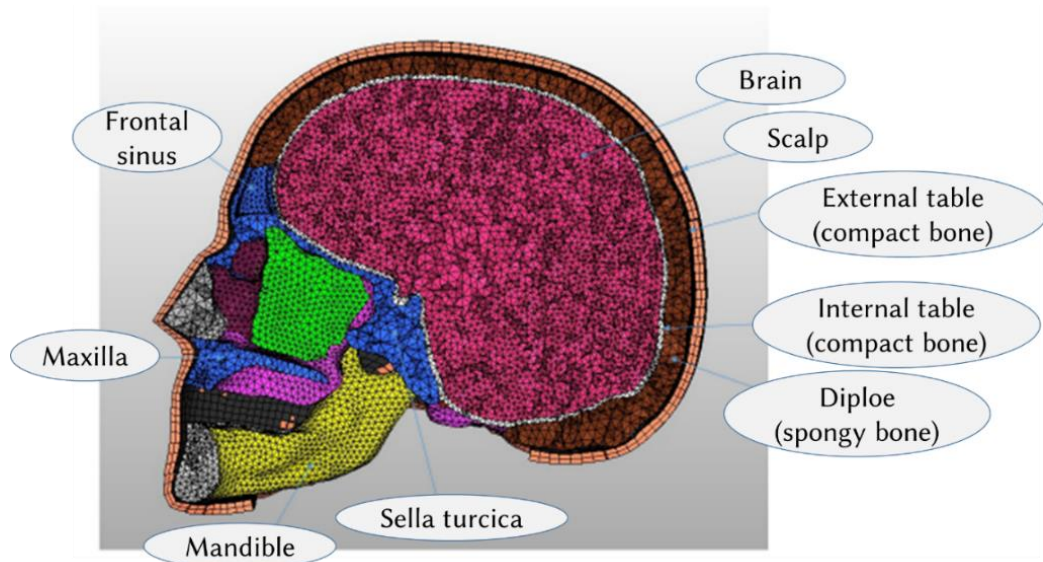
Fig. 2.18: 3D head model (sagittal section) developed by Tuchtan *et al.* (2015).

2-8 Modelling of skull growth and bone formation at the sutures

Modelling the bone formation has been investigated widely to understand the biomechanics of fracture fixation and fracture healing (for example see: Byrne, 2009; Fernández *et al.,* 2017; García-Aznar *et al.,* 2007; Garijo *et al.,* 2014; Kim *et al.*, 2010; Cheong *et al.*, 2018). Few studies have taken a closer look at the modelling of the calvarial growth and bone formation at the cranial sutures. These can be categorised into two main groups. First, the ones that have investigated the cranial sutures and how they are ossified regardless of the calvarial expansion and bone formation. Second, those studies that have investigated the pattern of the calvarial growth. These studies generally use an initial geometrical domain in which bone formation centres are considered to develop the final shape of the skull. They may be divided to two sub-categories, studies using finite element method, and those investigating the growth using other mathematical methods. The following sections provide an overview of the studies in each of the aforementioned groups, with more focus on the studies that have used finite element method.

2-8-1: Modelling ossification patterns in the cranial sutures

Eleven studies were found that had investigated specifically the biomechanics of the cranial sutures. They either modelled the pattern of suture formations subject to different loadings or investigated the possible correlations between different patterns of sutures and various biomechanical parameters such as their overall stiffness or stress and strain distribution patterns.

Hartwig (1991), Miura *et al.* (2009) and Yoshimura *et al.* (2016) used different mathematical modelling methods to study the overall pattern of cranial sutures. Miura *et al.*'s model, generated the interdigitated structure based on human and mouse skull data. They also incorporated the molecules involved in the developmental process, based on localization and function. Also, tissue differentiation state (u) and substrate concentration (v) were defined, to describe the situation. They formulated a two species reaction–diffusion model, and numerically

tested the behaviour of the model. Later, Yoshimura *et al.* (2016) expanded the same model to model more complicated pattern. However, the model was still only 2D.
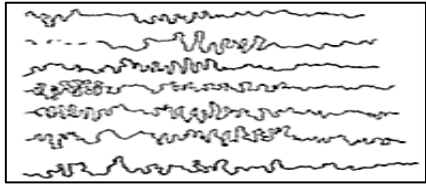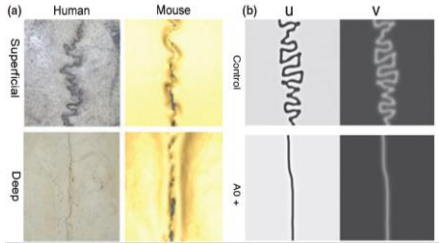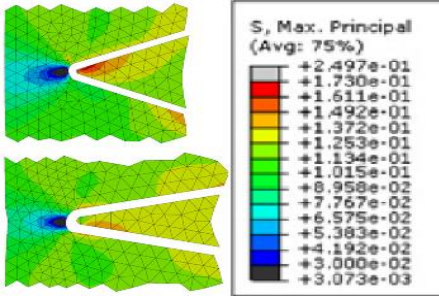
 Khonsari *et al.* (2013) developed a mathematical model and used finite element method to predict the pattern of suture closure during the development. Miroshnichenko *et al.* (2018) developed a model to investigate the effect of different tissue orientations and morphologies of layers for sutures, considering different mechanical properties.
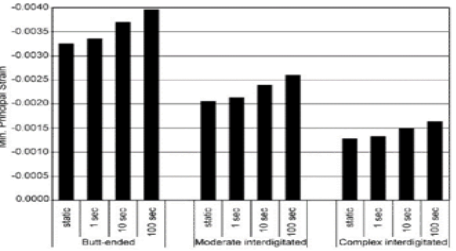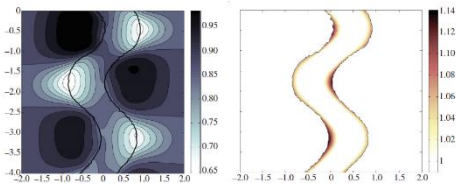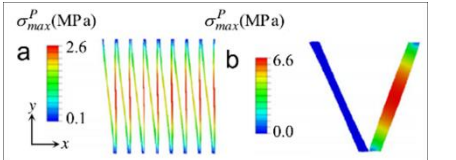
Other studies investigated the effect of different sutural shapes and material properties, show that they can affect the resultant stress and strain patterns within the sutures. For instance, Jasinoski *et al.* (2010 & 2012), investigated the effect of interdigitation index and mechanical properties (elastic vs. viscoelastic). Their results highlighted the significant role of suture morphology and anisotropy on sutural mechanics. Their results showed a correlation between the strain energy and interdigitation index. Although when the interdigitation index was increased, high stresses at the tips of the interdigitations, were shifted to the limbs of the suture. In their latter study, they investigated the effect of viscoelasticity of suture tissue and they suggested that it does not have a significant effect on the skull behaviour during masticatory loading. However, this may be different when investigating the early stages of cranial development (as in this project).
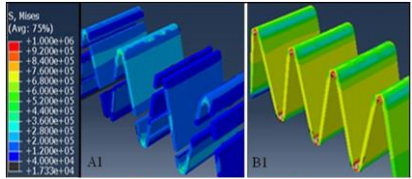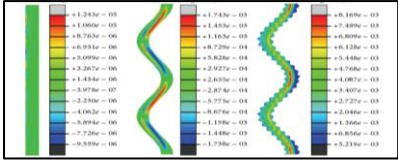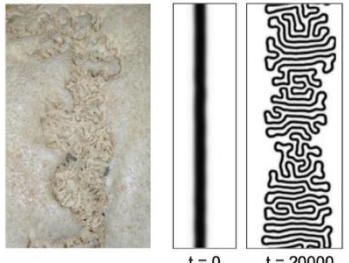
 Li *et al.* (2013), Maloul *et al.* (2014), Zhang *et al.* (2015), and Liu *et al.* (2017), studied different morphological aspects of sutures and how they affect the overall pattern of stress and strain distribution. They all used hypothetical geometries and only Maloul *et al.*'s model was 3D. Liu *et al.* used two different fibre orientations considering different levels of irregularity. Although they had used irregular patterns in their study (all other works had considered regular patterns of interdigitations).
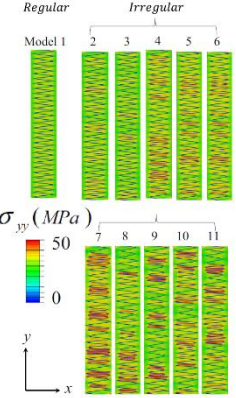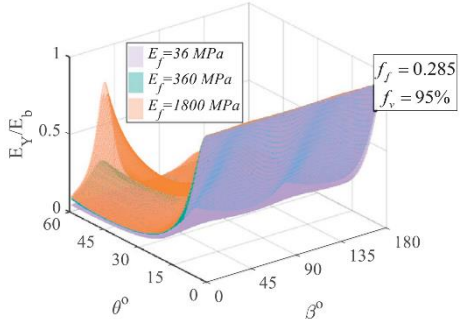
The need for a study which combines these two groups of studies is highly felt. To design a 3D a model which can get feedback from mechanical stimuli to predict the interdigitation patters in calvarial sutures. Table 2.6 summarises the overall aims of these studies, a brief review of their methods, results, and outcomes.

Table 2.6: Overall aims of the studies that have analysed the ossification patterns of the cranial sutures, a brief review of their methods, results and outcomes.

Authors	Aims/Objectives	Method	Outcome/discussion	Result - Fig.
Hartwig, 1991	To predict the pattern of sagittal suture formation in human.	Fractal analysis techniques was used at the sagittal suture to discriminate the separate morphological patterns of interfingering and interlocking.	Consistent degree of complexity at human sagittal sutures were visually observed. No significant correlation observed between the chord length of the suture and its degree of complexity.	Visual comparison of different samples.
Miura *et al.*, 2009	To establish a simple model that can generate the interdigitated structure based on experimental data, and experimentally verify the model.	A simple reaction–diffusion model is formulated using the tissue differentiation state (u) and substrate concentration (v) factors. Then the behaviour of the model was tested numerically and verified with various experimental methods.	The model could be extended to incorporate other factors such as cell lineage and tissue growth, which are known to be involved in the process. However, it showed some relationship with other skeletal structures.	Human and mouse sutures at surface and depth (a), and how some parameters affect the modelling results (b).
Jasinoski *et al.*, 2010	To investigate the response of different suture morphologies under tension and compression.	Finite Element- three suture morphologies were simulated with an increasing interdigitation index (I.I.)	The results highlighted the importance of suture morphology and anisotropy on sutural mechanics. The strain energy generally decreased with a decrease in I.I. However, high bone stress at the interdigitation apices shifted to the limbs of the suture with an increase in I.I.	1st principal stress plots of two interdigitation models in response to a tensile load.

Authors	Aims/Objectives	Method	Outcome/discussion	Result - Fig.
Jasinoski and Reddy, 2012	To investigate the effects of suture viscoelasticity on the pattern of stress, strain, and strain energy of different suture morphology under cyclic loading.	Finite Element- viscoelastic properties were applied to three idealised bone-suture models.	The results suggest that implementation of viscoelastic properties may not be necessary for computational studies of skull behaviour during masticatory loading.	3rd principal strain of each suture model for different loadings.
Khonsari *et al.*, 2013	To develop a mathematical model to predict the pattern of suture formation and bone deposition at the borders of the sutures, and validate it versus animal models.	Finite Element, considering self-organization of collagen fibres in the mesenchyme directed by mechanical stress, and mechanotransduction by migration of mesenchymal osteogenic cells along collagen fibres.	The model illustrates the patterning ability of simple mechanical processes, validated using histology, and synchrotron X-ray microtomography. The ossification speed was higher in the convex areas as a result of the distribution of collagen fibres.	1st principal stress (left), and mesenchymal cell density (right) after 30 days' simulation.
Li, Ortiz and Boyce, 2013	To formulate a generalised, composite mechanical model, to investigate the influence of suture morphology on various biomechanical factors such as load transmission, strength and overall stiffness.	Finite Element- four types of general trapezoidal suture interfaces under longitudinal and lateral tension, and shear.	The presented model provides insights into the relation between the mechanical function and the morphological diversity of suture interface geometries observed in natural systems.	1st principal stress due to bending for different tip angles.

Authors	Aims/Objectives	Method	Outcome/discussion	Result - Fig.
Maloul *et al.*, 2014	To quantify the impact of morphological features, direction of loading and suture material properties on the mechanical behaviour of sutures and surrounding bone in the craniofacial skeleton (CFS).	Several idealised finite element models were developed. One additional specimen-specific FE model was developed based on the morphology obtained from a μCT scan to represent the morphological complexity inherent in CFS sutures.	Suture mechanical behaviour is impacted by morphologic factors (interdigitation and connectivity), which may be optimised for regional loading within the CFS.	von Mises stresses in a complex suture with connectivity and without connectivity in sutures.
Zhang and Yang, 2015	To investigate how cranial suture morphology, suture material property, and the arrangement of sutural collagen fibres influence the dynamic responses of the suture and surrounding bone under impulsive loads.	Finite Element- a two-dimensional idealised bone-suture-bone complex model was used with a uniform impulsive loading.	Results showed that the suture strain energy and the patterns of von-Mises stress in both the suture and the surrounding bone were strongly dependent on the suture morphologies.	von Mises stress in different suture morphologies: straight suture, pure sinusoidal suture, and two-order hierarchical sinusoidal suture.
Yoshimura *et al.*, 2016	To introduce two mathematical concepts, an interface equation and effective range, to enable a mathematical analysis of pattern formation by cranial sutures. To present a new mathematical model that can reproduce the suture width maintenance and interdigitation formation.	A new mathematical model was developed in which the effects of diffusible differentiation factors were approximated as a circle around a producing mesenchymal cell. Effects of differentiation factors were assumed to be uniform inside the circle, and transformation of cranial sutures was simulated numerically.	The model could be used to gain a theoretical understanding of developmental diseases such as craniosynostosis. However, the diffuse circle maintains a certain distance between the neighbouring interfaces in order for the mesenchymal tissues to connect with each other. Thus, in principle, it is impossible to reproduce the formation of the wormian bone.	A complex fractal structure of human lambdoid suture (A), and the simulation of a model with noise (B).

Authors	Aims/Objectives	Method	Outcome/discussion	Result - Fig.
Liu *et al.*, 2017	To explore how the level of morphological irregularity together with suture complexity index influences the stiffness, strength and post-failure behaviour of interdigitated sutures.	Finite element- a Python script was developed in ABAQUS to randomly generate irregular suture models with certain degrees of irregularity. 11 suture models with three levels of morphological irregularity were set up. The theoretical mechanical model of irregular sutures was obtained, and anisotropic mechanical properties were assigned. Two different fibre orientations were considered and compared.	The results identified the mechanical advantages of the irregular nature of suture morphologies that are common in nature. Also, the theoretical and FE model results could provide a better understanding on how the mechanical properties of sutures were balanced via morphological variations.	Stress contour plots of 11 finite element models of sutures with different levels of morphological irregularity under tension in y direction.
Miroshnichenko *et al.*, 2018	To present a hierarchical theoretical strategy to systematically explore the synergistic effects of interfacial layer morphology and the fibre orientation of the connective layer.	A hierarchical homogenization methodology was developed. Investigated how the anisotropic mechanical properties and the wavy morphology of the fibrous interfacial layer jointly influence the overall mechanical properties of composites with wavy fibrous interfacial layer. Also, finite element mechanical models were developed. These were compared to evaluate the overall normal stiffness of suture joints as a function of wavy morphology of sutures, fibre orientation, fibre volume fraction, and the mechanical properties of fibres and matrix in the interfacial layer.	The modelling results provided an explanation on the developmental progression of the suture fibre alignment from the mechanics perspective. Also, this model prediction showed different optimal fibre orientations for sutures under overall tension and overall compression. This is consistent with the variation in collagen fibre orientations observed in sutures mainly taking tensile loads and compressive loads.	Theoretical prediction for the non-dimensionalised effective longitudinal suture stiffness for different fibre Young's modulus E_f.

2-8-2: Modelling craniofacial growth using finite element method

To the best of my knowledge there are fourteen studies that have used finite element method to investigate the cranial growth. These can be divided into three main groups. The first group simulated the overall bone formation patterns in the cranium using an initial simplified model with bone formation centres and applying the reaction-diffusion equations. Second group mainly have worked on craniosynostosis, and compared different surgical methods. Finally, the third group has used a growth function for the cranium and have investigated the resultant stress and strain patterns in sutures.

In one of the very initial studies on modelling the craniofacial growth, Moss *et al.* (1985), used a 2D finite element method to model rat's skull growth at the mid sagittal section from P7 to P150. Fig. 2.19 shows how they used 2D triangular mesh to develop their model with nodes at anatomical landmarks. Performing this initial study with several limitations such as, being 2D and having only 11 elements, they were trying to predict the growth aspect ratios and direction of growth for each element at various growth rates.
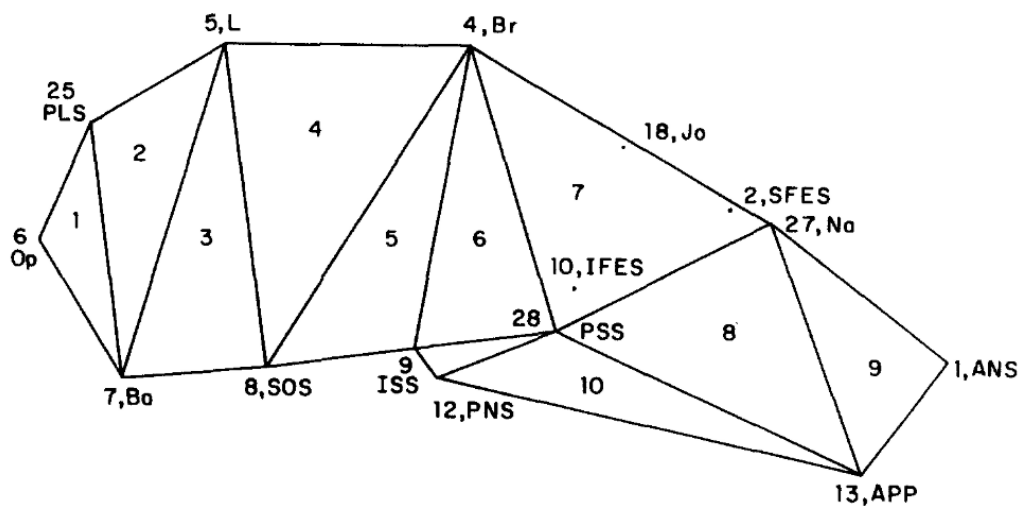
Fig. 2.19: The triangular elements used in studying of rat craniofacial growth using FE (from Moss *et al.*, 1985).

Burgos-Flórez *et al.* (2016) used preliminary growth factor concentration centres for sutures and bones. They used a system of reaction diffusion equations to model the suture interdigitation (Fig. 2.20). This developed spatio-temporal patterns of bone

formation and resorption. They could predict the bone formation from ossification centres, sutures and fontanels formation, and also bone formation and resorption along the sutures. Table 2.7 summarises the overall aims of these studies, a brief review of their methods, results, and outcomes.

Recent advances in image processing methods, combined with high performance computing facilities has made it possible to perform a more detailed patient-specific studies. Malde *et al.* (2018) reviewed the main studies that have used FE in modelling craniosynostosis. They highlighted the potentials of the FE to optimise management of various forms of craniosynostosis. Fig. 2.21 shows an overview of the key steps involve in these studies.

Although it has been shown that finite element method has a good potential in modelling calvarial growth, other mathematical methods are used as well. In the next section some of the studies that have used other methods to model the growth have been summarised.
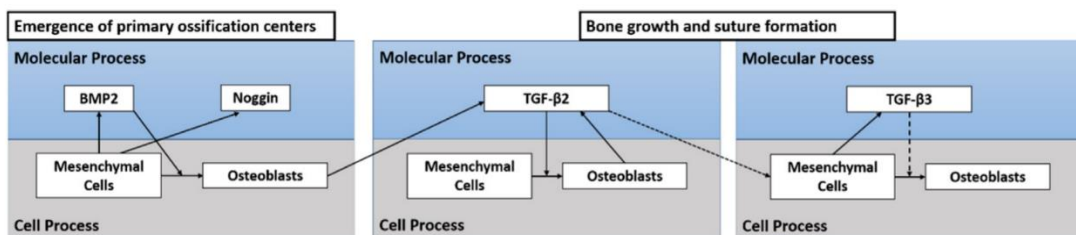
Fig. 2.20: Molecular and cellular processes involved in the stages of flat bone formation and growth and suture formation. Solid lines mean activation, dash lines inhibition, and dotted lines indicate a signal transduction (from Burgos-Flórez *et al.* 2016).
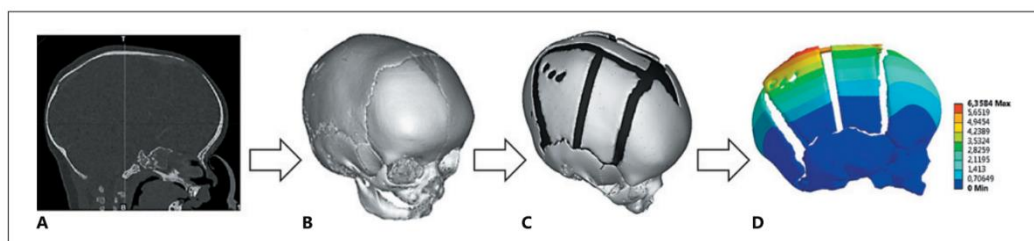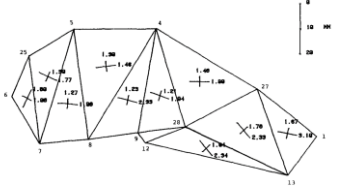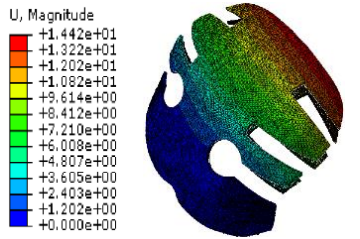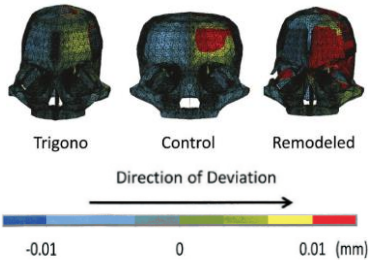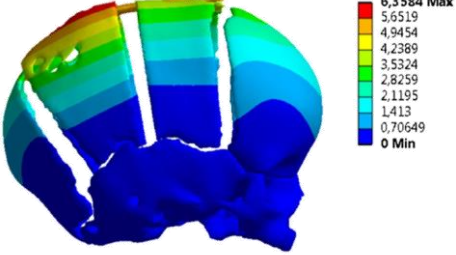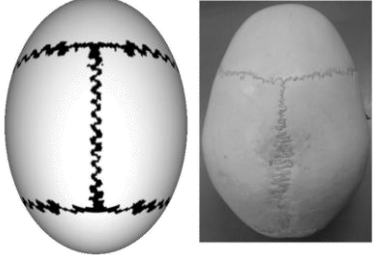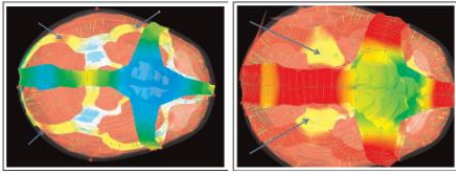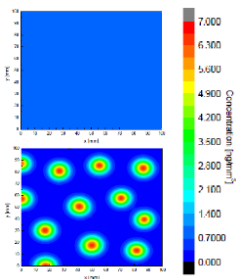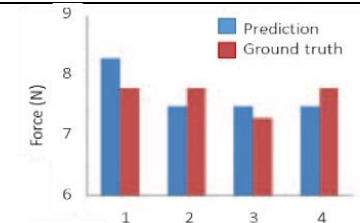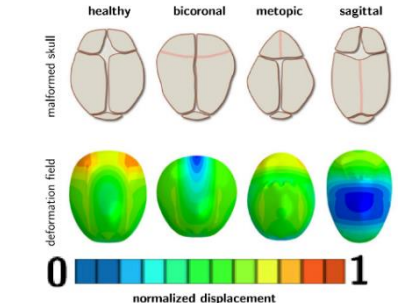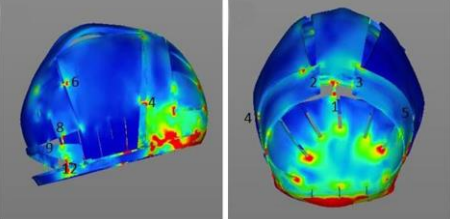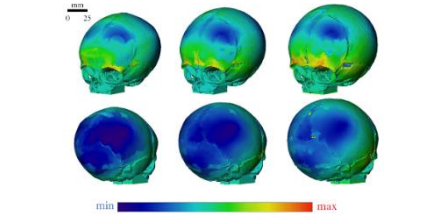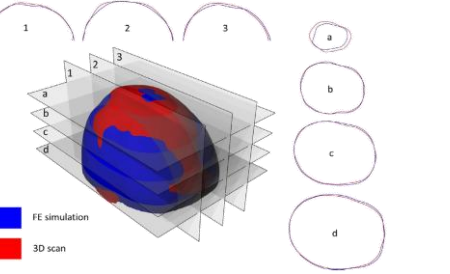
Fig. 2.21: General modelling approach in most of the FE studies. they start with CT data (A) to create a 3D model of the cranium (B), then reconstruct the pre-operation model (C) and finally run the FE analysis (D) (from Malde, Libby and Moazen, 2018)..

Table 2.7: Overall aims of the studies that have used FE to analyse the cranial growth, a brief review of their methods, results and outcomes.

Authors	Aims/Objectives	Method	Outcome	Result- Fig.
Moss *et al.*, 1985	To model rat skull growth using a basic finite element model.	Finite element- the cranial structure was modelled as a number of 2D elements. For each element, independently, both magnitude and direction of temporal size and shape changes occurring in that element relative to itself were described and depicted from P7 up to P150.	Quantitative descriptions of cranial skeletal shape and shape change with local growth were provided. The results were independent of any external frame of reference.	Principal extension ratios for rat craniofacial growth from 7 to 150 days.
You *et al.*, 2010	To analyse the relationship between different craniotomies and the overall skull rigidity in Pi-shape reconstruction.	Finite element- a surgery treatment plan was designed using a congenital craniosynostosis case. A modified PI-shape correction plan was used, and bone slots used for reconstructing the cranial suture were in variance to simulate the stress distribution.	Results indicated that cranial bone rigidity is a key factor with profound influence on postoperative outcomes, and lower bone rigidity leads to better results.	Displacement contour plot of the cranium after surgical cutting.
Nagasao *et al.*, 2010, 2011	To investigate how normal, preoperative metopic and postoperative metopic craniosynostosis orbital morphology are affected by the loading from intracranial pressure.	Finite element- CT data was used to produce for FE models for 10 patients with trigonocephaly (8.2 ± 4.5 months). A 15-mm Hg pressure was applied to the neurocranium to simulate the ICP. The amount of the change in the orbital distance was calculated. The same processes were repeated for 10 models simulating normal skulls and postoperative skulls. The changes in the orbital distance were compared among the three groups.	Results showed that the expansion of interorbital distances due to intracranial pressure is constrained structurally in metopic synostosis. The remodelling of the frontals during metopic synostosis treatment allowed the expansion of the frontals, and this increases the interorbital distance and improves the facial morphology.	Deformity patterns of the skull models. The colour scale indicates the value of horizontal displacement each part of the models presents

Authors	Aims/Objectives	Method	Outcome/discussion	Result - Fig.
Larysz *et al.*, 2012; Wolański *et al.*, 2013	To propose a method for preoperative planning of craniosynostosis based on 3D modelling and biomechanical analysis using finite element method.	Using CT or MRI data, patient specific 3D models were developed. Virtual reality was used for surgical correction planning and the head shape was modelled for after the surgery. Based on the FE results, the virtual model of the head shape was analysed, and a surgery method was proposed.	Pattern of skull deformation following patient-specific metopic and sagittal synostosis calvarial reconstruction were shown. Bone thickness and the loading levels required to cut the calvarial bones were also presented.	 Displacements plots after the correction.
Garzón-Alvarado, 2013; Garzón-Alvarado *et al.,* 2013; Burgos-Flórez *et al.,* 2016	To model and simulate prenatal growth of calvarial flat bones and formation of sutures and fontanels, and interdigitation and fusion of sutures during infancy.	Finite element- a system of reaction-diffusion equations was modelled combined with bone ossification centres in a simplified geometry.	The simulation results agreed with the morphological characteristics of calvarial bones and sutures throughout human prenatal development and infancy.	 Simulation results for suture interdigitation and adult calvaria.
Jin, Eagleson, *et al.*, 2014; Jin, Shahbazi, *et al.*, 2014; Jin *et al.,* 2018	To predict the result of various surgical interventions on the pattern of skull growth using FE.	A hybrid computational model was developed to simulate the relationship between the growing deformable brain and the rigid skull. The model was composed of the nine segmented skull plates as rigid surfaces, deformable sutures, and a volumetrically controllable deformable brain.	The results are expressed on the evolution of the Cranial Index as calculated using standard landmarks and are compared to the normal index, and evaluated by comparing with patient data. Potentially, by varying the properties of the sutures in the model, different craniosynostosis models, such as scaphocephaly and trigonocephaly can be simulated.	 Stress contour plots mid simulation (left), and at the end of simulation.

Authors	Aims/Objectives	Method	Outcome/discussion	Result - Fig.
Lee *et al.*, 2016	To develop a multiscale computational model to simulate the mechanisms associated with the growth of cranial vault in craniosynostosis, from cell activity to skull shape. Also, to investigate the effects of imbalance of the composition of proteins on abnormal ossification.	Reaction-diffusion-advection methods combined with the finite element method were used to investigate the skull growth in craniosynostosis phenotypes. Primary centres of ossification in cranial vault are identified using an activator-substrate model that represents the behaviour of key molecules for bone formation. Biomechanical effects due to the interaction between growing bone and soft tissue are also considered.	It was found that faster diffusion of substrate molecules than that of activator, leads to more intense pattern forming with smaller number of highly concentrated points. Primary centres of ossification in cranial vault were defined at the points where the concentration of activator molecules were high.	Activator concentration change at t=0 and t=18 weeks, in 2D.
Zhang *et al.*, 2016	To present and validate a system which can predict the optimal spring force for sagittal craniosynostosis reconstruction.	An elastic model was used to estimate the behaviour of the bone tissue for 23 patients. Using FE, the contact force was calculated on the skull strip with the springs. The relationships between biomechanical properties generated from spring force, bone thickness, and the change of cephalic index after surgery was modelled.	Development of a computer platform capable of predicting optimal spring force in spring-assisted surgery for sagittal synostosis was achieved. *In vivo* and clinical data results indicated that bone thickness and spring force play a crucial role in surgical outcome.	Force prediction performance for anterior spring on 2 age groups.
Weickenmeier *et al.*, 2017	To predict typical skull morphologies in most common forms of craniosynostosis.	An ellipsoid approximated the skull with sutures and fontanelles. Metopic and sagittal sutures were primarily responsible for widening, and coronal and lambdoid sutures for lengthening. Lengthening and widening were governed by two rates, γ_l and γ_t. The only free parameter of the simulation, their ratio $\gamma_l/\gamma_t = 2.11$, was selected such that it preserves a cephalic index of 78 at a circumference growth of 30% within 12 months.	Typical craniosynostotic skull shapes were predicted using simplified 2D and 3D elliptical models. The CI predictions based on the 2D model showed 0.5 – 12% difference with clinical data across sagittal, lambdoid, metopic, and uni/bi coronal synostosis. The 3D model showed 0.5 – 3.5% difference between the predicted and clinical CIs.	3D skull growth models, with normalised contours of skull displacement field.

Authors	Aims/Objectives	Method	Outcome/discussion	Result - Fig.
Li *et al.*, 2017	To quantify the positive outcome of using computer assisted preoperative planning such as biomechanical analysis and 3D printing.	Two groups of patients were treated with traditional preoperative strategy treatment method integrated with computer-assisted 3D simulations. Indexes such as length of operation, blood loss, operation cost, and postoperative complications were compared. The surgical effects were compared through the cranial index, head circumference, and cranial vault asymmetry indexes before and after treatment.	Stress and strain analysis of a single case for sagittal synostosis reconstruction was presented. Quantitative data, i.e., operative duration, blood loss, hospital cost, pre- and postoperative CIs were also presented comparing a preoperative planning cohort versus a non-preoperative planning cohort.	Stress contour plot of the reconstructed skull from different views.
Libby *et al.*, 2017	To develop a validated computational model of skull growth during the early postnatal period (0–12 months) based on the FE method.	Two *in silico* FE models were created with the same micro CT scan. The growing brain was assumed to be the driving force. The models were validated against a 3D printed *in vitro* model and also *in vivo* CT skulls (n=56).	Overall, the FE model results matched well with both the *in vitro* and *in vivo* data, which shows a potential to be used to assist in preoperative planning of craniofacial surgery procedures and help to reduce reoperation rates.	3D distance plots comparing *in silico* and *in vitro* models at different ages.
Borghi *et al.*, 2018	To develop a patient-specific computational model of spring-assisted cranioplasty, to predict individual overall head shape.	Pre-operative CT images of a spring-assisted cranioplasty patient were processed to extract a 3D model of the infant skull and simulate spring implantation. The distractors were modelled based on mechanical experimental data. Viscoelastic bone properties from the literature were tuned using the specific patient procedural information recorded during surgery and from x-ray measurements at follow-up.	A validated patient-specific model of spring-assisted sagittal synostosis was developed. The potentials of FEM to predict the skull shape of craniosynostotic patients following surgery was highlighted.	Comparison between the shapes of FE (blue) and Scan (red), and their cross sections.

2-8-3: Modelling craniofacial growth using other computational methods

Finite element method is one of the main methods that has been used in investigations and simulations of the cranial growth. However, there are other computational methods that have been used to model and study the cranial development as well. In this section three different studies that have used methods other than FEM will be reviewed briefly.

Zollikofer and De León (2006), used a shape analysis method to investigate the cranial growth in human. Their geometric-morphometric analyses investigated the kinematics of the shape change. They then related the change in the physical world with that in the shape space (Fig. 2.22). Each position in the shape space was correspondent to a defined landmark configuration in the physical space. As a result, in a sample, it is possible to switch between the physical and abstract representations of shape variability. This can be used to characterise complex patterns of the physical shape transformation as trajectories through the shape space, which provides invaluable information on how the craniofacial system grow during the development (Zollikofer and De León, 2006).
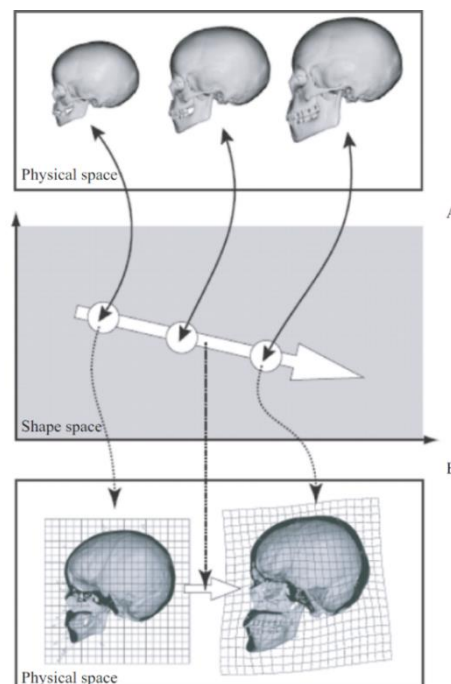
Fig. 2.22: Shape change in the physical world and in shape space. A: Correspondence between locations in multidimensional shape space (circles, middle graph) and cranial shapes in physical space. B: Correspondence between a shape trajectory in shape space (arrow, middle graph) and a pattern of shape transformation in physical space (transformation grid from juvenile to adult from Zollikofer and De León, 2006) .

Other novel methods have been used in order to model the abnormal development of the cranium. The influence of mechanical forces on the development and maintenance of the cranial sutures is well-established. However, the details of how they regulate the balance between sutural patency and fusion remains unclear. Scarr (2008), introduced a tensegrity structure for modelling the cranial vault with the aim to tackle the complexities of the cranial development. Considering that the stability of the vault is dependent on the underlying brain, sutural patency merely facilitates the cranial expansion. Fig. 2.23 shows how Scarr developed his model. Curved plates of cranial bone represented the compression struts, floating on the dura mater, and were modelled as elastic tension cords.
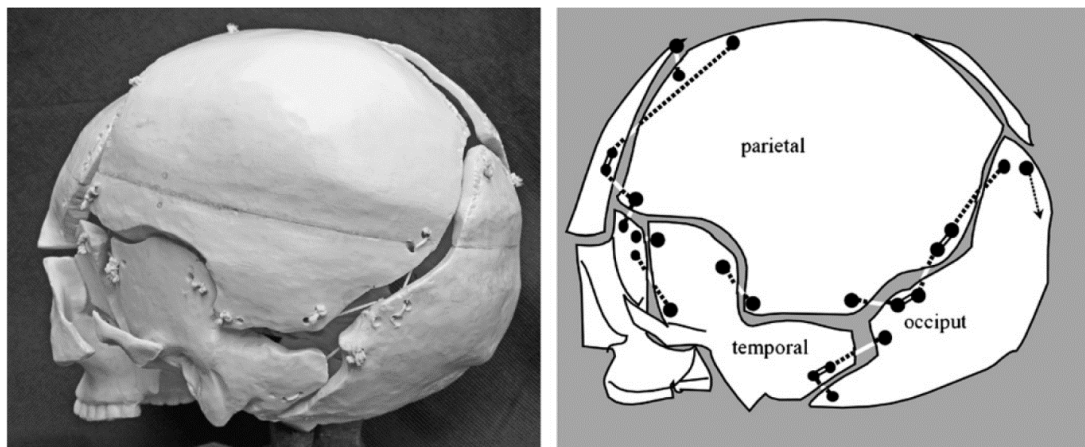
Fig. 2.23: Tensegrity skull model, posterolateral view (from Scarr, 2008).

Lee *et al.* (2015) used finite volume method to model the cranial growth using an initial geometry with preliminary bone growth centres. Two main agents of activator and inhibitor simulated the bone formation over time. Their analysis showed that osteoblast regions expanded from the ossification centres to form the sutures between the bones. One of the limitations of their study was that they hadn't considered the cranial vault expansion and their domain kept its initial geometry and only bone formation was modelled.

Fig. 2.24 shows the change of region of high concentration of osteoblast over time. The regions originally marked by the differentiation of osteoblasts expanded from the primary centres of ossification over time. The results showed two frontal bones, two parietal bones, and one interparietal bone. Sutures were formed between bones as bones grow according to repulsive effect between bones in the model.
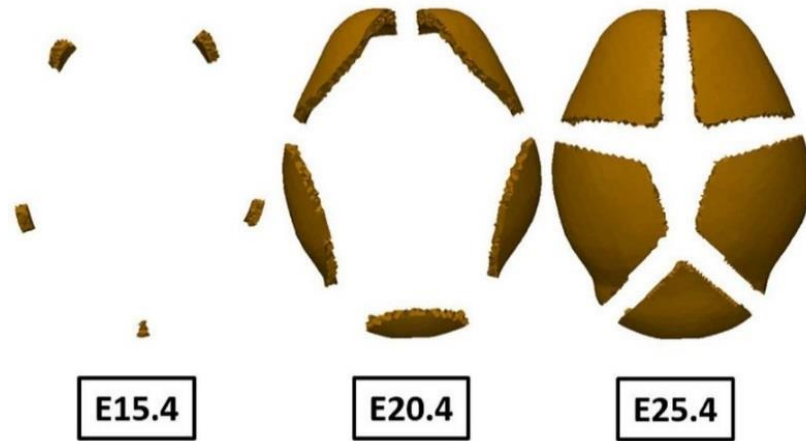
Fig. 2.24: Change of region of high concentration of the cranial osteoblast over time during the embryonic ages of E15.4 to E25.4 for a mouse model (from Lee *et al.*, 2015).

In summary, main limitations of previous studies of cranial development and suture ossification could be categorised based on their simulation methods. First, studies that investigated suture formation neglecting the skull growth. Then studies that investigated the bone formation, also had neglected the skull growth by considering an initial geometry which was far from what happens in reality. Although there were few studies that included the cranial growth, these models lacked simulating the cranial bone formation and suture ossification, or being able to be used in the patient specific studies of craniosynostosis. In the final section of this chapter, some of the existing theories of tissue differentiation will be reviewed briefly.

2-9 Mechanobiology of bone formation and adaptation

It's widely believed that the mechanical loads arising from the growing brain in a combination with the masticatory loads contributes to the pattern of the bone formation at the cranial sutures and their ossification (Herring, 2008; Moazen *et al.*, 2015; Weickenmeier *et al.*, 2017). For more than a century, several theories have been proposed and different models have been introduced to explain how biological processes are affected by the mechanical stimuli (Suárez, 2015). This section will provide a brief review of the fundamental concepts of the mechanobiology of tissue differentiation and bone adaptation.

Galileo Galilei (Galileo, 1638) was the first one to investigate the optimal shape and structure of bones in different animals (Pivonka, Park and Forwood, 2018). However, it wasn't until the 19th century that the combined observations of an engineer, Culmann, and an anatomist, von Meyer, showed the similarities between the stress patterns of a crane structure, and the trabecular patterns of human femur for the first time (Fig. 2.25). This led to major advances in the theories of bone adaptation (Pivonka, Park and Forwood, 2018).
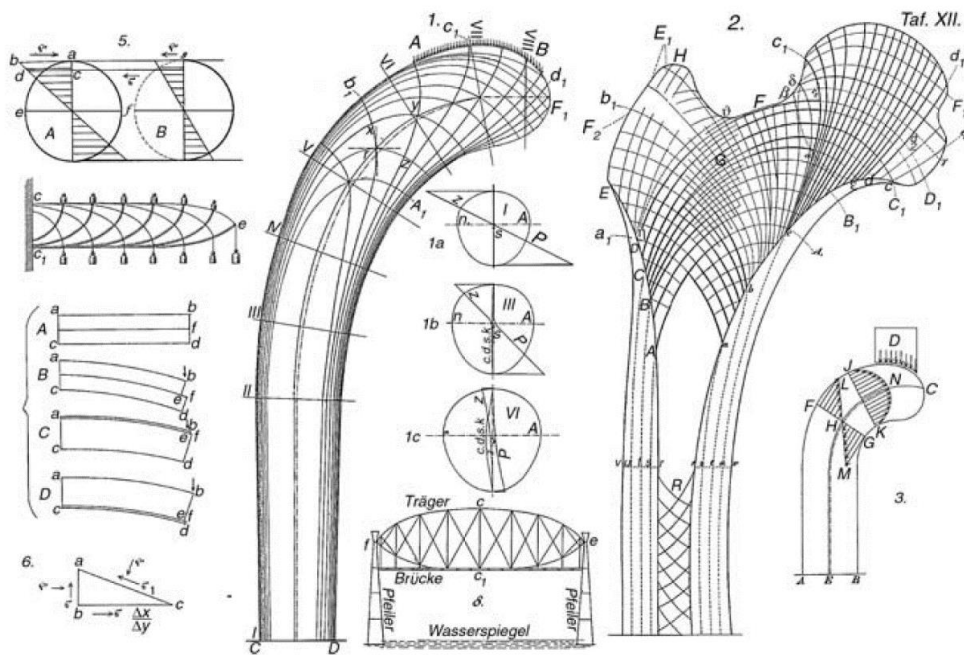
Fig. 2.25: Sketches drawn by Culmannn and von Meyer. Culmann's crane is left of the centre and Von Meyer's sketch is to the right of the centre (from Cowin, 2001).

These observations grabbed the attention of Wolff (1873) and Roux (1881). Their proposed theories were very similar and based on the relation between the bone structure and mechanical loading. Wolf's proposed theory was based on the trajectories of the structures of cancellous and compact bone, while Roux was the first one to use a term implying functional adaptation, he suggested that there is a relationship between the tissue differentiation and mechanical stimuli (Pivonka, Park and Forwood, 2018).

Almost one century later, Pauwels (1965) proposed a more detailed theory based on his clinical observation. While Roux's theory stated that the compression results in formation of bone tissue, tension in connective tissue, and both combined with shear results in cartilage, Pauwels stated that the elongation and hydrostatic pressure that

cells "feel", are the defining mechanical stimuli (Fig. 2.26). A few years later Weinans and Prendergast (1996) proposed their theory as "Tissue adaptation as a dynamical process far from equilibrium" (Fig. 2.27). The following year, Prendergast *et al.*, (1997) introduced the role of fluid flow in the cellular deformations. Later on, Carter *et al.* (1998) introduced the load history into Pauwels theory and assumed that the time variation in the mechanical loading triggers the tissue differentiation (Fig. 2.28).
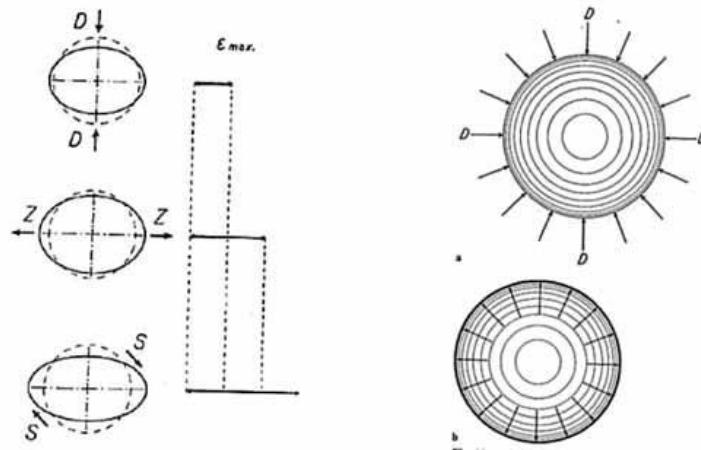
Fig. 2.26: Elongation due to tension (Z), compression (D), and shearing (S) – left, and the effect of hydrostatic pressure on a cell- right (from Pauwels, 1965).
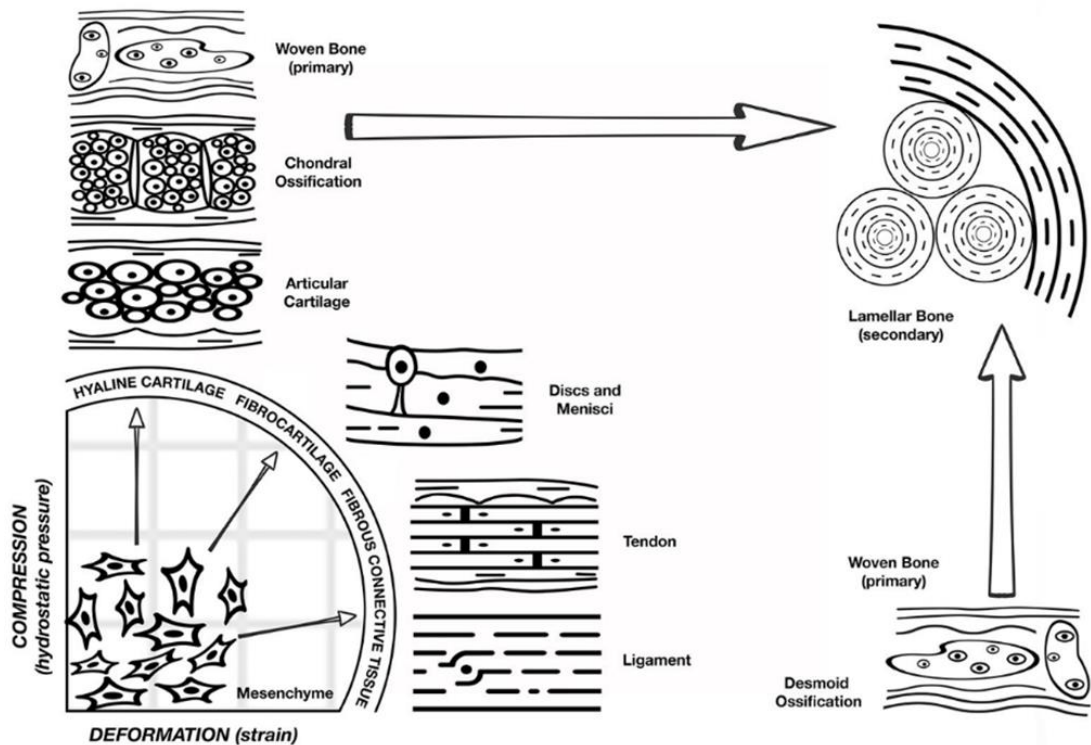
Fig. 2.27: A schematic representation of the hypothesis proposed by Pauwels, drawn by Weinans and Prendergast (1996), adapted by Glatt, Evans and Tetsworth (2017). Osteoblast proliferation and ossification can occur depending on the response of different tissues to the presence of mechanical stimuli (Glatt, Evans and Tetsworth, 2017).
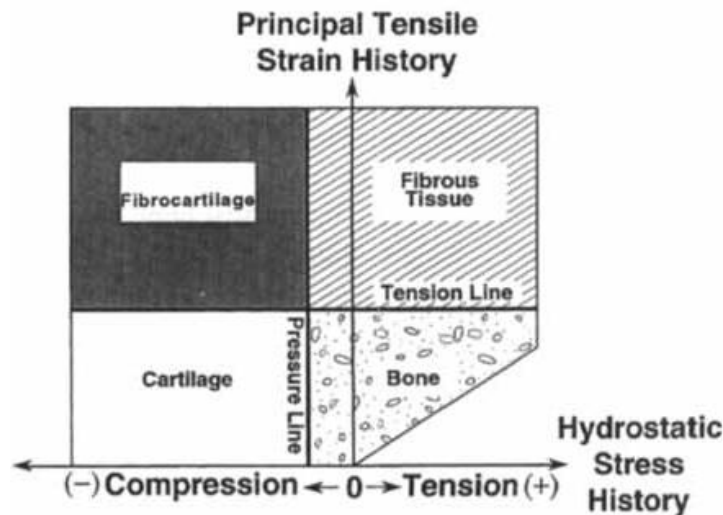
Fig. 2.28: The role of tissue's mechanical loading history on the skeletal tissue regeneration (from Carter *et al.*, 1998).

Claes and Heigele (1999), investigated the local stress and strain along bony surfaces to predict the course and type of fracture healing in long bones. Their proposed hypothesis indicated that the new bone formation mainly occurs along fronts of existing calcified tissue and local strain and stress magnitudes define the type of bone healing (intramembranous or endochondral- Fig. 2.29). For example, strain values of less than 5% can lead to intramembranous bone formation, or, strain values less than 15%, combined with the compression of more than 15%, would lead to endochondral ossification. Engler *et al.* (2006), investigated the physical effects of *in vivo* microenvironment by investigating the effect of matrix stiffness on the stem cell lineage. They reported a dramatic response in both morphology and lineage. This means that even without external forces, the elasticity of the environment can influence the cell movement.

In recent years, advances made in the computational powers have made it possible to simulate more complicated theories. Pivonka *et al.* (2018) reviewed the most recent theories that use parameters such as strain energy density, von Mises stress, axial strain, and dilatational strain to simulate bone resorption and formation by osteoclast and osteoblast cells. They suggested that despite significant ongoing work in the field of mechanobiology, much more work needs to be carried out to truly unravel the fundamentals of how cells and various biological tissues respond to the mechanical loads.
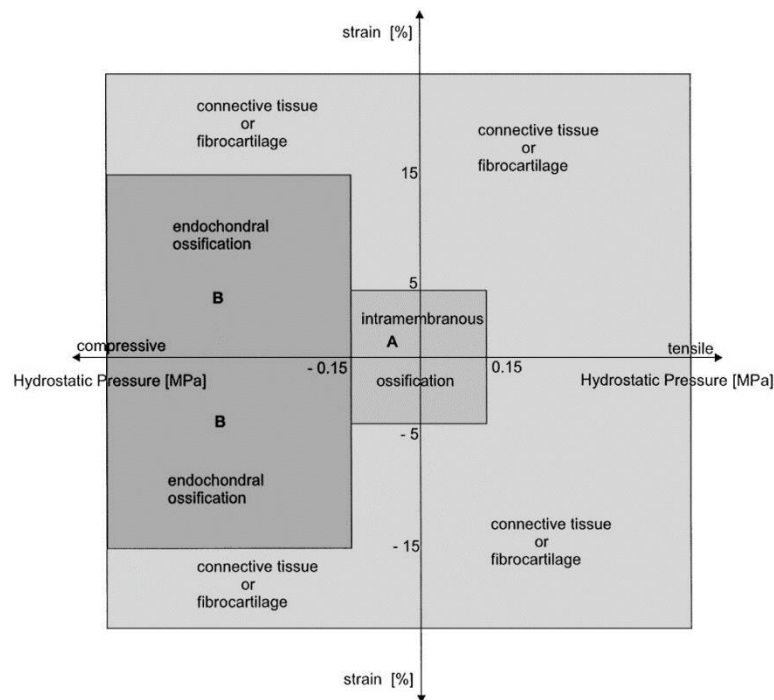
Fig. 2.29: Correlations between mechanical conditions and tissue differentiation in fracture healing (from Claes and Heigele, 1999).

2.10 Summary and discussion

A basic overview of the anatomy of the mouse skull was described in this chapter. This was very informative for the modelling work that is presented in Chapter 3 and 4. On the other hand, the morphological differences between the wild type and the Crouzon mouse were highlighted briefly. This is the main focus of Chapter 3, where detail analysis on two ontogenetic series of normal and Crouzon mouse is performed.

The modelling studies around the skull growth were reviewed in more details compare to other aspects of this project as this was the main focus of this work. Particular attention was paid to ensure if not all of the relevant studies are summarised here at least the key studies are reviewed. While the cranial bone formation is usually compared with bone fracture healing, it seems that bone distraction analogy may be suitable as well. However, there is little literature around it compared with fracture healing.

Overall, there were limited studies on the modelling of the calvarial growth using finite element method. This is in fact the main contribution of this work.

Review of the previous studies on the mechanical properties of the cranial sutures, calvarial bones and the brain highlighted that the measurements in the literature can vary considerably from one study to another. There are a number of variables between these studies and it is challenging to compare these studies directly. Nonetheless these studies provide invaluable data that can be used in computational studies. Obviously, these parameters can be varied in the computational studies to investigate their effect on the output parameter of the interest.

There is an extensive body of literature on the modelling of the bone formation during the fracture healing. However, there are limited studies on modelling the bone formation during the calvarial development. Nonetheless, the same modelling approaches can be applied to model the bone formation during the calvarial growth. This is also the main focus of this project and is presented in Chapter 5.

Chapter 3: Mouse skull development

3-1 Introduction

This Chapter describes several anatomical measurements that were aimed to quantify *ex vivo* mouse skull growth from P3 - 10. First, overall mouse skull morphology during the development was quantified. Then, changes in the cranial suture sizes were measured. This data will be used in further sections of this thesis for the finite element model development or validation purposes in the following Chapters.

3-2 Materials and methods

3-2-1 Specimens

Two ontogenetic series of mice, i.e. wild type and genetically modified *Fgfr2$^{C342Y/+}$*, were provided by Prof Andrew Wilkie at the University of Oxford. It must be noted that this is a well-established and described model in the literature (Table 2.2, in Chapter 2). The mice were from P1-42 with about ten specimens at each age in each group. For the purpose of this study the following specimens were randomly chosen and microCT scanned with a resolution of approximately 20μm (X-Tek Systems Ltd, UK): (1) two P3 skulls, one wild type and one mutant type, (2) ten P7, five wild type and five mutant type, and (3) ten P10, five wild type and five mutant type (Table 3.1). The aforementioned age groups were chosen since about 70% of mouse calvarial growth occur in this age range corresponding to about 1 year of age in human (please see section 2.4 in Chapter 2).

Table 3.1: A summary of specimens used in this Chapter. Please note specimen names are only for author's reference.

Age	Number of samples	Name of each sample				
Wild type P3	1	10.2				
Mutant type P3	1	10.1				
Wild type P7	5	7.3	7.7	7.8	8.5	8.10
Mutant type P7	5	7.4	7.5	7.6	8.2	8.11
Wild type P10	5	17.1	17.5	17.10	18.8	18.9
Mutant type P10	5	17.6	17.12	17.13	17.14	18.4

3-2-2 Skull alignment

MicroCT images were first aligned in a similar position. Here, the skulls in the transverse plane were aligned in a way that the inferior surface of the basisphenoid and presphenoid bones were forming the horizontal XY plane (Fig 3.1C) and the mid-sagittal plane formed the vertical XZ plane (Fig. 3.1A).
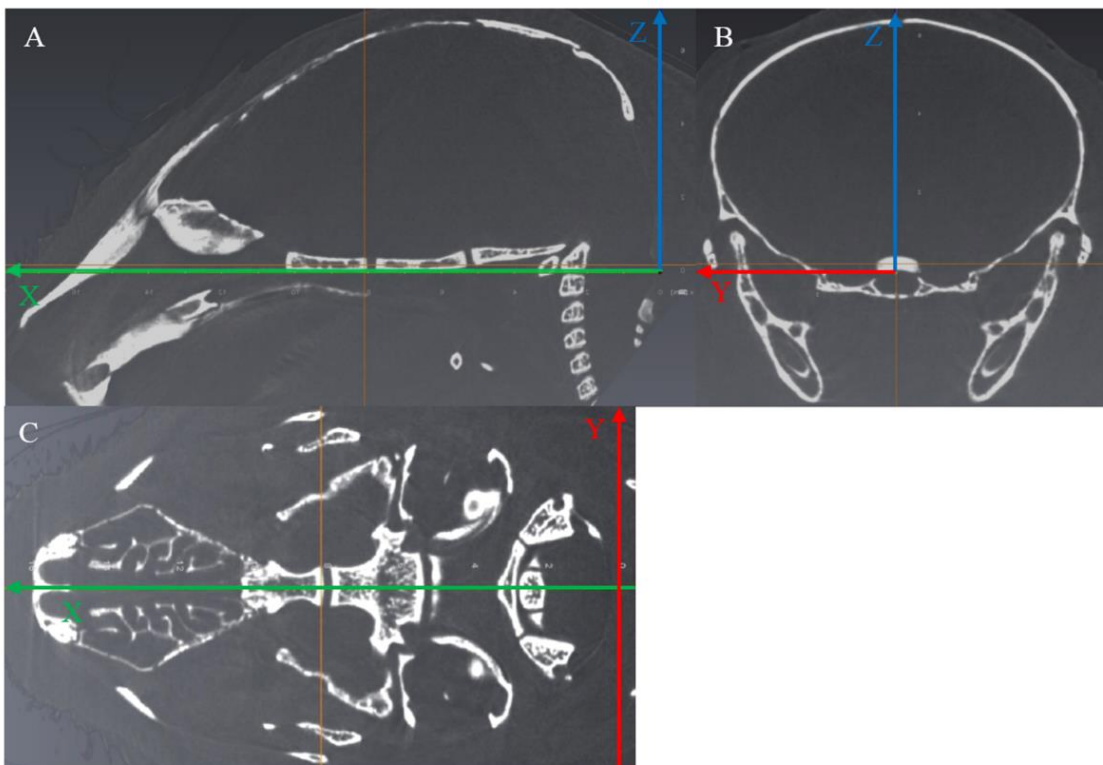
Fig 3-1: Skull alignments in the sagittal (A), coronal (B) and transverse (C) planes.

3-2-3 Skull measurements and average skull

Following alignment of all skulls in a same orientation, skull length, width, and height were measured. Skull (calvarial) length was measured in the mid-sagittal plane as the distance between the most anterior part of the frontal suture and the most posterior part of the skull (Fig. 3.2A). Skull height was also measured in the mid-sagittal plane as the distance between the presphenoid and the most superior part of the calvaria (Fig. 3.2B). Skull width was measured in the transverse view as the distance between the two most lateral points of the skull (Fig 3.2C).
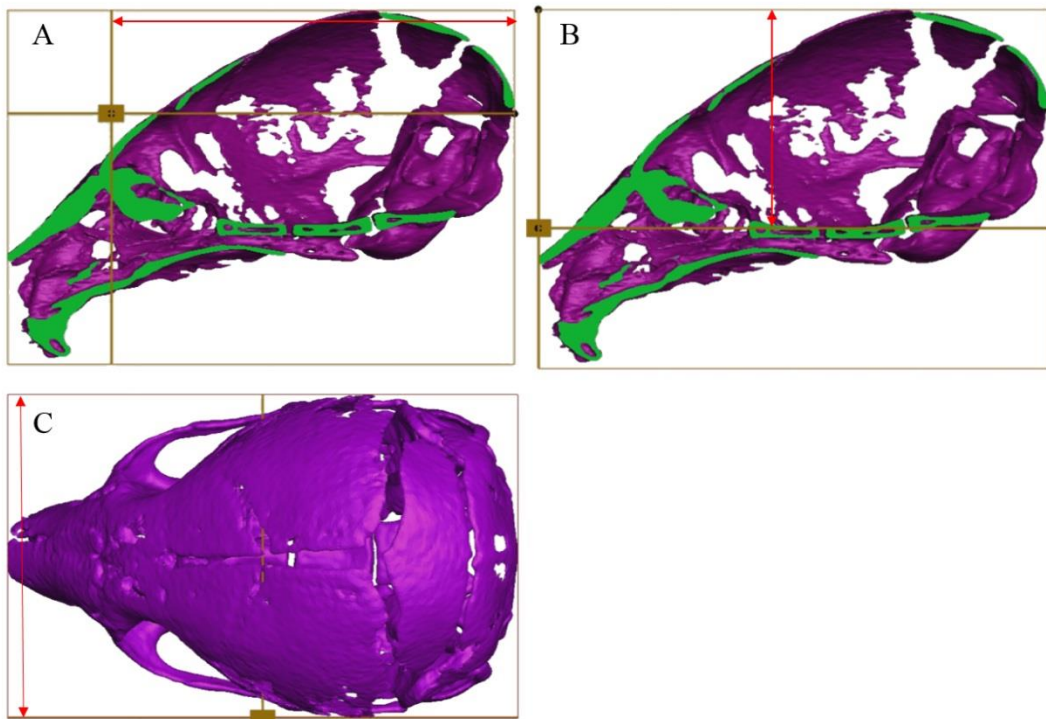
Fig 3-2: Skull measurements: length (A); height (B) and width (C) at P10.

3-2-4 Average skulls

The average skulls at P7 and P10 were determined based on the skull measurements. The specimen with the closest length, width, and height to the average values were chosen as the average specimens. The average specimens are used for the validation of the finite element results through the remaining Chapters of this thesis.

3-2-5 Sutures measurements

Using the original aligned CT images, suture sizes were measured at fourteen different regions across the P3, P7 and P10 skulls (see Fig 3.7). Fig. 3.7 highlights the position of this regions. Note that due to the quality of the CT images (voxel sizes were about 20µm to 40µm, and the coronal suture size from a parallel study by Moazen *et al.* (2015), was measured to be about 20µm and less) it was not possible to measure the size of the coronal sutures.
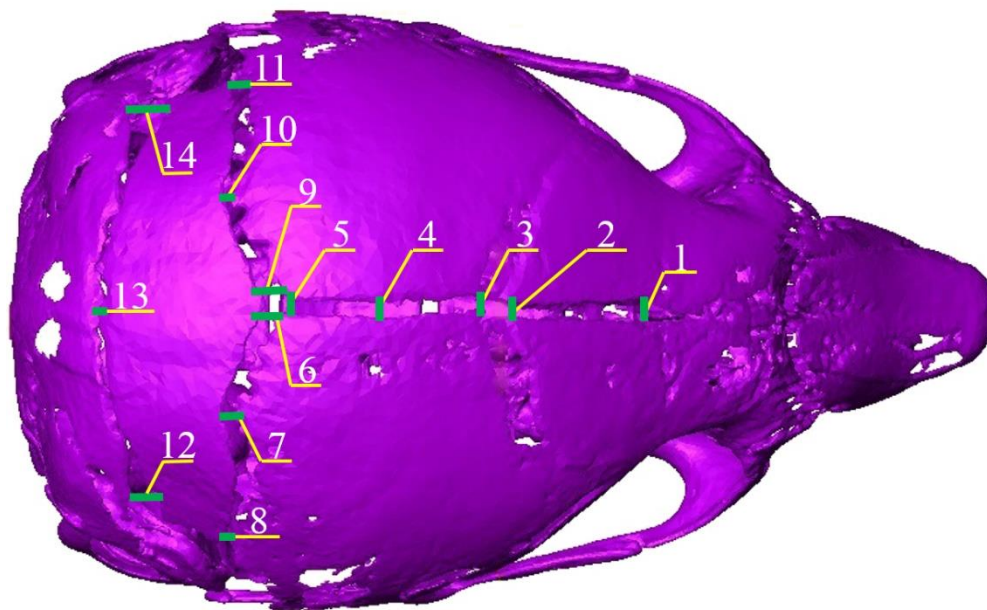
Fig. 3.3: Suture measurement at 14 different sections (P10). 1: Frontal suture, medial point; 2: Frontal suture, posterior point; 3: Sagittal suture, anterior point; 4: Sagittal suture, medial point; 5: Sagittal suture, posterior point; 6: Right Interparietal suture, nearest point to the midsagittal plane; 7: Right Interparietal suture, medial point; 8: Right Interparietal suture, most lateral point; 9: Left Interparietal suture, nearest point to the midsagittal plane; 10: Left Interparietal suture, medial point; 11: Left Interparietal suture, most lateral point; 12: Most lateral point of the Lambdoid suture- right ; 13: Lambdoid suture, medial point ; 14: Most lateral point of the Lambdoid suture- left.

3-3 Results

3-3-1 Skull measurements

WT and MT skulls' width, length and height at P3 were 8.43mm, 10.99mm and 6.02mm, and 8.27mm, 10.83mm and 6.41mm respectively. WT and MT skulls' width,

length, and height at P7 were 10.05±0.71mm, 12.45±0.55mm and 6.65±0.28mm, and 10.10±0.26mm, 11.85±0.41mm and 6.90±0.19mm respectively. The P10 WT and MT skulls' width, length, and height were 10.31±0.47mm, 13.14±0.62mm and 6.63±0.36mm, and 10.28±0.30mm, 12.59±0.41mm and 7.16±0.41mm, respectively. Mutant skulls had a higher width and height, and a shorter length in comparison with the wild type skulls.

Fig. 3-4 highlights the morphological variations between five P7 and five P10 specimens in the sagittal and coronal views. Despite a relatively large variation between the specimens at each age group, the pattern of skull growth from P3 to P7 and P10 was captured.

Table 3.2: Skull measurement comparison between the five wild type and mutant type specimens at P7 and P10 (all dimensions are in mm).

Age	Wild Type				Mutant Type			
	Name	Length	Width	Height	Name	Length	Width	Height
P3	10.2	10.99	8.43	6.02	10.1	10.83	8.27	6.41
P7	7.3	13.14	10.67	6.59	7.4	12.11	9.93	7.06
	7.7*	12.45	10.05	6.65	7.5	12.41	9.77	6.99
	7.8	12.43	9.97	6.13	7.6*	11.85	10.10	6. 90
	8.5	11.88	9.34	6.16	8.2	11.38	9.89	6.57
	8.10	11.77	8.81	6.75	8.11	11.57	9.41	6.93
	Average	12.33	9.77	6.44	Average	11.87	9.82	6.89
	SD	0.55	0.71	0.28	SD	0.41	0.26	0.19
P10	17.1	13.67	10.88	7.32	17.6	13.31	10.13	7.77
	17.5	13.60	10.9	7.26	17.12*	12.59	10.28	7.16
	17.10*	13.14	10.31	6.63	17.13	12.38	10.89	6.96
	18.8	12.45	9.90	6.66	17.14	12.25	10.28	7.17
	18.9	12.37	10.00	6.62	18.4	12.57	10.43	6.63
	Average	13.05	10.40	6.90	Average	12.62	10.40	7.14
	SD	0.62	0.47	0.36	SD	0.41	0.30	0.41

*: Average specimens of that group.
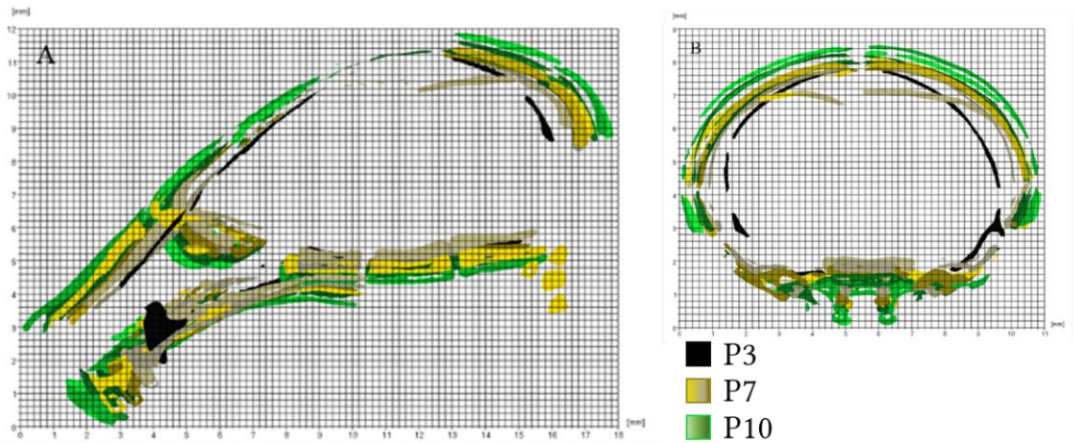
Fig 3-4: Morphological variation between the five WT specimens at P7 and P10 in the sagittal (A) and coronal (B) sections. Black outline is the single P3 skull; yellow shades are five P7 specimens and green shades are five P10 skulls.

3-3-2 Average P7 and P10

The sample with closest height, length and width to the average values at P7 and P10 were sample 7.7, 7.6 (WT and MT) and 17.10 and 17.12 (WT and MT), i.e. average specimens. Considering the average specimens, from P3 to P7, skull length, width and height increased by 13.28%, 19.22% and 10.47% in wild type, and 9.24%, 22.13% and 7.64% in mutant type. From P7 to P10 changed by 5.54%, 2.59% and -0.3% in wild type and 6.24%, 1.78%, and 3.77% in mutant type.

The slight decrease in the skull height from P7 to P10 in the wild type average skulls was because the average skulls were compared, not the average values and if the average values were compared (Table 3.2), a 7.14% increase was observed. Wild type and mutant type skull growth from P3 to P10 is shown in Fig. 3.5.

Table 3.3: Skull measurement comparison between P3 and the average specimens at P7 and P10 for both wild type and mutant type (all dimensions are in mm).

	Wild Type			Mutant Type		
	Length	Width	Height	Length	Width	Height
P3	10.99	8.43	6.02	10.83	8.27	6.41
Av. P7 Skull	12.45	10.05	6.65	11.85	10.1	6.90
P3 to P7 change %	13.28	19.22	10.47	9.42	22.13	7.64
Av. P10 skull	13.14	10.31	6.63	12.59	10.28	7.16
P7 to P10 change %	5.54	2.59	-0.30	6.24	1.78	3.77
Total change %	19.56	22.30	10.13	16.25	24.30	11.70
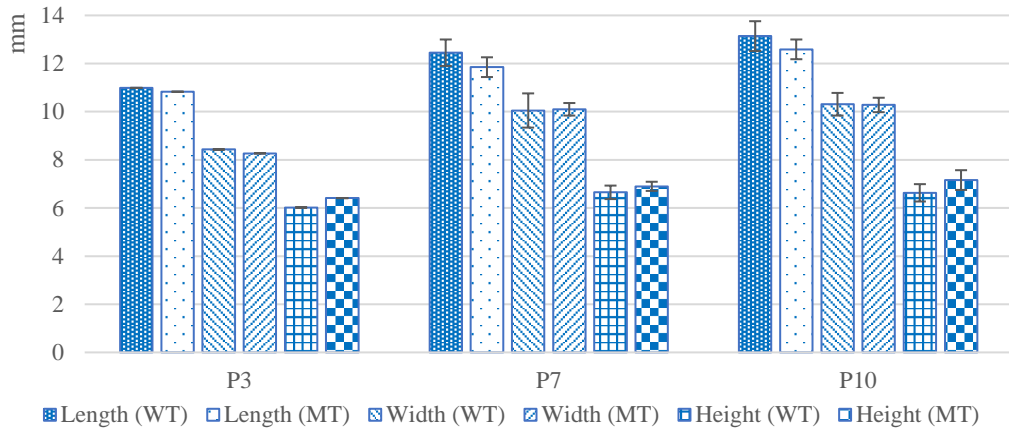
Fig 3-5: Skull measurement comparison between wild type (WT) and mutant type (MT) P3 and the average specimens at P7 and P10.

Figures 3.6 compares the morphological changes between the P3 and average P7 and P10 in the sagittal and coronal plane. While the calvarial bones grow radially, the bones on the palate e.g. basisphenoid and presphenoid grow eccentric to accommodate the growing brain. To predict the calvarial growth in following Chapters, these bones will be considered as centre of growth.
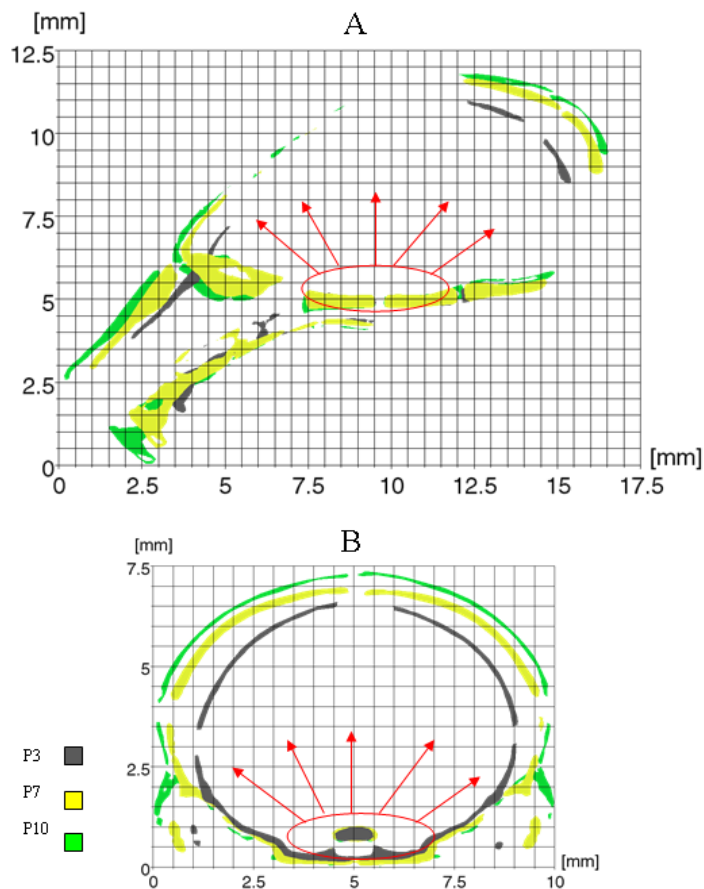
Fig 3.6: Comparison between the calvarial morphology of P3 and the average P7 and P10 in the sagittal (A) and coronal (B) views. Note the centre of growth indicated in the figure.

3-3-3 Suture sizes at P3, P7 and P10

Wild type:

Table 3.4 summarises suture measurements in the wild type specimens at P3, P7 and P10. In general, the size of the sutures decreased from P3 to P10 across all the measured regions. The posterior point of the frontal suture had the lowest suture size at P3 (0.46mm) and it decreased to 0.45±0.21mm and 0.23±0.03mm at P7 and P10 respectively. On the other hand, the posterior point of the sagittal suture had the largest suture size at P3 (3.24mm) and then decreased to 0.64±0.17mm and 0.43±18mm at P7 and P10 respectively.

At P7, the most lateral point of the left interparietal suture and the nearest point to the midsagittal plane of the right interparietal suture showed the highest standard deviations (0.3). While the anterior point of the sagittal suture had the lowest SD (0.07). At P10, the most lateral point of the left interparietal suture and the posterior point of the frontal suture with values of 0.27 and 0.03 had the highest and lowest SDs respectively.

The pie-charts in the Fig. 3.7, show percentage of reduction in sutures sizes from P3 to P7; P7 to P10 and P3 to P10 based on the average specimens. Considering the change between P3 and P10, sagittal suture showed the highest percentage of reduction (the average decrease percentage was 12%). While the frontal suture showed the lowest percentage of reduction (the average decrease percentage was 2%). Results show that the overall pattern of the suture closure is in a way that all the sutures have a similar size at P10 (minimum and maximum size for P3: 0.46mm and 3.24mm, for the Av. P7: 0.22mm and 0.80mm and for the Av. P10 are: 0.14mm and 0.49mm). This suggests that the fusion speed was highest at the sagittal suture and lowest at the frontal suture, and faster in early days than later days.

Fig. 3.8 shows the closure pattern at different sutures. It can be indicated that sutures fuse faster from P3 to P7 and fusion speed slows down from P7 to P10. Fig. 3.9 shows the lateral view of P3, Av. P7 and Av. P10 skulls. It can be seen that the big gap in the lateral side of the calvaria is closing, causing the interparietal suture to have the

highest rate of change. While the frontal and lambdoid sutures have the least change from P7 to P10. While there is a noticeable difference in suture size between interparietal and lambdoid sutures at P7, the suture sizes become more closed at P10 for these sutures.

The average suture closure rate is about 0.14mm per day for all sutures from P3 to P10. However, the minimum and maximum rates are 0.03mm/day and 0.43mm/day for second and fifth measuring points respectively. A relatively qualitative comparison of the bone formation patterns is presented in Fig. 3.9.

Table 3.5: The suture size at 14 sections for WT at P3, P7, and P10 (all dimensions are in mm).

Specimen Position	P3	P7							P10							Av daily closure
	10.2	7.3	7.7*	7.8	8.1	8.5	Av.	S. D.	18.8	17.1	17.5	17.10*	18.9	Av.	S.D	
1	0.63	0.7	0.6	0.27	0.61	0.48	0.53	0.17	0.56	0.47	0.36	0.21	0.35	0.39	0.13	0.03
2	0.46	0.3	0.39	0.28	0.81	0.46	0.45	0.21	0.19	0.26	0.2	0.23	0.25	0.23	0.03	0.03
3	1.2	0.55	0.56	0.61	0.6	0.72	0.61	0.07	0.29	0.38	0.26	0.21	0.42	0.31	0.09	0.13
4	1.46	0.43	0.44	0.24	0.54	0.46	0.42	0.11	0.31	0.56	0.31	0.15	0.27	0.32	0.15	0.16
5	3.24	0.48	0.68	0.53	0.9	0.59	0.64	0.17	0.52	0.68	0.44	0.23	0.29	0.43	0.18	0.40
6	1.11	0.81	0.95	0.48	0.35	1.05	0.73	0.3	0.41	0.52	0.3	0.2	0.24	0.33	0.13	0.11
7	1.16	0.29	0.64	0.46	0.06	0.77	0.44	0.28	0.24	0.32	0.31	0.15	0.1	0.22	0.1	0.13
8	1.24	0.5	0.89	0.54	0.95	0.57	0.69	0.21	0.22	1.48	1.07	0.15	0.37	0.31	0.14	0.13
9	1.1	0.63	0.92	0.5	0.87	1.09	0.8	0.24	0.58	0.81	0.38	0.22	0.26	0.45	0.25	0.09
10	1.36	0.16	0.62	0.52	0.26	0.73	0.46	0.24	0.41	0.5	0.15	0.1	0.12	0.26	0.19	0.16
11	1.41	0.36	0.98	0.67	0.51	1.05	0.71	0.3	0.46	1.39	1.55	0.54	0.33	0.49	0.27	0.13
12	1.53	0.36	0.3	0.43	0.58	0.89	0.51	0.24	0.13	0.63	0.52	0.41	0.18	0.37	0.22	0.17
13	1.11	0.1	0.24	0.03	0.38	0.35	0.22	0.15	0.21	0.13	0.1	0.13	0.13	0.14	0.04	0.14
14	1.3	0.61	0.32	0.52	0.53	0.75	0.55	0.16	0.64	0.72	0.3	0.58	0.16	0.48	0.24	0.12
Av	1.31	0.45	0.61	0.43	0.57	0.71	0.55		0.37	0.63	0.45	0.25	0.25	0.34		0.14

*: Average specimens of that group.

Fig. 3.7: Suture size changes for WT in percent, from P3 to P7, P7 to P10 and P3 to P10.

Fig. 3.8: Suture size changes (P3, Av. P7, and Av. P10) at different sutures. Suture closure rate decreases from P3 to P10. The lambdoid suture is more closed at the medial point at all ages.
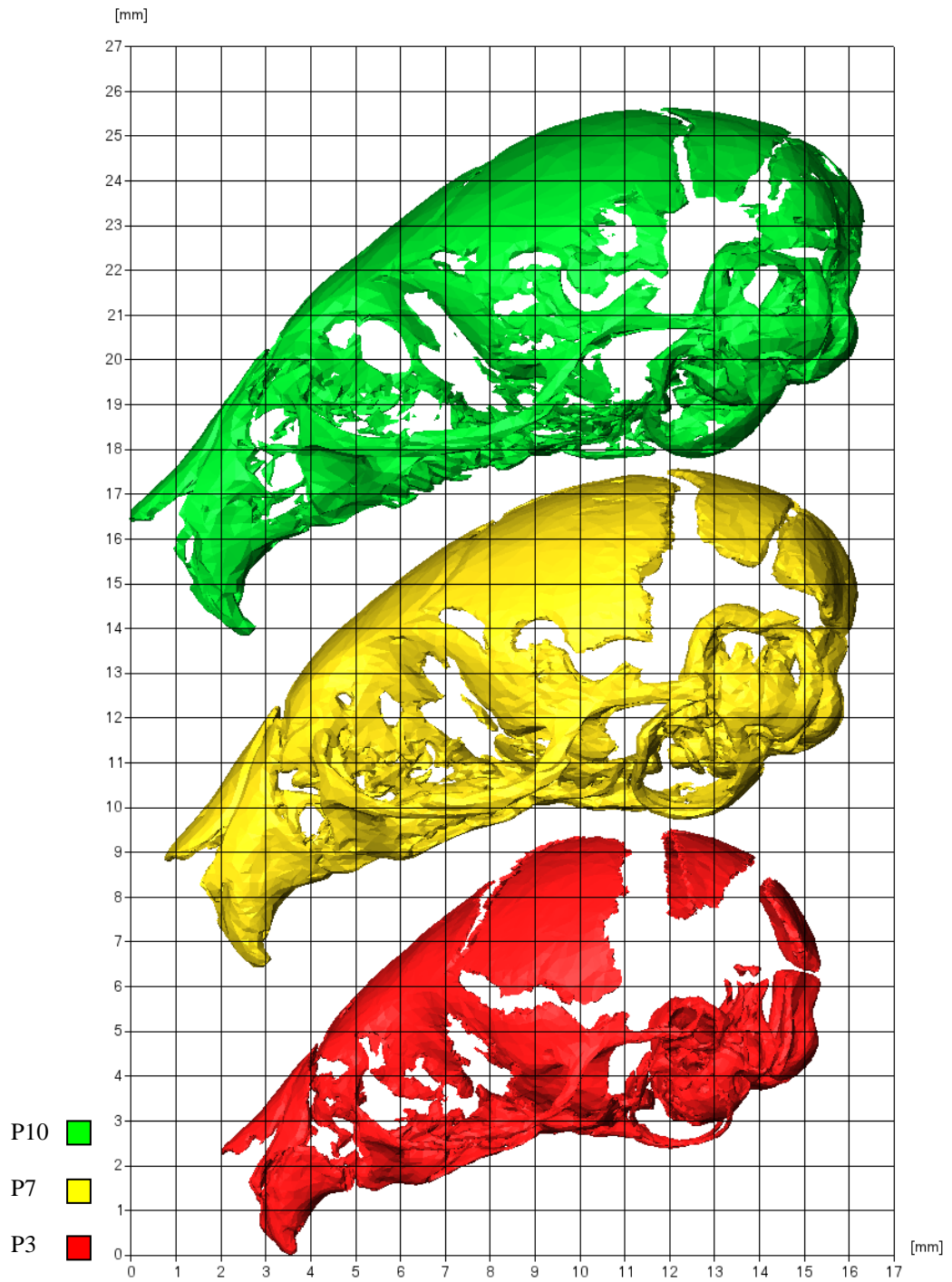
Fig 3.9: Average P3, P7, and P10 skulls. The lateral view showing the overall pattern of new bone generation.

Mutant type:

Table 3.5 summarises suture measurements in the mutant type specimens at P3, P7, and P10. Similar to the wild type pattern, the size of the sutures decreased from P3 to P10 across all the measured regions. The medial point of the lambdoid suture had

the lowest suture size at P3 (0.73mm) and it decreased to 0.17±0.13mm and 0.04±0.06mm at P7 and P10 respectively. On the other hand, the posterior point of the sagittal suture (like wild type) had the largest suture size at P3 (2.84mm) and then decreased to 0.69±0.33mm and 0.50±13mm at P7 and P10 respectively.

At P7, the posterior point of the sagittal suture showed the highest standard deviations (0.33). While the medial point and most lateral point (right) of the lambdoid suture had the lowest SD (0.13). At P10, the medial point of the right interparietal suture and the anterior point of the sagittal suture with values of 0.77 and 0.05 had the highest and lowest SDs respectively.

The pie-charts in the Fig. 3.10, show percentage of reduction in sutures sizes from P3 to P7; P7 to P10 and P3 to P10 based on the average specimens. Considering the change between P3 and P10, sagittal suture showed the highest percentage of reduction (similar to wild type), with the average decrease percentage of 15%. While the lambdoid suture showed the lowest percentage of reduction (the average decrease percentage was 2.7%). Results shows that the overall pattern of the suture closure is in a way that there is a big difference between all the suture sizes at P10 (minimum and maximum size for P3: 0.4mm and 2.4mm, for the Av. P7: 0.17mm and 1.13mm and for the Av. P10 are: 0.04mm and 0.88mm).

Fig. 3.11 shows the closure pattern at different sutures. It can be indicated that sutures width reduction is faster from P3 to P7 and it slows down from P7 to P10. While the frontal, sagittal, and lambdoid sutures have the least change from P7 to P10. The average bone formation rate is about 0.14mm per day for all sutures from P3 to P10. However, the minimum and maximum rates are 0.08mm/day and 0.33mm/day for thirteenth and fifth measuring points respectively.

Table 3.5: The suture size at 14 sections for MT at P3, P7, and P10 (all dimensions are in mm).

Specimen Position	P3	P7							P10							Av daily closure
	10.1	7.4	7.5	7.6*	8.2	8.11	Av.	S.D.	17.6	17.12	17.13	17.14*	18.4	Av.	S.D.	
1	1.03	0.67	0.18	0.38	0.32	0.36	0.38	0.18	0.22	0.63	0.08	0.35	0.52	0.36	0.22	0.10
2	0.84	0.09	0.17	0.28	0.49	0.38	0.28	0.16	0.23	0.26	0.09	0.27	0.19	0.21	0.07	0.09
3	1.88	0.21	0.41	0.22	0.63	0.34	0.36	0.17	0.25	0.20	0.28	0.30	0.34	0.27	0.05	0.23
4	1.41	0.13	0.49	0.11	0.79	0.50	0.40	0.29	0.48	0.37	0.22	0.38	0.15	0.32	0.13	0.16
5	2.84	0.40	0.71	0.44	1.22	0.68	0.69	0.33	0.62	0.44	0.32	0.64	0.48	0.50	0.13	0.33
6	1.86	1.06	0.95	1.00	1.56	1.10	1.13	0.24	1.36	0.47	0.17	0.86	0.33	0.64	0.48	0.17
7	1.58	0.92	0.91	0.91	0.61	1.08	0.89	0.17	0.95	0.46	0.31	0.81	0.48	0.60	0.27	0.14
8	1.40	0.78	0.59	0.60	0.49	0.89	0.67	0.16	0.80	0.54	0.00	0.65	0.46	0.49	0.30	0.13
9	1.16	0.26	0.29	0.25	0.52	0.50	0.36	0.13	0.54	0.18	0.32	0.36	0.26	0.33	0.13	0.12
10	1.24	0.61	0.16	0.72	0.34	0.98	0.56	0.32	0.59	0.16	0.69	0.81	0.35	0.52	0.26	0.10
11	0.91	0.26	0.36	0.40	0.61	0.65	0.46	0.17	0.19	0.09	0.17	0.19	0.29	0.19	0.07	0.10
12	1.37	0.62	0.62	0.97	0.42	1.07	0.74	0.27	2.21	0.32	0.45	0.86	0.58	0.88	0.77	0.07
13	1.33	0.63	0.75	0.80	0.73	1.22	0.83	0.23	1.61	0.75	0.05	0.85	0.60	0.77	0.56	0.08
14	0.73	0.05	0.04	0.19	0.32	0.27	0.17	0.13	0.00	0.00	0.00	0.11	0.10	0.04	0.06	0.10
Av	1.40	0.48	0.47	0.52	0.65	0.72	0.57		0.72	0.35	0.23	0.53	0.37	0.44		0.14
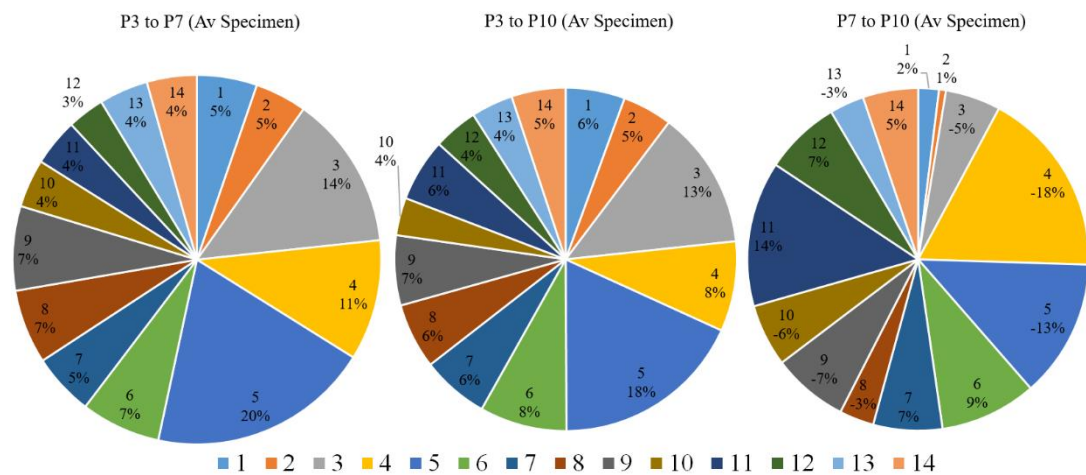
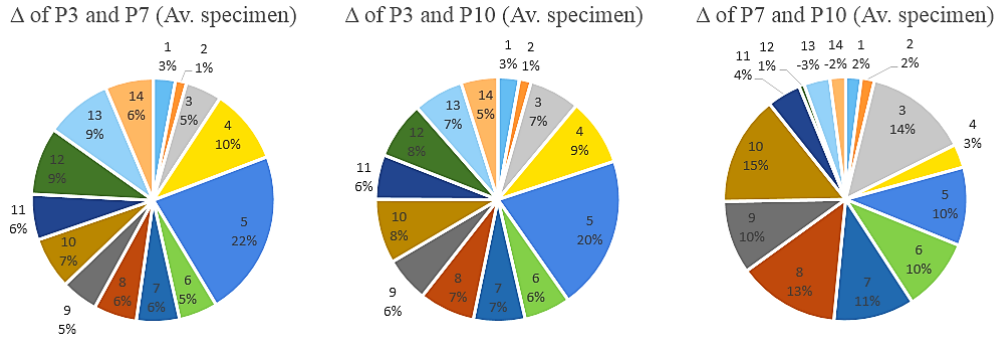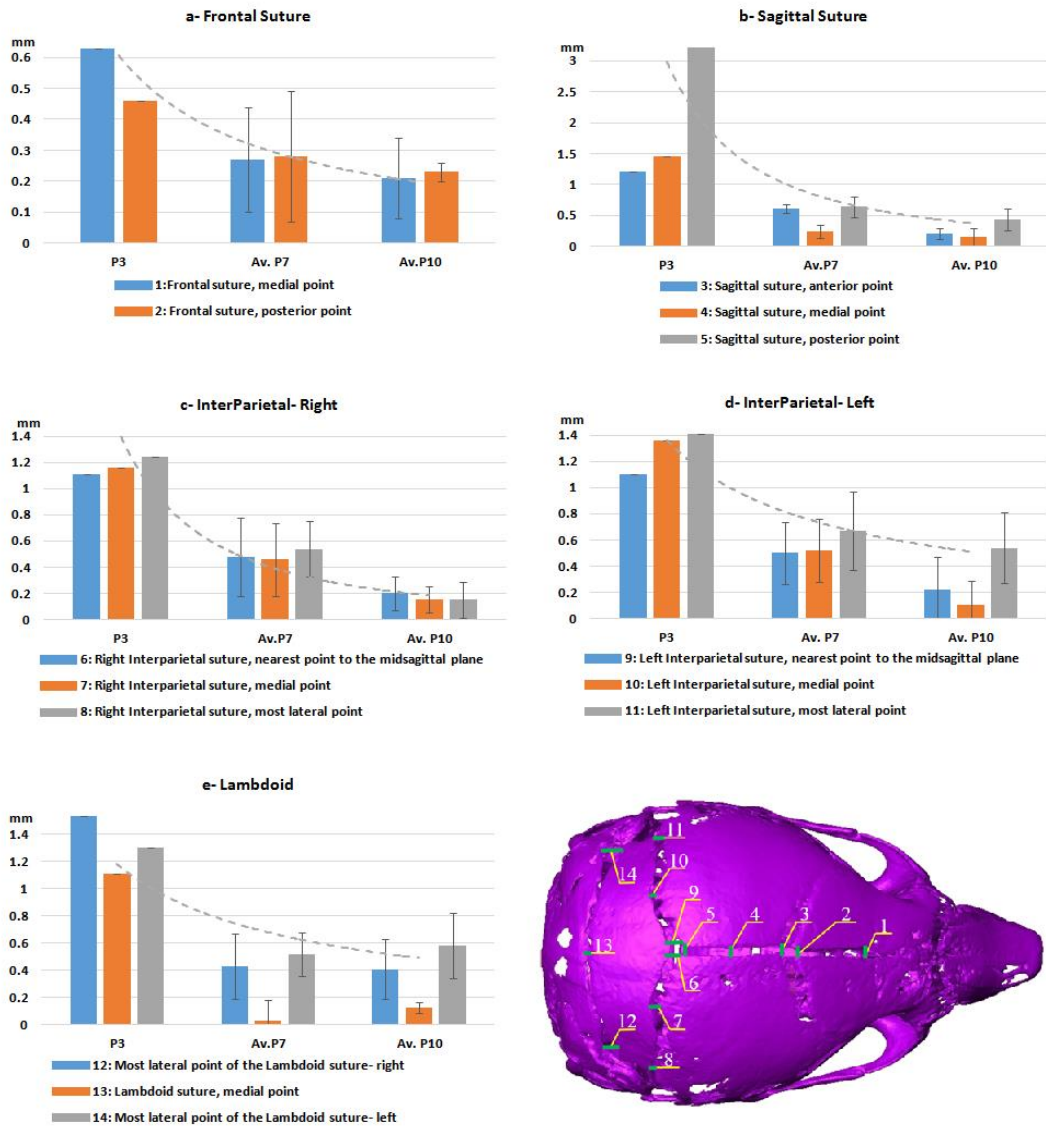**Fig. 3.10:** MT suture size changes in percent, from P3 to P7, P7 to P10 and P3 to P10.
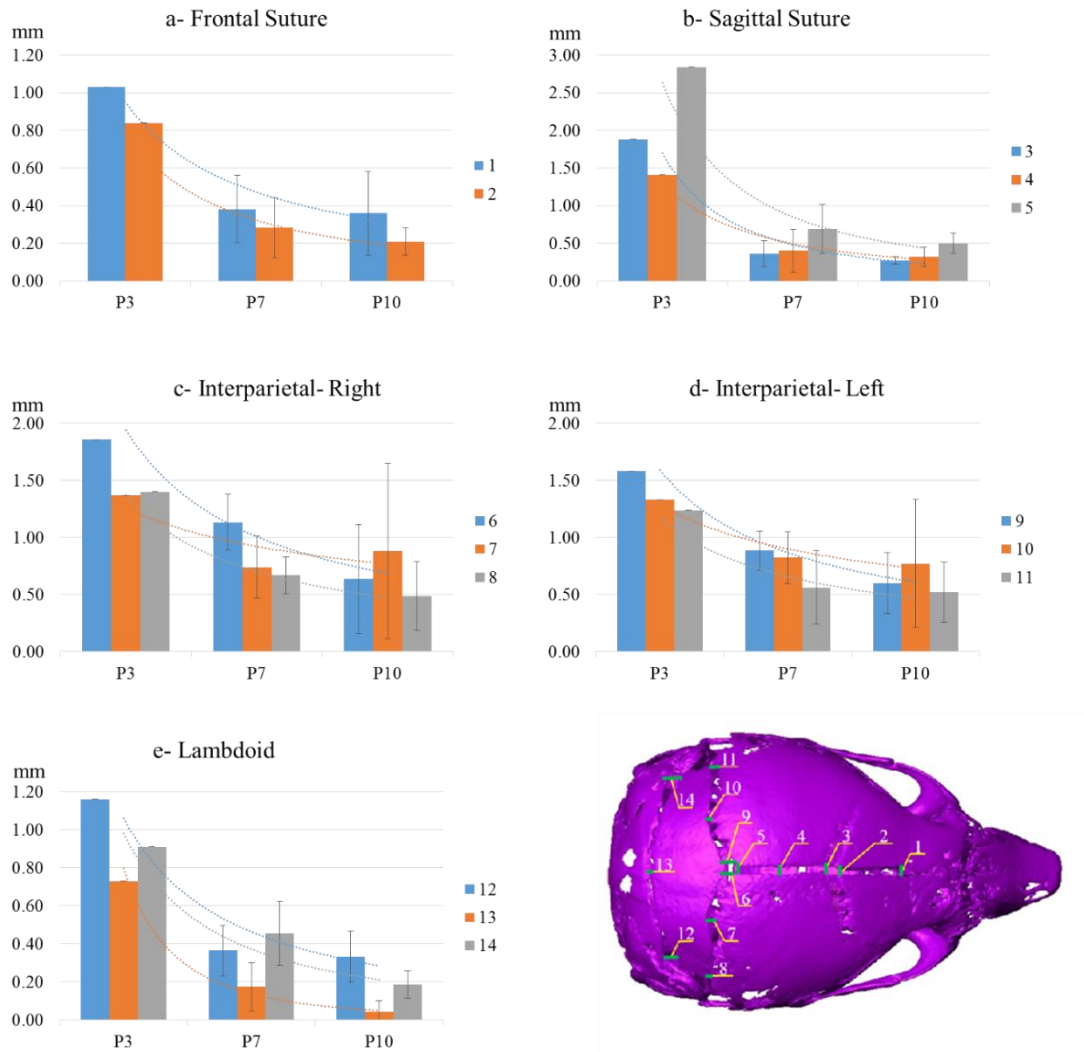
Fig. 3.11: Suture size changes (P3, Av. P7, and Av. P10) at different sutures. Suture closure rate decreases from P3 to P10. The lambdoid suture is more closed at the medial point at all ages.

3-4 Discussion

A series of morphological analysis were performed in this Chapter to find an average specimen at P7 and P10 and also to quantify the calvarial suture size changes during the development. Average specimens were found and a series of overall pattern of changes in the skull and suture sizes from P3-10 were identified.

Skull measurements

Findings of gross morphological measurements (Table 3.3, Fig. 3.5 and Fig. 3.10) highlighted that the overall skull height has little change from P7 to P10, while the width grows until about P20 and the length growth plateaus at about P30 (Nakata

1981 and Aggarwal *et al.* 2009). Our study showed similar findings to previous studies, however, this is to best of our knowledge the first study that quantify morphological changes of mouse skull in early postnatal ages i.e. P3-10.

Fig. 3.12 shows the lateral view of mutant and wild type P3, P7, and P10 skulls. Similar to previous studies of *Fgfr2*$^{C342Y/+}$ mouse model, our measurements showed a shorter length with increased width and height for MT calvaria. This is consistent with the previous finding of Perlyn *et al.* (2006) and Liu *et al.* (2013).
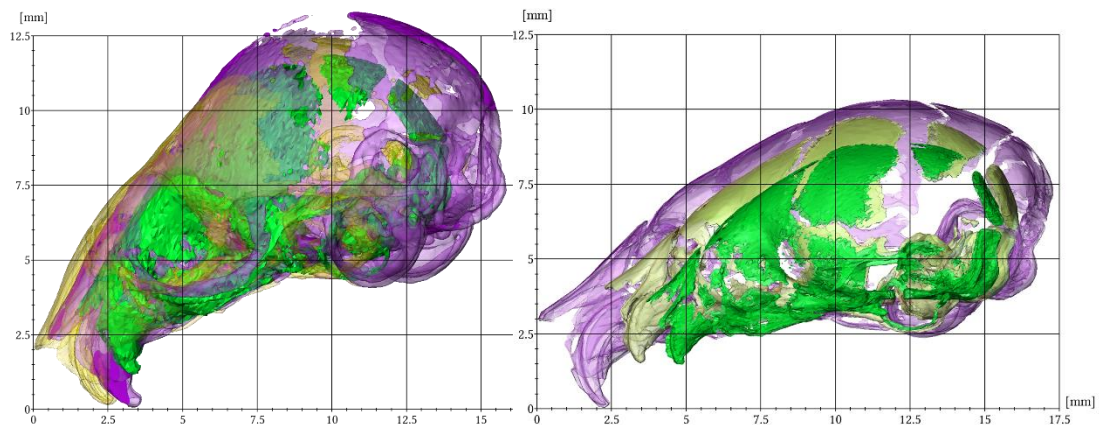
Fig 3.12: Overall skull growth pattern from P3 to P7 and P10 for MT (left) and WT (right) skulls. Mutant skulls, compared to the WT, show a smaller length with increased height at all ages.

Suture measurements:

Standard deviations for some of the suture measurements were relatively high. It should be noted that at this stage (P3 to P10), due to the fast growth rate, even a half a day difference in birth time can make a remarkable difference. Since it wasn't known if all specimen were from the same litter or not, this can be the main reason for the size differences at the same age. Another source of error can be the quality of segmentation and errors due to low resolution of the images (20μm to 40μm).

Fig. 3.13 compares the overall skull growth and suture closure pattern for WT and MT mice from P3 to P10. It can be seen that frontal suture is much wider in the MT while is almost fully fused at P7. This shows that there is a higher bone formation rate at this region for MT. On the other hand, interparietal suture has a wider gap at P10, compared to WT, while at P3 it is similar in WT and MT. Which indicates a slower bone formation rate at this region. Table 3.6 shows the suture closure rate

comparisons for WT and MT mice at 14 different points measured on P3, P7 and P10 specimens. Note that the overall P3 to P10 suture closure rates are very similar for WT and MT mice. Fig. 3.14 is a more visual comparison of suture closure rates. It shows WT/MT values for 14 section plus the average values. Red colour indicates higher suture closure rates for MT and yellow colour indicates higher suture closure rates for WT.

No measurements were taken on the coronal sutures due to their difference in mechanism of suture fusion and overlapping two adjacent bones (frontal and parietal) causing suture size change. The average skulls from skull measurements were measured to be the same as the average skull from the suture sizes. Based on the calvarial size and suture measurements evaluated in this Chapter, in the next two Chapters calvarial growth and bone formation at the sutures will be modelled from P3 to P10, using finite element modelling of the P3 skull.

In summary, the morphological studies in this Chapter indicated that the calvarial length, width, and height continuously increase from P3 to P10 for both WT and MT models. MT models were shorter in length compared to WT mice, while their height was increased. These observations are in line with previous studies (Eswarakumar *et al.*, 2004; Liu *et al.*, 2013; Martínez-Abadías *et al.*, 2013; Perlyn, DeLeon, *et al.*, 2006; Peskett *et al.*, 2017). The results and average models obtained in this Chapter are the validation reference points for the forthcoming Chapters that will simulate and model calvarial growth and bone formation at the sutures.
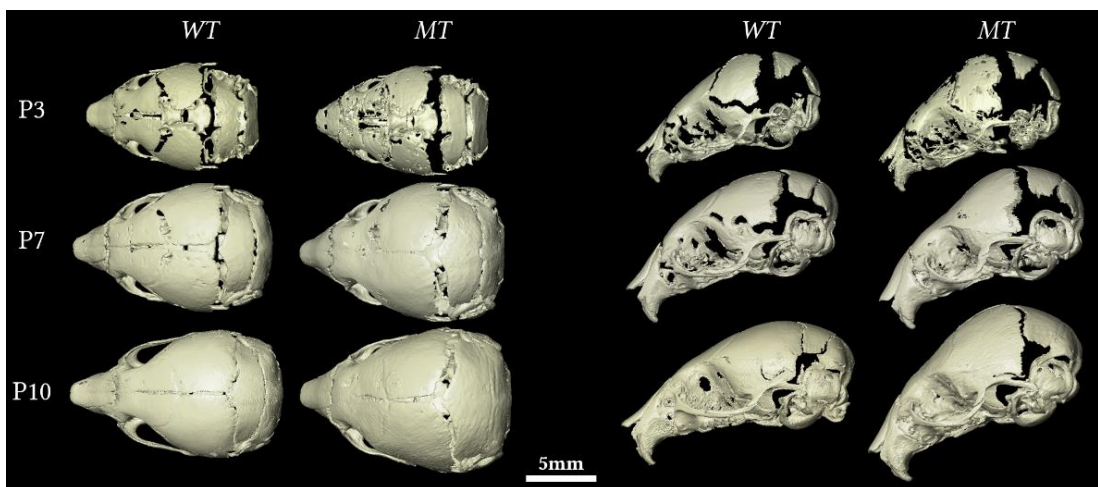
Fig 3.13: Overall skull growth and suture closure patterns from P3 to P10 for MT and WT skulls.

Table 3.6: A comparison of WT and MT bone formation rates from P3 to P10 at 14 measured sections. MT/WT bone formation rate ratios indicate higher (more than one) or lower (lower than one) bone formation rates in MT.

	WT	MT	MT/WT
1	0.03	0.1	3.33
2	0.03	0.09	3
3	0.13	0.23	1.77
4	0.16	0.16	1
5	0.4	0.33	0.82
6	0.11	0.17	1.55
7	0.13	0.14	1.08
8	0.13	0.13	1
9	0.09	0.12	1.33
10	0.16	0.1	0.62
11	0.13	0.1	0.77
12	0.17	0.07	0.41
13	0.14	0.08	0.57
14	0.12	0.1	0.83
Av	0.138	0.137	0.99
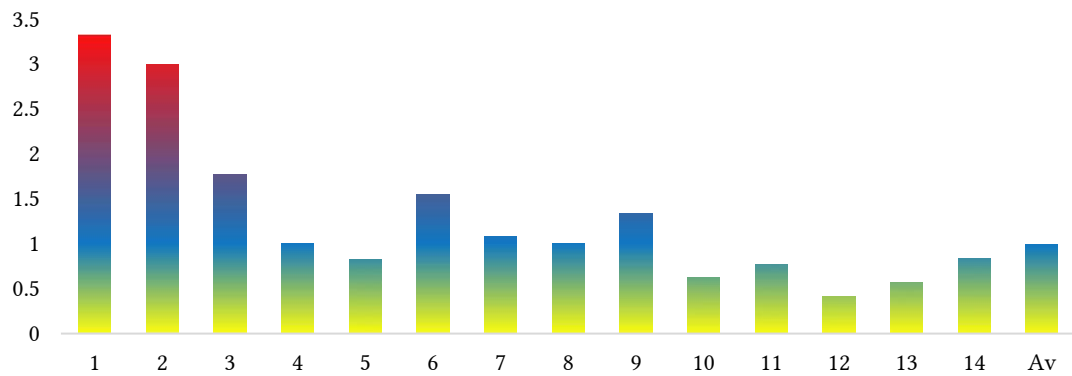
Fig 3.14: MT/WT bone formation rate ratios. WT/MT values for 14 section plus the average. Red colour indicates higher suture closure rates for MT, yellow indicates higher suture closure rates for WT, and blue shows a similar bone formation rate for WT and MT.

Chapter 4: Predicting the radial skull growth

4-1 Introduction

This chapter describes the development of finite element models of mouse skull growth. It is divided into two studies. Study 1 describes development of a finite element model of a mouse skull at postnatal day 3 (P3). This model was used to predict wild type mouse skull shape at P10. Here, several sensitivity tests were performed and summarised to the choice of input parameters. Study 2 uses the model that was developed in Study 1 to predict the skull shape of a mutant $Fgfr2^{C342Y/+}$ mouse at P10.

4-2 Study 1: Predicting wild type mouse skull shape at P10

To predict the mouse skull growth from P3 to P10, a finite element model of the mouse skull at P3 was developed. Several sensitivity tests were performed where the baseline values were altered to understand their effect on the predicted skull shape. Results were compared to micro computed topography (CT) images of the average *ex vivo* P10 skull as identified in Chapter 3.

4-2-1 Materials and methods

Model development

For the purpose of this study a wild type mouse at postnatal day 3 (P3) was scanned using an X-Tek HMX microCT scanner (X-Tek Systems Ltd, UK). MicroCT scan images were then imported into an image-processing software (AVIZO Image

Software version 6.0, TGS Inc, USA). Bone and sutures were segmented manually. The brain was segmented by filling the whole intracranial volume, hence it was required to ensure that the skull was fully enclosed. Therefore, the foramen magnum was filled and regions of the calvaria that were not fully developed were also manually segmented (Fig. 4.1). The model eventually consisted of twenty-three different sections. Surface model of the skull was then transformed into a meshed solid geometry using AVIZO and was then imported into a finite element software ANSYS v. 14.5 (ANSYS Inc., Canonsburg, PA, USA). The model was meshed using SOLID187 tetrahedral elements (10 node elements with quadratic displacement behaviours) that are well suited for modelling irregular geometries (ANSYS, 1997, 2010). The models consisted of about 144000 elements.
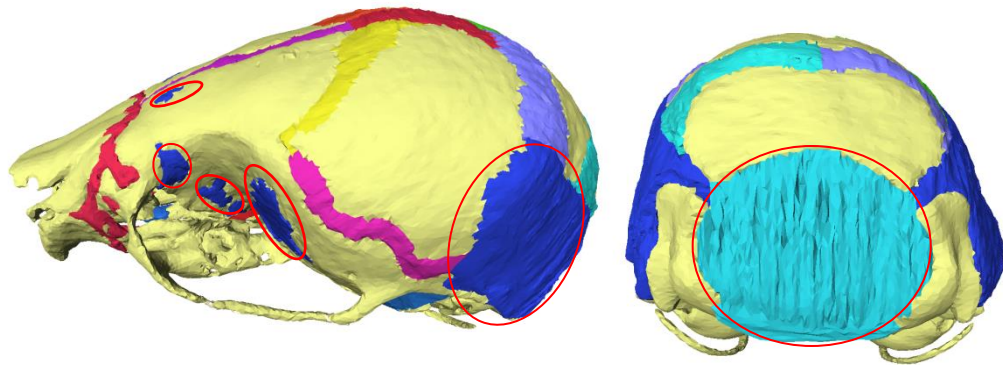
Fig. 4.1: Lateral and posterior views of the 3D model of the P3 skull. Light yellow is bone and all other colours are soft tissue. Red circles highlight the filling materials.

Material properties

All sections were assigned isotropic material properties. In the baseline model, an elastic modulus of 3500 MPa, and 30 MPa were assumed for the bone and sutures respectively. These were based on extrapolating in-house nanoindentation testing of frontal and parietal bone in mice at P10, P20, and P70 (Moazen *et al.*, 2015). Brain and the filling material at the foramen magnum were modelled with the elastic modulus of 150 MPa and 30 MPa. A Poisson's ratio of 0.3 was used for all the materials while 0.48 was used for the brain (Claessens, Sauren and Wismans, 1997). See Table 4.1 for a summary of the materials used in the baseline model. The filling material in the developing bone was assumed to have the same mechanical properties as the suture.

Table 4.1: Young's modulus and Poisson ratio for different materials used in the FE model.

	E (MPa)	ν	Reference
Bone Tissue	3500	0.3	Moazen *et al.* 2015
Suture Tissue	30	0.3	Moazen *et al.* 2015
Brain Tissue	150	0.48	Claessens *et al.* 1997
Filling Material	30	0.3	-

Boundary condition and loading

The intracranial volume (ICV) expansion during the calvarial growth was modelled by isotropic expansion of the ICV. This was achieved using thermal expansion analogy. Here a change of 100 degrees in the temperature was assumed and coefficient of thermal expansion was altered by trial and error to achieve the desired ICV (from about 243 mm^3 at P3 to about 393 mm^3 at P10). The thermal expansion that led to less than 5% difference between the predicted brain and actual brain volume (or intracranial volume) was considered acceptable. Note the compliance of the overlying bone and sutures were dictating the overall shape of the skull. For example, to predict the skull shape at P10 the brain volume of the P3 skull was expanded to the brain volume of the P10 based on the data available in the literature (see Fig 2.12 of Chapter 2). All degrees of freedom were constrained for 3 nodes on the presphenoid bone (Fig. 4.2). The presphenoid bone was constrained since quantifying the wild type mouse skull growth highlighted that this bone during the development grow centrically and it relatively remains at the same position (see section 3-3-2, Fig. 3.6 of Chapter 3).

Measurements

Twenty-four landmarks (LMs) were used (on anatomically observable positions) to quantify the difference between the *ex vivo* P10 (based on 3D reconstructions from CT data) and the predicted P10 skull (from the FE model). While more LMs would have clearly increased the accuracy of the measurements it was challenging to identify the same anatomical position in the P3 due to large areas of soft tissue. The

LMs were positioned on anatomical features that were identifiable in the P3. See Table 4.2 and Fig. 4.3 for LMs details.

Root mean square (RMS) between the position of actual and predicted LMs were calculated. RMS values were obtained using the coordinate of landmarks at P3 and P10 (derived from AVIZO), the resultant coordinates of P3 landmarks from ANSYS, and the following equation:

$$RMS = \sqrt[2]{\sum_{i=1}^{n} d_i^2 / n} \,,$$

where n is the number of landmarks (20 or 24) and d_i is the distance between two corresponding landmarks of P10 (AVIZO) and P10 (ANSYS). And d_i is obtained by:

$$d_i = \sqrt[2]{(x_{i+1} - x_i)^2 + (y_{i+1} - y_i)^2 + (z_{i+1} - z_i)^2} \,.$$

Two RMS values were calculated: (1) based on the LMs positioned only on the calvaria – RMS1 (2) based on the LMs position on the whole skull – RMS2 (see Fig. 4.4). It must be noted that (1) this study is mainly focused on the calvarial growth and not the facial growth hence RMS1 values are of main interest (2) RMS of zero would have meant identical match between the predicted shape and *ex vivo* results.
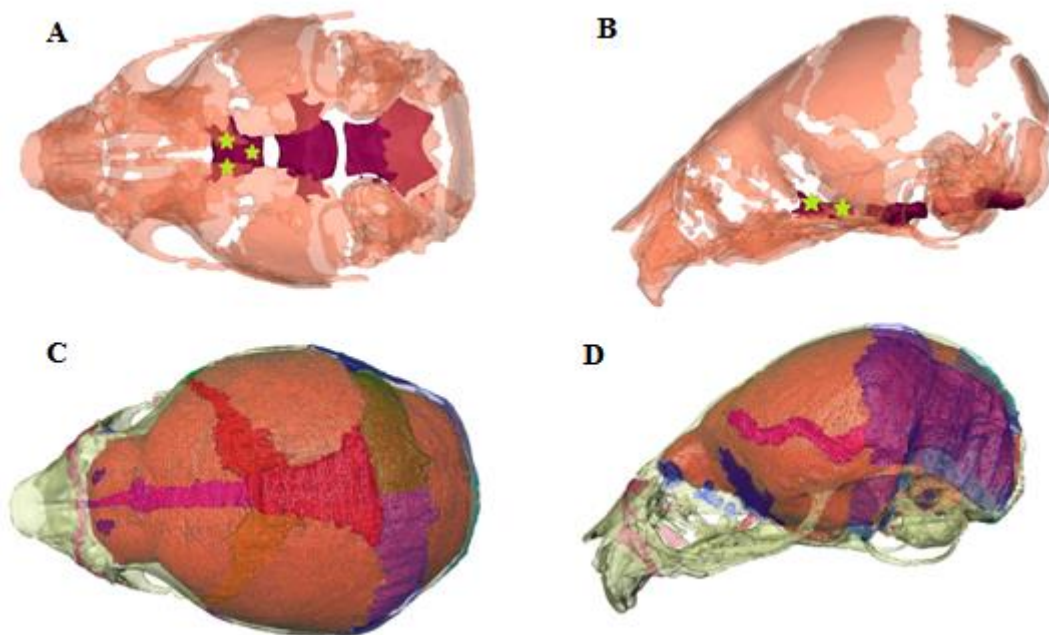
Fig. 4.2: Dorsal and lateral views of the P3 model. Boundary conditions were applied to the presphenoid bone (A and B- showing only bone tissue and stars indicate the constrained nodes). The thermal expansion was applied to the brain tissue (C and D- shown in orange).

Table 4.2: Landmark details.

1	Most anterior-medial point of the nasal bone
2	Most anterior-medial point of the premaxillae bone
3 & 4	Most anterior point at intersection of premaxillae and nasal bones (L & R)
5 & 6	Most medial intersection of the frontal and parietal bones, taken on the frontal (L & R)
7 & 8	Most medial intersection of the frontal and parietal bones, taken on the parietal (L & R)
9 & 10	Most lateral intersection of the frontal and parietal bones, taken on the frontal (L & R)
11 & 12	Midpoint on medial side of the parietal bone (L & R)
13 & 14	Most posterior-inferior point on the parietal (L & R)
15 & 16	Joining of squamosal body to zygomatic process of squamous portion of temporal bone (L & R)
17 & 18	Most posterior-inferior point on the interparietal (L & R)
19	Most anterior-medial point of the interparietal bone
20	Most anterior-medial point of the occipital bone
21 & 22	Most posterior-lateral point of the occipital bone
23	Most posterior-medial point of the occipital bone
24	Most posterior-medial point of the basioccipital bone
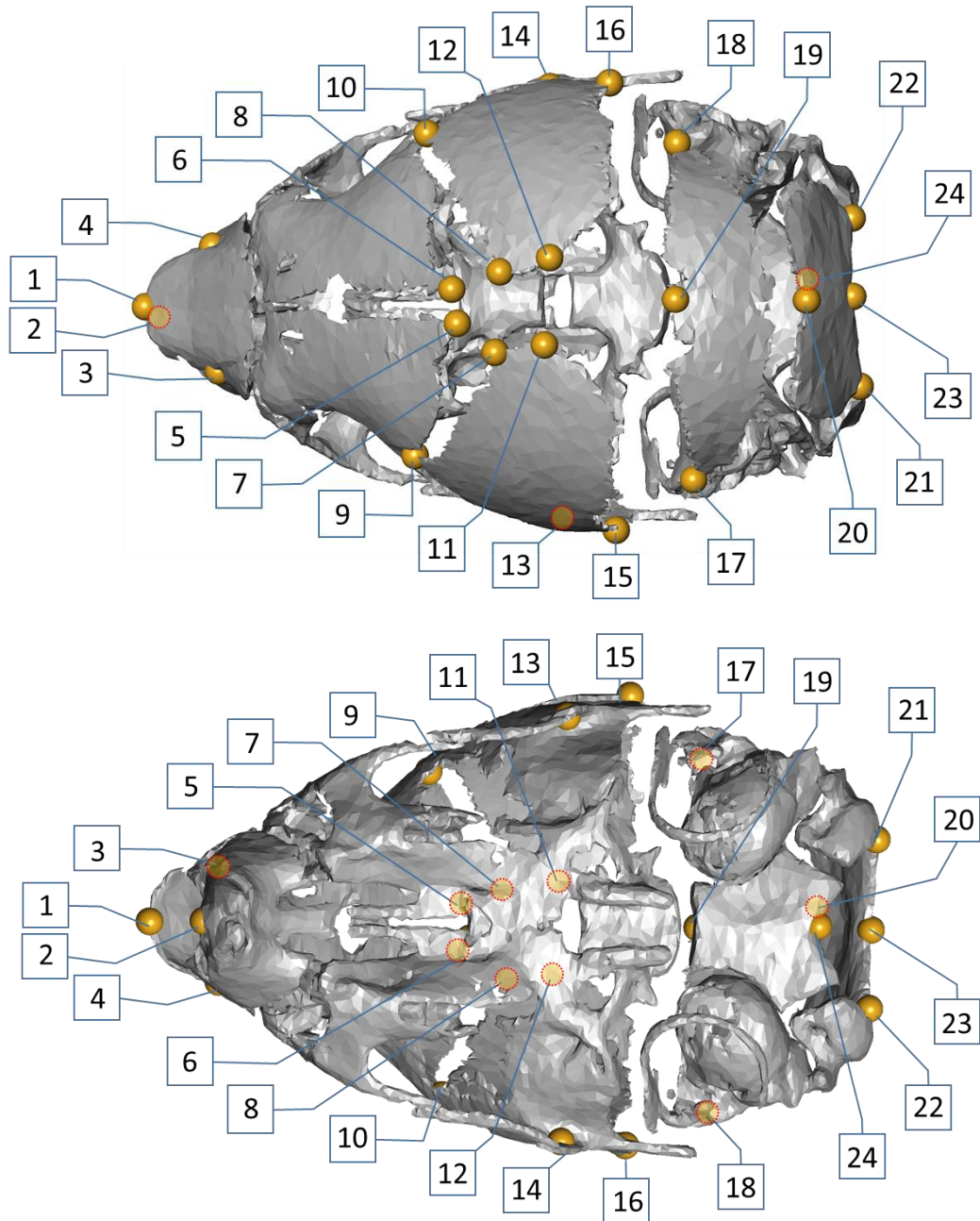
Fig. 4.3.1: Different views of mouse skull at P3 showing the landmark positions as indicated in Table 4.2.
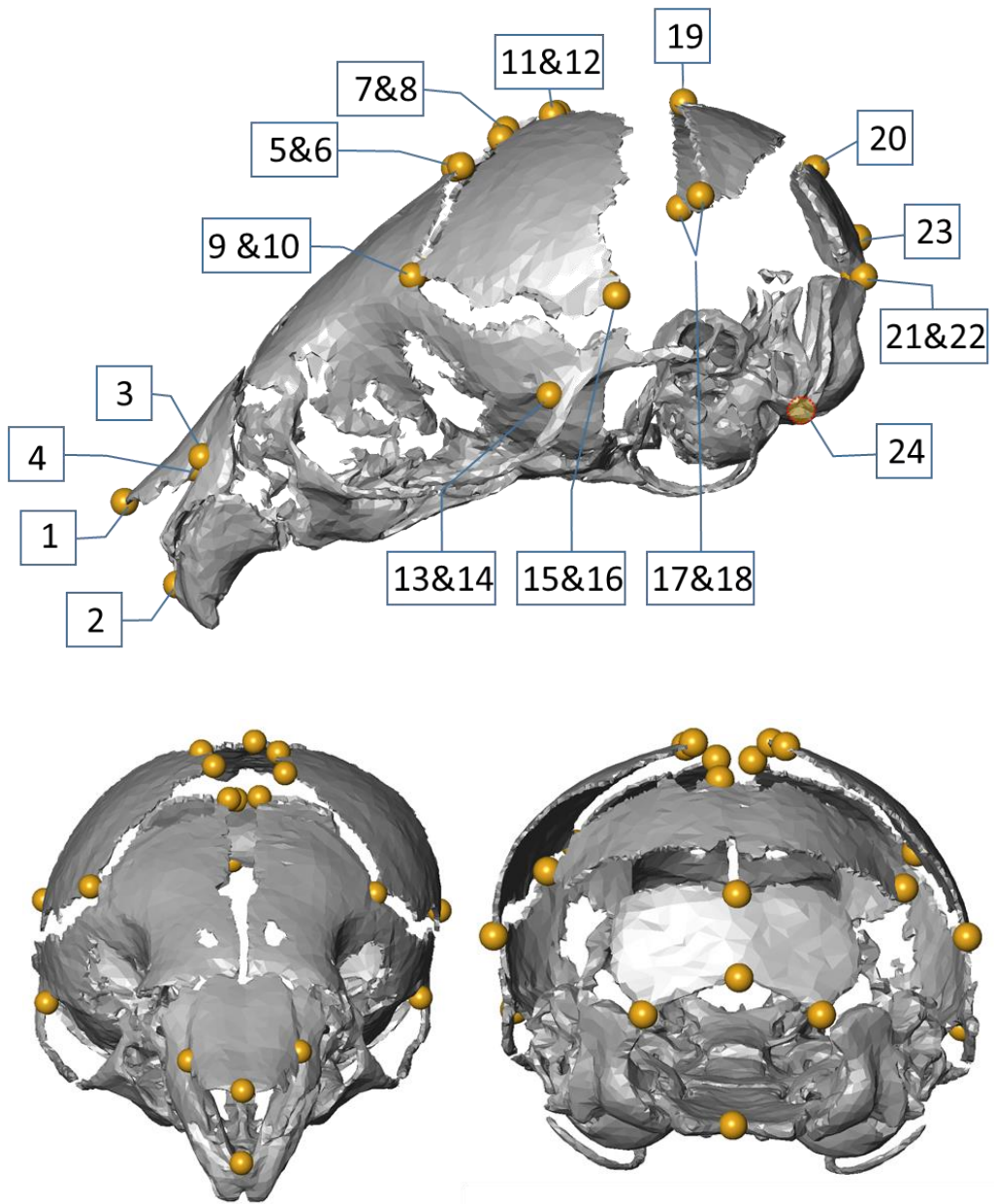
Fig. 4.3.2: Different views of mouse skull at P3 showing the landmark positions as indicated in Table 4.2.
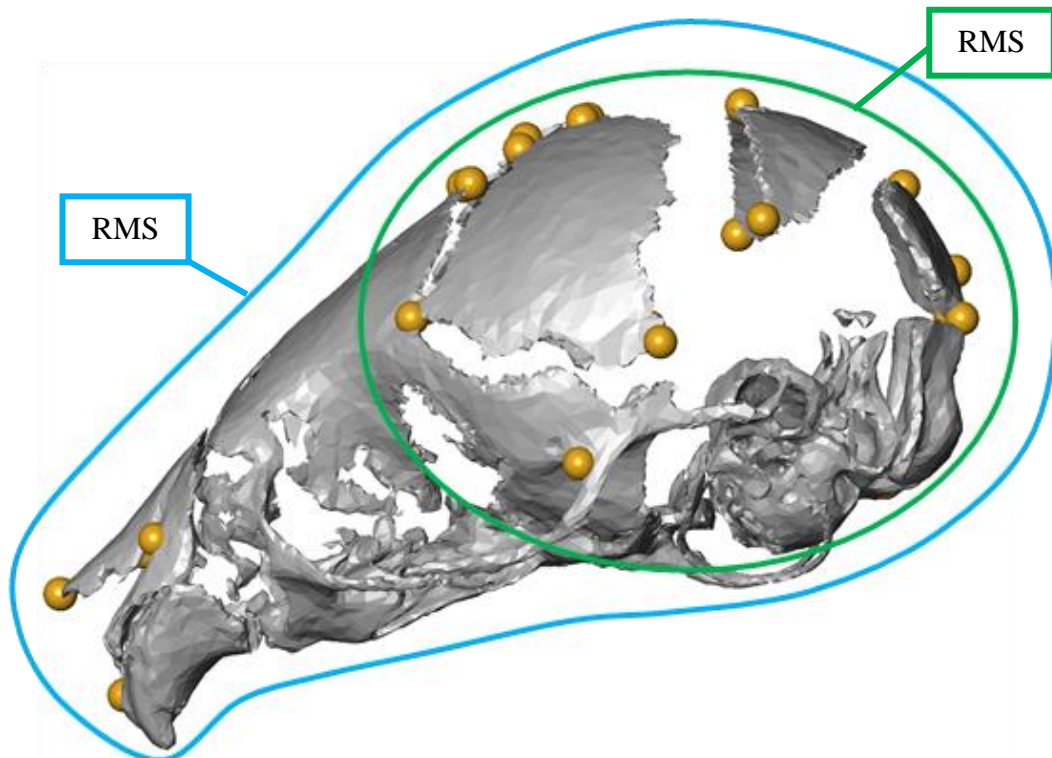
Fig. 4.4: Twenty four landmarks were used to indicate the shape difference between the *ex vivo* P10 (from CT data) and the P10 resultant from the FE predictions. RMS1 was calculated based on calvarial landmarks (20 landmarks) while RMS2 was calculated based on calvarial and facial landmarks.

Mesh convergence

Mesh convergence to the overall skull shape was tested by increasing the number of elements from about 144,000 to 7,500,000 in five steps. Overall skull shape and RMS were compared across the models. Note that, sensitivity studies were carried out on the model with 144,000 elements. Since our initial results highlighted that the overall skull shape was converged with this model. However, the exact values and pattern of strain distribution in the bone and suture were not converged and required higher mesh density.

At the first step the number of elements in the smallest model (with about 144,000 elements, model 1), were increased to about 450,000 elements (model 2). Next, the number of elements were increased such that sutures had at least two elements in their thickness but other sections, i.e. bone, had only one (about 870,000 elements, model 3). Then mesh density was increased to two elements for all of the sections (about 3,000,000 elements, model 4). Finally, there were at least four elements at the thickness of sutures and two elements for other sections (about 7,500,000 elements,

model 5). To reduce the huge number of elements that existed in the brain, it was meshed in a way that the model had bigger elements at the central areas and finer meshes at borders with bone and sutures (Fig. 4.6).

Model	Number of elements
1	144,368
2	436,345
3	870,415
4	3,096,159
5	7,523,779
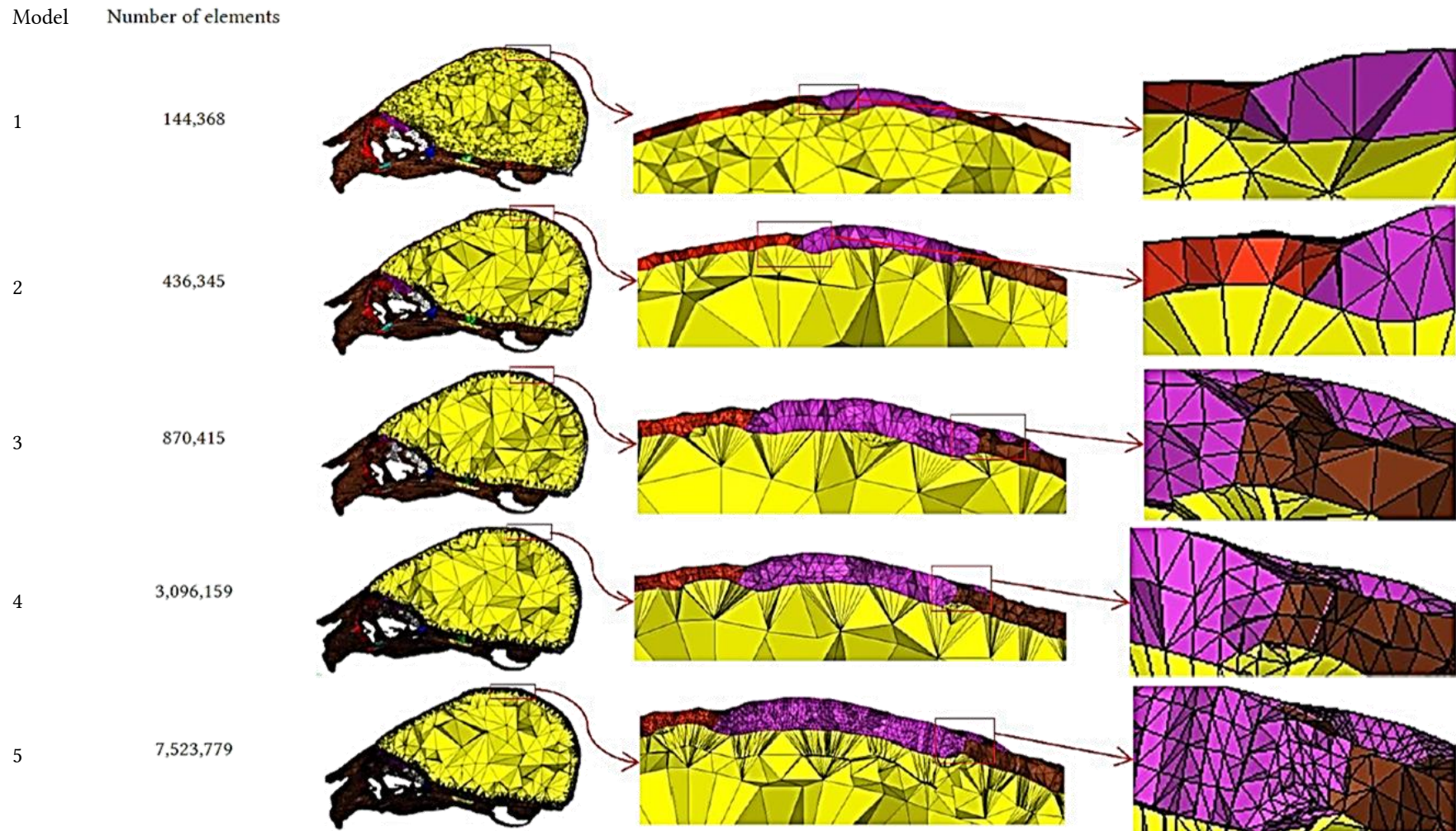
Fig. 4.5: Different number and configuration of meshes used to test the mesh convergence.
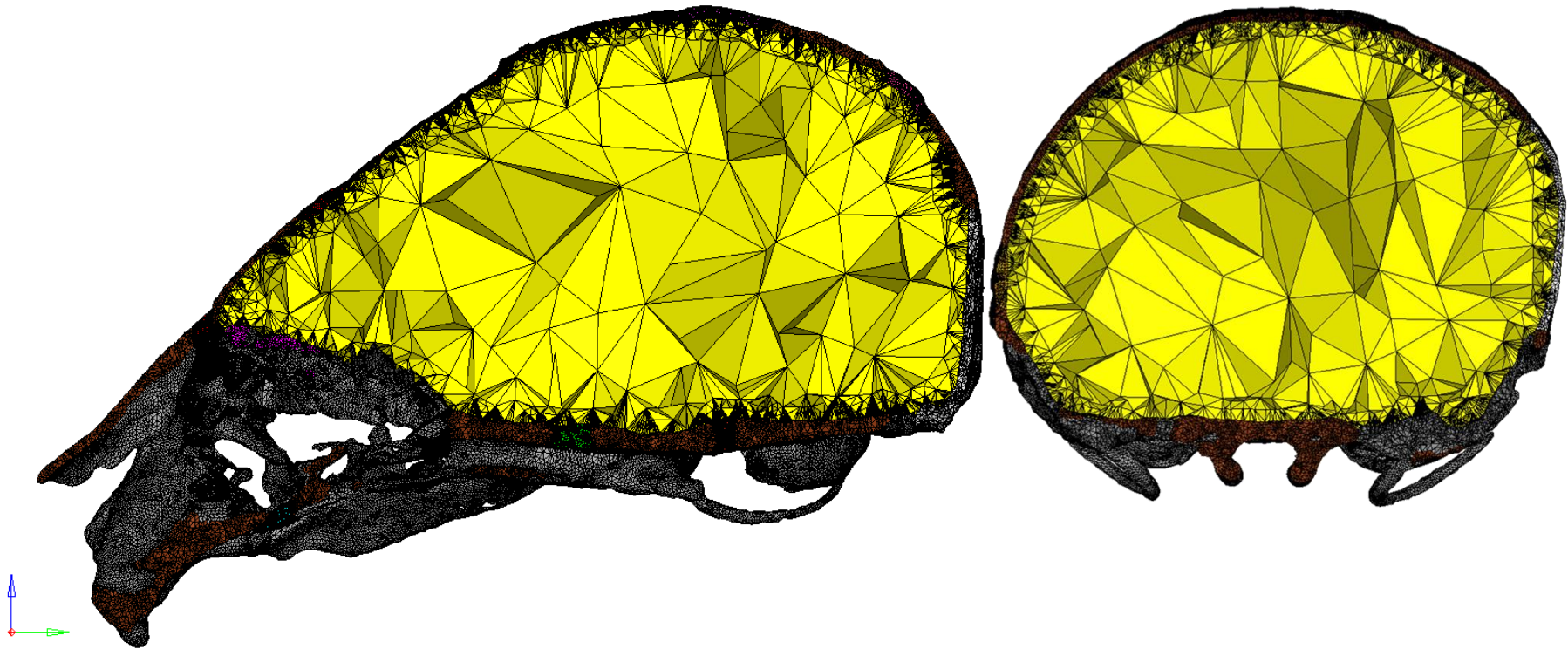
Fig. 4.6: Composition of elements in the model with the highest number of elements in mesh convergence analysis. All sutures have at least four elements in the thickness and all other sections have at least two elements in the thickness. In all of the models, the brain has a bigger mesh size in the middle and a finer mesh size in the outer areas.

Sensitivity tests

The key input parameters defined for the baseline model were altered in several sensitivity tests to understand the sensitivity of the model to these parameters. These tests included: (1) the elastic modulus of the bones; (2) the elastic modulus of the sutures; (3) the elastic modulus of the brain; (4) the Poisson's ratio of brain (Table 4.3) and (5) the boundary conditions (Fig. 4.7).

Table 4.3: Baseline input parameters and their variations for the convergence tests.

	Bone E (MPa), ν	Suture E (MPa), ν	Brain E (MPa), ν	Boundary condition
Baseline	3500, 0.3	30, 0.3	150, 0.48	2nd set
Sensitivity 1	E= 7000 and 1750	NA	NA	NA
Sensitivity 2	NA	E= 300 and 3	NA	NA
Sensitivity 3	NA	NA	E= 1500, 150, 15, 5 and 1	NA
Sensitivity 4	NA	NA	ν= 0.4 and 0.3	NA
Sensitivity 5	NA	NA	NA	1st and 3rd set

1st set

2nd set

3rd set
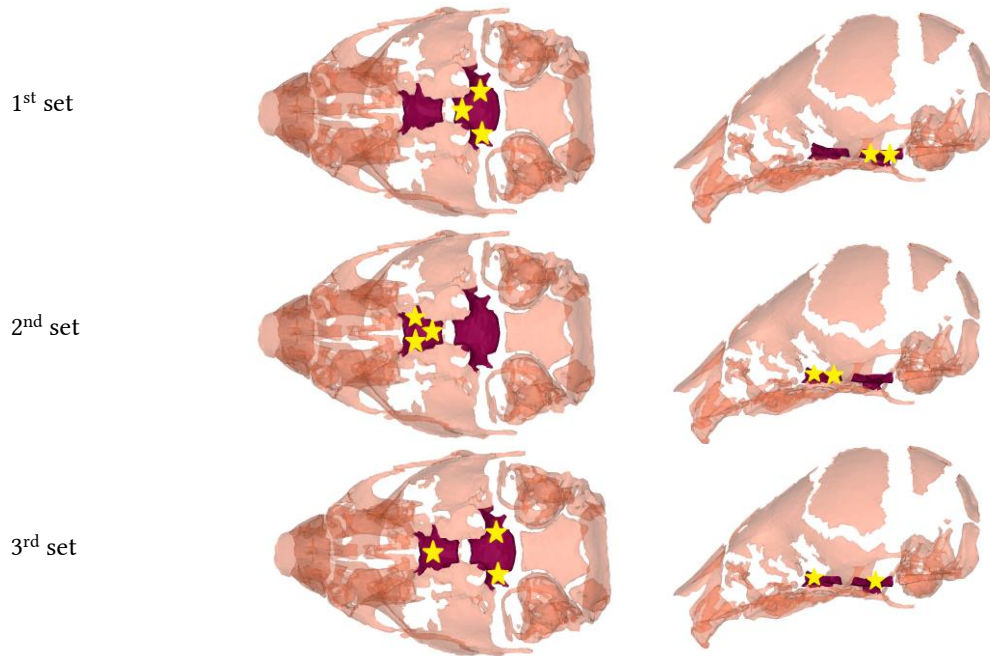
Fig. 4.7: Configurations of the sensitivity tests to the position of the constrained nodes.

4-2-2 Results

Mesh convergence

Fig. 4.8 compares the overall skull shape prediction of five different models with different mesh densities. There were negligible differences in the overall shape of the skulls between the considered models. Therefore, the model with about 144,000 elements was used for the initial sensitivity analysis where the sensitivity of the overall predicted shape to various parameters was assessed.

Fig. 4.9 and 4.10 compare the pattern of von- Mises strain and its average values over the frontal, sagittal, coronal, interparietal, and lambdoid sutures and parietal bones. The average strain values converge from the fourth model with 3,096,159 elements (the difference between 4th and 5th models was less than 5% in all areas). The same pattern was found for the first principal strain values on the sutures and bones (Fig. 4.11 and 4.12). Although the fifth model could be used as the model to study the pattern of stress and strain (in future chapters), the fourth model was chosen due to the high analysis time that was required for solving the fifth model and also considering the convergence pattern observed in Fig. 4.10 and 4.12.
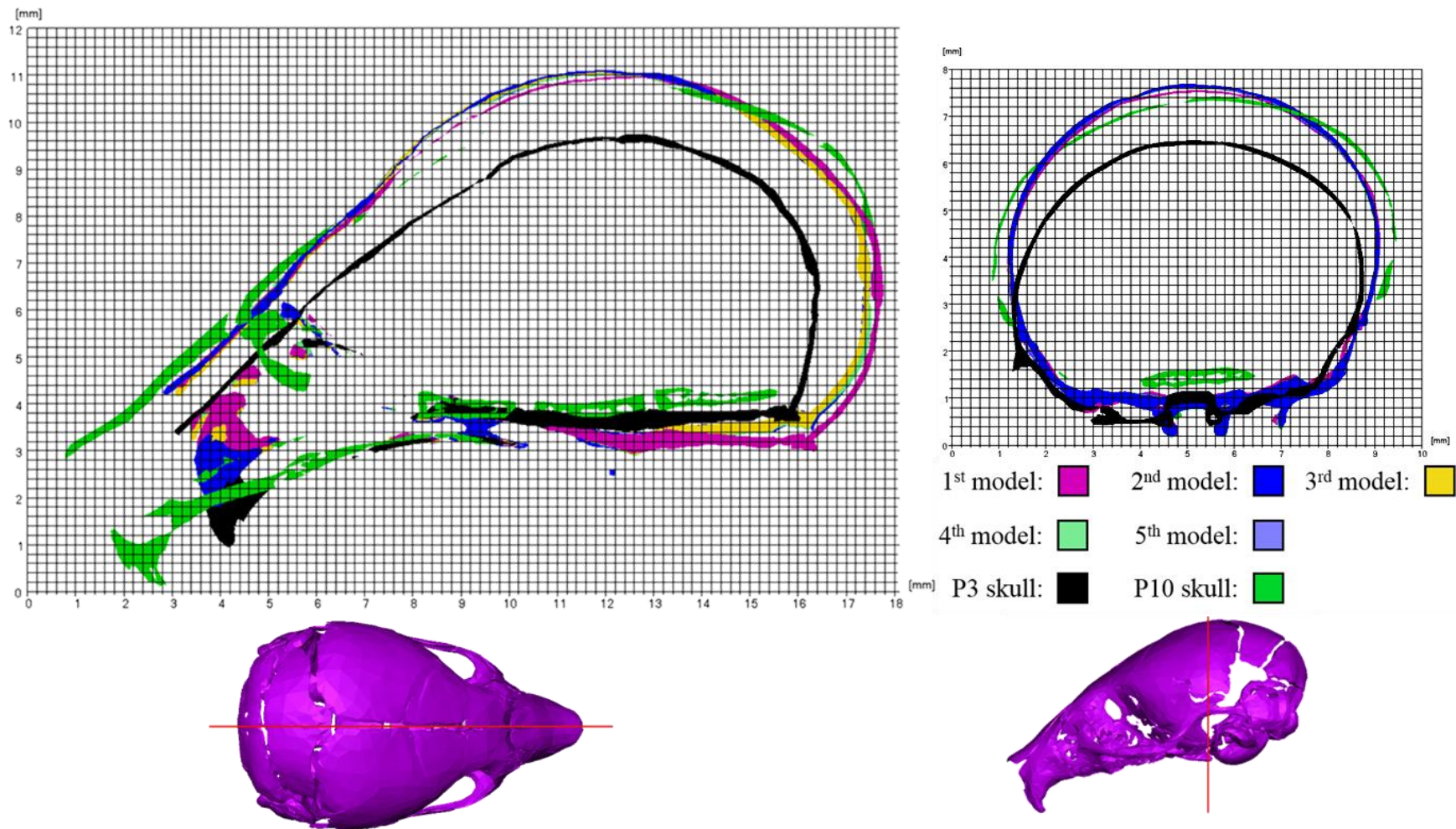
Fig. 4.8: Mesh convergence results. Overall skull shape prediction of the five different models with different mesh densities are compared. Negligible differences in the overall shape of skulls between the considered models were observed. Therefore, the model with about 144,000 elements was used for the initial sensitivity analysis where the sensitivity of the predicted shape to various parameters is assessed.
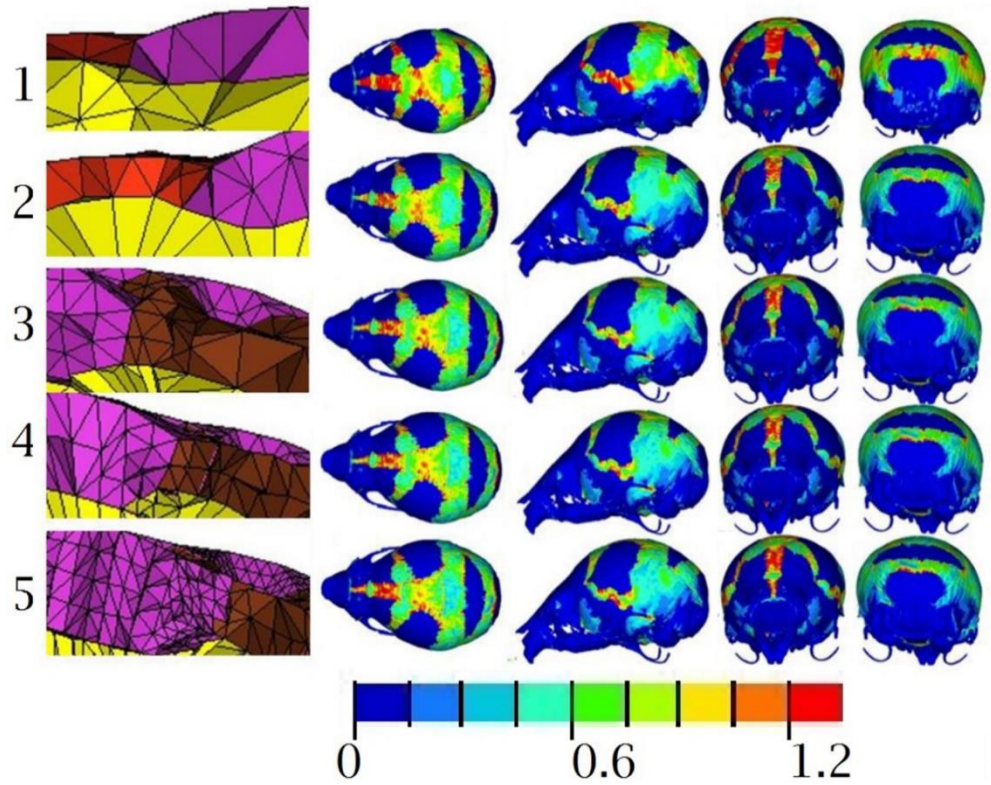
Fig. 4.9: Von Mises strain contour plot of different mesh sizes highlighting changes in the pattern of the strain distribution across the skull.
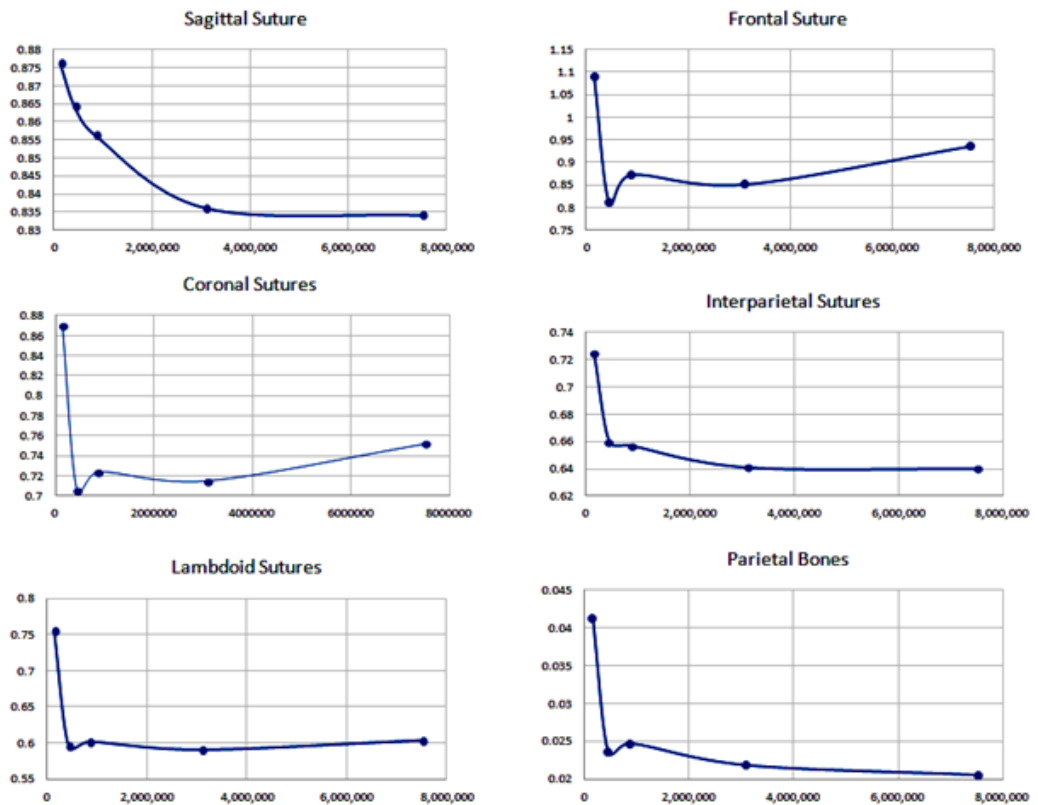
Fig. 4.10: Mesh convergence diagrams were plotted for the average von Mises strains (vertical axes) across the six regions of the skull. Horizontal axis represents number of elements at each specific area and the vertical axis, the average strain values.
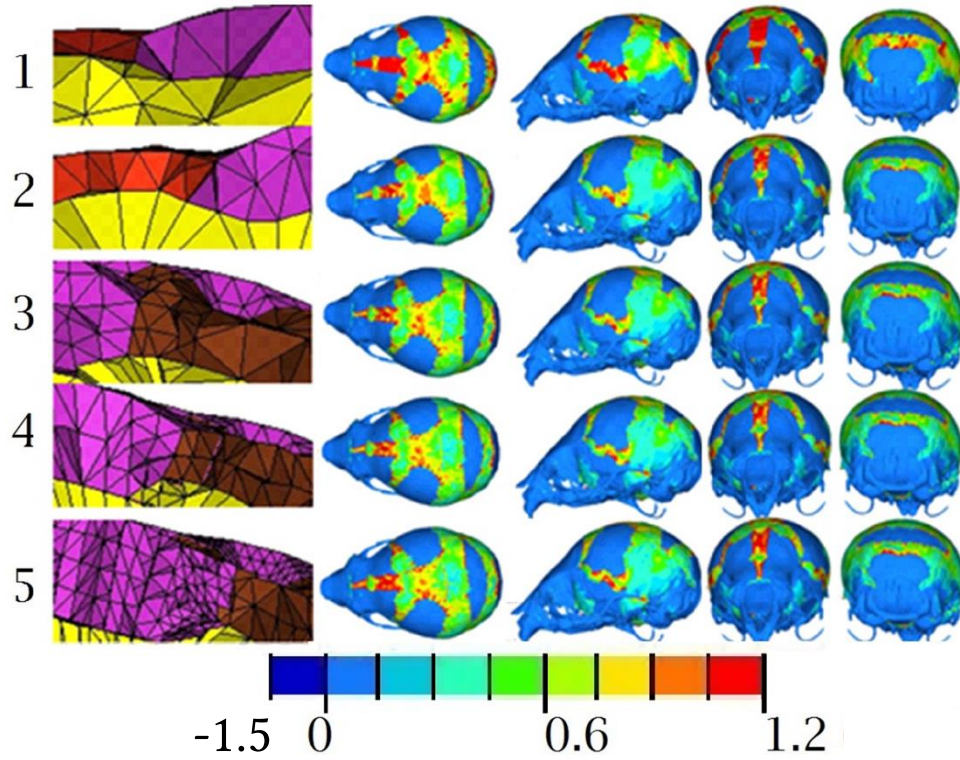
Fig. 4.11: 1st principal strain contour plot for different mesh sizes.
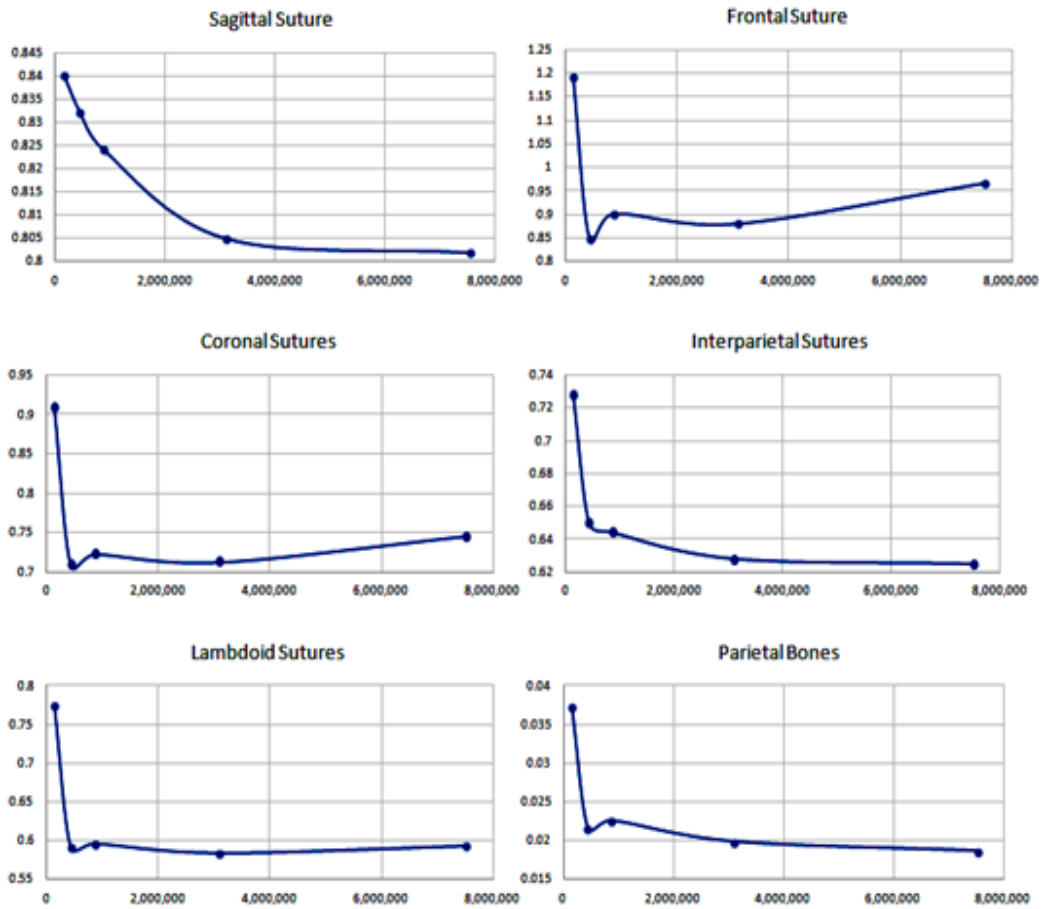
Fig. 4.12: Mesh convergence diagrams were plotted for the average 1st principle strains (vertical axes) across several regions of the skull. Horizontal axis represents the number of elements at that specific areas and the vertical axis, the average strain values.

Sensitivity analysis

Sensitivity 1: The elastic modulus of bones

There were minor differences in the overall shape of the predicted P10 skull within all three considered material properties for the bone (i.e. 1750, 3500, and 7000 MPa). In all three cases, the predicted P10 skull shapes were slightly taller across the posterior-frontal suture and the frontal regions compare to the *ex vivo* P10 skull. See e.g. the comparison between the results in the lateral view, shown in Fig. 4.13 *A*. In the posterior view the predicted P10 skull shape was slightly narrower than the *ex vivo* P10 skull (Fig. 4.13 *B*).

Varying the bone property of the baseline model from 3500 to 1750 and 7000MPa led to changes in RMS1 from 1.14 to 1.04 and 1.25, and in RMS2 from 1.44 to 1.34 and 1.55 respectively (see Fig. 4.14). RMS2 was consistently higher than RMS1 by 26%, 29%, and 24% for bone properties of 3500, 1750, and 7000 MPa respectively. Although 1750 MPa led to lower RMS values i.e. closer match with the FE predictions and *ex vivo* data, the elastic modulus of 3500 MPa was chosen as the baseline value since there wasn't a considerable difference in the overall shape and it was similar to the experimental measurements of Moazen *et al.* (2015).
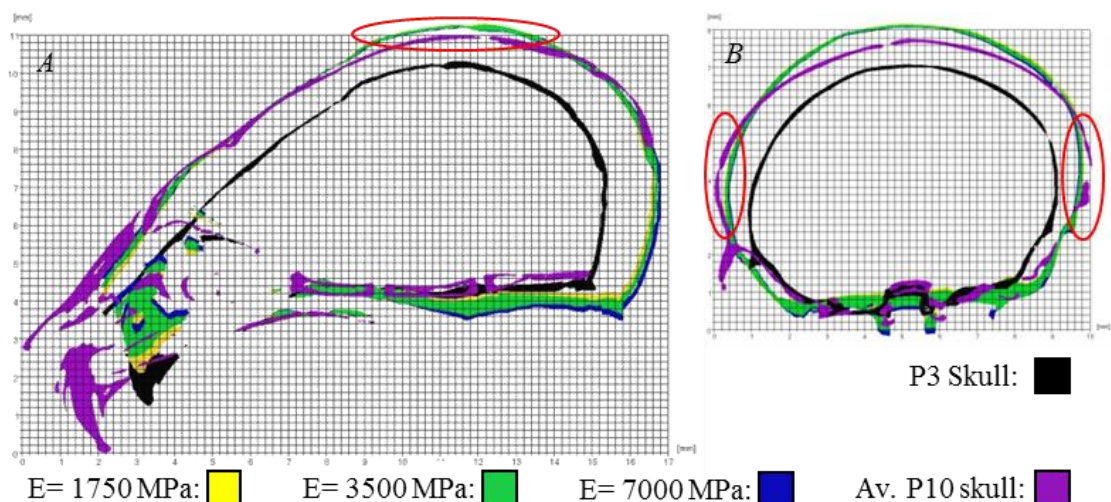
Fig. 4.13: Sensitivity test results to the elastic modulus of the bone tissue.
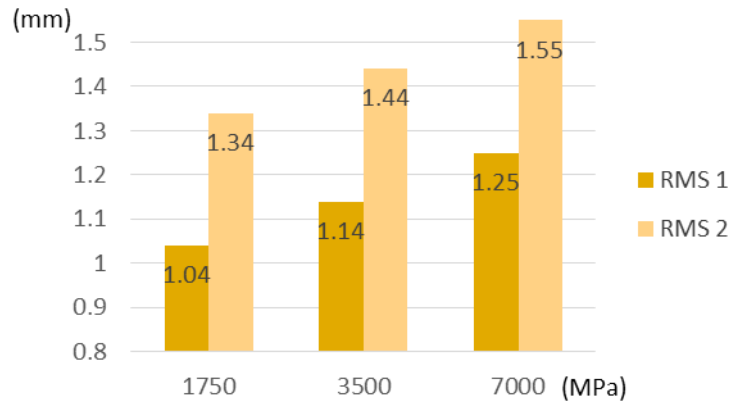
Fig. 4.14: RMS changes between models with a different elastic modulus of the bone.

Sensitivity 2: The elastic modulus of sutures

The elastic modulus of the sutures in the baseline model was assumed to be 30 MPa based on a recent study of Moazen *et al.* (2015). However, to understand the sensitivity of the model to this value, two additional models were tested with elastic modulus of 3 and 300 MPa. An elastic modulus of 300 MPa for all sutures led to bulging across the parietal bone. However, there was not a notable difference between the overall shape of the skull between the model with an elastic modulus of 3 MPa and 30 MPa (Fig. 4.15). RMS1 and RMS2 values were 1.18, 1.14, 0.99 and 1.5, 1.44 and 1.3 for 3, 30, and 300 MPa respectively. Although the value of 300 MPa resulted in smaller RMS values, 30 MPa was chosen as the baseline property as it was reported by the experimental studies of Moazen *et al.* (2015) and Henderson *et al.* (2004).
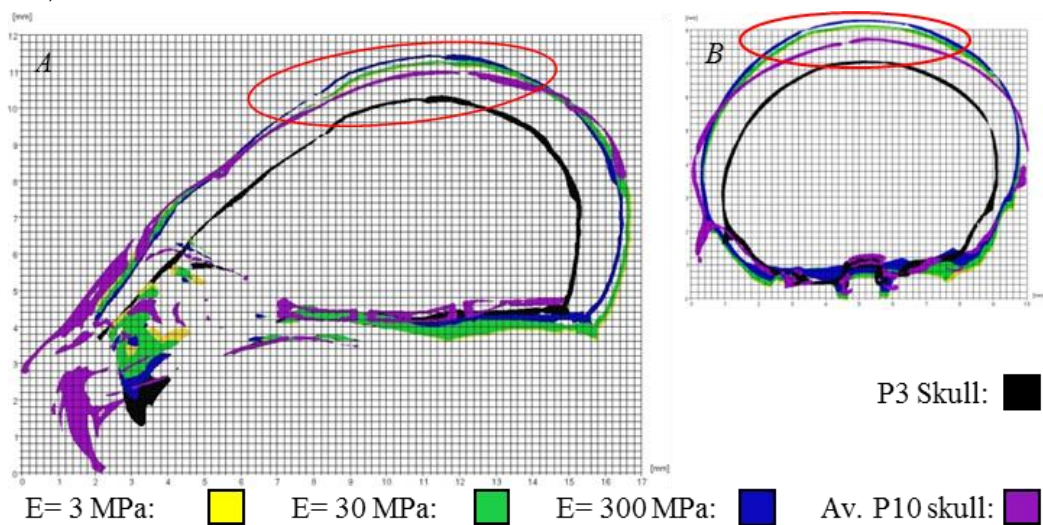
Fig. 4.15: Sensitivity test results to the elastic modulus of suture tissues.
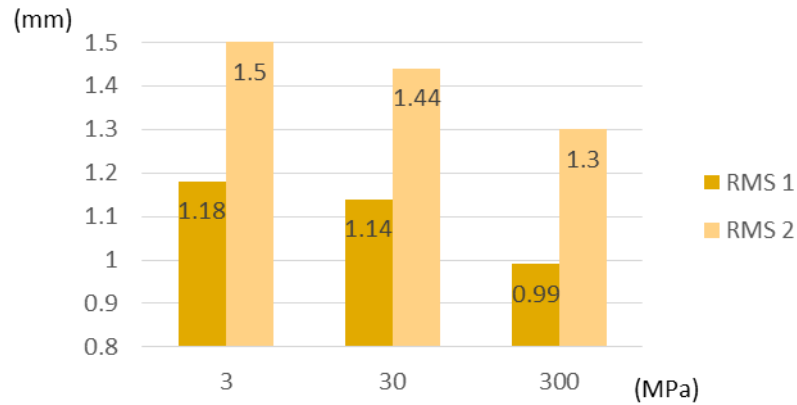
Fig. 4.16: RMS changes between models with different elastic modulus for the sutures.

Sensitivity 3: The elastic modulus of the brain

The elastic modulus of the brain tissues in the baseline models was 150 MPa. To understand the effect of this parameter on the results, it was changed from 150 MPa to 1, 5, 15, and 1500 MPa. Fig. 4.17 highlights that by increasing the elastic modulus of the brain from 1 to 1500 MPa the overall skull shape predictions converges to the *ex vivo* skull shape at P10. The RMS1 and RMS2 values were 1.39, 1.24, 1.28, 1.14, 0.95 and 1.54, 1.48, 1.55, 1.44 and 1.22 as elastic modulus of brain increased from 1MPa to 1500 MPa. Since the pattern of strain distribution in the brain is not the focus of this work elastic modulus of 150 MPa was used as the baseline value for the models.
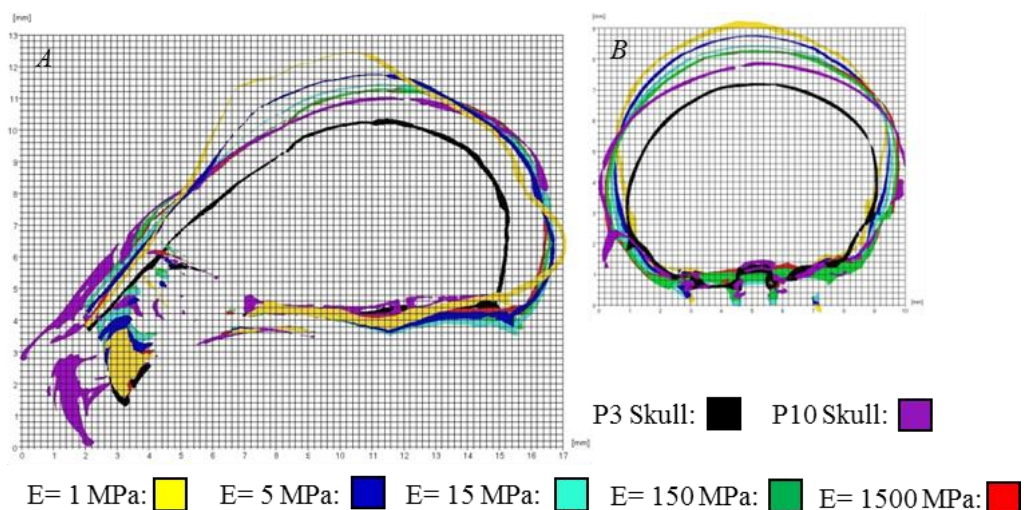
Fig. 4.17: FE results show that the higher the value of the modulus of elasticity of the brain, the smaller the bulging effect across the dorsal part of the skull.

102
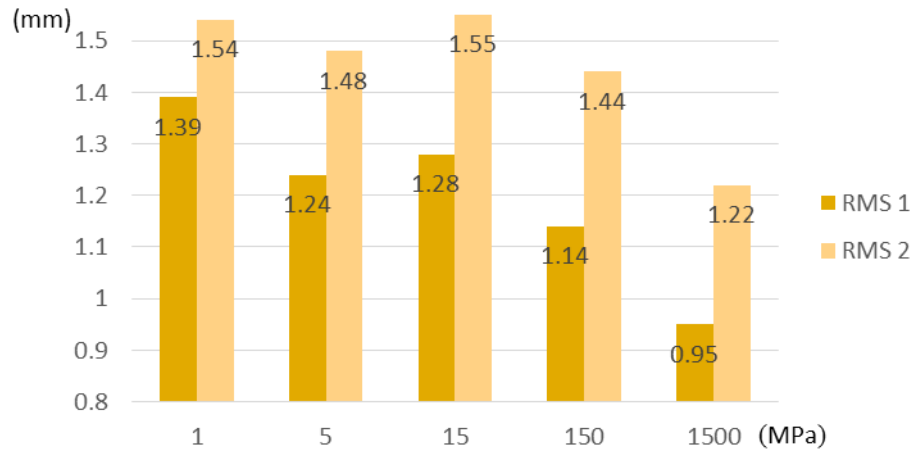
Fig. 4.18: RMS changes between models with different elastic modulus for the brain.

Sensitivity 4: Poisson ratio of the Brain

The Poisson's ratio of the brain was assumed to be 0.48 in the baseline model based on study of Claessens *et al.* (1997). To investigate the sensitivity of the model to this parameter, it was altered to 0.4 and 0.3. RMS1 and RMS2 values were 1.18, 1.23, 1.14 and 1.47, 1.5 and 1.44 for Poisson's ratio of 0.3, 0.4, and 0.48 respectively. Fig. 4.19 shows that there were minimal differences in the overall skull shape predictions when varying the Poisson ratio.

v= 0.3:   v= 0.4:   v= 0.48:   P3 Skull: Av. P10 skull:
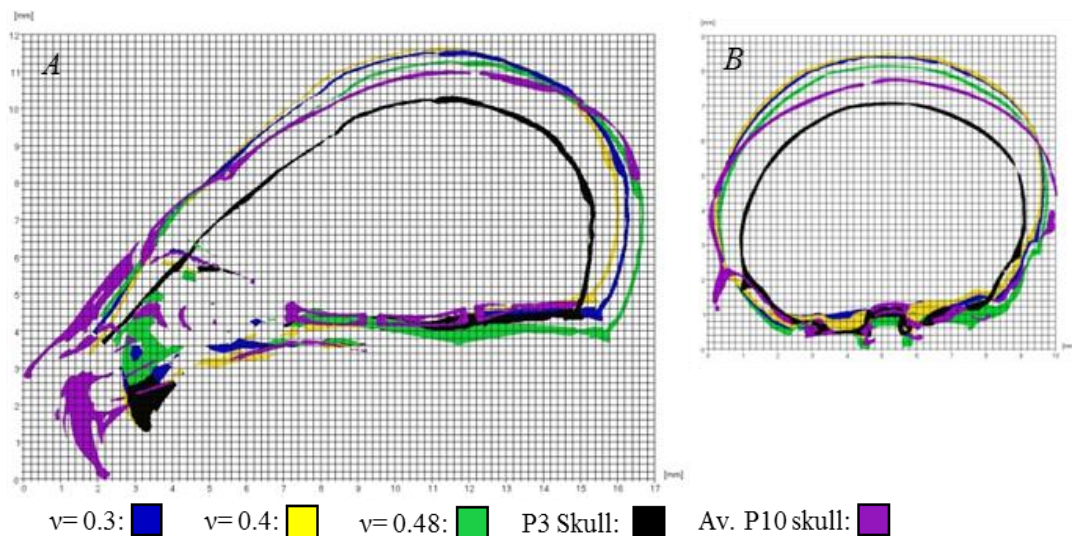
Fig. 4.19: Sensitivity test results to the Poisson ratio of the brain.
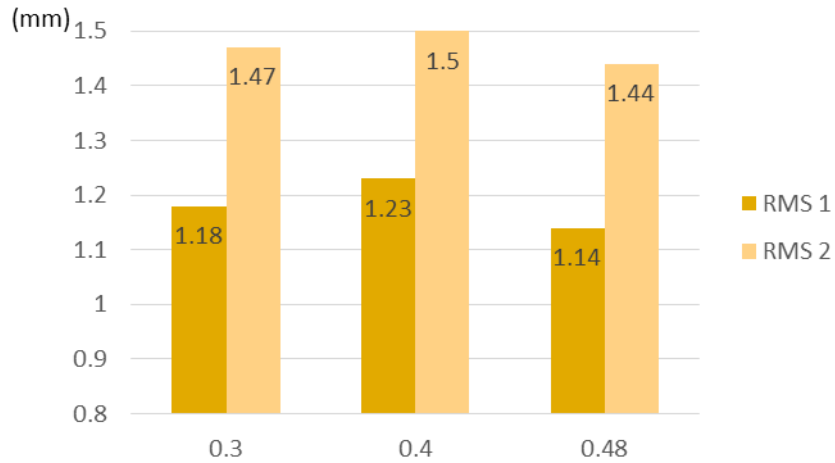
Fig. 4.20: RMS changes between models with different Poisson ratio for the brain.

Sensitivity 5: Boundary conditions

In the baseline FE model, the cranial base on the presphenoid was constrained in all directions based on morphological study in Chapter 3 that highlighted skull base perhaps grow around the presphenoid. To investigate the sensitivity of the results to this assumption two other alternative models were developed where basisphenoid was constrain in all directions (set 1) or presphenoid and basisphenoid both were constrained in all directions (set 3, Fig. 4.7). RMS1 and RMS2 values were 1.01, 1.14, 0.96 and 1.18, 1.44 and 1.21, respectively. Although the second set had higher RMS values, it was chosen as the main set for the analysis due to better overall shape (Fig. 4.21).

P3 Skull: ■

First set: ▢ Second set (baseline): ▢ Third set: ▢ Av. P10 skull: ▢
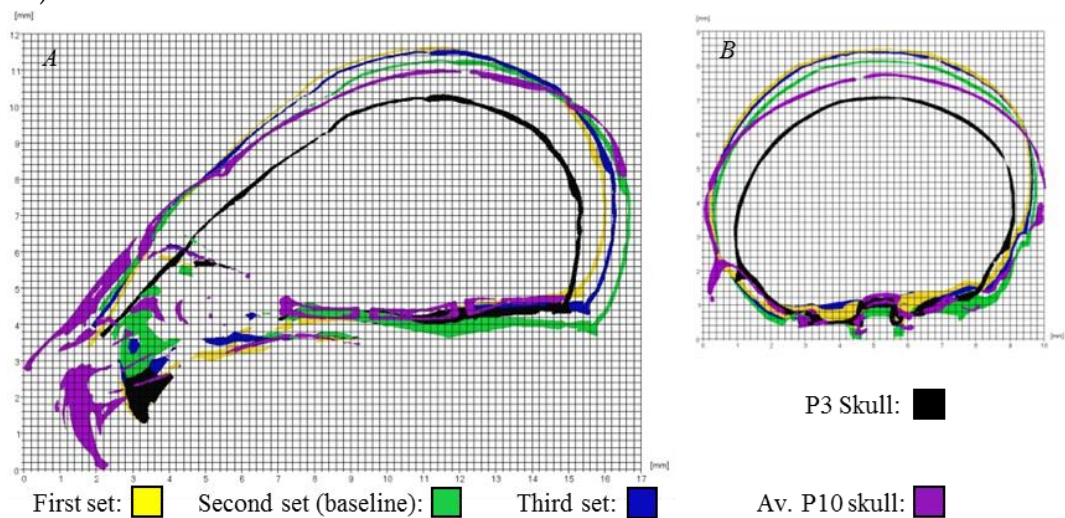
Fig. 4.21: Sensitivity test results to the position of the constrained nodes.
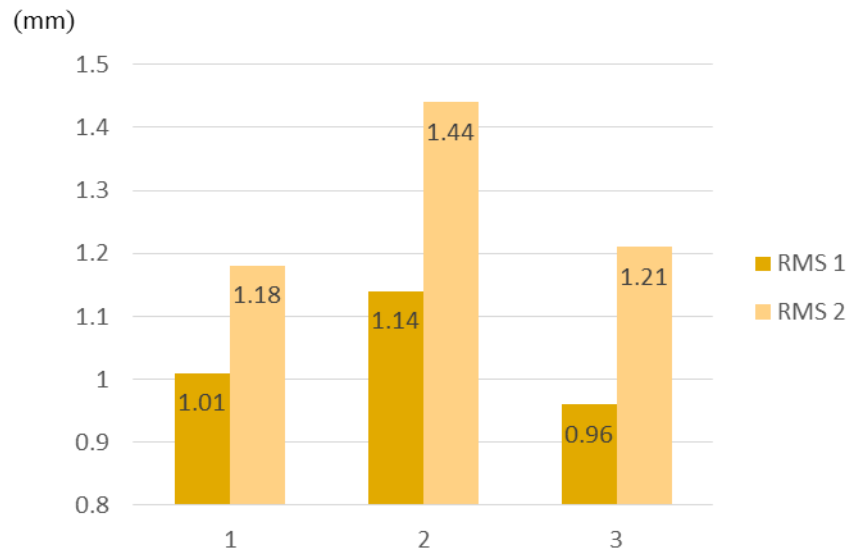
Fig. 4.22: RMS changes between models with different position of constrained nodes.

4-2-3 Discussion

The aim of this study was to predict the overall skull shape of a wild type mouse at P10 based on finite element model of a P3 skull. To understand the effect of different input parameters on the results, various sensitivity tests were performed, and results were compared against the *ex vivo* data in terms of overall skull shape and RMS values.

When investigating the effect of the elastic modulus of sutures, comparing the overall resultant shapes, showed that the RMS values cannot be the only parameter to take into account. Since the P3 skull has large areas that are consisted of the soft tissues (i.e. sutures) and were not captured within the microCT images, it was challenging to identify more homologous landmarks between the P3, P7, and P10 images. As a result, the RMS values of the base model (30 MPa, light green in Fig. 4.15) were higher than the third model (300 MPa, blue in Fig. 4.15).

Another point considering the RMS values is that, in this study only calvarial growth was modelled and the facial (nasal) growth was not modelled hence the shape of the nasal area did not change. This led to a systematic error in the total shape of the predicted P10 skull (Fig. 4.23). To address this point RMS1 and RMS2 were calculated based on two sets of landmarks. In all analysis the main focus was on the RMS values corresponding to the calvarial morphology i.e. RMS1 and it was interesting that

RMS1 values were consistently across all sensitivity tests smaller than RMS2 and closer to 1 i.e. 100% match between the model.

Mesh convergence is a crucial step in finite element studies hence a mesh convergence study was first performed followed by several sensitivity analysis where the FE predictions were compared against an *ex vivo* mouse skull shape at P10. Mesh convergence results highlighted that while low mesh density model (e.g. 144000 elements) was suitable to predict the overall skull shape, it was not suitable to predict the stress and strain values. Therefore, for the purpose of this chapter that was to predict the overall skull shape, this model was used. However, in Chapter 5, where the effect of bone deposition at the sutures on the overall predicted shapes will be considered, a higher mesh density model will be used.

Sensitivity analysis was performed to understand the effect of the input parameters on the model prediction. Bone and suture properties and Poisson's ratio of the brain had a minor effect on the overall predicted skull shape. However, modulus of elasticity of the brain had a more considerable impact on the model predictions. In the case of the modulus of elasticity of the brain, a value of 150 MPa was chosen eventually as the baseline value for the models forward, based on the sensitivity analysis.

The initial 3D model was segmented from the only WT P3 specimen, and the initial and the other age brain volumes were calculated based on that. However, when comparing with the *ex vivo* P10 skull, the average skull was determined from five specimens. This may cause an overestimation of the P10 volume and be a reason of the bulging. In all of the models, there was an overestimation of height and underestimation of the width of skulls. Another reason could be the isotropic expansion of the brain. As discussed in Chapter 3, the mouse skull grows more in length rather than height.
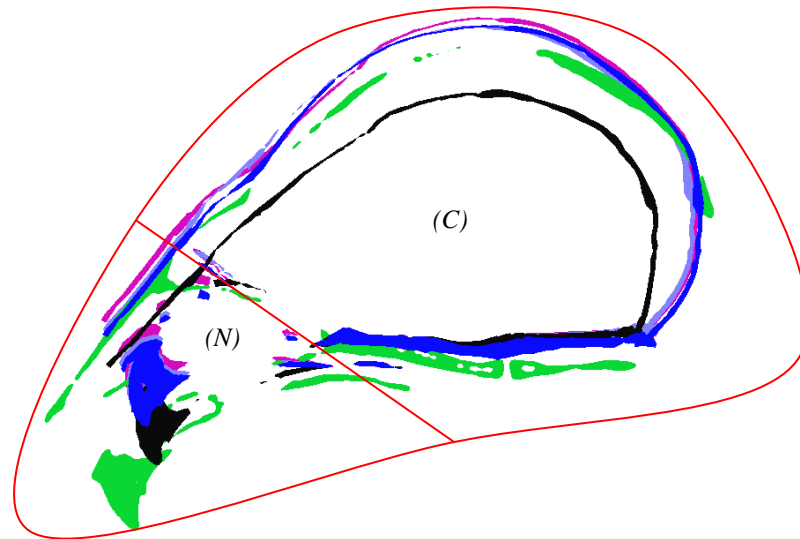
Fig 4.23: Skull growth is predicted in the Calvaria (C), while the nasal bones stay almost unaffected.

4-3 Study 2: Predicting mutant $Fgfr2^{C342Y/+}$ mouse skull shape at P10

The aim of this study was to predict the mutant mouse skull shape at P10. The model that was used for this study was the model that described in the Study 1 i.e. the wild type model at P3. The sutures that are fused in the $Fgfr2^{C342Y/+}$ *in vivo*, were fused on the FE model of the wild type model and the results were compared against microCT data of the mutant mouse at P10.

4-3-1 Materials and methods

The baseline model described in the Study 1 of this chapter was used to predict the mutant skull shape. Liu *et al.* (2013) showed that in the $FGFR2^{C342Y/+}$ mouse model, several sutures are fused. In most of the MT mice (more than 80%), Presphenoid-basisphenoid synchondrosis (PBS), frontal, coronal, and lambdoid sutures are fused. In the FE model of the MT mouse, these sutures were fused both independently and in combination, to investigate the effect of their fusion on the overall skull shape. Following models were developed and in each case suture fusion was modelled by assigning same material property as bone, i.e. 3500 MPa, to the fused suture:

(1) Only Presphenoid-basisphenoid synchondrosis (PBS) suture was fused;

(2) Only coronal sutures were fused;

(3) Only interfrontal suture was fused;

(4) PBS and coronal sutures were fused;

(5) PBS and interfrontal sutures were fused;

(6) Interfrontal and coronal sutures were fused;

(7) PBS, interfrontal and coronal sutures were fused;

(8) PBS, interfrontal, coronal and lambdoid sutures were fused.
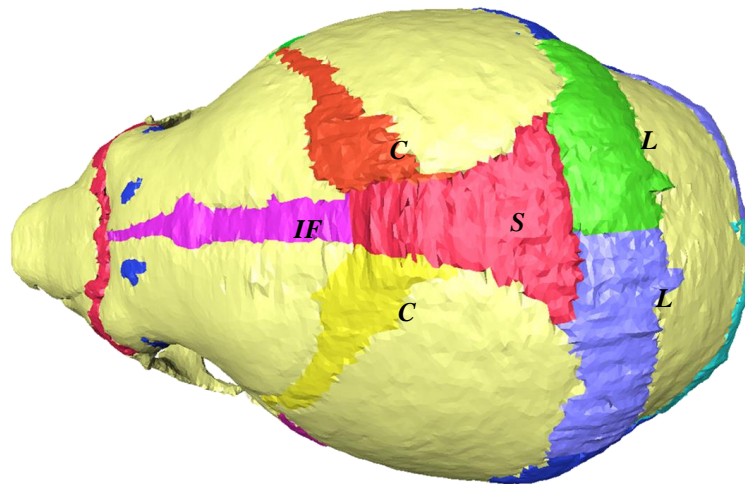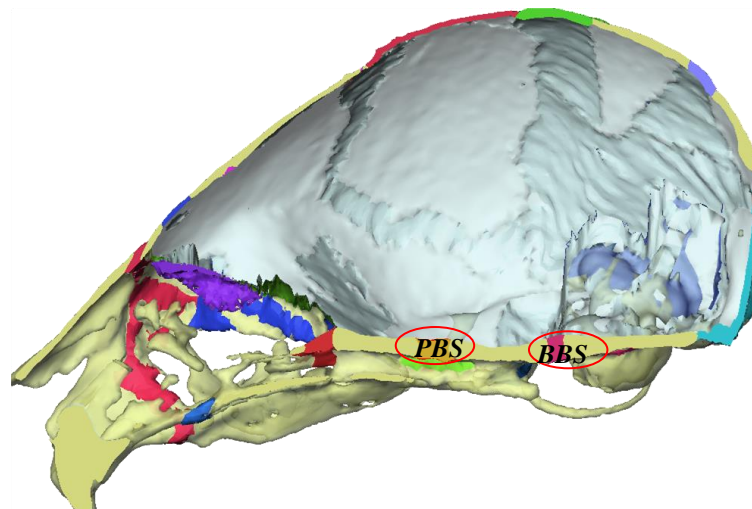
Fig. 4.24: Position of the interfrontal (*IF*), coronal (*C*), sagittal (*S*) and lambdoid (*L*) (A), basisphenoid-basioccipital synchondrosis (*BBS*) and presphenoid-basisphenoid synchondrosis (*PBS*) (B) sutures (based on the wild type model at P3).

4-3-2 Results

To study the effect of fusing different sutures on the skull growth various combinations of fusing sutures were investigated. RMS1, RMS2, width, length, and height values are reported in Table 4.4. Although all models show very similar RMS values, the model with both PBS and coronal sutures fused (6th model in Table 4.4) resulted in the minimum RMS1 value. There was a difference of 7% between the maximum and minimum RMS1 values. This difference was about 8% for the RMS2. Comparing the overall shape of the models with the *ex vivo* mutant P10 (Fig. 4.25 and Fig. 4.26), it was found that fusing all four sutures (frontal, coronals, PBS and lambdoid) led to closer match between the FE predictions and *ex vivo* data (as discussed in Chapter 3, MT skull is shorter and taller than WT skull).

Table 4.4: Width, length, height (in mm), and RMS values of various combinations of fused sutures. The last two columns are the RMS values of the baseline in wild type study and are presented here to compare with WT RMS values.

		width	length	height	RMS1	RMS2	WT RMS1	WT RMS2
	ex vivo mutant P10	10.28	12.59	7.16	----	----		
1)	F	9.60	13.00	7.38	1.21	1.52	1.14	1.44
2)	C	9.61	12.92	7.40	1.17	1.52	1.14	1.44
3)	P	9.62	12.89	7.36	1.13	1.40	1.14	1.44
4)	F & C	9.60	13.04	7.41	1.19	1.55	1.14	1.44
5)	F & P	9.61	12.96	7.38	1.14	1.42	1.14	1.44
6)	Cs & P	9.62	12.88	7.41	1.12	1.42	1.14	1.44
7)	F & C& P	9.61	12.90	7.43	1.13	1.45	1.14	1.44
8)	F & C & P & L	9.62	12.85	7.44	1.16	1.47	1.14	1.44
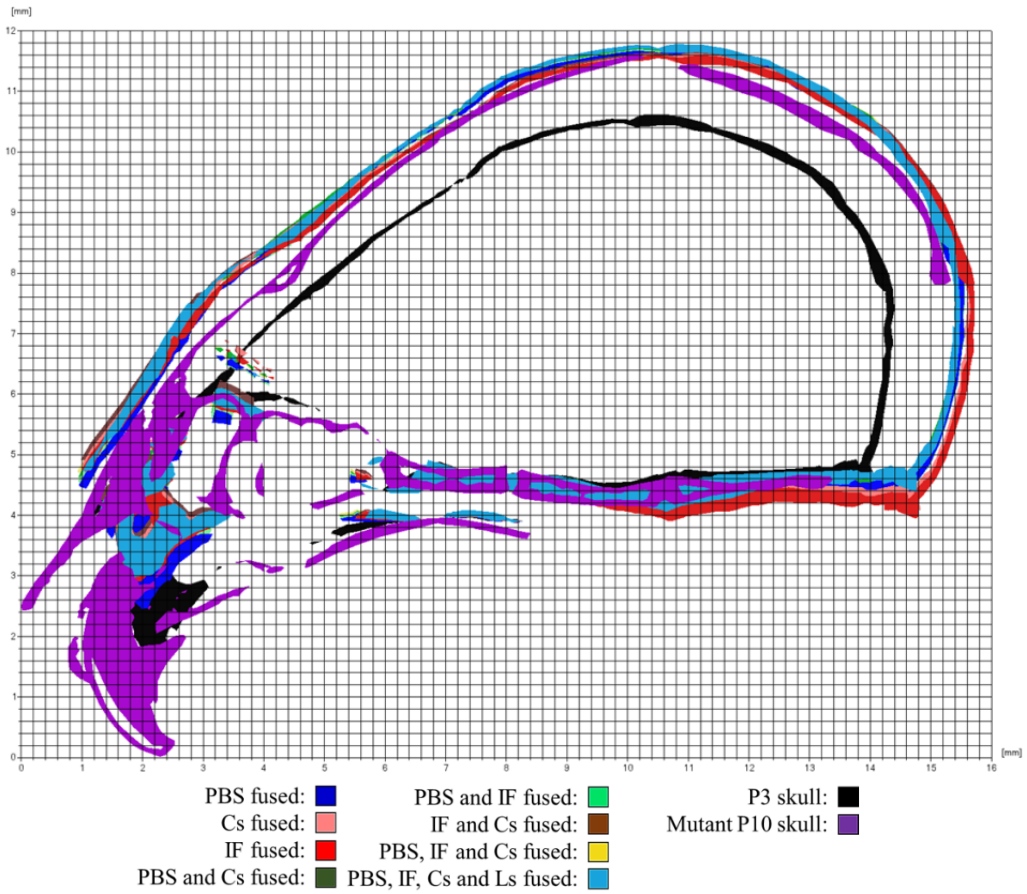
Fig. 4.25: Sagittal view of *ex vivo* P3 and MT P10 compared with various predictions of MT P10 skulls.
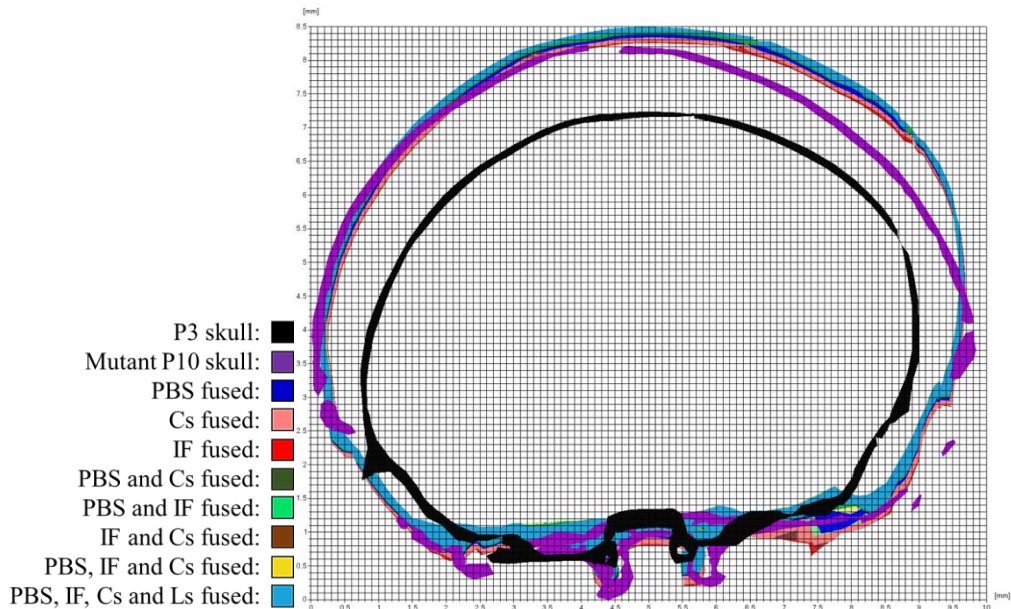
Fig 4.26: Anteroposterior section views of P3, mutant P10, and the predicted mutant P10 skulls.
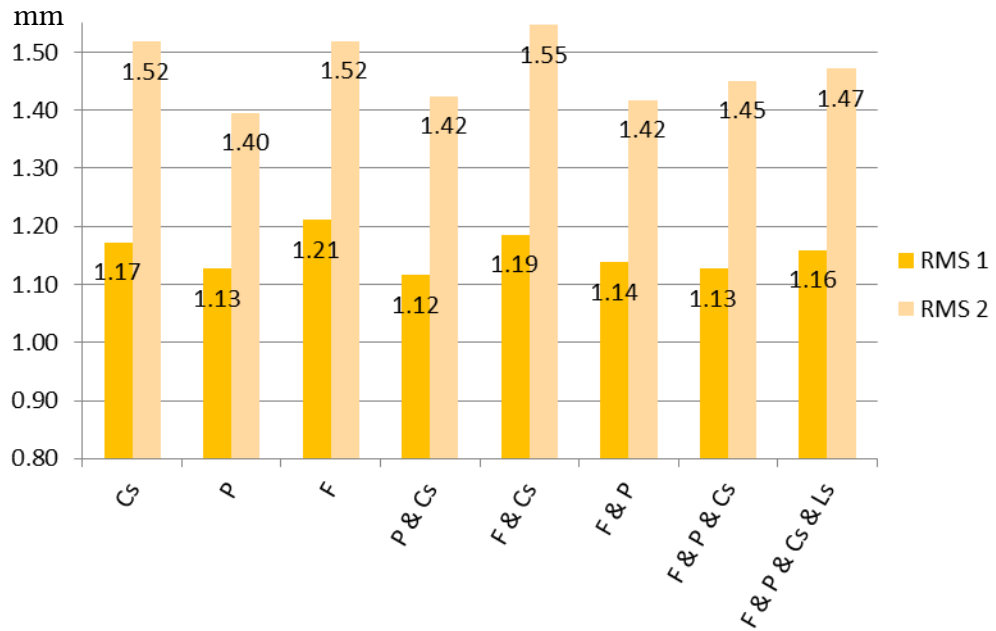
Fig. 4.27: RMS1 and 2 values comparison for different suture fusion.

4-3-3 Discussion

Fig. 4.28 shows a comparison of the average wild type and mutant type P10 *ex vivo* skulls in lateral views with the cranial study of WT and MT mice performed by Liu *et al.* (2013). Liu *et al.* showed that about 80% of $FGFR2^{C342Y/+}$ mice show suture fusion in frontal, coronal, lambdoid and PBS sutures.

Fig. 4.29 and 4.30 show the overall shape of predicted MT and WT P10 in comparison with the *ex vivo* data. Table 4.4 shows that the RMS values were in the same range for both types. The MT prediction was slightly shorter with increased calvarial height compared with WT prediction, the same pattern was observed in the *ex vivo* data (Fig. 4.28 and 4.29).
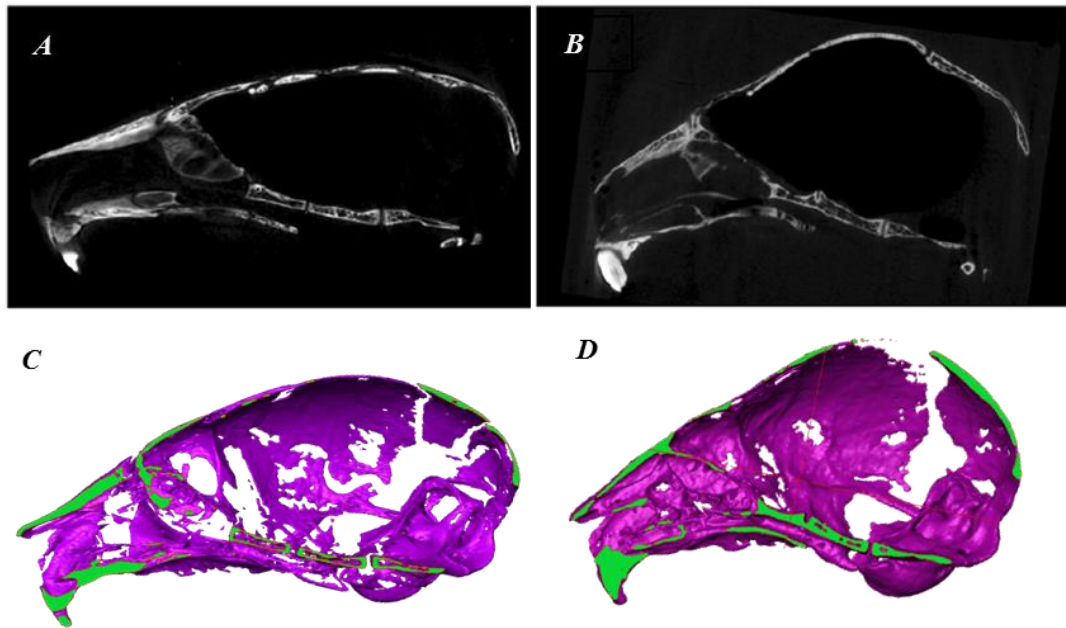
Fig. 4.28: A and B are wild type and mutant type mice at P28 from the study of Liu *et al.* (2013). C and D are wild type and mutant type mice at P10 from the same dataset as presented in Chapter 3. Note both studies are on same genetic background.

🟩 MT P10 (FE)	🟥 WT P10 (FE)
🟦 MT P10 (ex-vivo)	🟪 WT P10 (ex-vivo)
🟫 MT P3 (*ex-vivo*)	🟧 WT P3 (ex-vivo)
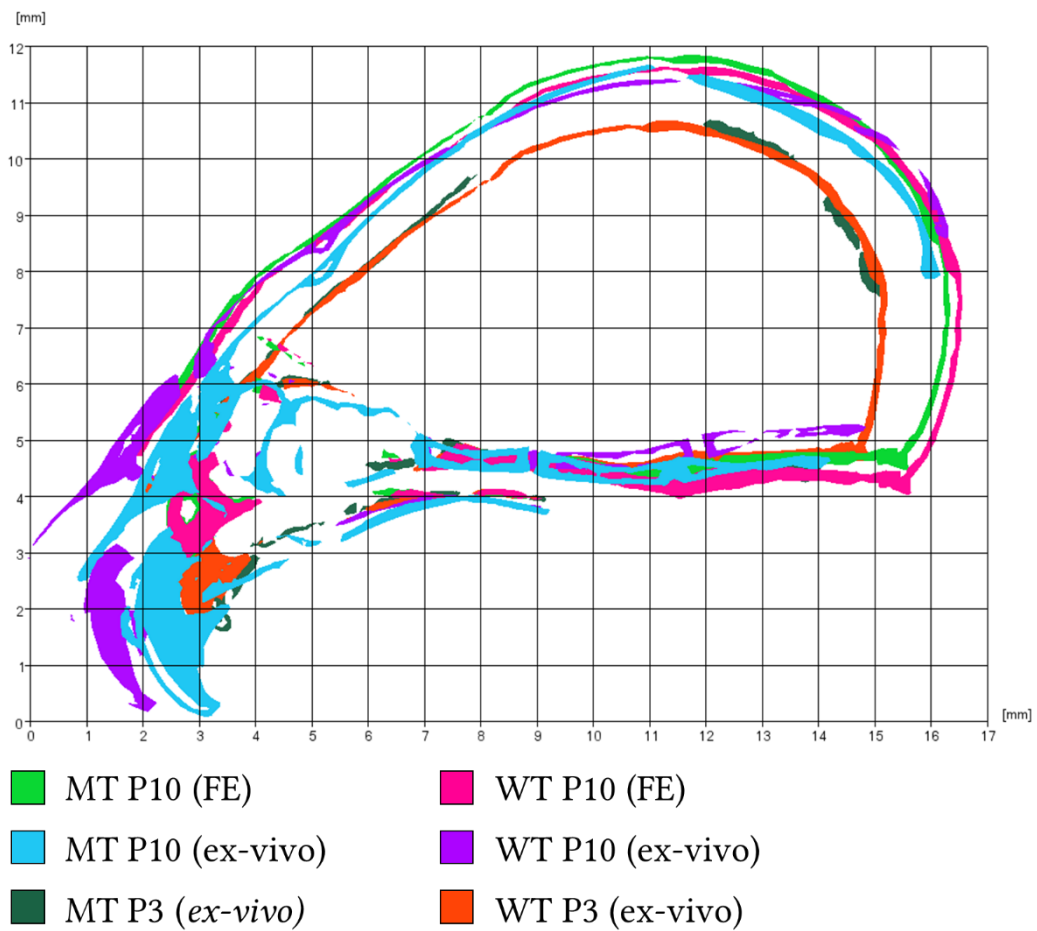
Fig. 4.29: Sagittal view of WT and MT *ex vivo* skulls compared with FE predictions.

4-4 Discussion

To the best of my knowledge, this is the first study that uses finite element method to predict skull growth in wild type and mutant type mice. Calvarial growth in wild type and mutant mice at P10 were predicted based on a WT model at P3 using finite element model. Surgical interventions to manage craniosynostosis usually happen at around six months up to one year of age in human babies. This age roughly correlates with P3 to P10 in mouse. Although the MT skulls already have a phenotype, in order to make sure of the robustness of the model, and the taken suture fusion approach, same WT, P3 model was used as the MT, P3 model. The only difference was changing the material properties of the fused sutures to that of bone.

Sensitivity analysis highlighted that results are sensitive to some of the input parameters (e.g. modulus of elasticity of the brain), while they are less sensitive to some other parameters (e.g. modulus of elasticity of the bone and the Poisson's ratio of the brain). Overall both wild type and mutant type predicted skull shapes at P10 were comparable to both our *ex vivo* data and literature and showed a relatively good match. However, it must be mentioned that facial growth was not captured in this study and emphasis was placed on the calvarial growth.

Generally, mouse cranium grows more in length than height (Fig. 2.10). However, in the simulation, the expansion was more spherical, leading to the bulging at the fronto-parietal region. This could be due to the effect of applying isotropic thermal expansion to the brain. While as it was mentioned earlier in Chapter 2 (section 2.6), mechanical properties of the brain are not isotropic. So, anisotropic thermal expansion should have been used. On the other hand, predicted MT models follow the same *ex* vivo pattern of shorter calvarial length and increased height.

When modelling the cranial growth based on the ICV expansion, one main simplification is that, there really exists a feedback loop between the brain growth and cranial bone formation. As brain expands, its growth is regulated by the pressure exerted by the skull, and the bone formation at the edges of cranial sutures, is regulated by the tensions generated by the brain. However, as a reasonable simplification, it is assumed that brain is growing independently of the pressure imposed by the skull.

The modelling approach presented in this chapter did not take into account the bone formation at the sutures during the radial expansion of the skull. Therefore, the next logical step for further development of the modelling approach described in this chapter was to include the bone formation at the suture in to the presented approach here. This is the focus of the next chapter.

Chapter 5: Modelling bone formation at the sutures

5-1 Introduction

This chapter focuses on predicting the bone formation at the cranial sutures. A strain-based tissue differentiation algorithm was developed to predict the bone formation at the cranial sutures. Results were compared throughout with the morphological data obtained in the Chapter 3.

This chapter is consisted of three studies describing the different stages of the tissue differentiation model development. In the first study, a simple algorithm was developed. Here, there was only one step of (suture) element selection in between different steps/days of development. In the second study, to ensure that number of elements selected in each step was converged, various convergence criteria were compared. In the third study, a mesh independent approach was used by selecting suture elements based on their distance from the hard/bone tissue. The distance was informed based on the bone formation rate data reported in the literature).

An additional study (section 5.5) investigates the effect of modelling the brain-bone interface on the pattern of bone formation at the sutures. Here contact elements were used as opposed to the fixed interface (at the brain-bone interface) that was used through the thesis up to this point. The final study of this chapter (section 5.6) applies the tissue differentiation approach described in the third study to the mutant mouse model.

5-2 Study 1: Bone formation- no convergence

An algorithm was developed to simulate the bone formation at the sutures while predicting the mouse skull growth from P3 to P10. Several sensitivity tests were

performed to understand the effect of different parameters on the predicted suture closure patterns. Results were compared to microCT images of the average *ex vivo* P7 and P10 mice as described in the Chapter 3.

5-2-1 Materials and methods

The baseline model developed in the Chapter 4 (a P3 wild type mouse) was used in this chapter. In brief, all sections were assigned isotropic material properties with an elastic modulus and Poisson's ratio of 3500 MPa and 0.3 for bones, 30MPa and 0.3 for sutures and 150 MPa and 0.48 for the brain respectively. Several sensitivity tests were performed by changing the input parameters such as: the strain type used for the algorithm, number of the elements selected across the sutures, and the strain range at which elements were selected, to investigate their effects on the results.

First, the brain volume at P3 was expanded to the brain volume at P4. At the end of expansion, suture elements with strain values in the defined range and type were changed to bone. The geometry of the model was updated i.e. to the deformed P3 geometry (or P4) was then used as the starting geometry for the following simulation i.e. P4 brain expansion to P5. Then the whole process was then repeated up to P10 (see Fig. 5.1).
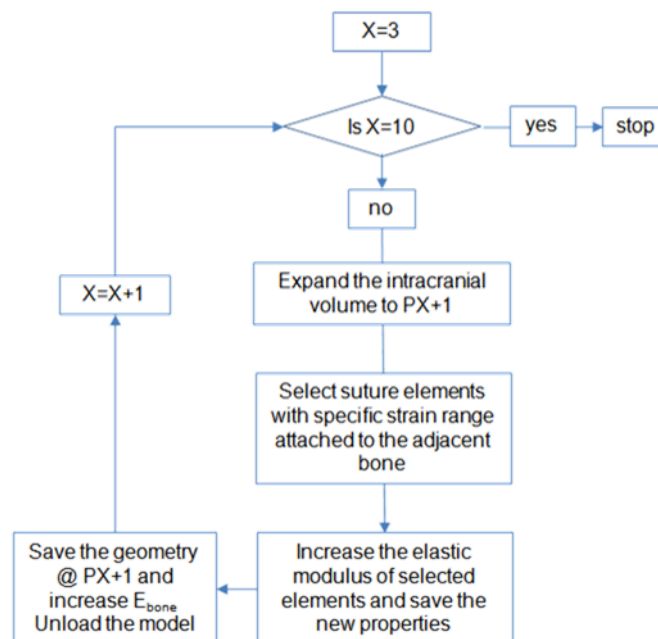
Fig. 5.1: The bone formation developed in study 1 during the calvarial growth from P3 to P10 in mouse.

Sensitivity to the number of suture elements

This sensitivity test was carried out on the hydrostatic strain of less than 5%. Three different methods for selecting suture elements were tested here. First, all of the suture elements were selected. Second, two layers of suture elements attached to bones were selected, and third only one layer of elements attached to the bone were selected. To select one layer of suture elements in ANSYS, first external nodes of the bone tissue were selected and then suture elements that were attached to those elements were selected. This was repeated to add more layers if needed. Note the third approach was set as the baseline element selection method for the subsequent sensitivity tests described in this study. Fig. 5.2 shows how the element selection algorithm selected different layers of suture elements. There were about 20 elements across the sagittal and coronal sutures, and 7 elements across the frontal suture. Fig 5.3 shows the mesh density at the sagittal, frontal, and coronal sutures.
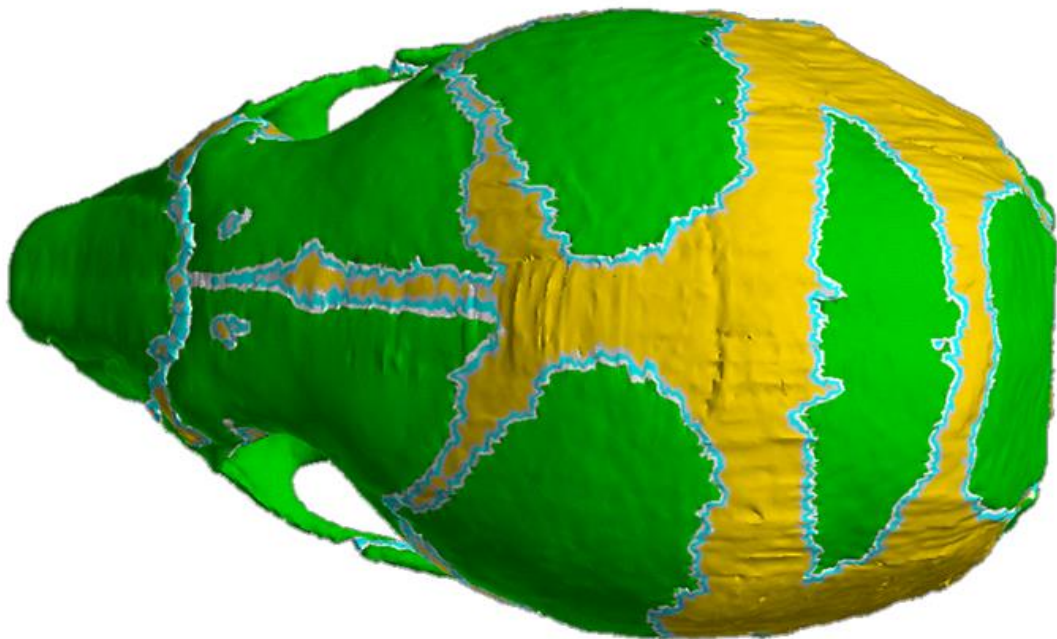
Fig. 5.2: Different layers of the suture elements attached to the bones in the element selection process illustrated on a P3 -WT model. Yellow is the suture, and green is the bone. White and light blue are two layers of the suture elements attached to the bones.
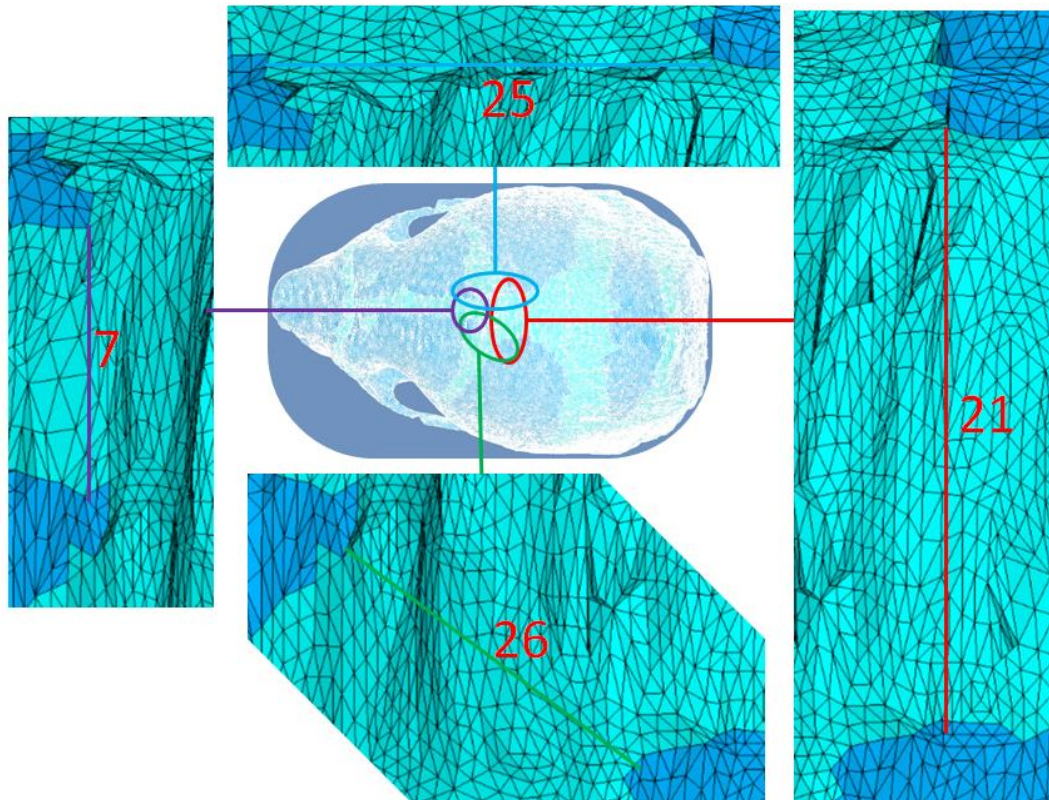
Fig. 5.3: Number of elements across the frontal, sagittal, and coronal sutures. There were about 20 elements across the sagittal and coronal sutures and 7 elements across the frontal suture.

Sensitivity to the strain type

Three different strain types were compared in the process of element selection: hydrostatic strain, first principal strain (P1), and von Mises strain. Since the maximum hydrostatic strain (0.17) was much smaller than the other two (1.76 and 1.66, respectively), a lower strain range was used for this type of strain. Based on the strain contour plots presented in Fig. 5.4, the strain selection range for the hydrostatic strain was defined as less than 2.5%, and less than 10% was used for the other two strain types. It can be seen that if a same range is defined for all three strain types, only a fraction would be included for P1 and von Mises strains (top row). On the other hand, increasing the selection range for these two (compared with the hydrostatic), a similar range would be selected (bottom row). See the next section for the sensitivity test to the strain ranges.

| Hydrostatic | P1 | von Mises |
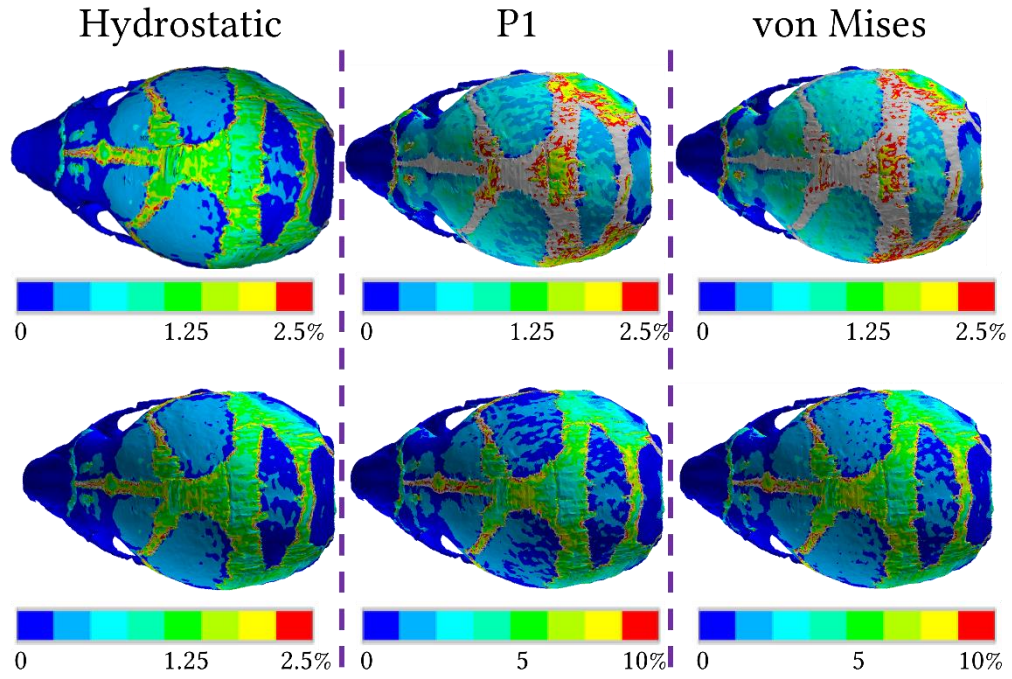
Fig. 5.4: Strain contour plots for hydrostatic, first principal (P1), and von Mises strains when expanding from P3 to P4. Red and grey areas have a value higher than the maximum threshold (2.5% or 10%). Using the value of 2.5% for all strain types highlights almost all suture elements. However, using different thresholds (2.5% for the hydrostatic strain, and 10% for P1 and von Mises) highlights a similar strain contour pattern. Max strains values are 0.17, 1.76 and 1.66 respectively.

Sensitivity to the strain range

To investigate the effect of the strain range used in the element selection process, the baseline strain selection range of $\varepsilon < 2.5\%$, was changed to $\varepsilon < 5\%$ and $\varepsilon < 1\%$. Fig. 5.5 shows how the strain contour plot changed when the maximum strain was changed. It was found that almost all of the suture elements experienced a hydrostatic strain in the range of 1-5% during the calvarial growth from P3 to P4.
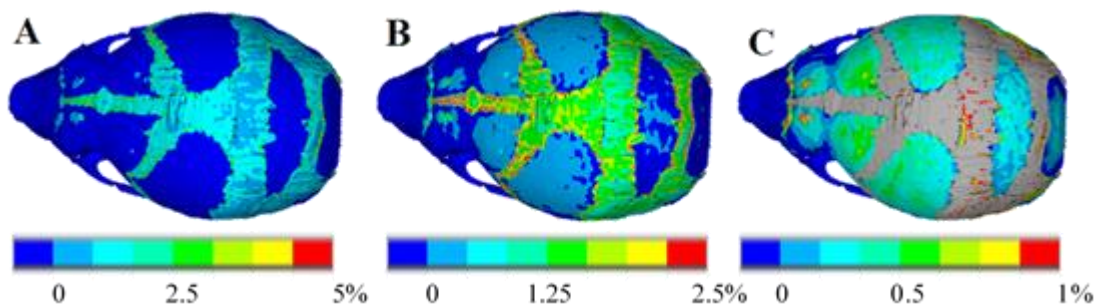
Fig 5.5: Hydrostatic strain contour plot with different ranges during the expiation from P3 to P4: grey regions have a strain value higher than A, 5%, B, 2.5%, C, 1%.

Measurements

Pattern of bone formation was compared between different cases. Also, the suture sizes were measured across 14 anatomical locations (see Fig 3.3) and results were compared against the measurements in Chapter 3.

5-2-2 Results

Sensitivity to the number of elements

Fig. 5.6 compares the pattern of suture closure obtained in the sensitivity test to the element selection process and the *ex vivo* microCT reconstructions at P7 and P10. The sensitivity analysis included selecting either two layers of suture elements attached to bone and changing them to bone based on their strain values (less than 2.5%), or only one layer of elements. Here all suture elements were not selected for the following reason. All suture elements were experiencing hydrostatic strain less than 2.5% during the growth from P3 to P4, if they all would have been selected, then all of the suture elements would have been turned into the bone, so the results in this section have excluded the selection of all suture elements.

Fig. 5.6 illustrates the overall shape of the skull and the bone formation pattern for these two methods and compares them with the *ex vivo* skulls at P7 and P10. It was found that, when only one layer of suture elements was selected, the sagittal suture was wider. Also, posterior-frontal suture remained open which was seen in some of the P10s in Chapter 3.
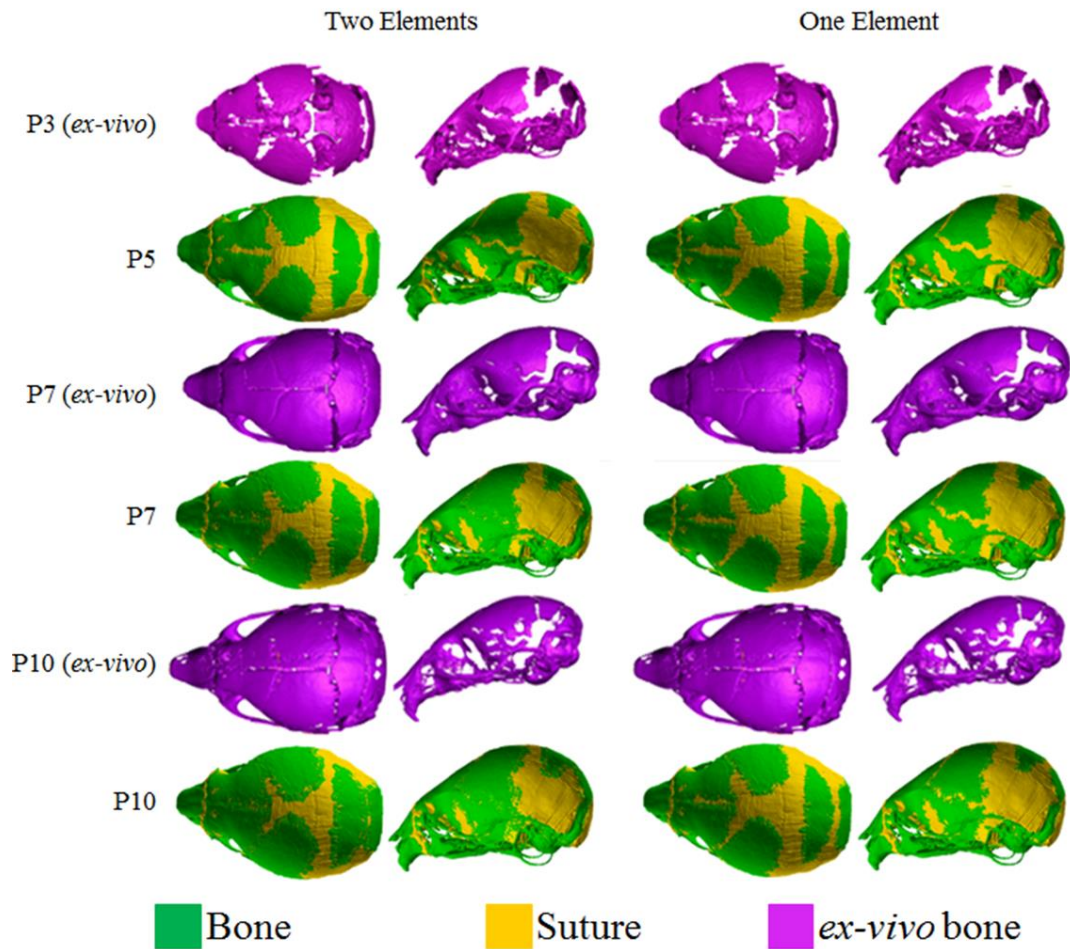
Fig 5.6: Comparing the overall shape of P5, P7 and P10 when two layers or only one layer of suture elements attached to bone is selected.

Sensitivity to the strain type

Fig. 5.7 shows the pattern of suture closure from P3 to P10 considering different strain types. Both von Mises and P1 showed a similar pattern at P10, while hydrostatic strain selection method, resulted in less bone formation. Considering the *ex vivo* skull *at* P10, sagittal suture was still open. As a result, hydrostatic strain was selected as the baseline. Note that the one layer of element selection method (as the baseline) was used in all these three strain types.
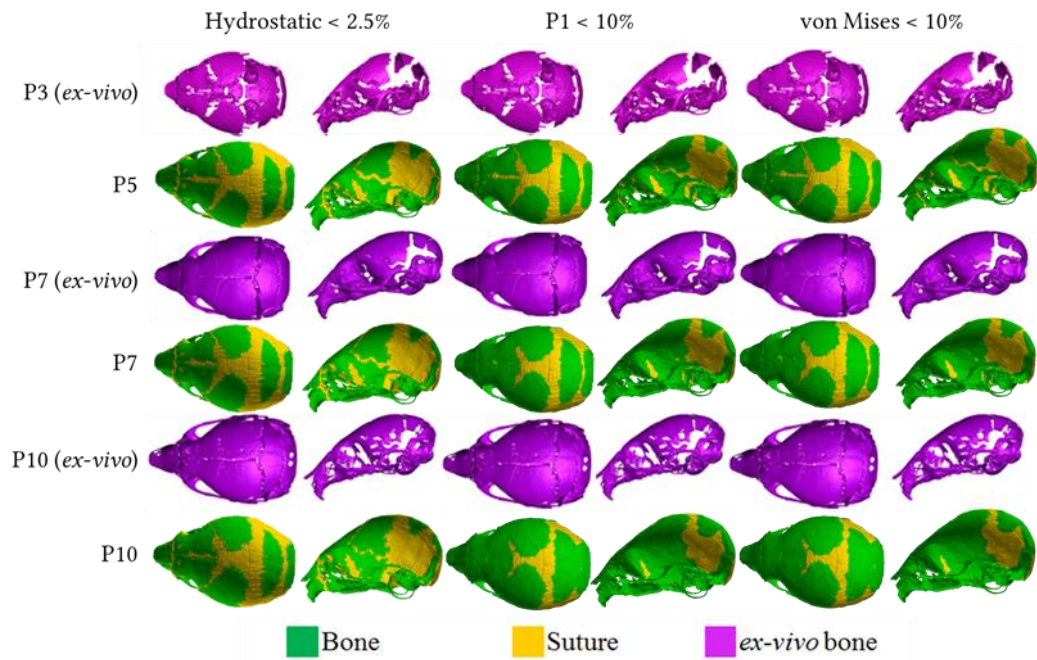
Fig. 5.7: Different strain types compared in the element selection process. Von Mises and P1 both showed a similar pattern of bone formation at P10 (all suture elements within a strain range less than 10% were selected), while hydrostatic strain resulted in less bone formation (all suture elements with a strain range higher than 2.5% were selected), which was very close to the *ex vivo* presented in Chapter 3.

Sensitivity to the strain range

Fig. 5.8 shows the sensitivity results when different hydrostatic strain values were used within only one layer of suture element selection. When 5% range was used in element selection process, frontal suture was almost fused at P7 and totally fused at P10. Using 2.5% range, results were comparable with the overall pattern of bone formation observed in the *ex vivo* P7 and P10. However, when 1% range was used almost no new bone formation was observed.
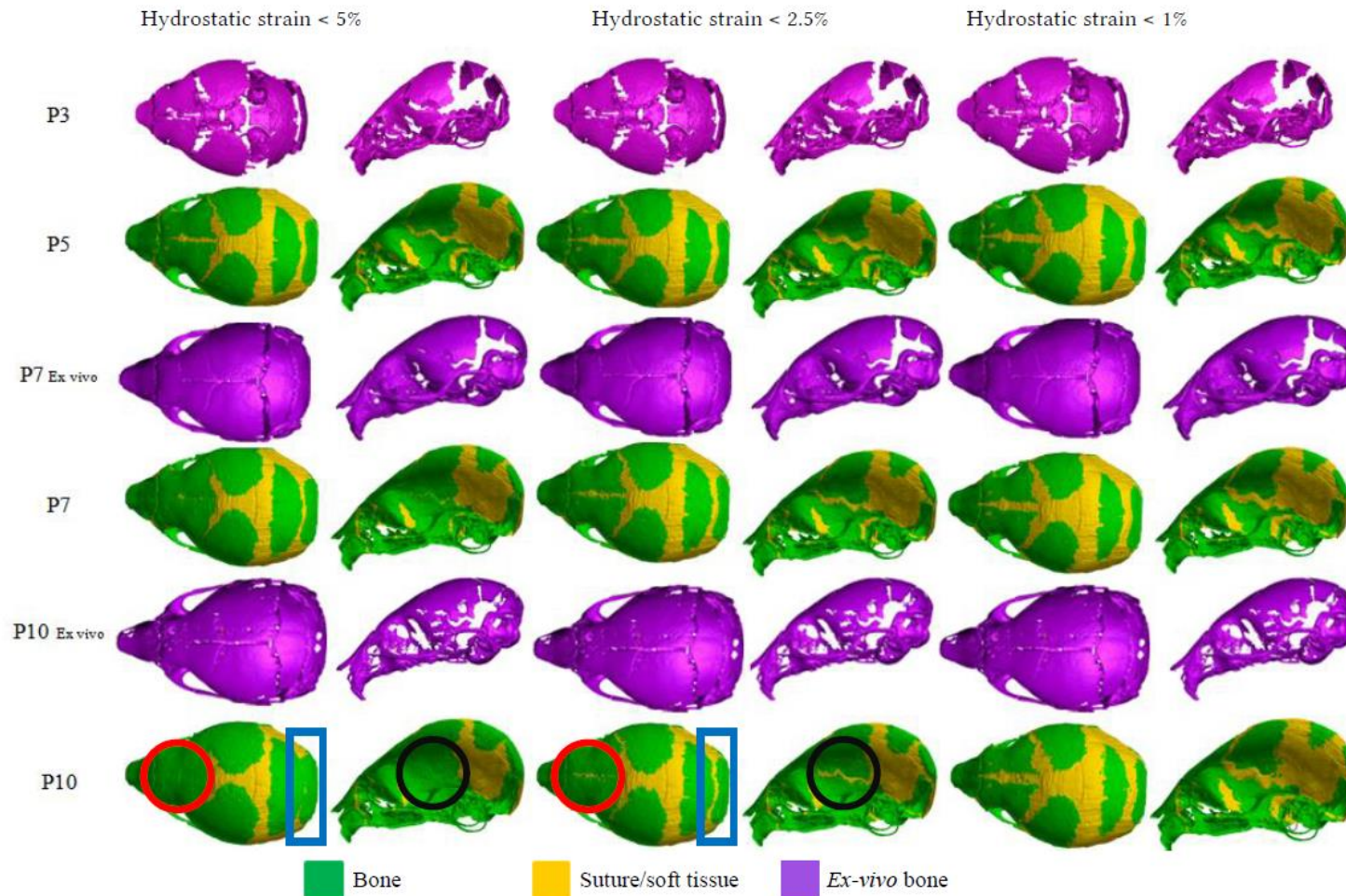
Fig. 5.8: Different hydrostatic strain ranges were compared in the element selection process. When 5% strain range was used, frontal (red circle), squamosal (black circle) and lambdoid (blue rectangle) sutures were almost fused at P7 and fully fused at P10, while using 2.5% range, resulted in a gap in all sutures up to P10, which was very similar to the *ex vivo* data.

Suture sizes at P10

Table 5.1 compares the suture width for the base model at this section (hydrostatic strain less than 2.5% within one layer of suture elements selected) versus *ex vivo* data at P10 for 14 measured sections. An over-estimation of suture sizes was found almost across all sections. The maximum overestimation was at point 12, with about 240% difference. The closest prediction was at point 4 with only 11% difference. Average difference across all regions was about 98%.

Table 5.1: Suture sizes (in mm) for the 1st model described in study 1 versus *ex vivo* measurements at P10. Note "Av *ex vivo*" abbreviates "average *ex vivo* measurements"; values are in mm.

		1st model	Av *ex vivo*	Δ%
Frontal suture	1: medial point	0	0.39	-
	2: posterior point	0	0.226	-
Sagittal suture	3: anterior point	0.76	0.312	143
	4: medial point	0.28	0.32	-11
	5: posterior point	0.92	0.432	113
Right Interparietal suture	6: closest point to the midsagittal plane	0.52	0.334	56
	7: medial point	0.58	0.224	157
	8: most lateral point	0.40	0.306	31
Left Interparietal suture	9: closest point to the midsagittal plane	0.74	0.45	65
	10: medial point	0.51	0.256	100
	11: most lateral point	1.02	0.492	108
Lambdoid suture	12: Most lateral point- Right	1.27	0.374	239
	13: medial point	0	0.14	-
	14: Most lateral point- Left	0.76	0.48	58

5-2-3 Discussion

The model described in this section was the first attempt to develop an algorithm to model the bone formation at the bone-suture interface during the calvarial growth from P3 to P10. The algorithm at this stage did not have a tissue differentiation step and it was simply altering the elastic modulus of the selected suture elements to elastic modulus of "bone" i.e. 3500 MPa depending on the level of strain that they were experiencing and the selection zone. Bearing in mind the simplicity of this approach, a range of sensitivity tests were performed to understand the effect of different parameters, and the results were compared against the *ex vivo* data in terms of overall pattern of bone formation at the sutures.

When the effects of different strain types were studied, a smaller strain range was used for the hydrostatic strain. This was comparable to the hydrostatic range that was proposed by Carter *et al.* (1998) and Claes *et al.* (1999) to lead to intramembranous bone formation. This was due to the lower range of hydrostatic strain in comparison with von Mises and P1 strains at P3 to P4 expansion.

Considering the effect of number of elements selected, if all of the suture element were selected (with the strain range of 2.5%), then all the sutures would have been converted to bone. Therefore, in the first step i.e. growth from P3 to P4, all suture elements would have changed into bone. This is clearly unrealistic hence here 1 or 2 layers of element were selected but it was noted that this is a mesh dependent approach that is not suitable moving forward. Hence the Study 2 and 3 focused on overcoming this limitation of this study.

5-3 Study 2 Bone formation - convergence

The algorithm developed in the Study 1 was further developed here to include tissue differentiation during the growth and as well as a step to ensure mesh independence of the results. Several sensitivity tests were performed to understand the effect of different parameters on the predicted suture closure pattern. Results were compared versus microCT images of the *ex vivo* P7 and P10 mice.

5-3-1 Materials and methods

Nanoindentation study of Moazen *et al.* (2015) quantified changes in the elastic modulus of the calvarial bones during the mouse development at P10, P20 and P70. Results of this study were used to extrapolate daily increase in the elastic modulus (E) of the bone and sutures. It was found that E_{suture} increases about 250 MPa per day from P3 to P10. This value was used in this study to model daily changes in the elastic modulus of the bones and sutures (Fig 5.9).

Material properties used for P3 were the same as the properties described in Study 1. At the end of radial expansion of the brain at P3 (i.e. expansion from P3 to P4), suture elements with strain values in the defined range (the baseline was kept at ε< 5%) and type (hydrostatic strain), were changed to a stiffer material (E=280 MPa), then the model was unloaded. These two steps were repeated until a convergence criterion was met. The convergence criterion was defined as the percentage of the difference between number of suture elements (n) in i^{th} and i-1th iterations (($^{n_i - n_{i-1}}/_{n_{i-1}}$) × 100). The baseline convergence criterion was 15% i.e. if there was less than 15% difference in the number of newly formed tissue (elements) compared to the previous step, the loop was stopped. Note 0% difference meant no new tissue was generated.

At the end of the convergence step, (1) the elastic modulus of the new tissue was increased by 250 MPa; (2) the geometry was updated i.e. the model was saved at deformed shaped (P4); (3) the material property of the bones was increased by 250 MPa, and saved as the new age (P4). This process was repeated day by day up to P10 (Fig 5.10). Fig 5.11 shows a schematic picture of the whole process of selecting suture elements at each age, and increasing their elastic modulus day by day from P3 to P10.
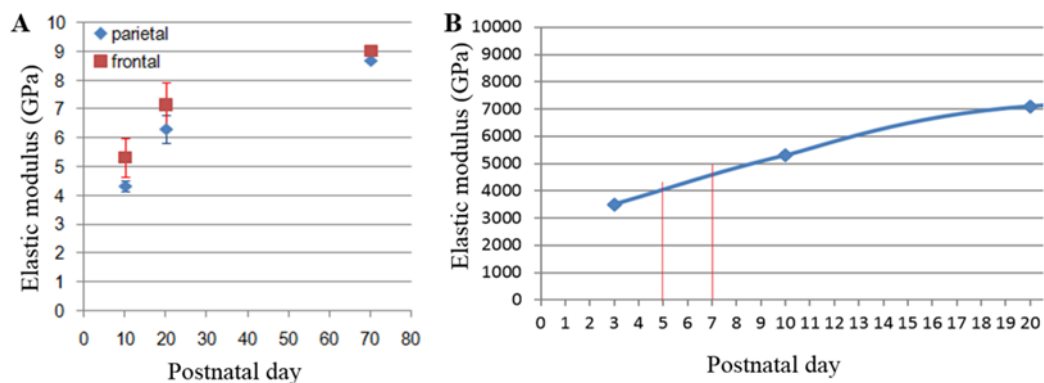
Fig. 5.9: The elastic modulus increases from P10 to P20 (A) and extrapolating the graph to P3 (B) shows a 250 MPa increase at each day (extracted and modified from Moazen *et al.*, 2015).
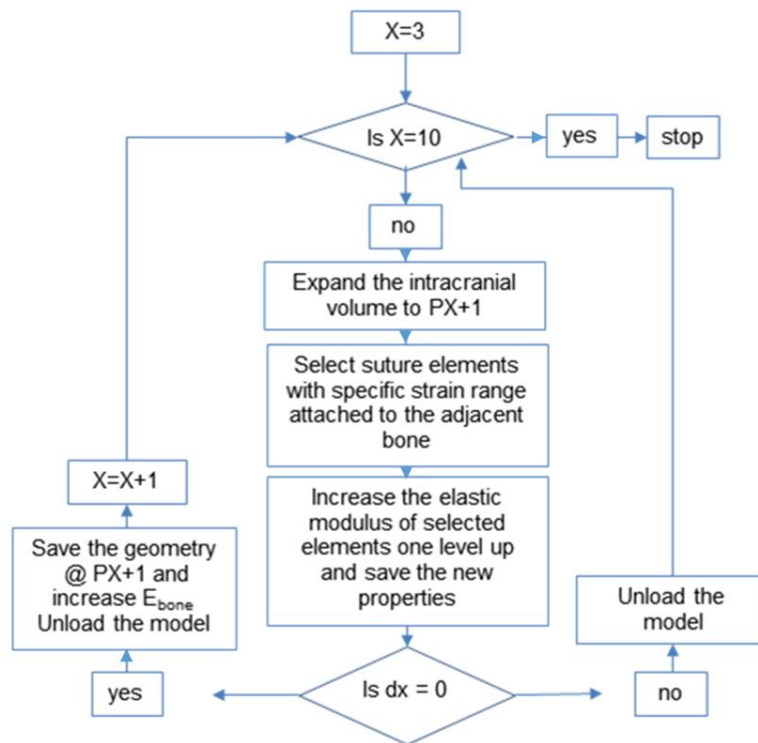
Fig. 5.10: The whole process of expanding P3 to P10 while stiffening suture elements. X is age and dx is the difference between numbers of suture elements between two iterations. A zero dx means no more suture elements are changed into bone.
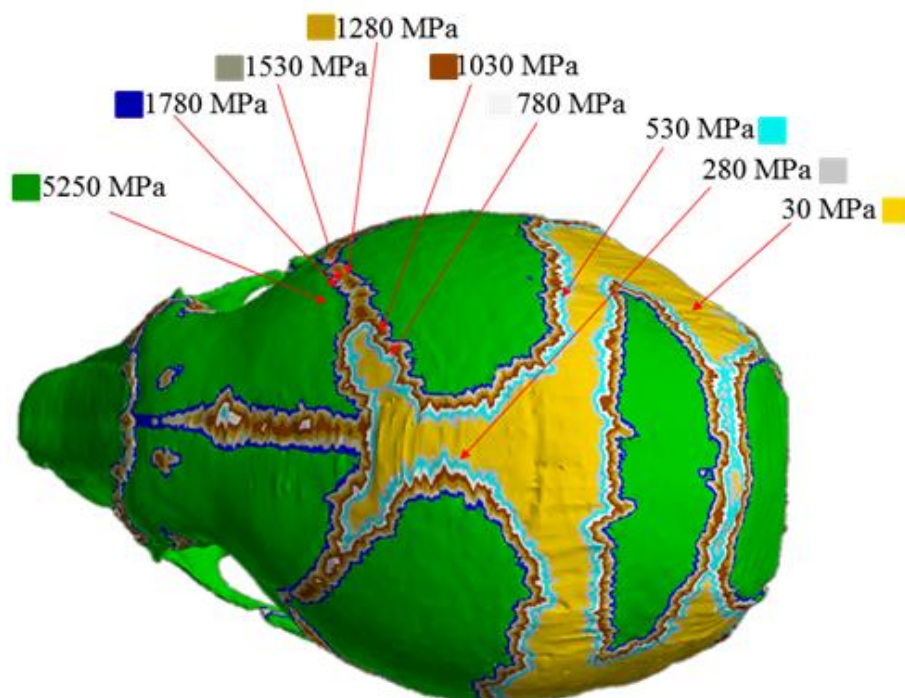
Fig. 5.11: Schematic presentation of the whole process of selecting different layers of elements and increasing the material properties step by step from P3 to P10.

Sensitivity to the strain range

The effect of strain range on the results was tested by changing the hydrostatic strain range from 0-1% to 0-2.5% and 0-5%. These values were used based on the initial observation of the level of hydrostatic strain that the sutures undergo during the growth from P3 – P4 as it is shown in Fig. 5.5.

Sensitivity to the convergence criterion

Convergence criterion defined here played an important role in the bone formation (suture fusion) rate. A low convergence rate could theoretically lead to a high rate of bone formation per day leading to the suture fusion at the early postnatal days that could be unrealistic. Nevertheless, convergence criterion was changed from 0% to 5% and 15% and its effect on the pattern of bone formation was investigated.

5-3-2 Results

Sensitivity to the strain range

Fig. 5.12 summarises the patterns of bone formation at the sutures with different hydrostatic strain ranges. Fig 5.12 corresponds to the initial analysis and runs from P3 to P4 only. At the end of each iteration the elastic modulus of the selected suture elements was updated (first iteration) without updating the geometry to that of P4. Then the model is loaded again (second iteration) and this process was repeated for several iterations. For the hydrostatic strain $\varepsilon<5\%$, all sutures were differentiated into bone after 25 iterations, while using 2.5% range some of the sutures were still open after 50 iterations. The simulation then stops because no new bone is generated. When using 1% range, after 50 iterations only a few elements were differentiated into bone and no more bone was generated.
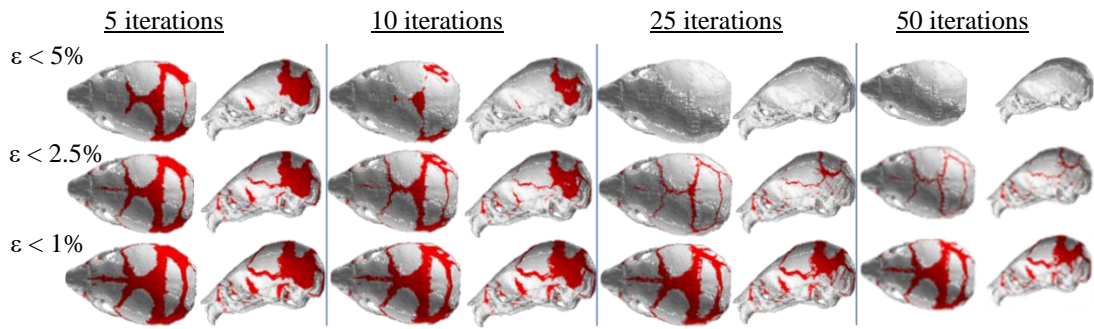
Fig. 5.12: Sensitivity to the hydrostatic strain range after several iterations (from P3 to P4). Selecting elements with hydrostatic strain (ε) less than 2.5% (top row), 2% (middle row), and 1% (bottom row). Note, grey highlights bones and red highlights sutures.

Sensitivity to the convergence criterion

Fig. 5.13 shows the pattern of bone formation at the sutures while changing the convergence criterion from 0% to 5% and 15%. Convergence criterion of 0% and 5% led to a selection of all of the suture tissue and changing it to a stiffer material. Then, again at the next age, all the elements across the new tissue were selected and gradually stiffened all the way up to P10 with elastic modulus of 530, 1030 and 1780 MPa at P5, P7, and P10 respectively. However, increasing the convergence criterion to 15% led to gradual day by day tissue differentiation across all the sutures.

Suture sizes at P10

Table 5.2 compares the predicted suture width for the baseline model in this study with the *ex vivo* measurements across fourteen anatomical positions across the skull. Note that elastic modulus equal or below 780 MPa was considered as sutures and above 1030 MPa was considered as bone. The baseline strain type and value used here was hydrostatic strain less than 5% with the convergence criterion of 15%. The FE results predicted full closure at the frontal suture and the mid lambdoid suture, while the *ex vivo* analysis highlighted that these sutures remain open by P10. The FE model over-estimated the suture sizes at all of the measurement points except point 4, with the maximum over prediction of 479% at point 5 and best match at point 4

with 5% difference. The average difference between the FE results and *ex vivo* was about 166%.
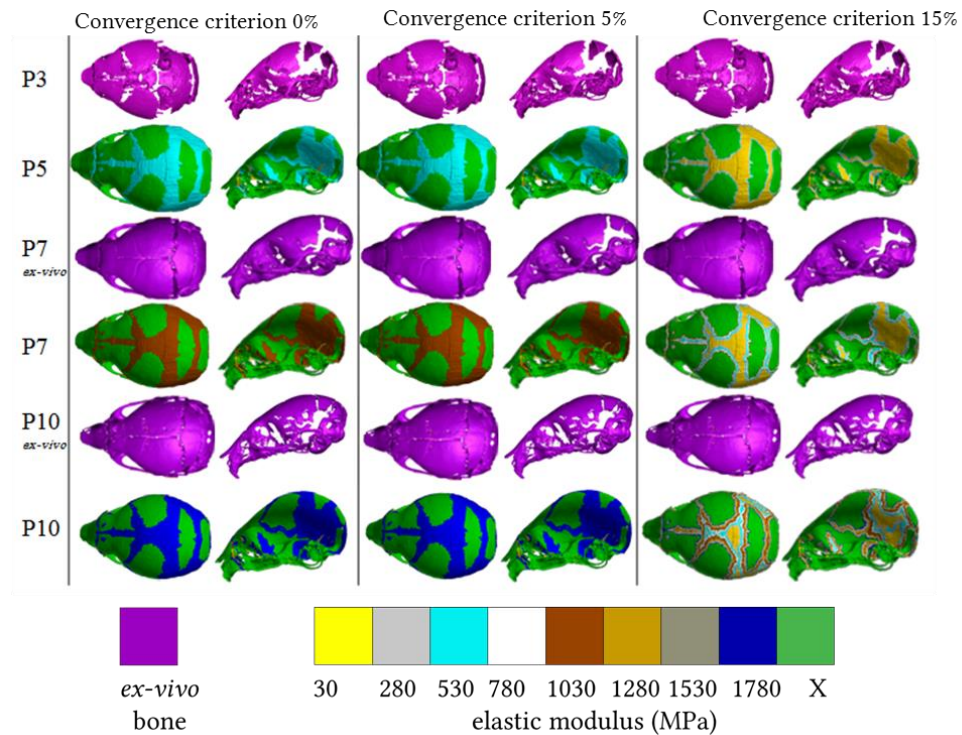
Fig. 5.13: Sensitivity to the convergence criterion in element selection with iteration method. 0% and 5% had same results. In both criteria, the process of stiffening the suture repeated until most of the suture elements were converted to a harder material with E=280 MPa at P4. This was repeated in the next ages until P10. At P10 there was only bone (E=5250 MPa) and the material coloured blue (E=1780). However, 15% criterion led to a proper tissue differentiation at sutures. The elastic modulus of bone (green, X) increased 250 MPa at the end of each age starting from 3500 MPa at P3 up to 5250 MPa at P10.

Table 5.2: Suture size predictions (in mm) based on the 2nd model presented in the study 2 versus *ex vivo* measurements at P10.

		2nd model	Av *ex vivo*	Δ%
Frontal suture	1: medial point	0	0.39	-
	2: posterior point	0	0.226	-
Sagittal suture	3: anterior point	1.12	0.312	261
	4: medial point	0.30	0.32	-5
	5: posterior point	2.50	0.432	479
Right Interparietal suture	6: closest point to the midsagittal plane	0.81	0.334	142
	7: medial point	0.50	0.224	125
	8: most lateral point	0.33	0.306	9
Left Interparietal suture	9: closest point to the midsagittal plane	1.01	0.45	125
	10: medial point	0.58	0.256	128
	11: most lateral point	1.75	0.492	255
Lambdoid suture	12: Most lateral point- Right	1.34	0.374	259
	13: medial point	0.00	0.14	-
	14: Most lateral point- Left	0.64	0.48	34

5-3-3 Discussion

Fig. 5.12 shows the pattern of bone formation at the sutures at P4 and for different hydrostatic strain ranges. It was found that when there was no limit stopping the bone generation process (i.e. convergence criterion of 0% with ε < 5%), all the sutures were turned to the bone tissue at P4. This is clearly not biological and the main reason behind it in the model described here is that, the hydrostatic strain is less than 5% across all the sutures. Even reducing the strain threshold to ε < 2.5% and running the simulations up to P10, did not result in a pattern of bone formation comparable to the *ex vivo* data. As Fig. 5.13 shows, it can be seen that with such criterion all suture elements were selected (mainly by P4) and from P5-P10 the elastic modulus of the whole sutures was increased without any tissue differentiation across the sutures.

However, altering the convergence criterion from 0 to 15% (see Fig 5.12) did generate a pattern of tissue differentiation across the sutures corresponding to the biological pattern observed in the study of Moazen *et al.* (2015). Nonetheless, 15% convergence criterion was a rather arbitrary criterion and it was felt that instead a more biological factor such as bone formation rate per day as a limit to control how much bone can be formed per day might be a more appropriate criterion. This was introduced and developed in the following section, Study 3.

5-4 Study 3 Bone formation - mesh independent

Considering the limitations of the convergence criterion that was used in the Study 2 here a different approach was used. In this Study a radius adjacent to the bone was used where the tissue-differentiation algorithm was only applied to that zone. Several sensitivity tests were performed to understand the effect of different parameters e.g. radius of the zone on the predicted suture closure pattern. Results were compared to microCT images of an average *ex vivo* P7 and P10 mice as described in the Chapter 3.

5-4-1 Materials and methods

The baseline P3 wild type mouse model developed in Chapter 4 was used in this study. In brief, all sections were assigned isotropic material properties with and elastic modulus and Poisson's ratio of 3500 MPa and 0.3 for bone, 30 MPa and 0.3 for suture and 150 MPa and 0.48 for brain respectively. First, the brain volume at P3 was expanded to the brain volume of P4. At the end of expansion, suture elements in a specific distance from bone (baseline radius: 0.1 mm) were selected. Out of the selected elements those with strain values in the defined range (baseline: strain less than 5%) and type (baseline: hydrostatic strain) were selected and their elastic modulus was increased by 250 MPa per day. At the same time the elastic modulus of the bone was also increased by 250 MPa per day. Then, the new geometry was updated to the deformed P3 geometry i.e. the starting point geometry for the P4 simulation. Then the whole process was repeated for the next age, up to P10 (see Fig 5.14). Several sensitivity tests were performed to analyse the effect of changing the strain type, the strain range, and the radius of the bone formation threshold across the sutures on the results.

In order to simulate the radial selection of elements in ANSYS, first the external nodes of the bone elements were selected. Then on each node, a spherical coordinate system was defined. Next, on each coordinate system, the nodes within the specific radius were started. Finally, the suture elements attached to these nodes were selected.

Sensitivity to the strain type

Three different strain types were compared in the process of element selection: von Mises strain, first principal strain (P1), and hydrostatic strain. Since the maximum hydrostatic strain was much smaller than the other two (Fig. 5.15), a lower range was used for this strain.

Sensitivity to the bone formation radius

Three different radiuses of 0.05mm, 0.1mm and 0.2mm were compared when suture elements were selected in a specified range. Fig. 5.16 shows how the element selection algorithm selected different layers of suture. Fig 5.3 shows the mesh density at the sagittal, frontal, and coronal sutures.

Sensitivity to the strain range

To investigate the effect of the range of strain used in the element selection process, the baseline strain selection range was ε < 5%, which changed was to 2.5% < ε < 5% and ε < 2.5%.
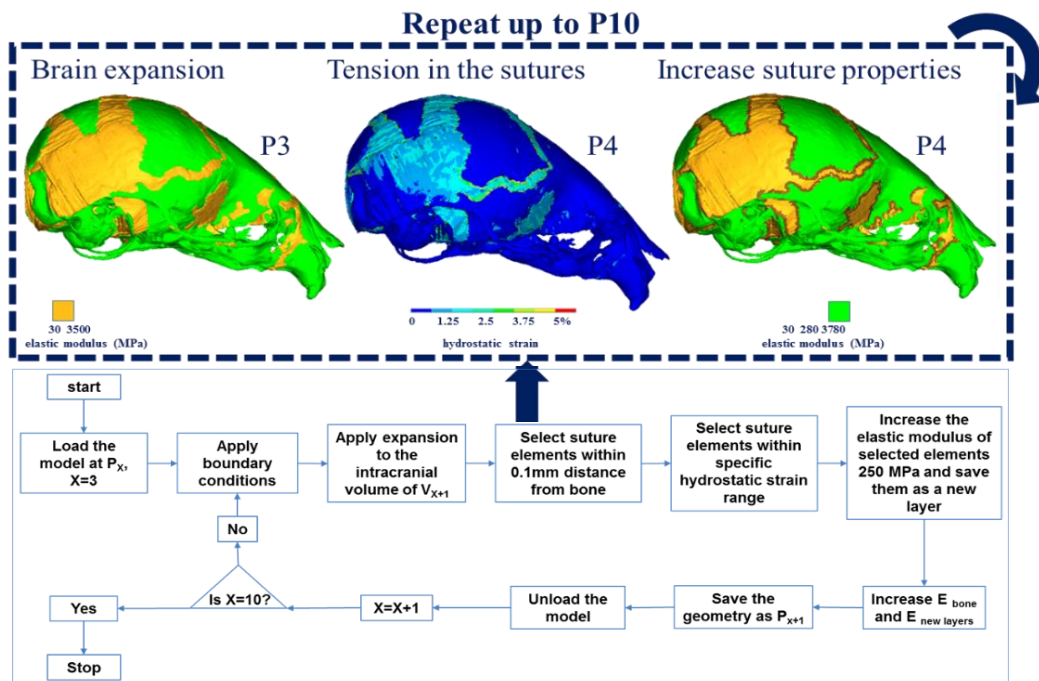
Fig. 5.14: The intracranial volume was expanded to the volume of the next age i.e. from P3 to P4. Then, material properties of the suture elements within the specified hydrostatic strain range and distance from the bone were updated. Also, elastic modulus of bone was increased, and the updated geometry was saved as P4. This process was repeated until P10. The flow diagram shows the overall process.
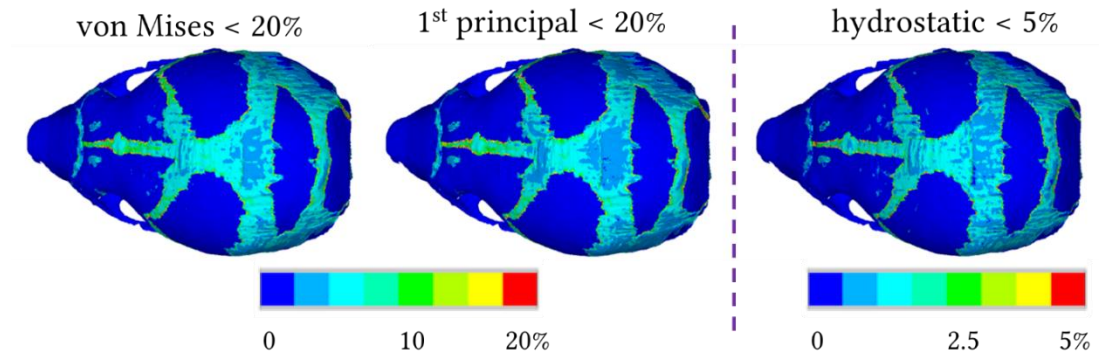
Fig. 5.15: Contour plots for different strain type: von Mises strain and 1st principal strain with the maximum value of 20% in legend and 5% for hydrostatic strain. Note that changing the legend range when the strain type is changed can lead to similar contour pattern
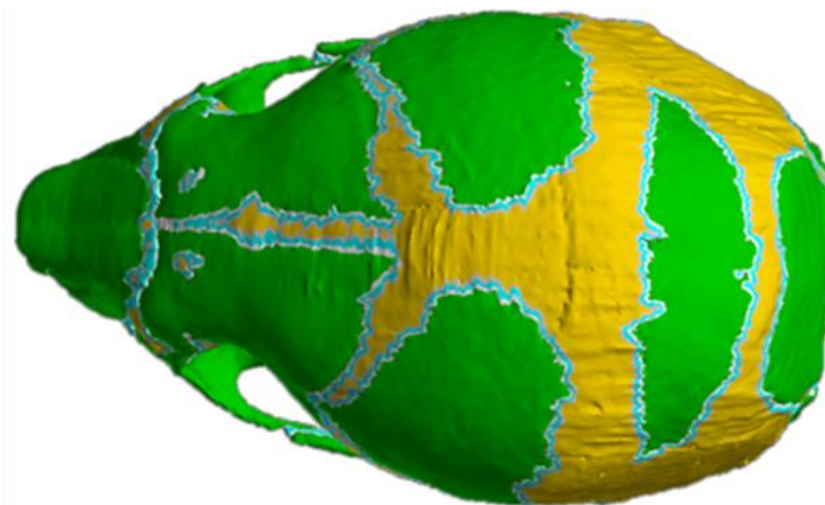
Fig. 5.16: Different layers of the suture elements attached to the bone element. Yellow is suture and green is bone. White and light blue are two layers of suture elements attached to bone, selected base on the distance of the suture elements from bone to increase their elastic modulus.

5-4-2 Results

Sensitivity to the strain type

Fig. 5.17 compares the pattern of tissue differentiation across the sutures with different strain types against the *ex vivo* data at P10. It was found that regardless of the strain type, i.e. von Mises, 1st principal or hydrostatic strain, a similar pattern of bone formation was found at P10. Since the hydrostatic strain was used in the previous studies on modelling bone formation in the long bones and takes into account the effect of all three principal strains, it was used as the baseline parameter for this study.

134
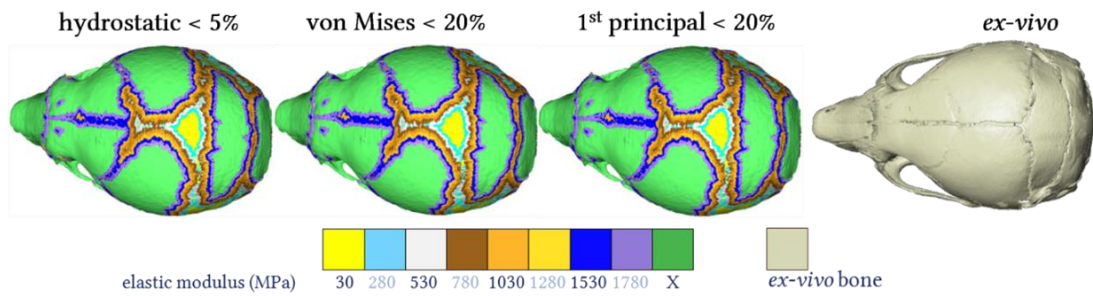
Fig. 5.17: Sensitivity test results for strain type: selecting suture elements with hydrostatic strain less than 5% as the baseline compared with von Mises strain and 1st principal strain less than 20%. Note that changing the selection range when the strain type is changed can lead to similar results.

Sensitivity to the distance from bone (r)

Fig. 5.18 shows the result of changing the radius of element selection on the bone formation pattern. It was found that the results were sensitive to the choice of the element selection radius. The same pattern of the tissue-differentiation was observed regardless of the exact radius. However, the higher radius showed a higher rate of bone formation. Comparing the three chosen radiuses, 0.1 mm radius showed a closer match with the *ex vivo* data.
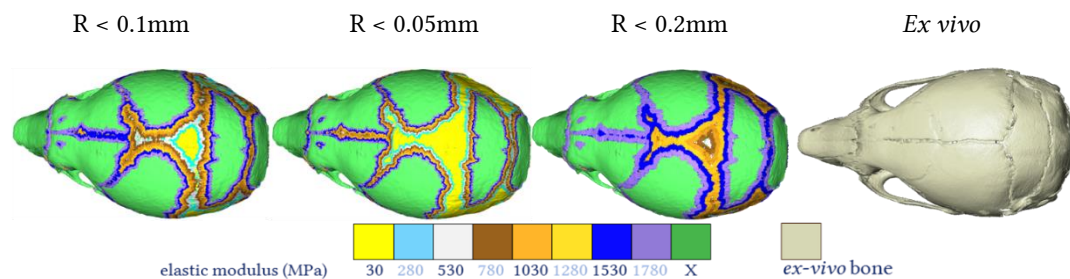
Fig. 5.18: Sensitivity test results for tissue differentiation radius: 0.1mm as the baseline compared with 0.05mm and 0.2mm. Note that the elastic modulus of the bone tissue (X) is increased 250 MPa at the end of each age, from 3500 MPa at P3 to 5250 MPa at P10.

Sensitivity to the strain range

Fig. 5.19 shows how changing the hydrostatic strain rage affected the predicted pattern of the tissue differentiation at P10. It was found that selecting elements with hydrostatic strain less than 5% led to a smooth tissue differentiation at P10 that could be similar to the *ex vivo*. Selecting the elements with strain less than 2.5% led to a similar pattern of tissue differentiation but with different layers intersecting with

135

one another and generated layers are not as distinct as 5% method. Selecting strain range between 5% and 2.5% did not predict the same pattern of bone formation and in fact almost all sutures remained wide open at P10.
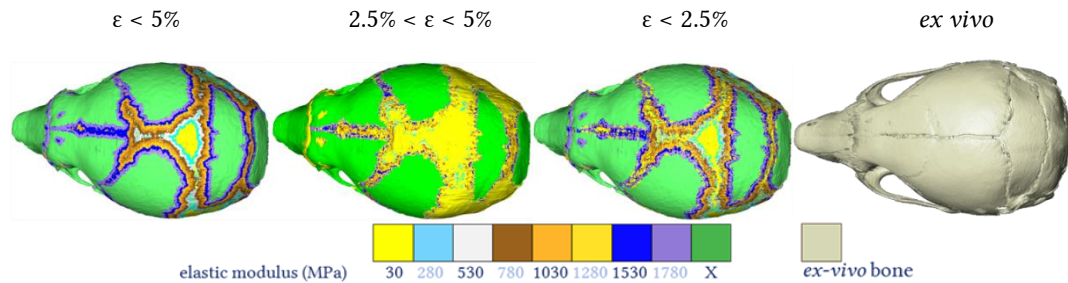
Fig. 5.19: Sensitivity test results for strain range: selecting suture elements with hydrostatic strain less than 5% as the baseline was compared with the strain ranges between 5% and 2.5%, and less than 2.5%.

Suture sizes at P10

Table 5.3 compares the suture width for the baseline model in this section (i.e. with hydrostatic strain less than 5% of suture elements selected within 0.1mm radius of bony edges) versus *ex vivo* microCT data at P10 at 14 measured sections. Similar to the previous two studies the FE results predicted closure of the frontal suture while *ex vivo* data suggest that this suture is still open at P10. There was a close match between the FE results and the *ex vivo* measurements at points 7 and 10 with a 6% difference between the measurements. Maximum difference was at point 5 with a difference of 361%. The average difference between the FE results and *ex vivo* measurements was about 90%.

Although predicted suture sizes were not exactly same as the *ex vivo* data, but overall there was a better match in this model (with an average difference of 90% compared with 166% for 2nd method and 98% for the 1st method).

Table 5.3: Suture size predictions (in mm) based on the 3rd model presented in the study 3 versus *ex vivo* measurements at P10.

		3rd model	Av *ex vivo*	Δ%
Frontal suture	1: medial point	0	0.39	-
	2: posterior point	0	0.23	-
Sagittal suture	3: anterior point	0.66	0.31	112
	4: medial point	0.25	0.32	-22
	5: posterior point	1.99	0.43	361
Right Interparietal suture	6: closest point to the midsagittal plane	0.66	0.33	98
	7: medial point	0.21	0.22	-6
	8: most lateral point	0.25	0.31	-18
Left Interparietal suture	9: closest point to the midsagittal plane	0.71	0.45	58
	10: medial point	0.24	0.26	-6
	11: most lateral point	1.04	0.49	111
Lambdoid suture	12: Most lateral point- Right	1.03	0.37	175
	13: medial point	0.00	0.14	-
	14: Most lateral point- Left	0.58	0.48	21

5-4-3 Discussion

Similar to Study 1 & 2 of this chapter, the effects of different strain types on the pattern of bone formation at the sutures were studied. A smaller strain range was used for the hydrostatic strain. This was due to the lower range of hydrostatic strain in comparison to the von Mises and 1st principal strains at the radial expansion of the calvaria from P3 to P4. It was also found that using different strain types had a minor effect on the final tissue differentiation pattern. The hydrostatic strain was used as the baseline strain type due to it being used in previous studies on modelling the bone formation during the fracture healing process (Claes and Heigele, 1999).

Altering the radius of the bone formation zone clearly altered the tissue differentiation pattern with over or under estimation of bone formation. A zone of 0.1mm away from the bony edges led to a close pattern of bone formation to what was observed on the reconstructed microCT images. This range was also similar to the finding of Henderson *et al.,* (2004) who reported a rate of 0.13mm/day bone formation across the sutures. Note results obtained from the quantification of the *ex vivo* data in Chapter 3 highlighted a rate of 0.14mm/day bone formation across the sutures (see section 3.4.3).

Changing the strain range also had a major effect on the resultant tissue differentiation pattern. It was found that changing the strain range from the baseline of less than 5% to between 5% and 2.5%, and less than 2.5% affected the final tissue differentiation results, with a more uniform bone formation pattern resulted in the range of less than 5% (the baseline).

5-5 Study 4 Bone formation - contact elements

One of the main limitations of the algorithm and approach developed in the Study 3 was that the relative motion that may exist at the brain-bone/suture interface during the calvarial development was not taken into account. The aim of this study was to include such relative motions in the modelling approach using contact elements and to investigate its effect on the pattern of the bone formation at the sutures.

5-5-1 Materials and methods

The same algorithm that was developed in the Study 3 was used here. The difference here was that contact elements were used at the brain-bone/suture interface (that were previously fixed/tied). Fig. 5.20 shows how contact elements were defined around the brain elements. Sensitivity tests were performed to investigate the effect of changing various key contact element parameters on the model i.e. contact stiffness, friction coefficient and penetration tolerance factor.

Sensitivity to the contact properties (stiffness, friction and penetration tolerance factor)

To study how contact properties, affect the bone formation at the suture, several sensitivity tests were performed. These parameters included the contact stiffness, friction coefficient and penetration tolerance factor. Allowable penetration was calculated based on the penetration tolerance factor (ANSYS, 2017).

Six different values were used to test the effect of contact stiffness. Contact stiffness was increased from 100 to 2000 N/mm in 5 steps (100, 250, 500, 750, 1000 and 2000 N/mm). Then, two values of friction coefficients were compared. The friction coefficient was changed from the baseline value of 0.1 to 0.05. Finally, three different values were used to investigate the effect of penetration tolerance factor. The tolerance factor's value was changed from the baseline value of 0.1 to 0.5 and 0.75. Appendix I provides a detailed explanation about how the contact method functions.
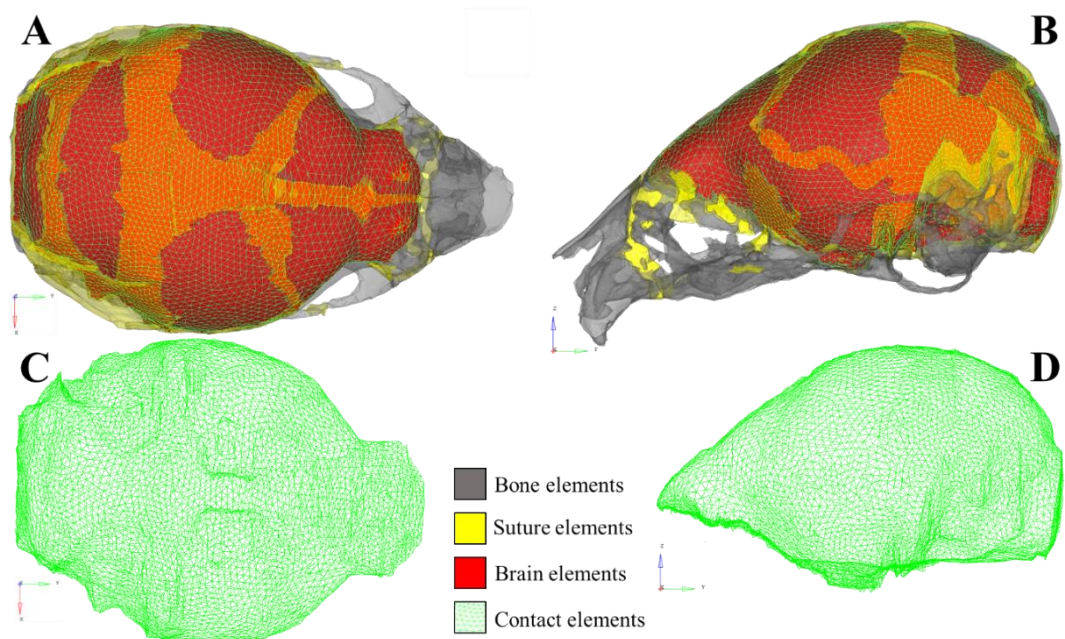
Fig. 5.20: Contact elements were defined at the brain-bone/suture interface. Bone and suture elements are shown in transparent mode.

5-5-2 Results

Sensitivity to the contact stiffness

Figs. 5.21 to 5.24 show the effect of changing the contact stiffness on the results. Von Mises strain contour plots (dorsal view Fig. 5.21 and lateral view Fig. 5.22) highlight that similar patterns of von Mises strain were obtained across the sutures with the contact stiffness above 500 N/mm. However, comparing the element plots (dorsal

view Fig. 5.23, and lateral view Fig. 5.24) highlighted that with contact stiffness of 500 N/mm, brain elements penetrated into bone and suture elements and this issue was addressed by increasing the contact stiffness to values larger than 1000 N/mm. So, this value was selected as the baseline value throughout the study.
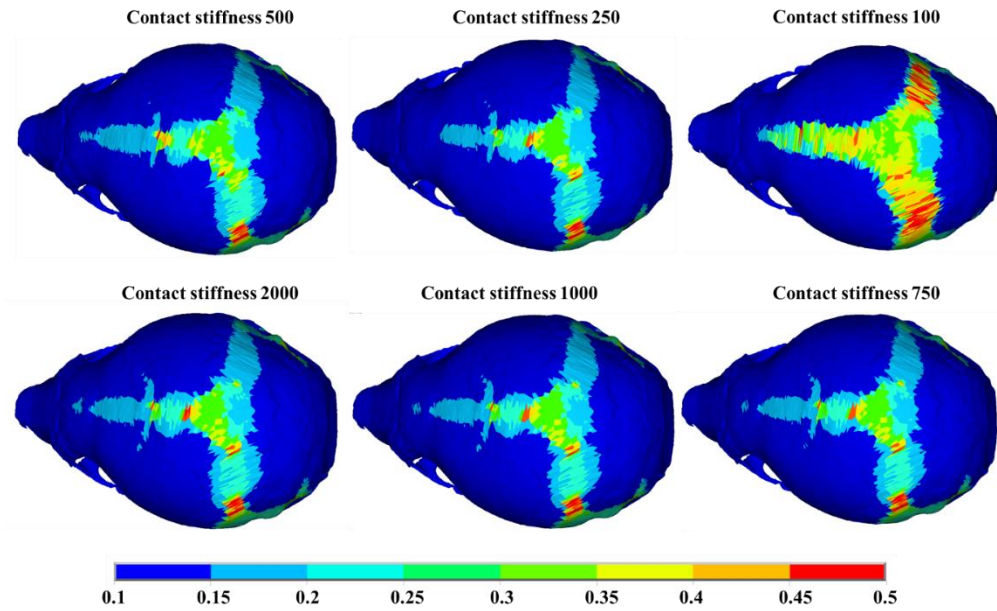
Fig. 5.21: Dorsal views of von Mises strain contour plots when contact stiffness was changed from 100 N/mm to 2000 N/mm at P10.
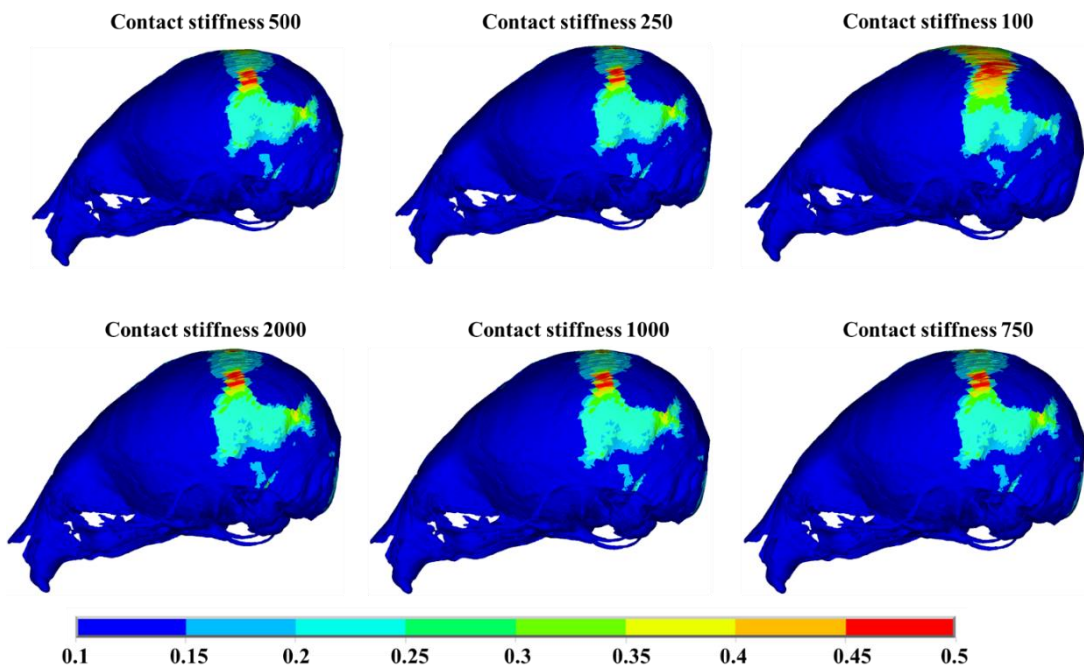
Fig. 5.22: Lateral views of von Mises strain contour plots when contact stiffness was changed 100 N/mm to 2000 N/mm at P10.
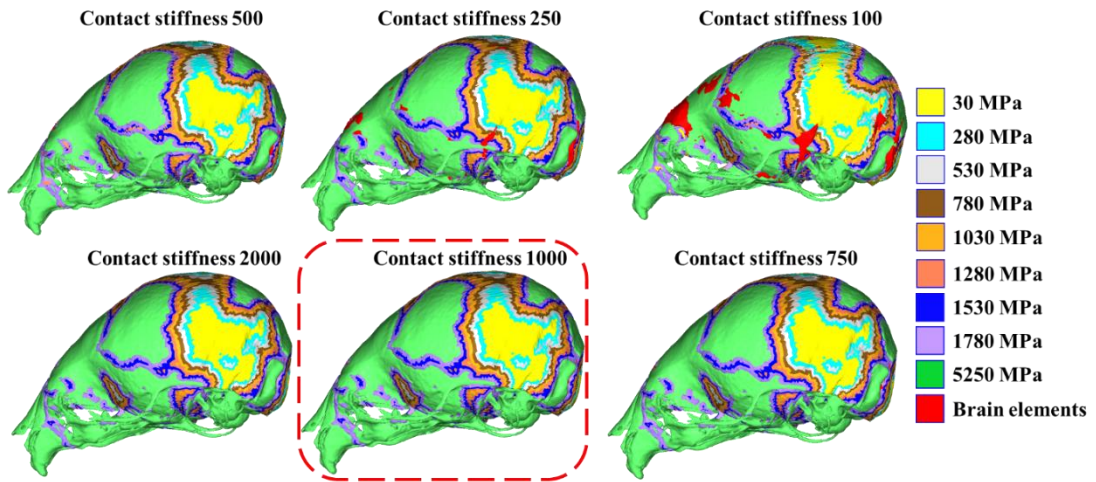
Fig. 5.23: Dorsal views of element plots when contact stiffness was changed from 100 N/mm to 2000 N/mm. In this view, it can be seen brain elements penetrate through the bone and suture elements when the contact stiffness is less than 500 N/mm (dashed red line rectangle is highlighting the baseline model).
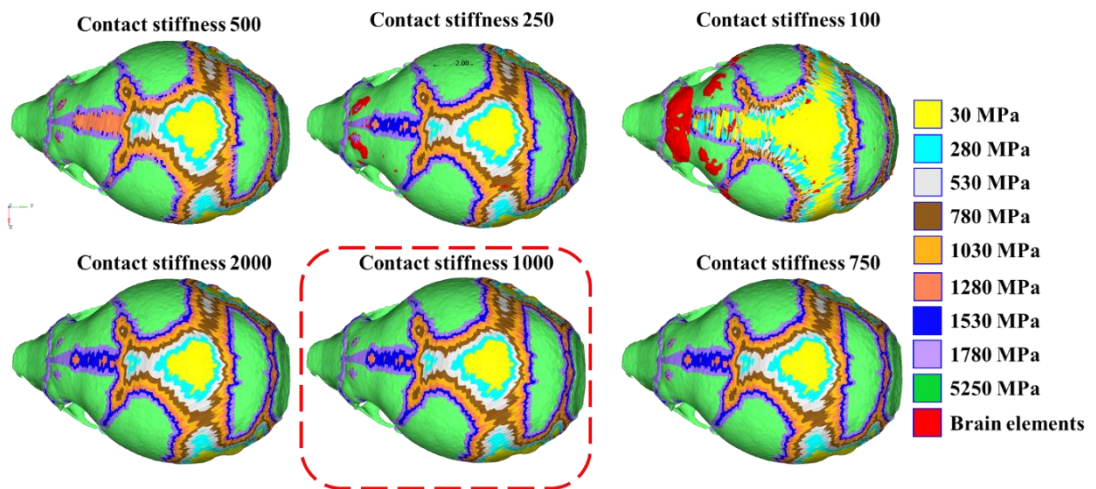
Fig. 5.24: Dorsal views of element plots when contact stiffness is changed from 100 N/mm to 2000 N/mm. In this view, it can be seen brain elements penetrate through the bone and suture elements when the contact stiffness is less than 1000 N/mm (dashed red line rectangle is highlighting the baseline model).

Sensitivity to the friction coefficient

Fig. 5.25 shows the result of changing the friction coefficient. It was found that decreasing the friction coefficient leads to bulging across the dorsal part of the skull and increased in the height prediction of the skull at P10. Friction coefficient of 0.1 was used throughout the study as the baseline value.
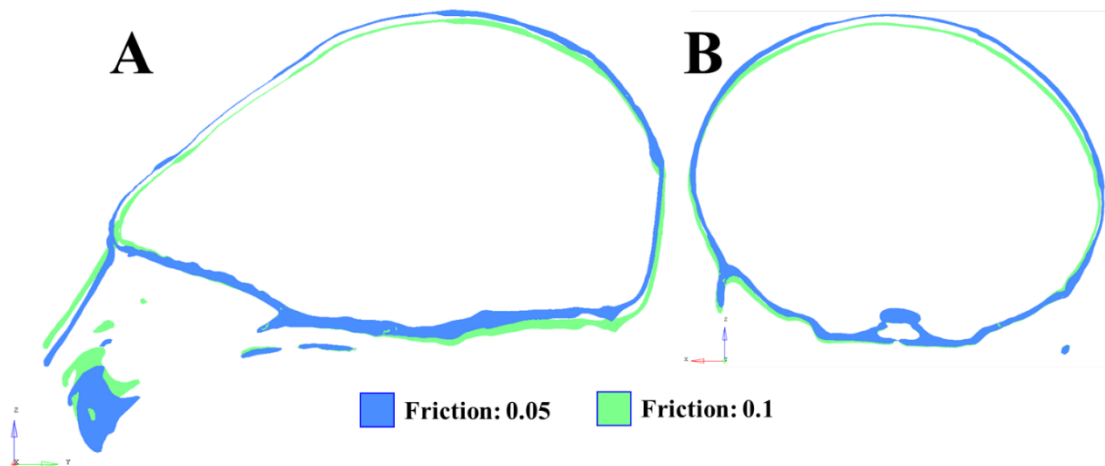
Fig. 5.25: Lateral (A) and anteroposterior (B) cross-section views of calvaria expanded to P10. When the value of contact friction is set as 0.1, there is less bulging across the calvaria which is desirable.

Sensitivity to the penetration tolerance factor

Fig. 5.26 shows the expansion of skull from P3 to P10 using the contact method. The effect of changing the contact penetration tolerance factor on the results was studied. It was observed that changing this factor from 0.1 to 0.5 and 0.75 had no effect on the results (all different results overlapped on top of each other at every age). Here value of 0.1 was selected as the baseline value throughout the study.
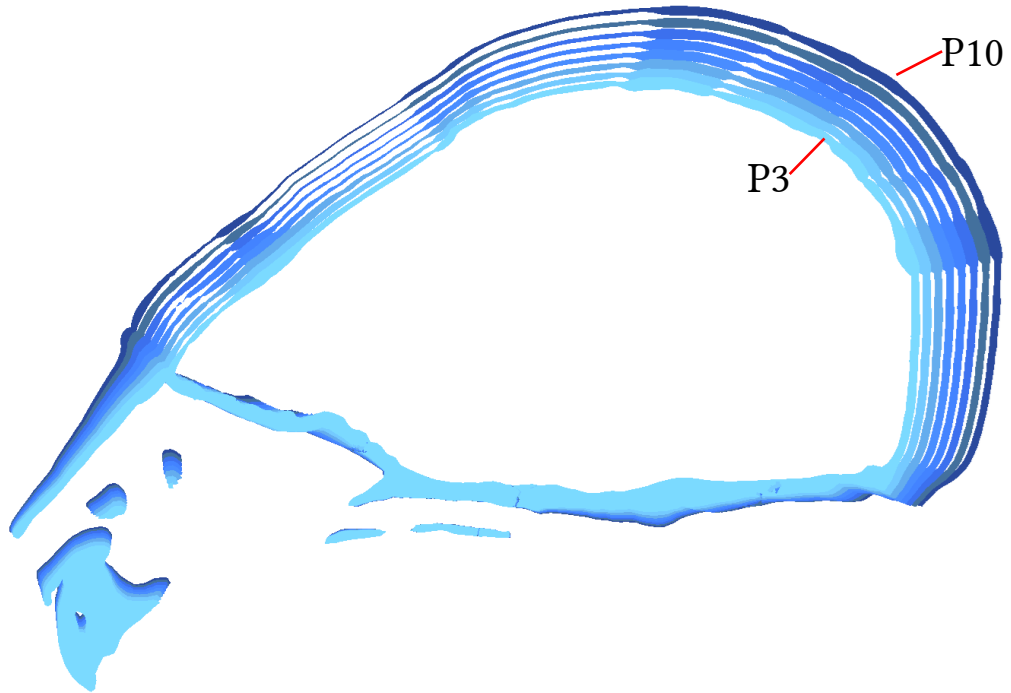
Fig. 5.26: Lateral cross-section views of calvaria expanded from P3 to P10. Changing values of the contact penetration tolerance factor from 0.1 to 0.5 and 0.75. The resultant sections from all three overlapped exactly on top of each other at each age, and it can be concluded that this factor had no effect on the results. Value of 0.1 was used as the baseline for this parameter.

Suture sizes at P10

Table 5.4 compares the suture width for the base model at this section (contact stiffness 1000 N/mm, initial friction 0.1 and penetration tolerance factor 0.1), versus *ex vivo* measurements at P10 at 14 measurement points as described in the Chapter 3 - section 3-2-5. This model was over-estimating the suture sizes almost at all sections (with exception of section 14). This method had extensively over-predicted suture sizes with a maximum difference percentage of about 1000% at point 5. Minimum difference was at point 14, which was the only under-estimated point, with a difference of 6%. Average percentage of the difference between the predations and *ex vivo* measurements across all the sections was 333%.

Table 5.4: Suture size predictions (in mm) based on the 4ᵗʰ model presented in the study 4 versus *ex vivo* measurements at P10.

		4ᵗʰ model	Av *ex vivo*	Δ%
Frontal suture	1: medial point	0	0.39	-
	2: posterior point	0	0.226	-
Sagittal suture	3: anterior point	1.43	0.312	357
	4: medial point	1.24	0.32	289
	5: posterior point	4.80	0.432	1011
Right Interparietal suture	6: closest point to the midsagittal plane	1.20	0.334	259
	7: medial point	0.89	0.224	297
	8: most lateral point	0.91	0.306	197
Left Interparietal suture	9: closest point to the midsagittal plane	0.92	0.45	105
	10: medial point	1.76	0.256	589
	11: most lateral point	2.41	0.492	390
Lambdoid suture	12: Most lateral point- Right	1.00	0.374	168
	13: medial point	0	0.14	-
	14: Most lateral point- Left	0.45	0.48	-6

5-5-3 Discussion

The aim of this study was to add contact elements to the algorithm developed in section 5-4 to take into account the relative movement that may exist at the brain-bone/suture interface. Various sensitivity tests were performed to investigate the effect of different contact parameters.

Considering the effect of changing the contact stiffness, larger values ensured the contact was made at the brain-bone/suture interface and that prevented the brain from penetrating into the bone and sutures. This can be explained as the higher contact stiffness values provide a stiffer contact surface between the interfaces.

It was also found that decreasing the contact tangential friction coefficient resulted in more bulging at the dorsal part of the calvaria. A value of 0.1 was used for this parameter as the baseline value. It was tried to use a low friction value to represent the frictionless environment between the brain and the skull/suture interface. On the other hand, it was found that changing the contact penetration tolerance factor had a minimal effect on the final results.

Fig. 5.27 compares P10 skull cross-sections of FE predictions for contact and noncontact (fixed interface) methods i.e. comparing the models described in this study section 5.5 and previous study section 5.4. A more anterior expansion of the skull was predicted near the Ethmoid bone (red oval). Also, the model that used the contact elements at the brain-bone/suture interface showed a more anteriorposterior growth and a lesser rotation across the constrained nodes (see Fig 5.27 for highlighted red stars) on the presphenoid bone.
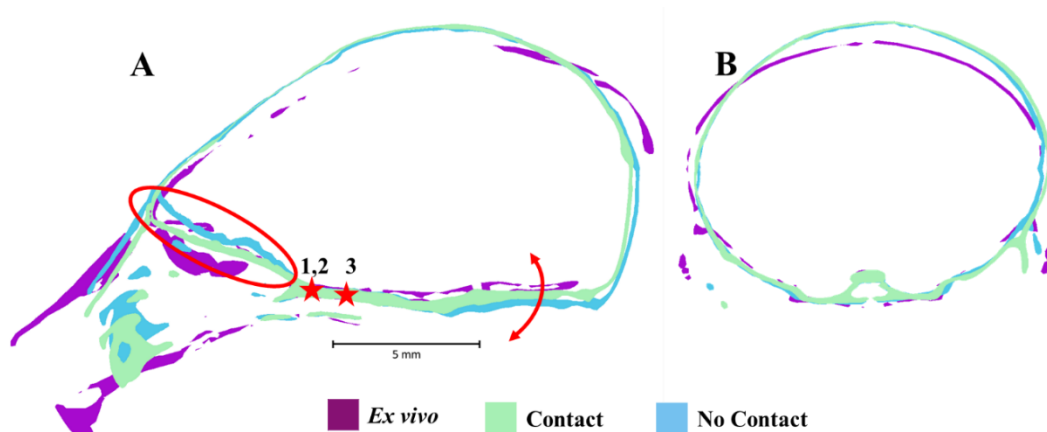
Fig. 5.27: Lateral (A) and anteroposterior (B) cross-section views of calvaria expanded to P10 comparing *ex vivo* versus contact and noncontact methods. Using the contact method increases the anterior expansion (red oval) while decreasing the rotation around the constrained nodes.

Considering that this study highlighted minimal differences in the pattern of the bone formation and morphological differences between the contact models and fix interface model i.e. at the brain-bone/suture interfaces. The fix interface model was used in the final study of this Chapter. Note that while the contact model is perhaps a more realistic approach to model the brain-bone/suture interface it has a huge computational time versus the fixed interface model. For example, a typical fixed interface model took about 10 minutes to be solved, and about 4 hours by the contact model.

5-6 Bone formation at the sutures in the MT mouse model

The aim of this study was to predict the pattern of bone formation at the sutures in the mutant mouse model from P3 to P10. The model that was used for this study was the model that described in the Study 3 i.e. the wild type model at P3 that assumes a

fixed boundary condition at the brain-bone/suture interfaces. The sutures that are fused in the *Fgfr2$^{C342Y/+}$* (frontal, coronal, and lambdoid sutures, and PBS- please see Chapter 2 –section 2.5), were fused on the FE model of the wild type mouse and the results were compared against suture measurements of the mutant mouse at P10 presented in Chapter 3 (please see Table 3.4).

5-6-1 Materials and methods

The baseline model described in the Study 3 of this chapter was used to predict the mutant skull shape. As mentioned in the previous chapters, several sutures are fused in the *FGFR2$^{C342Y/+}$* mouse model. These include Presphenoid-basisphenoid synchondrosis (PBS), frontal, coronal, and lambdoid sutures (see e.g. Liu et al 2013). In the FE model of the MT mouse, these sutures were fused in combination (based on the finding of previous chapters), to investigate the effect of their fusion on the bone formation pattern and dimensions of the cranial sutures. Suture fusion was modelled by assigning same material property as bone, i.e. 3500 MPa at P3, to the fused sutures.

5-6-2 Results

Fig. 5.28 compares dorsal and lateral views of the FE predictions for the non-contact (fixed interface) method with the *ex vivo* mouse skull reconstructions at P3, P7 and P10. It can be seen that the anterior-posterior closure pattern of the sagittal suture was comparable to the *ex vivo* calvarias. Similar to the previous sections, it was assumed that tissues with an elastic modulus equal to or less than 780 MPa, were still suture, while tissues with elastic modulus greater than 780 MPa were considered as bone or hard tissue.

Table 5.5 compares the FE suture measurements with the *ex vivo* data at P3, P7 and P10. To mimic the early fusion of these sutures in the Crouzon mouse, the sutures at 2nd and 13th points were assumed to be fused at P3. Hence, our predictions at P7 and P10 were also a fused suture with a width of 0, whereas the *ex vivo* measurements showed that these regions were not fully fused, but are very close to 0.
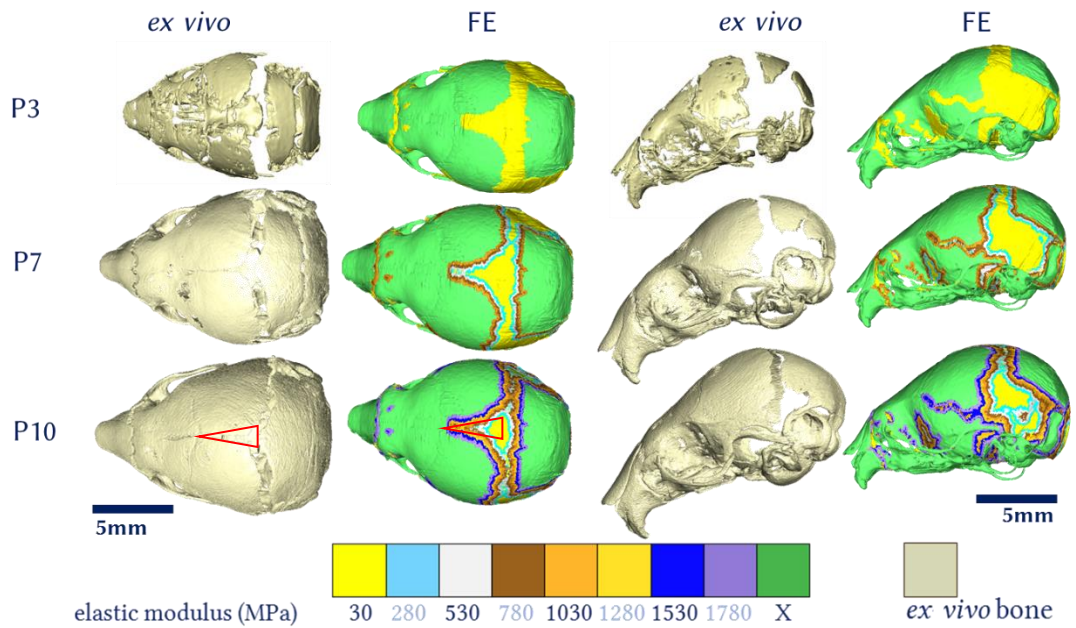
Fig. 5.28: Dorsal and lateral views of bone formation pattern for the MT model from P3 to P10 using the noncontact (fixed interface) model, compared with the *ex vivo*. Red tringles are highlighting the sagittal suture fusion pattern at P10.

Table 5.5: Finite element suture measurements of the MT model (in mm), compared with the *ex vivo* data at P3, P7 and P10.

	P3			P7			P10		
	Av *ex vivo*	SD*	FE	Av *ex vivo*	SD	FE	Av *ex vivo*	SD	FE
1	1.03	0	0	0.38	0.18	0	0.36	0.22	0
2	0.84	0	0	0.28	0.16	0	0.21	0.07	0
3	1.88	0	1.2	0.36	0.17	0.57	0.27	0.05	0
4	1.41	0	1.46	0.4	0.29	1.12	0.32	0.13	0.14
5	2.84	0	3.24	0.69	0.33	3.00	0.5	0.13	1.74
6	1.86	0	1.11	1.13	0.24	1.16	0.64	0.48	0.69
7	1.37	0	1.16	0.74	0.27	1.10	0.88	0.77	0.24
8	1.4	0	1.24	0.67	0.16	1.15	0.49	0.3	0.28
9	1.58	0	1.1	0.89	0.17	1.12	0.6	0.27	0.77
10	1.33	0	1.36	0.83	0.23	1.29	0.77	0.56	0.26
11	1.24	0	1.41	0.56	0.32	1.45	0.52	0.26	1.09
12	1.16	0	0	0.36	0.13	0	0.33	0.13	0
13	0.73	0	0	0.17	0.13	0	0.04	0.06	0
14	0.91	0	0	0.46	0.17	0	0.19	0.07	0

* Due to having only one specimen at P3, SD values are 0.

5-6-3 Discussion

The aim of this study was to use the baseline algorithm developed in the section 5-4 to simulate the bone formation pattern in mutant mouse calvaria. Since the baseline model was used, no more sensitivity tests were conducted here. To model the fused sutures, they were assumed to be same as bone tissue from the starting point of the simulation. The overall pattern of suture fusion and bone formation could be captured.

5-7 Discussion

The aim of this study was to develop an algorithm to model the bone formation at bone-suture interface during the calvarial growth from P3 to P10. Various sensitivity tests were performed to understand the effect of different parameters, and the results were compared against the *ex vivo* data in terms of overall pattern of bone formation at the sutures.

In this chapter, it was tried to simulate the bone formation at the sutures by increasing the elastic modulus of the sutures. Four different modelling strategies were developed starting from a simple approach to a more complex approach with contact elements at the brain-bone/suture interface. A series of sensitivity tests were performed to investigate the effect of different parameters on each model. It was shown that strain type, range, number of elements selected, convergence criterion, bone formation rate, and contact parameters such as contact stiffness and friction, could affect the results in different modelling approaches.

The main parameters that could affect the bone formation pattern were shown to be the strain range, and bone formation rate (which is represented by the number of element layers) in the first model, the convergence criterion in the second model, and distance from the bone (selection radius or bone formation rate) in the third and fourth models. The hydrostatic strain range that led to a close match between the FE results and *ex vivo* data was found to be $\varepsilon < 5\%$. However, using other strain types could be possible, but the strain range should be adjusted.

In the third and fourth models, in order to make the bone formation algorithm mesh independent, the elastic modulus of some of the suture elements were increased at the end of each age, in a step by step and layer by layer approach, based on their distance from the bone. Comparing the estimated suture sizes (Table 5.5) shows that the third model was the best model. Using the contact method aimed to increase the longitudinal growth of the calvaria (Fig. 5.27). However, this affected the bone formation pattern by applying a higher tension across the suture elements and resulting in wider sutures at P10 (4th model in Fig. 2.29).
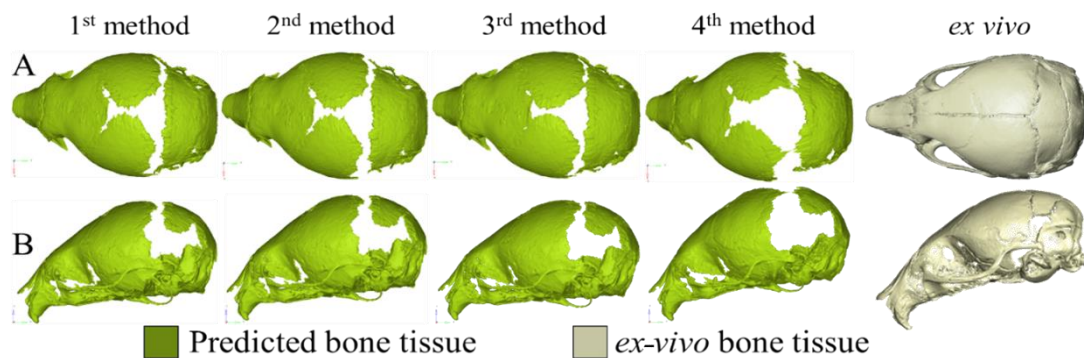
Fig. 5.29: Dorsal (A) and lateral (B) views of calvaria expanded to P10 comparing *ex vivo* vs. four suture formation methods. Suture tissue is hidden while bone tissue is coloured as green to provide a better overall view.

Table 5.5: Estimated suture sizes (in mm) for four modelling methods compared with *ex vivo* at P10.

		1st	2nd	3rd	4th	Av *ex vivo*
Frontal suture	1: medial point	0	0	0	0	0.39
	2: posterior point	0	0	0	0	0.23
Sagittal suture	3: anterior point	0.76	1.12	0.66	1.43	0.31
	4: medial point	0.28	0.30	0.25	1.24	0.32
	5: posterior point	0.92	2.50	1.99	4.80	0.43
Right Interparietal suture	6: closest point to the midsagittal plane	0.52	0.81	0.66	1.20	0.33
	7: medial point	0.58	0.50	0.21	0.89	0.22
	8: most lateral point	0.40	0.33	0.25	0.91	0.31
Left Interparietal suture	9: closest point to the midsagittal plane	0.74	1.01	0.71	0.92	0.45
	10: medial point	0.51	0.58	0.24	1.76	0.26
	11: most lateral point	1.02	1.75	1.04	2.41	0.49
Lambdoid suture	12: Most lateral point- Right	1.27	1.34	1.03	1.00	0.37
	13: medial point	0	0	0	0.00	0.14
	14: Most lateral point- Left	0.76	0.64	0.58	0.45	0.48

Previous studies have suggested that mechanical strain must be a key factor in regulating the bone formation at the sutures, in addition to the complex mix of chemical and biological signalling (Carter and Beaupre, 2000; Hall, 2015; Weickenmeier *et al.*, 2017). In this chapter, it was tried to develop an algorithm to model this phenomenon based on mechanical strains experienced by the sutures during the skull growth.

Moazen *et al.* (2015) showed that the bone tissue has a lower elastic modulus in the suture vicinity, and our current modelling approach simulates it (Fig. 5.30). However, further experimental measurements are required to validate the tissue differentiation that current model predicted across the sutures (Leong and Morgan, 2008; Moazen *et al.*, 2015).

Suture, 30MPa — Bone, 5250 MPa

Suture differentiation, 280 to 1780 MPa
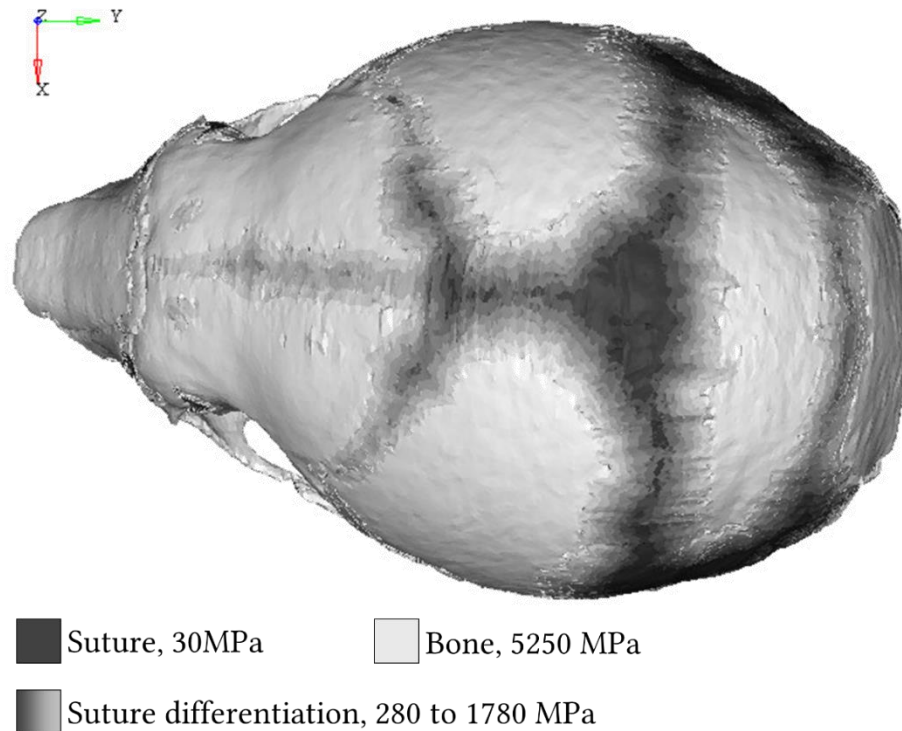
Fig. 5.30: Dorsal views of the calvaria expanded to P10 with tissue differentiation at sutures in grey scale. Darker sections have lower elastic modulus from 280 MPa at the vicinity of sutures to 1780 MPa at the vicinity of bone.

A number of assumptions and approximations had to be made in the simulations, but still there was good agreement in the pattern of bone formation across the sutures and with the *ex vivo* results. Some of the main simplifications that had to be considered in this section were as follows:

- Linear elastic properties were assumed for sutures while they are known to be nonlinear and viscoelastic.

- Bone formation was assumed to be uniform at all sutures and at all ages, while results in the Chapter 3 shows that not only this rate is both age and region dependant, it also varies between the WT and MT mice.

- Many biological and non-biological factors play a role in cranial bone formation, however, only hydrostatic strain was included in this study. It can be assumed that the bone formation rate could be a compensating factor including all other factors.

- Same P3 model (from geometrical point of view) was used when modelling cranial growth and suture ossification in the MT mouse. However, in Chapter 3 it was shown how WT and Crouzon mouse skulls are different.

- Average element size in sutures was in the range of 0.1 mm or 100 microns (Fig. 5.3), while in order to be able to capture the suture interdigitation, suture elements sizes require to be in the range of 10 to 20 micron or even less.

Main findings of this chapter can be summarised as:

- Fixed interface method:
    o Increasing the elastic modulus of the sutures in daily increments was a good imitation of biological nature of growth.
    o Bone formation rate of 0.1 mm/day within the 5% of hydrostatic strain level, led to reasonable results.
- Contact method:
    o Higher contact stiffness values decreased the penetration of ICV into bone/suture. However, it increased the solving time.
    o Lower contact friction values caused an increased bulging across the sagittal suture.
    o The penetration tolerance factor did not have a significant effect on the results.

In summary, it can be said that the proposed modelling method here has a great potential in the modelling the calvarial growth and bone formation. Different

reconstruction methods for the treatment of craniosynostosis can be simulated and compared using this method, which can provide significant advancement in terms of understanding the optimum management of various forms of this condition (Malde, Libby and Moazen, 2018), with a the long term goal of reducing the complications currently associated with the treatment of craniosynostosis.

Chapter 6: Discussion

6-1   Introduction

Calvarial development is thought to involve a series of complex biological, chemical and perhaps mechanical signals between a number of soft and hard tissues such as the growing brain, dura mater, sutures and bones (Morriss-Kay and Wilkie, 2005; Richtsmeier and Flaherty, 2013; Al-Rekabi, Cunningham and Sniadecki, 2017). Premature fusion of cranial sutures, or Craniosynostosis, is a medical condition that occurs in about 1 in 2500 births with reports of increases in its reoccurrence for unknown reasons (Boulet, Rasmussen and Honein, 2008; Van Der Meulen *et al.*, 2009; Johnson and Wilkie, 2011; Cornelissen *et al.*, 2016).

Usually, surgical interventions take place during infancy. The treatment process involves a multidisciplinary working group of neurosurgeons, plastic and reconstructive surgeons, maxillofacial surgeons, orthodontists, and anaesthetists to manage this condition. There is also a larger team of psychology, speech and language therapy as well as genetics experts who support the surgical team (Mathijssen, 2015; Malde, Libby and Moazen, 2018).

This study aimed to first obtain the morphological characteristics of wild type and Craniosynostotic type mice skulls from postnatal day 3 to 10 (which corresponds to about first year of age in humans). Then to use finite element method to predict the calvarial growth and bone formation at the cranial sutures in both WT and MT mouse models using the growing brain as the driving force. Results of the latter sections were validated using the average values of skull and suture dimensions collected in the first part. In this chapter an overview of the key findings of the work conducted throughout this project is discussed.

6-2   Morphological investigation of the WT and MT mouse skulls

Morphological characterisation showed that the calvarial length, width and height continuously increase from P3 to P10 for both the WT and MT models, as expected. The MT mouse skulls were wider and shorter compared to the WT mice, with an increase in their height. These observations were in line with previous studies on the same MT mouse model (Eswarakumar *et al.*, 2004; Liu *et al.*, 2013; Martínez-Abadías *et al.*, 2013; Perlyn, DeLeon, *et al.*, 2006; Peskett *et al.*, 2017). The results and average models obtained following this characterisation were then used for the validation of the finite element model.

There were several limitations within the morphological characterisation study. For example, (1) the results are obviously affected by the resolution of the microCT images. While high resolution CT scans were carried out future studies can for instance use synchrotron imaging facilities or maybe histological sectioning to characterise the suture sizes. (2) The standard deviations for some of the skull and suture measurements were relatively high. One reason could be that, at the age range that this study was focused on i.e. P3 to P10, due to the fast growth rate, even a half a day difference in birth time can make a remarkable difference in the measurements. Another reason could be that some of the specimens collected for this study may have been from different litter and the exact timing of birth might have been difficult to identify. Nonetheless, the relative differences in terms of morphological variations between the WT and MT mice at different ages were captured.

6-3   Mechanical properties

It is critical to use realistic material properties when it comes to any numerical analysis, and especially finite element method. In section 2.6, different material properties that have been reported for the cranial sutures, bones, and the brain were summarised. It was found that there is a wide range of elastic modulus reported for each of these tissues, especially for the brain. For example, the elastic modulus of the brain has been reported to be in a quite wide range, from 60 Pa for mouse at 6 weeks

(Koser *et al.* 2018) to 16 MPa for human at 6 months of age (Coats *et al.,* 2006). Some of the main factors that may affect the experimental results could be: the variation between the specimens within the same species and between different species; the regional variability in the brain properties and also various parameters that need to be used during the experiments as well as the experimental approach (i.e. indentation vs. tensile testing).

Considering the uncertainties around the choice of various material properties that were used in this study, several sensitivity tests were performed to understand the effect of this parameter on the outputs of the FE models. All three parts of the cranium (bones, sutures, and the brain) were assumed to have linear isotropic elastic properties. Although as discussed before, they show nonlinear, non-isotropic, and viscoelastic properties nonetheless given that the simulations were performed day by day where the geometry of the model was also updated day by day perhaps a linear material model could be accepted.

6-4   Radial expansion of the cranium

Radial expansion of the WT and MT mice calvarias were modelled from P3 to P10. Overall the modelling approach could capture the relative differences between the WT and MT calvarias however the differences that FE results predicted were not as large as those observed *in vivo* (see Fig 4.28 and 4.29 in Chapter 4). This could have been due to various limitations of the study.

Brain growth is likely to be anisotropic. Considering the *in vivo* growth observed in the WT mice from P3 to P10 (see e.g. Fig. 2.8 and 3.4) it can be interpreted that, the brain growth rate in the anteroposterior direction is larger than the dorsoventral direction. However, the modelling approach developed here assumed an isotropic expansion of the brain during the development while it is likely to be anisotropic (see section 2.6).

Another limitation of this section of the project was that various other tissues present between the brain and the calvaria were not modelled. For example if dura

mater was added to the model, given its higher elastic modulus compared to the brain (McGarvey, Lee and Boughner, 1984; Prange and Margulies, 2002), it might have altered the predicted calvarial morphology. Also the gradual thickening of the calvarial bones, suture ossification, and increase in its material properties were neglected at this stage (Richtsmeier and Flaherty, 2013; Chen, 2014; Moazen *et al.*, 2015, 2016) all of which could have contributed to the differences observed between the FE predictions and the *in vivo* data.

6-5   Modelling the bone formation at sutures

Bone formation in the cranial sutures is widely considered to be of intramembranous bone formation nature (Shapiro and Robinson, 1980; Hall and Miyake, 2000; Opperman, 2000; Chan *et al.*, 2009; Burgos-Flórez, Gavilán-Alfonso and Garzón-Alvarado, 2016), in which the mechanical loads induced by growing brain in a combination with the masticatory loads trigger the cranial suture ossification (Herring, 2008; Moazen *et al.*, 2015; Weickenmeier *et al.*, 2017). Our knowledge and understanding of the level of mechanical stimulus that sutures experience during the calvarial growth, and the mechanobiology of the cranial sutures is limited (Carter and Beaupre, 2000; Mao, 2002; Herring, 2008; Khonsari *et al.*, 2013; Weickenmeier *et al.*, 2017). However, several researchers have tried to use computational methods to investigate the suture ossification in the cranium (see Table 2.6).

In the last part of this project, it was tried to model the bone formation process in the cranial sutures. Several tissue differentiation theories developed in the literature, were summarised in section 2.8. In this project given the complex morphology of the skull and also that sutures are mainly under tension during the calvarial growth a rather simple strain-based tissue differentiation approach was developed. The initial primitive approach was gradually improved by implementing a bone formation rate into the algorithm. Obtained results were in a reasonable agreement with the *in vivo* pattern of the bone formation. For example, considering the sagittal suture WT models (both *ex vivo* and FE – see Fig 5.18) showed a rectangular pattern of bone formation i.e. the rate of bone formation seems to be similar in the anterior and posterior segments of the suture. However, the MT mouse had a triangular form i.e.

156

a higher rate of bone formation in the anterior part of the sagittal suture as oppose to its posterior segments (see Fig 5.28). Comparing the measured suture widths also showed a reasonable similarity between the FE and *ex vivo* suture sizes at P10 (3rd model- Table 5.5).

The main modelling approach used in this part was based on the level of hydrostatic strain experienced by the sutures at each age. While this is a huge simplification i.e. ignore the role of various biological signalling, perhaps it can be said that the bone formation radius that was specified in the approach took into account the effect of the various complex biological and non-biological factors involved in the process. In the current model, the bone adjacent to the suture tissue has a lower elastic modulus, which is similar to results Moazen *et al.* (2015) reported for similar mouse models. However, further experimental measurements are required to validate the tissue differentiation that the model predicted (see e.g. Leong and Morgan, 2008). The approach developed here can be further improved by incorporating various signalling events into the modelling approach, and addressing other limitations of the work.

Similar to the previous sections, several approximations were needed to be considered. For example, the sutures were modelled as a linear elastic material with isotropic properties, while they have a nonlinear and viscoelastic nature (McLaughlin *et al.*, 2000). This assumption was made due to the short timescale of the simulation (P3 to P10). However, due to the rapid morphological changes happening at this age, using nonlinear properties would have been more realistic. Other limitation of this work was assuming same bone formation rate and same material properties for all of the sutures for both MT and WT models. While it was already discussed how bone formation rates (Table 3.3 and 3.4), and material properties (Section 2-6-1) vary in different sutures.

Chapter 7: Conclusions and future work

7-1 Conclusions

Our understanding of the mechanobiology of the cranial sutures and the overall biomechanics of the cranium during the natural calvarial growth is still limited. However, it is crucial to have this knowledge to develop new technologies and approaches to improve the management of conditions such as craniosynostosis.

The main aim of this thesis was to first characterise the changes in the cranium and calvarial suture sizes in a series of *ex vivo* WT and MT mice. Then, to develop a platform to predict calvarial morphology i.e. both modelling the radial expansion of the skull as well as bone formation at the sutures. It is crucial to validate the FE results hence throughout the FE results were compared with the *ex vivo* data collected from a series of WT and MT mice. The main conclusions from this work are summarised below:

- finite element (FE) method can be used to predict the calvarial growth and has great potential to compare different management strategies for calvarial reconstructions to optimise the management of different form of craniosynostosis.
- care must be taken in terms of validation of the FE models as the results of these models are sensitive to the choice of input parameters.
- considering the various sensitivity analysis that were carried out in this study, perhaps modelling the brain-bone interface, realistic choice of the material properties and taking into account the anisotropic pattern of brain growth, are crucial parameters to be considered in future studies.

Considering the initial aim of investigating the effect of brain growth on the cranial bone growth, it can be concluded that modelling the cranial growth can be performed to a reasonable grade, based on considering the brain growth. Also bone formation at the edges of cranial sutures can be modelled to a reasonable detail.

7-2 Future work

The modelling approach developed and described in this study can be on one hand further developed, and on the other hand, it can be applied to many other areas and complications associated with the craniofacial growth to advance our understanding of the mechanobiology of this complex system. Some examples of future work are highlighted here.

Several limitations of the modelling approach developed in this study were highlighted throughout this thesis, e.g. anisotropic modelling of brain growth and using viscoelastic properties for sutures. Addressing these limitations all can be considered as future avenues to further develop this modelling approach in future. For instance, a multiscale method could be used to model the sutures in a micro level, and bone growth in macro. At the same time various biological and chemical signalling events that occur during the growth can be added to mechanical approach considered here i.e. modelling the growth only based on the forces arising from the brain growth. Also, adding some stochastic parameters would increase the similarity of simulations to natural phenomenon. However, stochastic models are considerably complicated.

It has also been shown that calvarial loading can alter the pattern of bone formation across the sutures (Soh, Rafferty and Herring, 2018). The effect of such loading regimes on the whole skull, sutures and the underlying brain during the development can be investigated using the modelling approach described here. It would be interesting to investigate how the calvarial loading would alter the natural level strain that cranial sutures experience during the development and if that would be captured by the strain thresholds that were used in this study or further amendment are required.

One of the main conclusions from this work was that the modelling approach described here can be used to optimise the management of craniosynostosis where different surgical options are available for treatment of a particular form of craniosynostosis. Currently a PhD student (Mr Connor Cross) in Moazen Lab is working in this area and applying the same methodologies to optimise management

159

of sagittal craniosynostosis in children. The same approach can be applied to all other forms of craniosynostosis as outlined in the introduction.

In conclusion, future steps will first include improving current bone formation algorithm by considering different suture fusion rates for different sutures and for WT and MT. Then nonlinear material properties can be used for sutures in combination with different material properties for each suture. On the other hand, experimental characterisations will be needed to specify each suture's properties at different ages. In parallel, current method can be used for patient specific models, while improvements are being investigated.

References

Advani, S., Powell, W., Huston, J. and Ojala, S. (1975), "Human head impact response: Experimental data and analytical simulations", *Proceedings of the 2nd International Conference on the Biomechanics of Serious Trauma*, pp. 153–163.

Advani, S.H., Ommaya, A.K., Yang, W.J., Collins, R., Kivity, K., Kalliers, D., Mathern, R., et al. (1982), "Head injury mechanisms - Characterizations and clinical evaluation", in Ghista, D.N. (Ed.), *Human Body Dynamics: Impact, Occupational and Athletic Aspectsmics*, Oxford University Press, Oxford.

Aggarwal, M., Zhang, J., Miller, M.I., Sidman, R.L. and Mori, S. (2009), "Magnetic resonance imaging and micro-computed tomography combined atlas of developing and adult mouse brains for stereotaxic surgery", *Neuroscience*, IBRO, Vol. 162 No. 4, pp. 1339–1350.

Al-Rekabi, Z., Cunningham, M.L. and Sniadecki, N.J. (2017), "Cell mechanics of craniosynostosis", *ACS Biomaterials Science and Engineering*, Vol. 3 No. 11, pp. 2733–2743.

Allsop, D.L., Perl, T.R. and Warner, C.Y. (1991), "Force/Deflection and fracture characteristics of the temporo-parietal region of the human head", *SAE Technical Paper Series*, 912907.

Allsop, D.L., Warner, C.Y., Wille, M.G., Schneider, D.C. and Nahum, A.M. (1988), "Facial impact response — A comparison of the hybrid III dummy and human cadaver", *SAE Technical Paper Series*, 881719.

ANSYS®. (2010), "ANSYS Mechanical – Introduction to Contact", December,.

ANSYS®. (2017), *ANSYS Mechanical APDL Contact Technology Guide*, ANSYS, Inc., Canonsburg, PA, USA.

ANSYS®. (1997), "Structural nonlinearities, User's guide for revision 5.5".

ANSYS®. (2010), "Mechanical APDL modeling and meshing guide", Vol. 3304, November.

Badea, A., Ali-Sharief, A.A. and Johnson, G.A. (2007), "Morphometric analysis of the C57BL/6J mouse brain", *NeuroImage*, Vol. 37 No. 3, pp. 683–693.

Badve, C.A., Mallikarjunappa, M.K., Iyer, R.S., Ishak, G.E. and Khanna, P.C. (2013), "Craniosynostosis: Imaging review and primer on computed tomography", *Pediatric Radiology*, Vol. 43 No. 6, pp. 728–742.

Ballell, A., Moon, B.C., Porro, L.B., Benton, M.J. and Rayfield, E.J. (2019), "Convergence and functional evolution of longirostry in crocodylomorphs", edited by Benson, R.*Palaeontology*, Vol. 62 No. 6, pp. 867–887.

.Baloch, S., Verma, R., Huang, H., Khurd, P., Clark, S., Yarowsky, P., Abel, T., et al. (2009), "Quantification of brain maturation and growth patterns in C57BL/6J mice via computational neuroanatomy of diffusion tensor images", *Cerebral*

Cortex, Vol. 19 No. 3, pp. 675–687.

Bannink, N., Nout, E., Wolvius, E.B., Hoeve, H.L.J., Joosten, K.F.M. and Mathijssen, I.M.J. (2010), "Obstructive sleep apnea in children with syndromic craniosynostosis: long-term respiratory outcome of midface advancement", *International Journal of Oral and Maxillofacial Surgery*, Vol. 39 No. 2, pp. 115–121.

Borghi, A., Rodriguez-Florez, N., Rodgers, W., James, G., Hayward, R., Dunaway, D., Jeelani, O., et al. (2018), "Spring assisted cranioplasty: A patient specific computational model", *Medical Engineering & Physics*, Vol. 53, pp. 58–65.

Bouchonville, N., Meyer, M., Gaude, C., Gay, E., Ratel, D. and Nicolas, A. (2016), "AFM mapping of the elastic properties of brain tissue reveals kPa μm-1 gradients of rigidity", *Soft Matter*, Vol. 12 No. 29, pp. 6232–6239.

Boulet, S.L., Rasmussen, S.A. and Honein, M.A. (2008), "A population-based study of craniosynostosis in metropolitan Atlanta, 1989-2003", *American Journal of Medical Genetics, Part A*, Vol. 146 No. 8, pp. 984–991.

Bradley, J.P., Levine, J.P., Roth, D. a, McCarthy, J.G. and Longaker, M.T. (1996), "Studies in cranial suture biology: IV. Temporal sequence of posterior frontal cranial suture fusion in the mouse", *Plastic and Reconstructive Surgery*, Vol. 98 No. 6, pp. 1039–1345.

Bright, J.A. (2014), "A review of paleontological finite element models and their validity", *Journal of Paleontology*, Vol. 88 No. 4, pp. 760–769.

Brusatte, S.L., Sakamoto, M., Montanari, S. and Harcourt Smith, W.E.H. (2012), "The evolution of cranial form and function in theropod dinosaurs: Insights from geometric morphometrics", *Journal of Evolutionary Biology*, Vol. 25 No. 2, pp. 365–377.

Budday, S., Nay, R., de Rooij, R., Steinmann, P., Wyrobek, T., Ovaert, T.C. and Kuhl, E. (2015), "Mechanical properties of gray and white matter brain tissue by indentation", *Journal of the Mechanical Behavior of Biomedical Materials*, Vol. 46, pp. 318–330.

Budday, S., Ovaert, T.C., Holzapfel, G.A., Steinmann, P. and Kuhl, E. (2019), *Fifty Shades of Brain: A Review on the Mechanical Testing and Modeling of Brain Tissue*, *Archives of Computational Methods in Engineering*, Springer Netherlands, No. 0123456789.

Budday, S., Sommer, G., Birkl, C., Langkammer, C., Haybaeck, J., Kohnert, J., Bauer, M., et al. (2017), "Mechanical characterization of human brain tissue", *Acta Biomaterialia*, Vol. 48, pp. 319–340.

Burgos-Flórez, F.J.J., Gavilán-Alfonso, M.E.E. and Garzón-Alvarado, D.A.A. (2016), "Flat bones and sutures formation in the human cranial vault during prenatal development and infancy: A computational model", *Journal of Theoretical Biology*, Vol. 393, pp. 127–144.

Button, D.J., Barrett, P.M. and Rayfield, E.J. (2016), "Comparative cranial myology and biomechanics of Plateosaurus and Camarasaurus and evolution of the sauropod feeding apparatus", *Palaeontology*, Vol. 59 No. 6, pp. 887–913.

Byrne, D.P. (2009), *Computational Modelling of Bone Regeneration Using a Three-Dimensional Lattice Approach*, Trinity College (Dublin, Ireland), available at: http://www.tara.tcd.ie/handle/2262/88812.

Carretero, A., Ruberte, J., Navarro, M., Nacher, V. and Mendes-Jorge, L. (2017), "Osteology", *Morphological Mouse Phenotyping*, Elsevier, pp. 7–53.

Carter, D.R. and Beaupre, G.S. (2000), *Skeletal Function and Form: Mechanobiology of Skeletal Development, Aging, and Regeneration*, Cambridge University Press, Cambridge.

Carter, D.R., Beaupre, G.S., Giori, N.J. and Helms, J.A. (1998), "Mechanobiology of Skeletal Regeneration", *Clinical Orthopaedics and Related Research*, Vol. 355S No. 355 SUPPL., pp. S41–S55.

Chan, C.K.F., Chen, C.C., Luppen, C.A., Kim, J.B., DeBoer, A.T., Wei, K., Helms, J.A., et al. (2009), "Endochondral ossification is required for haematopoietic stem-cell niche formation", *Nature*, Vol. 457 No. 7228, pp. 490–494.

Chen, Y. (2014), "Mechanical Properties of Cranial Bones and Sutures in 1–2-Year-Old Infants", *Medical Science Monitor*, Vol. 20, pp. 1808–1813.

Cheong, V.S., Blunn, G.W., Coathup, M.J. and Fromme, P. (2018), "A novel adaptive algorithm for 3D finite element analysis to model extracortical bone growth", *Computer Methods in Biomechanics and Biomedical Engineering*, Vol. 21 No. 2, pp. 129–138.

Christ, A.F., Franze, K., Gautier, H., Moshayedi, P., Fawcett, J., Franklin, R.J.M., Karadottir, R.T., et al. (2010), "Mechanical difference between white and gray matter in the rat cerebellum measured by scanning force microscopy", *Journal of Biomechanics*, Vol. 43 No. 15, pp. 2986–2992.

Chuang, N., Mori, S., Yamamoto, A., Jiang, H., Ye, X., Xu, X., Richards, L.J., et al. (2011), "An MRI-based atlas and database of the developing mouse brain", *NeuroImage*, Vol. 54 No. 1, pp. 80–89.

Claes, L.E. and Heigele, C.A. (1999), "Magnitudes of local stress and strain along bony surfaces predict the course and type of fracture healing", *Journal of Biomechanics*, Vol. 32 No. 3, pp. 255–266.

Claessens, M., Sauren, F. and Wismans, J. (1997), "Modeling of the human head under impact conditions: a parametric study", *Sae Conference Proceedings P.*

Coats, B. and Margulies, S.S. (2006), "Material Properties of Human Infant Skull and Suture at High Rates", *Journal of Neurotrauma*, Vol. 23 No. 8, pp. 1222–1232.

Cook, M.J. (1965), *The Anatomy of the Laboratory Mouse, Academic Press Inc.*

Cornelissen, M., Ottelander, B. den, Rizopoulos, D., van der Hulst, R., Mink van der Molen, A., van der Horst, C., Delye, H., et al. (2016), "Increase of prevalence of craniosynostosis", *Journal of Cranio-Maxillofacial Surgery*, Vol. 44 No. 9, pp. 1273–1279.

Cowin, S.C. (2001), "The False Premise in Wolff's Law", *Bone Mechanics Handbook*, p. 981.

Curtis, N., Jones, M.E.H., Shi, J., O'Higgins, P., Evans, S.E. and Fagan, M.J. (2011),

"Functional relationship between skull form and feeding mechanics in sphenodon, and implications for diapsid skull development", *PLoS ONE*, Vol. 6 No. 12, pp. 31–33.

Curtis, N., Jones, M.E.H.H., Evans, S.E., O'Higgins, P. and Fagan, M.J. (2013), "Cranial sutures work collectively to distribute strain throughout the reptile skull", *Journal of the Royal Society Interface*, Vol. 10 No. 86, pp. 1–9.

Dixit, P. and Liu, G.R. (2017), "A Review on Recent Development of Finite Element Models for Head Injury Simulations", *Archives of Computational Methods in Engineering*, Vol. 24 No. 4, pp. 979–1031.

Doro, D., Liu, A., Grigoriadis, A. E., & Liu, K. J. (2019) "The osteogenic potential of the neural crest lineage may contribute to craniosynostosis", *Molecular Syndromology*, Vol. 10, No. 1–2, pp. 48-57.

Engler, A. J., Sen, S., Sweeney, H. L., and Discher, D. E. (2006), "Matrix Elasticity Directs Stem Cell Lineage Specification", *Cell*, Vol. 126, No. 4, 2006, pp. 677–89.

Engström, C., Kiliaridis, S. and Thilander, B. (1986), "The relationship between masticatory function and craniofacial morphology. II A histological study in the growing rat fed a soft diet", *European Journal of Orthodontics*, Vol. 8 No. 4, pp. 271–279.

Eswarakumar, V.P., Horowitz, M.C., Locklin, R., Morriss-Kay, G.M. and Lonai, P. (2004), "A gain-of-function mutation of Fgfr2c demonstrates the roles of this receptor variant in osteogenesis.", *Proceedings of the National Academy of Sciences of the United States of America*, Vol. 101 No. 34, pp. 12555–60.

Eswarakumar, V.P., Ozcan, F., Lew, E.D., Bae, J.H., Tome, F., Booth, C.J., Adams, D.J., et al. (2006), "Attenuation of signaling pathways stimulated by pathologically activated FGF-receptor 2 mutants prevents craniosynostosis", *Proceedings of the National Academy of Sciences*, Vol. 103 No. 49, pp. 18603–18608.

Fernandes, F.A.O. and Sousa, R.J.A. De. (2015), "Head injury predictors in sports trauma - A state-of-the-art review", *Proceedings of the Institution of Mechanical Engineers, Part H: Journal of Engineering in Medicine*, Vol. 229 No. 8, pp. 592–608.

Fernández, J.R., García-Aznar, J.M. and Masid, M. (2017), "Numerical analysis of an osteoconduction model arising in bone-implant integration", *ZAMM Zeitschrift Fur Angewandte Mathematik Und Mechanik*, Vol. 97 No. 9, pp. 1050–1063.

Fish, J.L. (2016), "Developmental mechanisms underlying variation in craniofacial disease and evolution", *Developmental Biology*, Vol. 415 No. 2, pp. 188–197.

Flaherty, K., Singh, N. and Richtsmeier, J.T. (2016), "Understanding craniosynostosis as a growth disorder", *Wiley Interdisciplinary Reviews: Developmental Biology*, Vol. 5 No. 4, pp. 429–459.

Galileo, G. (1638), "Discorsi e demonstrazioni matematiche, intorno a due nuove scienze attentanti all meccanica ed a muovementi locali".

García-Aznar, J.M., Kuiper, J.H., Gómez-Benito, M.J., Doblaré, M. and Richardson, J.B. (2007), "Computational simulation of fracture healing: Influence of interfragmentary movement on the callus growth", *Journal of Biomechanics*,

Vol. 40 No. 7, pp. 1467–1476.

Garijo, N., Fernández, J.R., Pérez, M.A. and García-Aznar, J.M. (2014), "Numerical stability and convergence analysis of bone remodeling model", *Computer Methods in Applied Mechanics and Engineering*, Vol. 271, pp. 253–268.

Garzón-Alvarado, D.A. (2013), "A hypothesis on the formation of the primary ossification centers in the membranous neurocranium: A mathematical and computational model", *Journal of Theoretical Biology*, Vol. 317, pp. 366–376.

Garzón-Alvarado, D.A., González, A. and Gutiérrez, M.L. (2013), "Growth of the flat bones of the membranous neurocranium: A computational model", *Computer Methods and Programs in Biomedicine*, Vol. 112 No. 3, pp. 655–664.

Gefen, A., Gefen, N., Zhu, Q., Raghupathi, R. and Margulies, S.S. (2003), "Age-Dependent Changes in Material Properties of the Brain and Braincase of the Rat", *Journal of Neurotrauma*, Vol. 20 No. 11, pp. 1163–1177.

Glatt, V., Evans, C.H. and Tetsworth, K. (2017), "A concert between biology and biomechanics: The influence of the mechanical environment on bone healing", *Frontiers in Physiology*, Vol. 7 No. JAN, pp. 1–18.

Grau, N., Daw, J.L., Patel, R., Evans, C., Lewis, N. and Mao, J.J. (2006), "Nanostructural and nanomechanical properties of synostosed postnatal human cranial sutures", *Journal of Craniofacial Surgery*, Vol. 17 No. 1, pp. 91–98.

Grova, M., Lo, D.D., Montoro, D., Hyun, J.S., Chung, M.T., Wan, D.C. and Longaker, M.T. (2012), "Models of Cranial Suture Biology", *Journal of Craniofacial Surgery*, Vol. 23 No. 4, pp. S12–S16.

Hall, B.K. (2015), *Bones and Cartilage: Developmental and Evolutionary Skeletal Biology. Second Edition*, *British Poultry Science*, Vol. 56.

Hall, B.K. and Miyake, T. (2000), "All for one and one for all: Condensations and the initiation of skeletal development", *BioEssays*, Vol. 22 No. 2, pp. 138–147.

Hammelrath, L., Škokić, S., Khmelinskii, A., Hess, A., van der Knaap, N., Staring, M., Lelieveldt, B.P.F., et al. (2016), "Morphological maturation of the mouse brain: An in vivo MRI and histology investigation", *NeuroImage*, Vol. 125, pp. 144–152.

Hartwig, W.C. (1991), "Fractal analysis of sagittal suture morphology", *Journal of Morphology*, Vol. 210 No. 3, pp. 289–298.

Henderson, J.H., Chang, L.Y., Song, H.J.M., Longaker, M.T. and Carter, D.R. (2005), "Age-dependent properties and quasi-static strain in the rat sagittal suture", *Journal of Biomechanics*, Vol. 38 No. 11, pp. 2294–2301.

Henderson, J.H., Longaker, M.T. and Carter, D.R. (2004), "Sutural bone deposition rate and strain magnitude during cranial development", *Bone*, Vol. 34 No. 2, pp. 271–280.

Herring, S.W. (2008), "Mechanical Influences on Suture Development and Patency", *Matrix Biology*, Vol. 7446, pp. 41–56.

Holmes, G. (2012), "The role of vertebrate models in understanding craniosynostosis", *Child's Nervous System*, Vol. 28 No. 9, pp. 1471–1481.

Hrapko, M., Van Dommelen, J.A.W., Peters, G.W.M. and Wismans, J.S.H.M. (2008), "The influence of test conditions on characterization of the mechanical properties of brain tissue", *Journal of Biomechanical Engineering*, Vol. 130 No. 3, pp. 1–10.

Huang, H., Yamamoto, A., Hossain, M.A., Younes, L. and Mori, S. (2008), "Quantitative cortical mapping of fractional anisotropy in developing rat brains", *Journal of Neuroscience*, Vol. 28 No. 6, pp. 1427–1433.

Hume, A., Mills, N.J. and Gilchrist, A (1995), "Industrial head injuries and the performance of the helmets", *Proceedings of the international IRCOBI Conference on Biomechanics of Impact, Switzerland*.

Hunt, H.R. (1924), *A laboratory manual of the anatomy of the rat*, Macmillan, New York.

Ishii, M., Sun, J., Ting, M.C. and Maxson, R.E. (2015), "The development of the calvarial bones and sutures and the pathophysiology of craniosynostosis", *Current Topics in Developmental Biology*, 1st ed., Vol. 115, Elsevier Inc., pp. 131–156.

Jacobs, B. (2001), "Regional dendritic and spine variation in human cerebral cortex: a quantitative golgi study", *Cerebral Cortex*, Vol. 11 No. 6, pp. 558–571.

Jasinoski, S.C. and Reddy, B.D. (2012), "Mechanics of cranial sutures during simulated cyclic loading", *Journal of Biomechanics*, Elsevier, Vol. 45 No. 11, pp. 2050–2054.

Jasinoski, S.C., Reddy, B.D., Louw, K.K. and Chinsamy, A. (2010), "Mechanics of cranial sutures using the finite element method", *Journal of Biomechanics*, Elsevier, Vol. 43 No. 16, pp. 3104–3111.

Jaslow, C.R. (1990), "Mechanical properties of cranial sutures", *Journal of Biomechanics*, Vol. 23 No. 4, pp. 313–21.

Jerome, C. and Hoch, B. (2012) '5 - Skeletal System', In eds. Piper M Treuting and Suzanne M B T - Comparative Anatomy and Histology Dintzis. San Diego: Academic Press, 53–70.

Jin, J., Eagleson, R. and Ribaupierre, S. (2018), "Skull Development Simulation Model for Craniosynostosis Surgery Planning", *Biology, Engineering and Medicine*, Vol. 3 No. 2.

Jin, J., Eagleson, R., de Ribaupierre, S. and Fels, S. (2014), "Simulation of Brain-skull Development Utilizing a Hybrid Model", *Proceedings of the 2014 Summer Simulation Multiconference*, Vol. 1 No. 519, pp. 46:1–46:8.

Jin, J., Shahbazi, S., Lloyd, J., Fels, S., de Ribaupierre, S. and Eagleson, R. (2014), "Hybrid simulation of brain–skull growth", *Simulation*, Vol. 90 No. 1, pp. 3–10.

Johnson, D. and Wilkie, A.O.M. (2011), "Craniosynostosis", *European Journal of Human Genetics*, Vol. 19 No. 4, pp. 369–376.

Jones, M.E.H., Gröning, F., Dutel, H., Sharp, A., Fagan, M.J. and Evans, S.E. (2017), "The biomechanical role of the chondrocranium and sutures in a lizard cranium", *Journal of the Royal Society Interface*, Vol. 14 No. 137.

Kang, H.-S., Willinger, R., Diaw, B.M. and Chinn, B. (1997), "Validation of a 3D anatomic human head model and replication of head impact in motorcycle accident by finite element modeling", *SAE Technical Paper Series, 973339.*

Kaster, T., Sack, I. and Samani, A. (2011), "Measurement of the hyperelastic properties of ex vivo brain tissue slices", *Journal of Biomechanics*, Vol. 44 No. 6, pp. 1158–1163.

Katsianou, M.A., Adamopoulos, C., Vastardis, H. and Basdra, E.K. (2016), "Signaling mechanisms implicated in cranial sutures pathophysiology: Craniosynostosis", *BBA Clinical*, Vol. 6, pp. 165–176.

Kawakami, M. and Yamamura, K.I. (2008), "Cranial bone morphometric study among mouse strains", *BMC Evolutionary Biology*, Vol. 8 No. 1, pp. 1–11.

Khonsari, R.H., Olivier, J., Vigneaux, P., Sanchez, S., Tafforeau, P., Ahlberg, P.E., Di Rocco, F., et al. (2013), "A mathematical model for mechanotransduction at the early steps of suture formation", *Proceedings of the Royal Society B: Biological Sciences*, Vol. 280 No. 1759, p. 20122670.

Kim, S.H., Chang, S.H. and Jung, H.J. (2010), "The finite element analysis of a fractured tibia applied by composite bone plates considering contact conditions and time-varying properties of curing tissues", *Composite Structures*, Vol. 92 No. 9, pp. 2109–2118.

Kimonis, V., Gold, J.A., Hoffman, T.L., Panchal, J. and Boyadjiev, S.A. (2007), "Genetics of Craniosynostosis", *Seminars in Pediatric Neurology*, Vol. 14 No. 3, pp. 150–161.

Koser, D.E., Moeendarbary, E., Kuerten, S. and Franze, K. (2018), "Predicting local tissue mechanics using immunohistochemistry", *BioRxiv*, p. 358119.

Larysz, D., Wolański, W., Kawlewska, E., Mandera, M. and Gzik, M. (2012), "Biomechanical aspects of preoperative planning of skull correction in children with craniosynostosis", *Acta of Bioengineering and Biomechanics*, Vol. 14 No. 2, pp. 19–26.

Laurita, J., Koyama, E., Chin, B., Taylor, J.A., Lakin, G.E., Hankenson, K.D., Bartlett, S.P., et al. (2011), "The Muenke syndrome mutation (FgfR3[P244R]) causes cranial base shortening associated with growth plate dysfunction and premature perichondrial ossification in murine basicranial synchondroses", *Developmental Dynamics*, Vol. 240 No. 11, pp. 2584–2596.

Lee, C., Richtsmeier, J.T. and Kraft, R.H. (2014), "A multiscale computational model for the growth of the cranial vault in craniosynostosis", *Volume 9: Mechanics of Solids, Structures and Fluids*, American Society of Mechanical Engineers, p. V009T12A061.

Lee, C., Richtsmeier, J.T. and Kraft, R.H. (2015), "A Computational Analysis of Bone Formation in the Cranial Vault in the Mouse", *Frontiers in Bioengineering and Biotechnology*, Vol. 3 No. March, pp. 1–11.

Lee, K. K. L., Peskett, E., Quinn, C. M., Aiello, R., Adeeva, L., Moulding, D. A., Stanier, P., and Pauws, E. (2018), "Overexpression of Fgfr2c causes craniofacial bone hypoplasia and ameliorates craniosynostosis in the Crouzon mouse", *Disease*

Models and Mechanisms, Vol. 11, No. 11, p. dmm035311

Lee, K.K.L., Stanier, P. and Pauws, E. (2019), "Mouse models of syndromic craniosynostosis", *Molecular Syndromology*, Vol. 10 No. 1–2, pp. 58–73.

Leong, P.L. and Morgan, E.F. (2008), "Measurement of fracture callus material properties via nanoindentation", *Acta Biomaterialia*, Vol. 4 No. 5, pp. 1569–1575.

Li, X., Zhu, W., He, J., Di, F., Wang, L., Li, X., Liu, W., et al. (2017), "Application of computer assisted three-dimensional simulation operation and biomechanics analysis in the treatment of sagittal craniosynostosis", *Journal of Clinical Neuroscience*, Vol. 44, pp. 323–329.

Li, Y., Ortiz, C. and Boyce, M.C. (2013), "A generalized mechanical model for suture interfaces of arbitrary geometry", *Journal of the Mechanics and Physics of Solids*, Vol. 61 No. 4, pp. 1144–1167.

Li, Z., Hu, J., Reed, M.P., Rupp, J.D., Hoff, C.N., Zhang, J. and Cheng, B. (2011), "Development, validation, and application of a parametric pediatric head finite element model for impact simulations", *Annals of Biomedical Engineering*, Vol. 39 No. 12, pp. 2984–2997.

Li, Z., Wang, G., Ji, C., Jiang, J., Wang, J. and Wang, J. (2019), "Characterization of the mechanical properties for cranial bones of 8-week-old piglets: the effect of strain rate and region", *Biomechanics and Modeling in Mechanobiology*, Vol. 18 No. 6, pp. 1697–1707.

Libby, J., Marghoub, A., Johnson, D., Khonsari, R.H., Fagan, M.J. and Moazen, M. (2017), "Modelling human skull growth: a validated computational model", *Journal of The Royal Society Interface*, Vol. 14 No. 130, p. 20170202.

Liu, J., Nam, H.K., Wang, E. and Hatch, N.E. (2013), "Further analysis of the crouzon mouse: Effects of the FGFR2^{C342Y} mutation are cranial bone-dependent", *Calcified Tissue International*, Vol. 92 No. 5, pp. 451–466.

Liu, L., Jiang, Y., Boyce, M., Ortiz, C., Baur, J., Song, J. and Li, Y. (2017), "The effects of morphological irregularity on the mechanical behavior of interdigitated biological sutures under tension", *Journal of Biomechanics*, Vol. 58, pp. 71–78.

Malde, O., Libby, J. and Moazen, M. (2018), "An Overview of Modelling Craniosynostosis Using the Finite Element Method", *Molecular Syndromology*, pp. 1–9.

Maloul, A., Fialkov, J. and Whyne, C. M. (2013), "Characterization of the bending strength of craniofacial sutures", *Journal of Biomechanics*, Vol. 46 NO 5, pp. 912–917.

Maloul, A., Fialkov, J., Wagner, D. and Whyne, C.M. (2014), "Characterization of craniofacial sutures using the finite element method", *Journal of Biomechanics*, Vol. 47 No. 1, pp. 245–252.

Mao, J.J. (2002), "Mechanobiology of craniofacial sutures", *Journal of Dental Research*, Vol. 81 No. 12, pp. 810–816.

Margulies, S.S. and Thibault, K.L. (2000), "Infant Skull and Suture Properties: Measurements and Implications for Mechanisms of Pediatric Brain Injury",

Journal of Biomechanical Engineering, Vol. 122 No. 4, pp. 364–371.

Martínez-Abadías, N., Motch, S.M., Pankratz, T.L., Wang, Y., Aldridge, K., Jabs, E.W. and Richtsmeier, J.T. (2013), "Tissue-specific responses to aberrant FGF signaling in complex head phenotypes", *Developmental Dynamics*, Vol. 242 No. 1, pp. 80–94.

Mathijssen, I.M.J. (2015), "Guideline for Care of Patients With the Diagnoses of Craniosynostosis", *Journal of Craniofacial Surgery*, Vol. 26 No. 6, pp. 1735–1807.

McElhaney, J.H., Fogle, J.L., Melvin, J.W., Haynes, R.R., Roberts, V.L. and Alem, N.M. (1970), "Mechanical properties of cranial bone", *Journal of Biomechanics*, Vol. 3 No. 5, pp. 495–511.

McGarvey, K.A., Lee, J.M. and Boughner, D.R. (1984), "Mechanical suitability of glycerol-preserved human dura mater for construction of prosthetic cardiac valves", *Biomaterials*, Vol. 5 No. 2, pp. 109–117.

McLaughlin, E., Zhang, Y., Pashley, D., Borke, J. and Yu, J. (2000), "The load-displacement characteristics of neonatal rat cranial sutures", *Cleft Palate-Craniofacial Journal*, Vol. 37 No. 6, pp. 590–595.

McPherson, G.K. and Kriewall, T.J. (1980), "The elastic modulus of fetal cranial bone: A first step towards an understanding of the biomechanics of fetal head molding", *Journal of Biomechanics*, Vol. 13 No. 1, pp. 9–16.

Melott, M.J. (1999), "Apert syndrome: A case report and discussion", *Clinical Eye and Vision Care*, Vol. 11 No. 4, pp. 215–220.

Van Der Meulen, J., Van Der Hulst, R., Van Adrichem, L., Arnaud, E., Chin-Shong, D., Duncan, C., Habets, E., et al. (2009), "The increase of metopic synostosis: A pan-European observation", *Journal of Craniofacial Surgery*, Vol. 20 No. 2, pp. 283–286.

Miller, K. and Chinzei, K. (2002), "Mechanical properties of brain tissue in tension", *Journal of Biomechanics*, Vol. 35 No. 4, pp. 483–490.

Miller, K., Chinzei, K., Orssengo, G. and Bednarz, P. (2000), "Mechanical properties of brain tissue in-vivo: experiment and computer simulation.", *Journal of Biomechanics*, Vol. 33 No. 11, pp. 1369–76.

Miroshnichenko, K., Liu, L., Tsukrov, I. and Li, Y. (2018), "Mechanical model of suture joints with fibrous connective layer", *Journal of the Mechanics and Physics of Solids*, Vol. 111, pp. 490–502.

Miura, T., Perlyn, C.A., Kinboshi, M., Ogihara, N., Kobayashi-Miura, M., Morriss-Kay, G.M. and Shiota, K. (2009), "Mechanism of skull suture maintenance and interdigitation", *Journal of Anatomy*, Vol. 215 No. 6, pp. 642–655.

Moazen, M., Alazmani, A., Rafferty, K., Liu, Z.J., Gustafson, J., Cunningham, M.L., Fagan, M.J., et al. (2016), "Intracranial pressure changes during mouse development", *Journal of Biomechanics*, Vol. 49 No. 1, pp. 123–126.

Moazen, M., Costantini, D. and Bruner, E. (2013), "A Sensitivity Analysis to the Role of the Fronto-Parietal Suture in Lacerta Bilineata: A Preliminary Finite Element Study", *Anatomical Record*, Vol. 296 No. 2, pp. 198–209.

Moazen, M., Curtis, N., Evans, S.E., O'Higgins, P. and Fagan, M.J. (2008), "Rigid-body analysis of a lizard skull: Modelling the skull of Uromastyx hardwickii", *Journal of Biomechanics*, Vol. 41 No. 6, pp. 1274–1280.

Moazen, M., Curtis, N., O'Higgins, P., Evans, S.E. and Fagan, M.J. (2009), "Biomechanical assessment of evolutionary changes in the lepidosaurian skull", *Proceedings of the National Academy of Sciences*, Vol. 106 No. 20, pp. 8273–8277.

Moazen, M., Curtis, N., O'Higgins, P., Jones, M.E.H., Evans, S.E. and Fagan, M.J. (2009), "Assessment of the role of sutures in a lizard skull: a computer modelling study.", *Proceedings. Biological Sciences*, Vol. 276 No. 1654, pp. 39–46.

Moazen, M., Peskett, E., Babbs, C., Pauws, E. and Fagan, M.J. (2015), "Mechanical Properties of Calvarial Bones in a Mouse Model for Craniosynostosis", edited by Jeffery, N.*PLOS ONE*, Vol. 10 No. 5, p. e0125757.

Morriss-Kay, G.M. and Wilkie, A.O.M. (2005), "Growth of the normal skull vault and its alteration in craniosynostosis: insights from human genetics and experimental studies", *Journal of Anatomy*, Vol. 207 No. 5, pp. 637–653.

Moss, M.L., Skalak, R., Patel, H., Sen, K., Moss-Salentijn, L., Shinozuka, M. and Vilmann, H. (1985), "Finite element method modeling of craniofacial growth.", *American Journal of Orthodontics*, Vol. 87 No. 6, pp. 453–72.

Motherway, J.A., Verschueren, P., Van der Perre, G., Vander Sloten, J. and Gilchrist, M.D. (2009), "The mechanical properties of cranial bone: The effect of loading rate and cranial sampling position", *Journal of Biomechanics*, Vol. 42 No. 13, pp. 2129–2135.

Nagasao, T., Miyamoto, J., Jiang, H., Kaneko, T. and Tamaki, T. (2011), "Biomechanical analysis of the effect of intracranial pressure on the orbital distances in trigonocephaly", *Cleft Palate-Craniofacial Journal*, Vol. 48 No. 2, pp. 190–196.

Nagasao, T., Miyamoto, J., Uchikawa, Y., Tamaki, T., Yamada, A., Kaneko, T., Jiang, H., et al. (2010), "A biomechanical study on the effect of premature fusion of the frontosphenoidal suture on orbit asymmetry in unilateral coronal synostosis", *Cleft Palate-Craniofacial Journal*, Vol. 47 No. 1, pp. 82–91.

Nahum, A.M., Gatts, J.D., Gadd, C.W. and Danforth, J. (1968), "Impact Tolerance of the Skull and Face", *SAE Technical Paper Series*, Vol. 1, 680785.

Nakata, S. (1981), "Relationship between the development and growth of cranial bones and masticatory muscles in postnatal mice", *Journal of Dental Research*, Vol. 60 No. 8, pp. 1440–1450.

Opperman, L.A. (2000), "Cranial sutures as intramembranous bone growth sites", *Developmental Dynamics*, Vol. 219 No. 4, pp. 472–485.

Pauwels, F. (1965), "Grundriß einer Biomechanik der Frakturheilung", *Gesammelte Abhandlungen Zur Funktionellen Anatomie Des Bewegungsapparates*, Springer Berlin Heidelberg, Berlin, Heidelberg, pp. 139–182.

Perlyn, C.A., DeLeon, V.B., Babbs, C., Govier, D., Burell, L., Darvann, T., Kreiborg, S., et al. (2006), "The craniofacial phenotype of the Crouzon mouse: Analysis of a model for syndromic craniosynostosis using three-dimensional microCT", *Cleft*

Palate-Craniofacial Journal, Vol. 43 No. 6, pp. 740–747.

Perlyn, C.A., Morriss-Kay, G., Darvann, T., Tenenbaum, M. and Ornitz, D.M. (2006), "Model for the Pharmacologic Treatment of Crouzon Syndrome", *Neurosurgery*, Vol. 59 No. 1, pp. 210–215.

Peskett, E., Kumar, S., Baird, W., Jaiswal, J., Li, M., Patel, P., Britto, J.A., et al. (2017), "Analysis of the *Fgfr2* [C342Y] mouse model shows condensation defects due to misregulation of *Sox9* expression in prechondrocytic mesenchyme", *Biology Open*, Vol. 6 No. 2, pp. 223–231.

Pivonka, P., Park, A. and Forwood, M.R. (2018), "Functional adaptation of bone: The mechanostat and beyond", in Pivonka, P. (Ed.), *Multiscale Mechanobiology of Bone Remodeling and Adaptation*, Springer International Publishing, Cham, pp. 1–60.

Popowics, T.E. and Herring, S.W. (2007), "Load transmission in the nasofrontal suture of the pig, Sus scrofa", *Journal of Biomechanics*, Vol. 40 No. 4, pp. 837–844.

Prange, M.T. and Margulies, S.S. (2002), "Regional, directional, and age-dependent properties of the brain undergoing large deformation", *Journal of Biomechanical Engineering*, Vol. 124 No. 2, pp. 244–252.

Prendergast, P.J., Huiskes, R. and Søballe, K. (1997), "Biophysical stimuli on cells during tissue differentiation at implant interfaces", *Journal of Biomechanics*, Vol. 30 No. 6, pp. 539–548.

Rahmoun, J., Auperrin, A., Delille, R., Naceur, H. and Drazetic, P. (2014), "Characterization and micromechanical modeling of the human cranial bone elastic properties", *Mechanics Research Communications*, Vol. 60, pp. 7–14.

Rasmussen, S.A., Yazdy, M.M., Frías, J.L. and Honein, M.A. (2008), "Priorities for public health research on craniosynostosis: Summary and recommendations from a Centers for Disease Control and Prevention-sponsored meeting", *American Journal of Medical Genetics Part A*, Vol. 146A No. 2, pp. 149–158.

Rayfield, E.J. (2007), "Finite element analysis and understanding the biomechanics and evolution of living and fossil organisms", *Annual Review of Earth and Planetary Sciences*, Vol. 35 No. 1, pp. 541–576.

Rice, D.P. (2008), "Developmental anatomy of craniofacial sutures", *Craniofacial Sutures*, Vol. 12, Karger, Basel, Switzerland, pp. 1–21.

Rice, D.P.C. (2003), "Molecular mechanisms in calvarial bone and suture development, and their relation to craniosynostosis", *The European Journal of Orthodontics*, Vol. 25 No. 2, pp. 139–148.

Richtsmeier, J.T. and Flaherty, K. (2013), "Hand in glove: Brain and skull in development and dysmorphogenesis", *Acta Neuropathologica*, Vol. 125 No. 4, pp. 469–489.

Robert, A. (2014), *Human anatomy the definitive visual guid*, 2014th ed., DK Publishing, New York.

Roux, W. (1881), "Der zuchtende Kampf der Teile, oder die 'Teilauslese' im

Organismus (Theorie der 'funktionellen Anpassung')", *Leipzig: Wilhelm Engelmann.*

Sakamoto, M. (2010), "Jaw biomechanics and the evolution of biting performance in theropod dinosaurs", *Proceedings of the Royal Society B: Biological Sciences*, Vol. 277 No. 1698, pp. 3327–3333.

Scarr, G. (2008), "A model of the cranial vault as a tensegrity structure, and its significance to normal and abnormal cranial development", *International Journal of Osteopathic Medicine*, Vol. 11 No. 3, pp. 80–89.

Schneider, D.C. and Nahum, A.M. (1972), "Impact studies of facial bones and skull", *Proceedings of the 16th Stapp Car Crash Conference*, Vol. 1, pp. 186–203.

Shapiro, R. and Robinson, F. (1980), *The embryogenesis of the human skull: An anatomic and radiographic atlas*, Harvard University Press.

Simmons, D. (2008), "The use of animal models in studying genetic disease", No. 2008, pp. 1–4.

Soh, S.H., Rafferty, K. and Herring, S. (2018), "Cyclic loading effects on craniofacial strain and sutural growth in pigs", *American Journal of Orthodontics and Dentofacial Orthopedics*, Vol. 154 No. 2, pp. 270–282.

Suárez, D.R. (2015), "Theories of mechanically induced tissue differentiation and adaptation in the musculoskeletal system", *Ingenieria y Universidad*, Vol. 20 No. 1, pp. 21–40.

Sun, Z., Lee, E. and Herring, S.W. (2004), "Cranial sutures and bones: Growth and fusion in relation to masticatory strain", *The Anatomical Record Part A: Discoveries in Molecular, Cellular, and Evolutionary Biology*, Vol. 276A No. 2, pp. 150–161.

Tuchtan, L., Piercecchi-Marti, M.D., Bartoli, C., Boisclair, D., Adalian, P., Léonetti, G., Behr, M., et al. (2015), "Forces transmission to the skull in case of mandibular impact", *Forensic Science International*, Vol. 252, pp. 22–28.

Viano, D.C., Casson, I.R., Pellman, E.J., Bir, C.A., Zhang, L., Sherman, D.C. and Boitano, M.A. (2005), "Concussion in professional football: Comparison with boxing head impacts - Part 10", *Neurosurgery*, Vol. 57 No. 6, pp. 1154–1170.

Voo, L., Pintar, F.A., Yoganandan, N., Sances, A., Ewing, C.L., Thomas, D.J. and Snyder, R.G. (1994), "Biomechanical analysis of tractor induced head injury", *SAE Technical Paper Series*, Vol. 1, 941726.

Vora, S.R., Camci, E.D. and Cox, T.C. (2016), "Postnatal ontogeny of the cranial base and craniofacial skeleton in male C57BL/6J mice: A reference standard for quantitative analysis", *Frontiers in Physiology*, Vol. 6 No. JAN, pp. 1–14.

Wang, Q., Wood, S.A., Grosse, I.R., Ross, C.F., Zapata, U., Byron, C.D., Wright, B.W., et al. (2012), "The role of the sutures in biomechanical dynamic simulation of a macaque cranial finite element model: Implications for the evolution of craniofacial form", *Anatomical Record*, Vol. 295 No. 2, pp. 278–288.

Weickenmeier, J., Fischer, C., Carter, D., Kuhl, E. and Goriely, A. (2017), "Dimensional, geometrical, and physical constraints in skull growth", *Physical*

Review Letters, Vol. 118 No. 24, p. 248101.

Weinans, H. and Prendergast, P.J. (1996), "Tissue adaptation as a dynamical process far from equilibrium.", *Bone*, Vol. 19 No. 2, pp. 143–9.

Weinzweig, J., Kirschner, R.E., Farley, A., Reiss, P., Hunter, J., Whitaker, L.A. and Bartlett, S.P. (2003), "Metopic synostosis: Defining the temporal sequence of normal suture fusion and differentiating it from synostosis on the basis of computed tomography images", *Plastic and Reconstructive Surgery*, Vol. 112 No. 5, pp. 1211–1218.

Weisbecker, V., Guillerme, T., Speck, C., Sherratt, E., Abraha, H.M., Sharp, A.C., Terhune, C.E., et al. (2019), "Individual variation of the masticatory system dominates 3D skull shape in the herbivory-adapted marsupial wombats", *BioRxiv*, Vol. 8 No. 5, p. 692632.

Wilkie, A.O.M. (2005), "Bad bones, absent smell, selfish testes: The pleiotropic consequences of human FGF receptor mutations", *Cytokine and Growth Factor Reviews*, Vol. 16 No. 2 SPEC. ISS., pp. 187–203.

Wolański, W., Larysz, D., Gzik, M. and Kawlewska, E. (2013), "Modeling and biomechanical analysis of craniosynostosis correction with the use of finite element method", *International Journal for Numerical Methods in Biomedical Engineering*, Vol. 29 No. 9, pp. 916–925.

Wolff, J. (1873), "Zur Lehre von der Fracturenheilung", *Deutsche Zeitschrift Für Chirurgie*, Vol. 2 No. 6, pp. 546–551.

Wolfinbarger, L., Zhang, Y., Adam, B.-L.T., Homsi, D., Gates, K. and Sutherland, V. (1994), "Biomechanical aspects on rehydrated freeze-dried human allograft dura mater tissues", *Journal of Applied Biomaterials*, Vol. 5 No. 3, pp. 265–270.

Wu, J.Z., Pan, C.S., Wimer, B.M. and Rosen, C.L. (2017), "An improved finite element modeling of the cerebrospinal fluid layer in the head impact analysis", *Bio-Medical Materials and Engineering*, Vol. 28 No. 2, pp. 187–199.

Yoganandan, N., Pintar, F., A, J.S., Walsh, P., Ewing, C., Thomas, D. and Snyder, R. (1995), "Biomechanics of skull fracture", *Journal of Neurotrauma*, Vol. 12 No. 4, pp. 659–668.

Yoshimura, K., Kobayashi, R., Ohmura, T., Kajimoto, Y. and Miura, T. (2016), "A new mathematical model for pattern formation by cranial sutures", *Journal of Theoretical Biology*, Vol. 408, pp. 66–74.

You, J., Jiang, X., Hu, M., Wang, N., Shen, Z., Li, J. and Peng, W. (2010), "The bone slot effect study of PI procedure for craniosynostosis correction plan based on finite element method", *Proceedings - 3rd International Conference on Biomedical Engineering and Informatics, BMEI 2010*, IEEE, Vol. 2 No. Bmei, pp. 605–608.

Zhang, G., Tan, H., Qian, X., Zhang, J., Li, K., David, L.R. and Zhou, X. (2016), "A systematic approach to predicting spring force for sagittal craniosynostosis surgery", *Journal of Craniofacial Surgery*, Vol. 27 No. 3, pp. 636–643.

Zhang, J., Miller, M.I., Plachez, C., Richards, L.J., Yarowsky, P., Van Zijl, P. and Mori, S. (2005), "Mapping postnatal mouse brain development with diffusion tensor microimaging", *NeuroImage*, Vol. 26 No. 4, pp. 1042–1051.

Zhang, Z.Q. and Yang, J.L. (2015), "Biomechanical Dynamics of Cranial Sutures during Simulated Impulsive Loading", *Applied Bionics and Biomechanics*, Vol. 2015, pp. 1–11.

Zollikofer, C.P.E. and De León, M.S.P. (2006), "Cranial growth models: heterochrony, heterotopy, and the kinematics of ontogeny", *Vertebrate Paleobiology and Paleoanthropology*, No. 9781402051203, pp. 89–111.

Appendix I: Contact interface

When two separate surfaces touch each other such that they become mutually tangent, they are said to be in contact. In the common physical sense, surfaces that are in contact have these characteristics:

– They do not interpenetrate,

– They can transmit compressive normal forces and tangential friction forces,

– They often do not transmit tensile normal forces.

They are therefore free to separate and move away from each other.

Contact is a changing-status nonlinearity. That is, the stiffness of the system depends on the contact status, whether parts are touching or separated (ANSYS®, 2010, 2017).

Physical contacting bodies do not interpenetrate. Therefore, the program must establish a relationship between the two surfaces to prevent them from passing through each other in the analysis. When the program prevents interpenetration, it is said that it enforces contact compatibility (Fig. A.1).
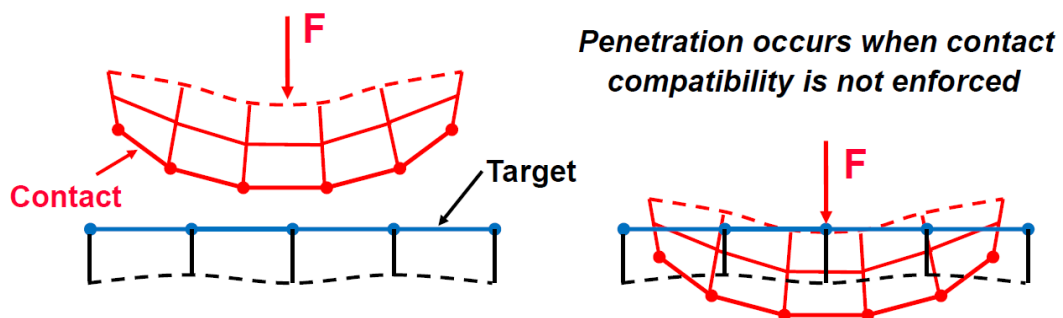

Fig. A.1: Illustration of contact surfaces without enforced contact compatibility (ANSYS®, 2010).

To achieve an enforced contact compatibility in the normal and tangential plane, a specific algorithm is implemented to represent the interaction between the two surfaces. Multiple options are available in the FEA software such that a relationship between the PDE of each system can be established. The most common types of algorithms for nonlinear solid bodies are the Pure Penalty, and Augmented Lagrange. The main difference between the two is the fact that Augmented Lagrange method (indicated by its name) augments the contact force (pressure) calculations making it less sensitive to contact parameters such as normal penetration stiffness k_{normal}. Therefore, the *Pure Penalty* method were used for this study such that optimal contact parameters could be identified through sensitivity tests.

(1) Pure Penalty: $$F_{normal} = k_{normal} \, x_{penetration}$$

(2) Augmented Lagrange: $$F_{normal} = k_{normal} \, x_{penetration} + \lambda$$

Both equations use the same method for contact detection in the normal plane, called integration point detection (IPD) while other formulations use a method called nodal detection (ND). As Fig. A.2 indicates, the use of IPD provides more detection points than ND. This causes ND to be better at handling contact scenarios at edges. However, this can be alleviated by refining the mesh around edges when using IPD.
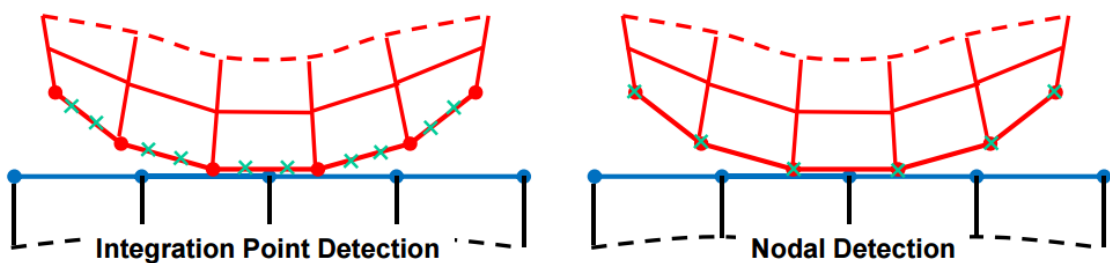

Fig. A.2: Two different contact detection methods used for various contact formulations (ANSYS®, 2010).

When considering friction between the surfaces, one needs to refer to the tangential contact stiffness parameter. Depending on the expected behaviour between the surfaces *in vivo,* such as friction between the brain and calvarial bones, an appropriate friction coefficient is defined. As in the aforementioned options relating contact interaction in the normal direction, similar relations occur in the tangential plane. In contrast to the normal plane, tangential forces (friction) can only be formulated by the Penalty method and thus, the use of Augmented Lagrange method is ideal for frictionless situations. However, tangential forces also occur due to geometric constraints such as the complex morphology seen inside the neurocranial vault. Therefore, if friction or any form of constraints (Sticking) occur a tangential force is generated as seen in equation 6. It should also be noted that an ideal situation with not slip (sliding) $x_{sliding}$ equals zero.

(3) $F_{tangential} = k_{tangential}x_{sliding}$

It should be clear that the normal penetration stiffness is the primary parameter to be considered in a contact simulation. Higher values provide a more accurate solution, but the simulations suffer from high computation costs and convergence issues could arise. Additionally, if the normal stiffness exceeds a certain point the model might start oscillating, meaning that the distinct parts bounces of each other (Fig. A.3). On the contrary, a much to low value of stiffness could cause incorrect force estimates and thus a poor accuracy of the interaction between the surfaces is calculated. This is often seen clearly in the model as one surface entering the other.
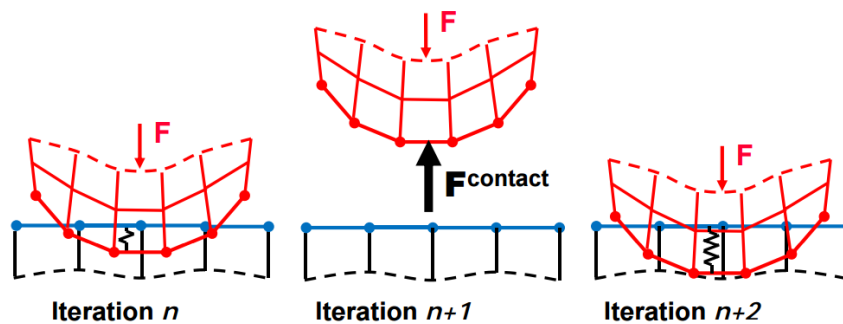

Fig. A.3: Visualisation of a contact simulation with an excessive value of normal penetration stiffness, causing oscillation of the model (ANSYS®, 2010).

Appendix II: List of publications

<u>Journal Papers:</u>

- O. Malde; C. Cross, C. L. Lim, **A. Marghoub**, M. L. Cunningham, R. A. Hopper, M. Moazen, 2020, "***Predicting calvarial morphology in sagittal craniosynostosis***" Scientific Reports (In press).

- M. E. Dolack, C. Lee, Y. Ru, **A. Marghoub**, J. T. Richtsmeier, E. W. Jabs, M. Moazen, D. A. Garzón-Alvarado, R. H. Kraft, 2020, "***Computational Morphogenesis of Embryonic Bone Development: Past, Present, and Future***", in *Mechanobiology.* Elsevier, pp. 197–219.

- **A. Marghoub**, J. Libby, C. Babbs, Y. Ventikos, M. J. Fagan, M. Moazen, 2019, "***Characterizing and modelling bone formation during mouse calvarial development***" Physical Review Letters, 122(4):048103.

- **A. Marghoub**, J. Libby, C. Babbs, E. Pauws, M. J. Fagan, M. Moazen, 2018, "***Predicting calvarial growth in normal and craniosynostotic mice using a computational approach***" Journal of Anatomy, 232:440-448.

- J. Libby, **A. Marghoub**, D. Johnson, R. H. Khonsari, M. J. Fagan, M. Moazen, 2017, "***Modelling human skull growth: a validated computational model***" Journal of The Royal Society Interface, 14:20170202.

- M. Moazen, A. Leonidou, J. Pagkalos, **A. Marghoub**, M. J. Fagan, E. Tsiridis, 2016, "***Application of far cortical locking technology in periprosthetic femoral fracture fixation – a biomechanical study***", 31:1849-1856.

<u>Conferences:</u>

- Moazen, C. Babbs, E. Pauws, M. J. Fagan, **A. Marghoub** "***Modelling Calvarial Development in Mice Using Finite Element Method***" The 12th International Congress of Vertebrate Morphology, Prague, Czech Republic, 21st - 25th July, 2019.

- Moazen, **A. Marghoub**, C. Babbs, E. Pauws, S. W. Herring, M. J. Fagan "***Biomechanics of craniofacial development in mice***" Experimental Biology 2019, Orlando, USA, 6th - 9th April, 2019.

- **<u>A. Marghoub</u>**, J. Libby, C. Babbs, Y. Ventikos, M. J. Fagan, M. Moazen "*Modelling bone formation at the cranial sutures in normal and craniosynostotic mice*" The 8th world congress of biomechanics, Dublin, Ireland, 8th - 12th July 2018.

- **<u>A. Marghoub</u>**, J. Libby, C. Babbs, E. Pauws, M. J. Fagan, M. Moazen "*Modelling bone formation at the cranial sutures in wild type mouse*" The 17th congress of international society of craniofacial surgery, Cancun, Mexico, 24th - 28th October 2017.

- J. Libby, **<u>A. Marghoub</u>**, D. Johnson, R. H. Khonsari, M. J. Fagan, M. Moazen "*A validated computational model of normal calvarial growth in humans*" The 17th congress of international society of craniofacial surgery, Cancun, Mexico, 24th - 28th October 2017.

- **<u>A. Marghoub</u>**, J. Libby, C. Babbs, A. O. Wilkie, M. J. Fagan, M. Moazen "*Predicting calvarial growth in a mouse model for craniosynostosis*" The 23rd congress of the European society of biomechanics, Sevilla, 2nd - 5th July 2017.

- J. Libby, **<u>A. Marghoub</u>**, D. Johnson, R. H. Khonsari, M. J. Fagan, M. Moazen "*Modelling growth of the human skull: a validated computational model approach*" The 23rd congress of the European society of biomechanics, Sevilla, 2nd - 5th July 2017.

- J. Xue, **<u>A. Marghoub</u>**, S. Bertazzo, S. E. Evans, M. Moazen "*Biomechanics of osteoderms in a lizard skull – a preliminary finite element study*" Anatomical Society Winter Meeting 19th - 21st December 2016, London, UK.

- **<u>A. Marghoub</u>**, J. Libby, C. Babbs, A. O. Wilkie, M. J. Fagan, M. Moazen "*Predicting calvarial growth in normal and craniosynostotic mice using finite element analysis*" The 11th International Congress of Vertebrate Morphology Washington DC, 29th June - 3rd July 2016.

- J. Libby, **<u>A. Marghoub</u>**, R. H. Khonsari, M. J. Fagan, M. Moazen "*Modelling human skull development*" The 11th International Congress of Vertebrate Morphology Washington DC, 29th June - 3rd July 2016.

- **<u>A. Marghoub</u>**, J. Libby, C. Babbs, A. O. Wilkie, M. J. Fagan, M. Moazen "*Predicting skull growth in normal and caniosynostotic mice*" The 16th congress of international society of craniofacial surgery, Tokyo, Japan, 14th – 18th September 2015.

- J. Libby, **<u>A. Marghoub</u>**, D. Johnson, R. H. Khonsari, M. J. Fagan, M. Moazen "*Biomechanics of Normal Human Skull Growth*" The 16th congress of international society of craniofacial surgery, Tokyo, Japan, 14th – 18th September 2015.

Appendix III: Published papers

Predicting calvarial growth in normal and craniosynostotic mice using a computational approach

Arsalan Marghoub[1], Joseph Libby[2], Christian Babbs[3], Erwin Pauws[4], Michael J Fagan[2], Mehran Moazen[1]

[1]Department of Mechanical Engineering, University College London, Torrington Place, London, WC1E 7JE, UK

[2]Medical and Biological Engineering, School of Engineering and Computer Science, University of Hull, Hull, HU6 7RX, UK

[3]MRC Molecular Haematology Unit, MRC Weatherall Institute of Molecular Medicine, University of Oxford, Oxford, OX3 9DS, UK

[4]Great Ormond Street, Institute of Child Health, University College London, Guilford St, London, WC1N 1EH, UK

Corresponding author:

Mehran Moazen; Department of Mechanical Engineering, University College London, Torrington Place, London, WC1E 7JE, UK; T: +44 (0) 207 679 3862; E: M.Moazen@ucl.ac.uk

Abstract

During postnatal calvarial growth the brain grows gradually and the overlying bones and sutures accommodate that growth until the later juvenile stages. The whole process is coordinated through a complex series of biological, chemical and perhaps mechanical signals between various elements of the craniofacial system. The aim of this study was to investigate to what extent a computational model can accurately predict the calvarial growth in wild type (WT) and mutant type (MT) $Fgfr2^{C342Y/+}$ mice displaying bicoronal suture fusion. A series of morphological studies were carried out to quantify the calvarial growth at P3, P10 and P20 in both mouse types. Then, microCT images of a P3 specimen were used to develop a finite element model of skull growth to predict the calvarial shape of WT and MT mice at P10. Sensitivity tests were performed and the results compared to *ex vivo* P10 data. While the models were sensitive to the choice of input parameters, they predicted the overall skull growth in the WT and MT mice. The models also captured the difference between the *ex vivo* WT and MT mice. This modelling approach has the potential to be translated to human skull growth and enhance our understanding of the different reconstruction methods used to clinically manage the different forms of craniosynostosis, and in the long term possibly reduce the number of re-operations in children displaying this condition and thereby enhance their quality of life.

Keywords: biomechanics; development; calvarial bones; sutures; finite element method; craniosynostosis

Running title: Modelling calvarial growth

1- Introduction

The mammalian cranial vault principally consists of five flat bones joined along their edges by soft tissues termed sutures (Opperman, 2000; Morriss-Kay & Wilkie 2005; Herring, 2008). The sutures are the sites where most skull vault growth occurs and they also function to give bones flexibility for birth and to allow the skull to expand and grow as the brain enlarges (Cohen, 2005; Richtsmeier & Flaherty, 2013). Premature closure of the sutures, or craniosynostosis, is a medical condition that occurs in about 1 in 2500 births, the question of an occurrence rate increase has also been raised (Boulet et al. 2008; van der Meulen et al. 2009; Johnson & Wilkie, 2011; Cornelissen et al. 2016). The majority of cases (70%) are non-syndromic i.e. single suture synostosis, with the remaining instances being syndromic (e.g. Crouzon and Apert), in which more than one suture fuses and where additional features are present such as midfacial hypoplasia (Morriss-Kay & Wilkie, 2005). Children displaying craniosynostosis generally require a surgical procedure that in majority of cases is carried out at 6-12 months of age.

Research to understand the genetic basis and clinical course of craniosynostosis (Wilkie, 1997; Morriss-Kay & Wilkie, 2005; Al-Rekabi et al. in press) has led to the development of various animal models (Mooney et al. 1998; Grova et al. 2012; Holmes, 2012). Mice have been investigated extensively in this work because murine calvarial morphology and genetics share several similarities with humans with the advantage that the developmental process occurs over a much shorter period (Morriss-Kay & Wilkie, 2005). In terms of calvarial development the intracranial volume of wild type mice typically reaches 70% of the adult size by postnatal day 10 (P10) with minimal further growth after P20 (Aggarwal et al. 2009; Moazen et al. 2016). In contrast, human intracranial volume reaches 65% of the adult volume by 1 year, with minimal further growth after 10 years (Dekaban, 1977; Sperber, 1989).

The Crouzon mouse model ($Fgfr2^{C342Y/+}$) has been extensively studied and has become a well-established model for investigating craniosynostosis (Eswarakumar et al. 2004; Perlyn et al. 2006; Liu et al. 2013; Martinez-Abadias et al. 2013; Peskett et al. 2017). This line is particularly interesting since it exhibits robust phenotypic abnormalities with features recapitulating clinical abnormalities observed in patients. The coronal sutures (joining the parietal and frontal bones) are primarily affected in these mice, as well as other joints on the cranial base (e.g. intersphenoidal synchondrosis joining the presphenoid and basisphenoid bones), causing a predictable bracycephalic (wide and short) head shape also characteristic of Crouzon patients (Eswarakumar et al. 2004; Perlyn et al. 2006; Liu et al. 2013). Coronal sutures in the wild type mouse are immediately adjacent, while never fully ossified, i.e. with micro-meter gap being present between the adjacent bones. In the Crouzon mouse overlapping of the frontal and parietal bones at this suture begins at the embryonic stages (E18.5) with full ossification (closure) occurring at ~P20 (Eswarakumar et al. 2004; Perlyn et al. 2006; Peskett et al. 2017). Thus, Crouzon $Fgfr2^{C342Y/+}$ mutant type (MT) and wild type (WT) mice provide an invaluable tool with which to understand the biomechanics of craniosynostotic and normal skull growth during postnatal development.

The finite element (FE) method is a computational modelling technique that has been widely used to understand general craniofacial biomechanics (e.g. Ross et al. 2005; Rayfield, 2007; Curtis et al. 2011; Cox et al. 2012; Moazen et al. 2013; Gussekloo et al. 2017), but it also has great potential in the simulation of growth and development of the craniofacial system. It can be used to predict the calvarial growth and to optimize reconstruction of various forms of craniosynostosis (Wolanski et al. 2013; Li et al. 2013; Libby et al. 2017). However, FE models require several input parameters and results produced must be validated using experimental data generated *in vitro* or *in vivo* (e.g. Kupczik et al. 2007; Szwedowski et al. 2011; Toro-Ibacache. et al. 2016). To best of our knowledge, there have not been any detailed simulations of skull growth (normal or craniosynostotic), which could lead to improvements in patient management or improvement of craniofacial surgery.

98   This study tests the hypothesis that brain expansion during postnatal development drives
99   calvarial growth and the response of the calvarial bone and sutures govern the resulting skull
100   shape. We tested this hypothesis in a FE study to simulate calvarial growth, specific aims were
101   to: (1) quantify the postnatal calvarial growth in WT and MT mice at P3, 10 and 20; (2) to
102   develop a FE model of mouse calvarial growth; and (3) to validate the FE predictions by
103   comparing them to *ex vivo* measurements of the calvaria in WT and MT mouse models.

104

105   2- Materials and Methods

106   Micro-computed tomography (microCT) images were obtained from wild type and mutant,
107   *Fgfr2*$^{C342Y/+}$, mice. A series of morphological studies were carried out to quantify the calvarial
108   growth at P3, P10 and P20. The microCT data of a single P3 mouse were then used to develop
109   a finite element model to simulate skull growth and in particular to predict mean calvarial shape
110   at P10. P10 was chosen since 70% of skull growth has been completed at this stage, with the
111   P20 data included to confirm this (see also Chuang et al. 2011; Moazen et al. 2016). Several
112   modelling sensitivity tests were performed with the results compared to a mean specimen
113   identified from the morphological study. This FE model was then used in the same way but
114   with specified premature fusion of the presphenoid-basisphenoid synchondrosis (PBS),
115   frontal, coronal, and lambdoid sutures to simulate growth to the equivalent P10 (MT) mutant
116   geometry.

117   *2-1 Morphological analysis*

118   MicroCT scans of a total of 22 WT and MT mice at P3 (n=1 for WT and MT), P10 (n=5 for WT
119   and MT), and P20 (n=5 for WT and MT), were obtained using an X-Tek HMX160 microCT
120   scanner (XTek Systems Ltd, Hertfordshire, UK). The images had a voxel size of 0.02mm in all
121   directions. Avizo image processing software (FEI Visualization Sciences Group, Merignac
122   Cedex, France) was used to reconstruct these data into three dimensional models. The
123   models were positioned so that in the mid-sagittal and transverse planes the basisphenoid
124   and preshenoid bones were aligned with the horizontal axis. Following this alignment, calvarial
125   length was measured in the mid-sagittal plane as the distance between the most anterior part
126   of the frontal suture and the most posterior part of the calvaria (Fig. 1). Calvarial height was
127   measured in the mid-sagittal plane as the distance between the basisphenoid and the most
128   superior part of the calvaria. Finally, calvarial width was measured in the transverse plane as
129   the distance between the two most lateral points of the calvaria. An average specimen at each
130   age and in each group was identified based on the specimen with the closest length, width
131   and height to the mean values.

132

133   *2-2 Finite element analysis*

134   ***Model development***: A three dimensional model of the P3 WT mouse was developed from
135   the microCT data (Fig. 2), with bone and sutures segmented and reconstructed in Avizo. The
136   intracranial volume was defined by filling the whole intracranial volume, hence it was
137   necessary to ensure that the skull was fully enclosed. Thus the foramen magnum was filled
138   and areas of the calvaria that were not fully developed were also defined manually. The model
139   eventually consisted of twenty-three different sections. A surface model of the skull was then
140   transformed into a meshed solid geometry using Avizo and was then imported into a finite
141   element software ANSYS v.14.5 (ANSYS Inc., Canonsburg, PA, USA). The model was
142   meshed using SOLID187 tetrahedral elements (10 node elements with quadratic
143   displacement behaviours) that are well suited for modelling irregular geometries (ANSYS
144   Theoretical Manual, v. 14.5). Mesh convergence was carried out, with the final model defined
145   by over 144,000 elements.

146

147   ***Material properties***: All regions were assigned isotropic material properties. In the baseline
148   model, an elastic modulus of 3500 MPa was assumed for the bone. This was based on
149   extrapolation of the frontal and parietal bone properties measured in mice at P10, P20, and

P70 (Moazen et al. 2015). Sutures and undeveloped areas of bone were assigned an elastic modulus of 30 MPa (Henderson et al. 2005; Moazen et al. 2015) while brain (the intracranial volume) was modelled with an elastic modulus of 150 MPa. A Poisson's ratio of 0.3 was used for all the materials, except 0.48 for the brain (Claessens et al. 1997).

Boundary condition and loading: The intracranial volume expansion during calvarial enlargement was modelled by expansion of the intracranial volume (Fig. 2) by applying a thermal expansion to the intracranial volume (ICV) in the FE model to increase its volume. Isotropic linear expansion was assumed using the following equation:

$$\Delta V = V_1 \times \alpha \times \Delta T \tag{1}$$

where α is the expansion coefficient, ΔV the change in volume, equal to the target volume of the next age V2 minus the current volume V1. The change in temperature ΔT was set at an arbitrary constant value of 100°C, and then α was altered by to achieve the desired ICV volume. A thermal expansion that finally led to less than 5% difference between the predicted brain and actual brain volume was considered acceptable. Thus, the P3 calvarium was initially expanded to the intracranial volume of the wild type P10 (Chuang et al. 2011). All degrees of freedom were constrained at three nodes on the presphenoid bone. The presphenoid bone was constrained since quantification of the wild type mouse skull growth revealed that this bone grows centrically during development and can be considered to effectively remain at the same position in the skull.

Measurements: Twenty landmarks (LMs) were used to quantify any differences between the predicted P10 skull (from the FE model) and the *ex-vivo* P10 (based on a 3D reconstruction from the CT data). While more LMs might have increased the sensitivity of the measurements, it was challenging to reliably identify more positions in the P3 geometry due to large areas of soft tissue. See Fig. 1 for the LMs details.

Root mean square (RMS) differences between the position of the actual and predicted LMs were then calculated by the following equation:

$$RMS = \sqrt{\left(\sum_{i=1}^{n} d_i^2\right)\big/ n} \, , \tag{2}$$

where, n is the number of landmarks and d_i is the distance between two corresponding landmarks of *ex vivo* P10 (in Avizo) and simulated P10 (expanded P3 geometry in ANSYS), with d_i obtained by:

$$d = \sqrt{(x_2 - x_1)^2 + (y_2 - y_1)^2 + (z_2 - z_1)^2}. \tag{3}$$

It should be highlighted again that this study is focused on calvarial growth and not facial growth, hence no LMs were assigned to the facial bones and an RMS of zero would have meant an identical match between the predicted shape and *ex-vivo* results.

To quantify the change in the overall shape and to visualise the differences between the skulls, 3D distance plots were also created using Avizo. The models were aligned and the points on the expanded FE surface mesh were measured to the closest point on the average *ex vivo* skull at P10. The areas at which the two surfaces differed (both positively or negatively) showed where the FE models over or under-predicted skull growth. The maximum differences in both the positive and negative directions were calculated and plotted on a colour contour plot.

Sensitivity tests: Three sensitivity tests were carried out on the WT model to investigate the sensitivity of the results to some of the key input parameters. In particular: (1) boundary

200 condition: the baseline model in this study was constrained at the presphenoid bone; this was
201 altered to basisphenoid or both presphenoid and basisphenoid; (2) brain properties: there is a
202 large range of data reported in the literature for brain properties (e.g. Miller et al. 2000; Gefen
203 & Margulies 2004; Bouchonville et al. 2016) hence the baseline value of 150 MPa was altered
204 within the range from 1 MPa to 1500 MPa; (3) suture properties: our previous experimental
205 measurements (Moazen et al. 2015) showed a large standard deviation for the suture
206 properties hence the baseline value of 30 MPa was varied between 3 MPa and 300 MPa.

207 ***Predicting mutant Fgfr2$^{C342Y/+}$ mouse calvarial shape at P10:*** The baseline wild type model
208 was used to predict the mutant skull shape at P10 after fusion of some of the sutures (Fig. 3).
209 Lui et al. (2013) showed that in this mouse model, several sutures including the presphenoid-
210 basisphenoid synchondrosis (PBS), frontal, coronal, and lambdoid sutures fuse prematurely.
211 Hence, they were effectively fused in the wild type model described above by changing their
212 elastic modulus from suture material to that of bone (3500 MPa). The ICV was expanded the
213 same as the WT models and the results were compared against the microCT data of the MT
214 mice at P10. Fig. 3 shows the 3D elastic modulus distribution across the WT and MT FE
215 models.

216

217 **Results**

218 ***Morphological analysis:***

219 Fig. 4 summarises the calvarial length, width and height measurements at P3, P10 and P20
220 for the WT and MT models. While all measurements gradually increased from P3 to P20,
221 calvarial length and height of the WT mice were consistently higher and lower than the MT
222 mice respectively. This pattern is also evident in the 2D sagittal cross-sections of the WT and
223 MT mice (Fig. 5).

224 Fig. 6 compares the overall morphological differences between the *ex vivo* WT and MT mice
225 at P10 using 3D distance colour plots. In the dorsal view, the highlighted square shows the
226 over growth of the MT skull across the parietal region (bulging). In the posterior view, the
227 highlighted oval shows the under growth of the lambdoid region in the MT mouse (Fig. 6).

228 ***Finite element analysis:***

229 ***Sensitivity tests:*** Altering the boundary conditions from the baseline model i.e. at the
230 presphenoid bone (set 2 in Fig. 7A), to the basisphenoid (set 1 in Fig. 7) or both the
231 presphenoid and basisphenoid (set 3, Fig. 7A) leads to overestimation of the calvarial height.
232 At the same time, the RMS difference values were decreased from the baseline value of 1.14
233 to 1.01 and 0.96, for set 1 and 3 respectively. Altering the elastic modulus of the brain had the
234 greatest impact on the overall skull shape (Fig. 7B). Reducing the elastic modulus of the brain
235 led to an increase in the skull height and bulging of the fronto-parietal region. However,
236 increasing the elastic modulus of the brain from 15 MPa to 150 MPa and 1500MPa led to a
237 closer match with the overall skull shape of the *exvivo* data and reduced the RMS values from
238 1.28 to 0.95 for an elastic modulus change of 15 to 1500 MPa. Increasing the elastic modulus
239 of the sutures from 3 MPa to 300 MPa led to a gradual increase in skull height and decrease
240 of RMS values from 1.18 to 0.99 (Fig. 7C).

241

242 ***Predicted WT and MT calvarial shape at P10:*** Fig. 7 compares the overall geometric
243 differences (in 2D and 3D) between the FE prediction of skull shape at P10 versus the *ex vivo*
244 P10 skull using on the baseline model parameters. The FE model overestimates the skull
245 height by 0.56 mm (highlighted square in Fig. 8, 7.19 mm vs. 6.63 mm) and underestimates
246 the skull length by 0.21 mm (highlighted oval in Fig. 8 - 12.93 mm vs. 13.14 mm). In contrast,
247 using the same parameters, the FE model simulating the MT mice skull shape also
248 overestimates the skull height by 0.16mm (Fig. 9 - 7.32 mm vs. 7.16 mm) and underestimates
249 the skull length by 0.13mm (Fig. 9 - 12.72 mm vs. 12.59 mm).

Discussion

Calvarial growth is thought to involve a series of complex biological, chemical and perhaps mechanical signalling between a number of soft and hard tissues such as the growing brain, dura mater, sutures and bone (Morriss-Kay & Wilkie, 2005; Richtsmeier & Flaherty, 2013; Al-Rekabi et al. in press). This study aims to investigate whether a simple biomechanical approach simulating expansion of the brain can predict calvarial growth in wild type and a mouse model of craniosynostosis. The study focuses on prediction of calvarial growth up to P10, using FE metholodology, which corresponds to about one year of age in humans, the point at which there is clinical consensus advocating surgical treatment of craniosynostosis. To validate the FE results a series of morphological studies on WT and MT mice were carried out.

The morphological studies highlighted: (1) expansion of the calvaria up to P20 in both WT and MT; (2) centric growth of the cranial base; (3) the MT mice have a shorter skull length compared to WT mice and display bulging across the parietal region in line with previous studies (Eswarakumar et al. 2004; Perlyn et al. 2006; Liu et al. 2013; Martinez-Abadias et al. 2013; Peskett et al. 2017); and most importantly (4) they provided the reference data required for validation of the FE modelling approach.

Sensitivity analysis to investigate the choice of input parameters is a key step in any FE study, therefore a series of sensitivity tests were carried out initially to understand their impact on the results. In the studies performed, the FE results consistently overestimated the calvarial height and underestimated the calvarial width (Fig. 7). The results highlighted that the brain (or here the intracranial filling material) properties had the highest impact on the predictions. The elastic modulus of the brain is reported to be in the range of 1-30 kPa (Bouchonville et al. 2016). This is three to four orders of magnitude lower than the baseline value of 150MPa used in this study. This may appear un-realistic, nonetheless since it generally leads to a similar degree of calvarial expansion to the *ex vivo* data it may have compensated the effect of other tissues not included here. For instance, dura mater was not modelled explicitly in this study and is expected to have an elastic modulus in the range of 1-1000 MPa (e.g. van Noort et al. 1981; Mikos et al. 2008). While it is not clear what the combined elastic modulus of the intracranial soft tissues is, it is likely to be higher than each of its individual components and it is perhaps covered in the range of properties tested in the sensitivity tests here. Although higher values of elastic modulus for brain lead to a better match with the *ex vivo* data, 150 MPa was chosen as the baseline as this is within the range of the experimental data (brain properties) reported in the literature.

Overall, the finite element models predicted the expansion of the WT and MT model skulls from P3 to P10 reasonably well. However, there were differences between the FE results and the *ex vivo* measurements at P10 (Fig. 8 and Fig. 9). The fact that the FE prediction constantly overestimates the skull height might be due to not modelling the soft tissues that cover the brain and perhaps constrain it to the base of the skull i.e. dura mater. On the other hand, while we believe that at early stages of postnatal development perhaps a uniform growth of the brain is not an unrealistic assumption but it is likely that in mouse from about P10 onward, brain growth deviates from a uniform radial growth in line with the bone formations at the sutures to exhibit a more posterior growth (see also Fig. 5).

To the best of our knowledge this is the first attempt to predict calvarial growth in WT and craniosynostotic MT mice using finite element analysis. A similar approach was recently tested in humans to predict normal calvarial growth up to one year of age, and it also showed promising results (Libby et al. 2017). Nonetheless, there are a number of limitations with the current approach that can be improved. These include: (1) several anatomical structures were not explicitly modelled. For example, the dura mater will constrain the brain expansion to some degree; (2) bone forms gradually at the suture, its thickness and elastic modulus increases

during the development, coincident with skull expansion (Richtsmeier & Flaherty, 2013; Moazen et al. 2015 & 16). It is likely that addition of these changes to the model described in this study can enhance the presented prediction and may lead to better matching of the skull height predictions.

Considering the limitations mentioned above, modelling an expanding brain using our methodology, seems to predict skull expansion reasonably well. This suggests that brain growth may be a key factor in the morphogenesis of the calvarial growth. Future studies are required to address the limitations of the approach, nonetheless this approach may have applications in improving management of craniosynostosis, for example through optimisation of the reconstruction methods for the different various forms of the condition. In the longer term, this could reduce the number of re-operations for children displaying the condition and enhance their quality of life.

Authors' contribution
MM, CB and MJF designed the study, AM performed the study, AM, JL and EP performed the analysis, AM, MM, MJF, CB and EP wrote the paper. All authors gave final approval for publication.

References:

Al-Rekabi Z, Cunningham ML, Sniadecki NJ (in press). Cell mechanics of craniosynostosis. *ACS Biom Sci Eng*.

Aggarwal M, Zhang J, Miller MI, Sidman RL, Mori S (2009). Magnetic resonance imaging and micro-computed tomography combined atlas of developing and adult mouse brains for stereotaxic surgery. *Neuroscience*. **162**,1339-1350.

Bouchonville N, Meyer M, Gaude C, Gay E, Ratel D, Nicolas A (2016). AFM mapping of the elastic properties of brain tissue reveals kPa µm(-1) gradients of rigidity. *Soft Matter*. **12**, 6232-6239.

Boulet SL, Rasmussen SA, Honein MA (2008). A population-based study of craniosynostosis in metropolitan Atlanta, 1989-2003. *Am J Med Genet A*. **146A**, 984-991.

Chuang N, Mori S, Yamamoto A, Jiang H, Ye X, Xu X, Richards LJ, Nathans J, Miller MI, Toga AW, Sidman RL, Zhang J (2011). An MRI-based atlas and database of the developing mouse brain. *Neuroimage*. **54**, 80-89.

Claessens M, Sauren F, Wismans J (1997). Modeling of the human head under impact conditions: a parametric study. *SAE Technical Paper*. 973338.

Cohen MM (2005). Editorial: perspectives on craniosynostosis. *Am J Med Genet A*. **136A**, 313-326.

Cornelissen M, Ottelander Bd, Rizopoulos D, van der Hulst R, Mink van der Molen A, van der Horst C, Delye H, van Veelen ML, Bonsel G, Mathijssen I (2016). Increase of prevalence of craniosynostosis. *J Cranio-Max-Fac Surg*. **44**,1273-1279.

Cox PG, Rayfield EJ, Fagan MJ, Herrel A, Pataky TC, Jeffery N (2012). Functional evolution of the feeding system in rodents. *PLoS One* **7**: e36299.

Curtis N, Jones MEH, Shi J, O'Higgins P, Evans SE, Fagan MJ (2011). Functional relationship between skull form and feeding mechanics in *Sphenodon* and implications for Diapsid skull development. *PLoS ONE* **6(12)**, e29804.

Dekaban AS (1977). Tables of cranial and orbital measurements, cranial volume, and derived indexes in males and females from 7 days to 20 years of age. *Ann. Neurol*. **2**, 485-491.

Eswarakumar VP, Horowitz MC, Locklin R, Morriss-Kay GM, Lonai P (2004). A gain-of-function mutation of Fgfr2c demonstrates the roles of this receptor variant in osteogenesis. *Proc Natl Acad Sci USA*. **101**,12555-12560.

Gefen A, Margulies SS (2004). Are in vivo and in situ brain tissues mechanically similar? *J Biomech*. **37**,1339-1352.

Grova M, Lo DD, Montoro D, Hyun JS, Chung MT, Wan DC, Longaker MT (2012). Models of cranial suture biology. *J Craniofac Surg*. **23**,1954–1958.

Gussekloo SW, Berthaume MA, Pulaski DR, Westbroek I, Waarsing JH, Heinen R, Grosse IR, Dumont ER (2017). Functional and evolutionary consequences of cranial fenestration in birds. *Evolution*. **71**, 1327-1338.

Henderson JH, Chang LY, Song HM, Longaker MT, Carter DR (2005). Age-dependent properties and quasi-static strain in the rat sagittal suture. *J Biomech*. **38**, 2294-2301.

Herring SW (2008). Mechanical influences on suture development and patency. *Front Oral Biol*. **12**, 41-56.

Holmes G (2012). The role of vertebrate models in understanding craniosynostosis. *Childs Nerv Syst*. **28**,1471–1481.

Johnson D, Wilkie AOM (2011). Craniosynostosis. *Eur J Hum Genet*. **19**, 369–376.

Kupczik K, Dobson CA, Fagan MJ, Crompton RH, Oxnard CE, O'Higgins P (2007). Assessing mechanical function of the zygomatic region in macaques: validation and sensitivity testing of finite element models. *J Anat*. **210**, 41–53.

Li Z, Luo X, Zhang J (2013). Development/ global validation of a 6-month-old pediatric head finite element model and application in investigation of drop-induced infant head injury. *Comput Methods Programs Biomed*. **112**, 309-319.

Libby J, Marghoub A, Johnson D, Khonsari RH, Fagan MJ, Moazen M (2017). Modelling human skull growth: a validated computational model. *J Roy Soc Int.* **14**, 20170202.

Liu J, Nam HK, Wang E, Hatch N (2013). Further analysis of the Crouzon mouse: effects of the FGFR2(C342Y) mutation are cranial bone-dependent. *Calcif Tissue Int.* **92**, 451-466.

Martínez-Abadías N, Motch SM, Pankratz TL, Wang Y, Aldridge K, Jabs EW, Richtsmeier JT (2013). Tissue-specific responses to aberrant FGF signaling in complex head phenotypes. *Dev Dyn.* **242**, 80-94.

Maikos JT, Elias RA, Shreiber DI (2008). Mechanical properties of dura mater from the rat brain and spinal cord. J Neurotrauma. **25**, 38-51.

Miller K, Chinzei K, Orssengo G, Bednarz P (2000). Mechanical properties of brain tissue in-vivo: experiment and computer simulation. J Biomech. **33**,1369-1376.

Moazen M, Alazmani A, Rafferty K, Liu ZJ, Gustafson J, Cunningham ML, Fagan MJ, Herring SW (2016). Intracranial pressure changes during mouse development. *J. Biomech.* **49**, 123-126.

Moazen M, Costantini D, Bruner E (2013). A sensitivity analysis to the role of fronto-parietal suture in *Lacerta bilineata:* a preliminary finite element approach. *Anat Rec.* **296**,198-209.

Moazen M, Peskett E, Babbs C, Pauws E, Fagan MJ (2015). Mechanical properties of calvarial bones in a mouse model for craniosynostosis. *PloS ONE.* **10**, e0125757.

Mooney MP, Siegel MI, Burrows AM, Smith TD, Losken HW, Dechant J, Cooper G, Kapucu MR (1998). A rabbit model of human familial, nonsyndromic, unicoronal suture synostosis: part 1. Synostotic onset, pathology, and sutural growth patterns. *Childs Nerv Syst.* **14**, 236-246.

Morriss-Kay GM, Wilkie AOM (2005). Growth of the normal skull vault and its alteration in craniosynostosis: insights from human genetics and experimental studies. *J Anat.* **207**, 637-653.

Opperman LA (2000). Cranial Sutures as intramembranous bone growth sites. *Dev Dyn.* **485**, 472-485.

Perlyn CA, DeLeon VB, Babbs C, Govier D, Burell L, Darvann T, Kreiborg S, Morriss-Kay G (2006). The craniofacial phenotype of the Crouzon mouse: analysis of a model for syndromic craniosynostosis using three-dimensional MicroCT. *Cleft Palate J.* **43**, 740-748.

Peskett E, Kumar S, Baird W, Jaiswal J, Li M, Patel P, Britto JA, Pauws E (2017). Analysis of the $Fgfr2^{C342Y}$ mouse model shows condensation defects due to misregulation of Sox9 expression in prechondrocytic mesenchyme. *Biol Open.* **6**, 223-231.

Rayfield EJ (2007). Finite element analysis and understanding the biomechanics and evolution of living and fossil organisms. *Annu Rev Earth Planet Sci.* **35**, 541–576.

Ross CF, Patel BA, Slice DE, Strait DS, Dechow PC, Richmond BG, Spencer MA (2005). Modeling masticatory muscle force in finite element analysis: sensitivity analysis using principal coordinates analysis. *Anat Rec.* **283A**, 288–299.

Richtsmeier JT, Flaherty K (2013). Hand in glove: brain and skull in development and dysmorphogenesis. *Acta Neuropathol.* **125**, 469-489.

Sperber GH (1989). Craniofacial embryology, 4th edition, p. 102. London: Wright, Butterworths.

Szwedowski TD, Fialkov J, Whyne CM (2011). Sensitivity analysis of a validated subject-specific finite element model of the human craniofacial skeleton. *Proc Inst Mech Eng H.* **225**, 58-67.

Toro-Ibacache V, Fitton LC, Fagan MJ, O'Higgins P (2016). Validity and sensitivity of a human cranial finite element model: implications for comparative studies of biting performance. *J Anat.* **228**, 70-84.

van der Meulen J, van der Hulst R, van Adrichem L, Arnaud E, Chin-Shong D, Duncan C, Habets E, Hinojosa J, Mathijssen I, May P, et al. (2009). The increase of metopic synostosis a pan-european observation. *J Craniofac Surg.* **20**, 283-286.

447   **van Noort R, Black MM, Martin TR, Meanley S** (1981). A study of the uniaxial mechanical
448   properties of human dura mater preserved in glycerol. *Biomaterials.* **2**, 41-5.
449   **Wilkie AOM** (1997). Craniosynostosis : genes and mechanisms. *Hum Mol Genet.* **6**, 1647-
450   1656.
451   **Wolanski W, Larysz D, Gzik M, Kawlewska E** (2013). Modeling and biomechanical
452   analysis of craniosynostosis correction with the use of finite element method. *Int J Numerl*
453   *Method Biomed Eng.* **29**, 916-925.

454

455

456

457

458

459

460

461

462

463

464

465

466

467

468

469

470

471

472

473

474

475

Figure captions:

Fig. 1: Lateral and dorsal view of a P3 mouse skull, highlighting landmark positions, length, height and width measurement. Note: 1& 2 Most medial intersection of the frontal and parietal bones, on the frontal (left & right); 3&4 Most medial intersection of the frontal and parietal bones, on the parietal (left and right); 5&6 Most lateral intersection of the frontal and parietal bones, on the frontal (left and right); 7&8 Midpoint on medial side of the parietal bone (left & right); 9&10 The posterior root of the zygomatic process (left & right); 11 &12 Most posterior-inferior point on the parietal (left and right); 13&14 Most posterior-inferior point on the interparietal (left & right); 15 Most anterior-medial point of the interparietal bone; 16 Most anterior-medial point of the occipital bone; 17&18 Most posterior-lateral point of the occipital bone; 19 Most posterior-medial point of the occipital bone; 20 Most posterior-medial point of the basioccipital bone.

Fig. 2: Finite element model development and loading. Micro-CT images (A) were used to develop the 3D FE model (B). Brain volume at P3 (C and yellow elements shown in B) was expanded to P10 and P20 (D and E). Note colours in (C) and (D) highlight different sections segmented i.e. bone and sutures.

Fig. 3: 3D elastic modulus distribution of WT and MT for FE models. Presphenoid-basisphenoid synchondrosis (PBS), frontal, coronal, and lambdoid sutures are fused prematurely by changing their elastic modulus from suture material to that of bone (3500 GPa).

Fig. 4: Length, width and height measurement at P3 (n=1), P10 (n=5) and P20 (n=5). Error bars indicate the SD of each group.

Fig. 5: Sagittal sections of *ex vivo* wild type (WT) and mutant type (MT) mice at P3, P10 and P20.

Fig. 6: 3D morphological comparison between the *ex vivo* P10 wild type (WT) and mutant type (MT) mice. The highlighted oval shows the overall shorter length of the MT skull in comparison with the WT skull, while the square shows its extended height.

Fig. 7: Sensitivity analysis to the choice of (A) boundary condition, (B) elastic modulus of the brain, and (C) sutures. Dashed outlines highlight the baseline values and results. The sagittal section of the average *ex vivo* P10 is shown in green, while the purple figures show the FE predictions.
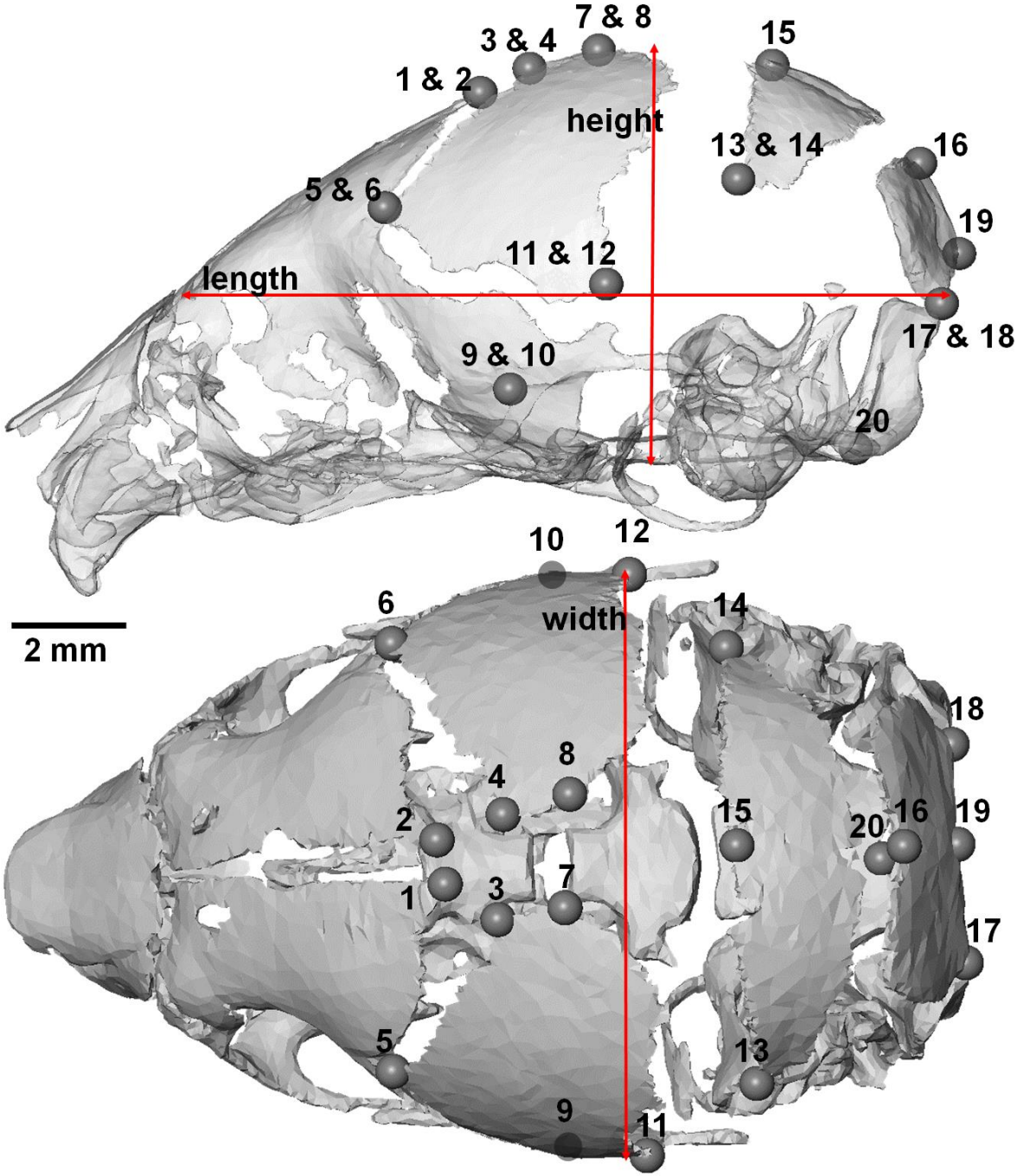
Fig. 8: 3D morphological comparison between the finite element (FE) predicted and *ex vivo* wild type (WT) mouse at P10. The length is under estimated (the oval), while the height is over estimated (the square).

Fig. 9: 3D morphological comparison between the finite element (FE) predicted and *ex vivo* mutant type (MT) mouse at P10. There is a relatively good match between the FE prediction and ex vivo.
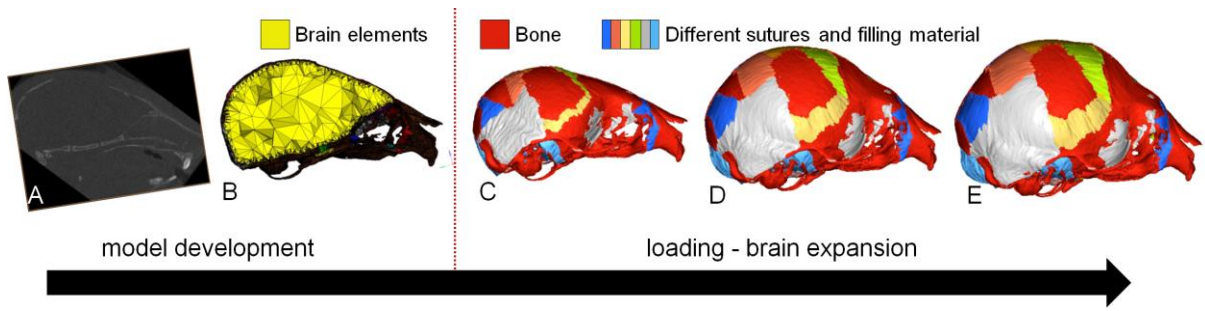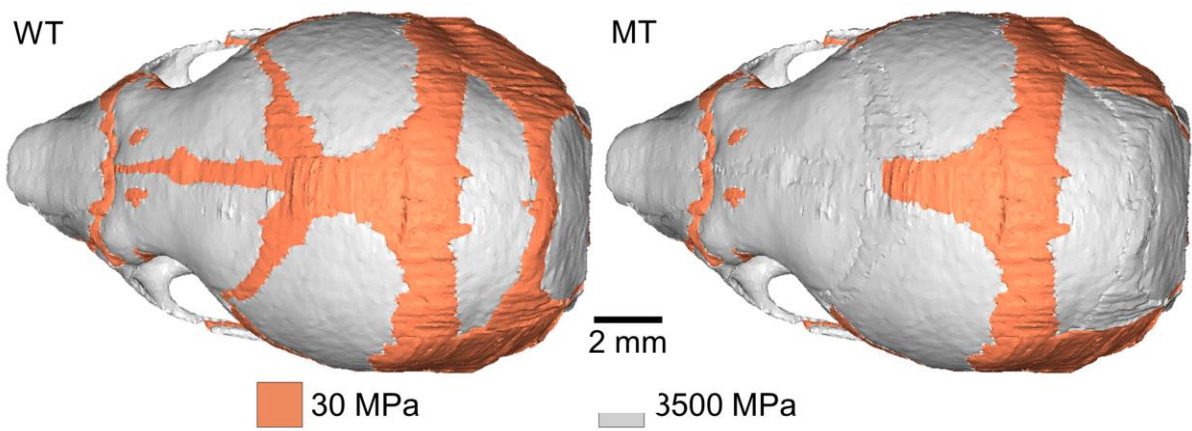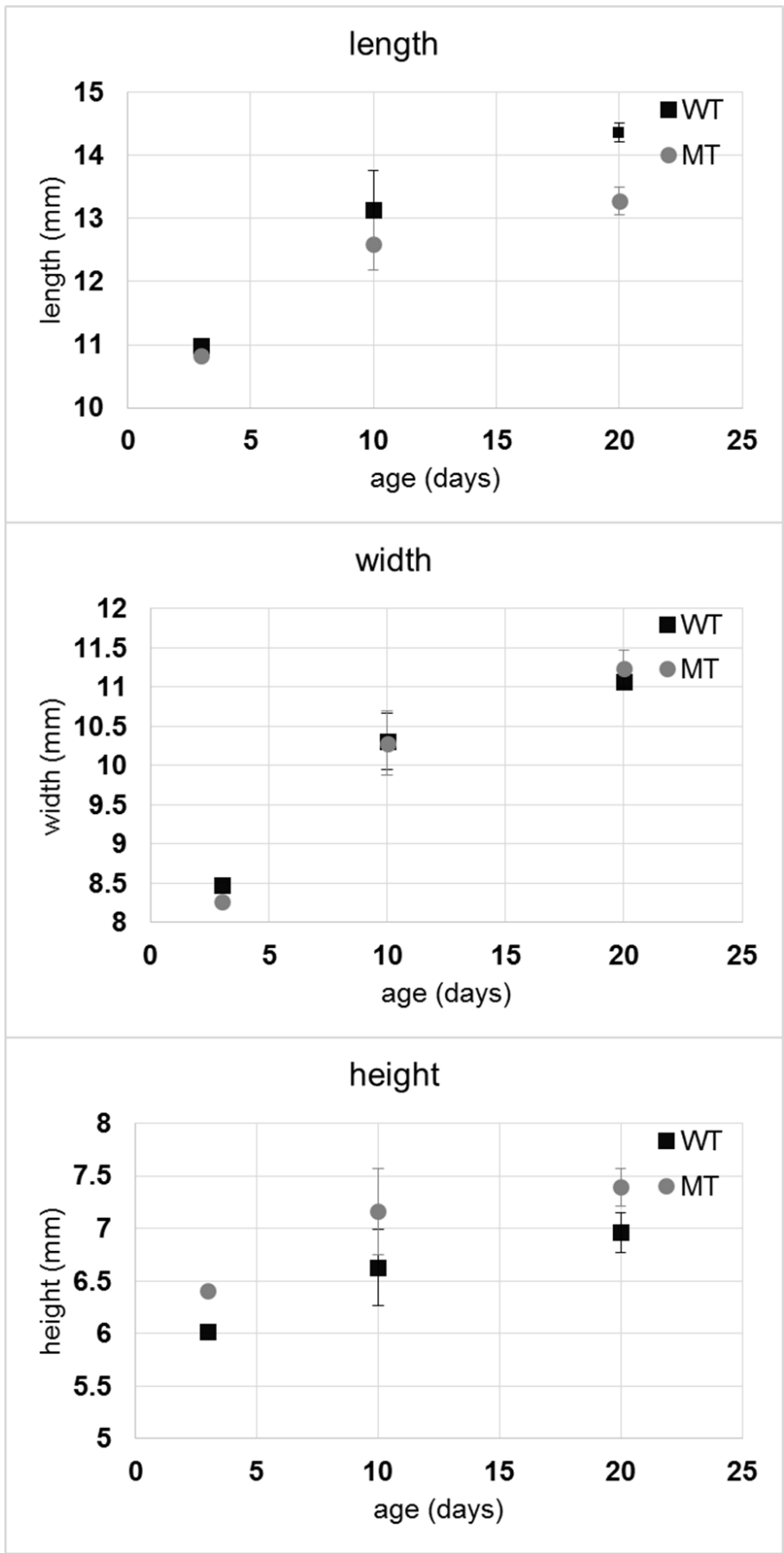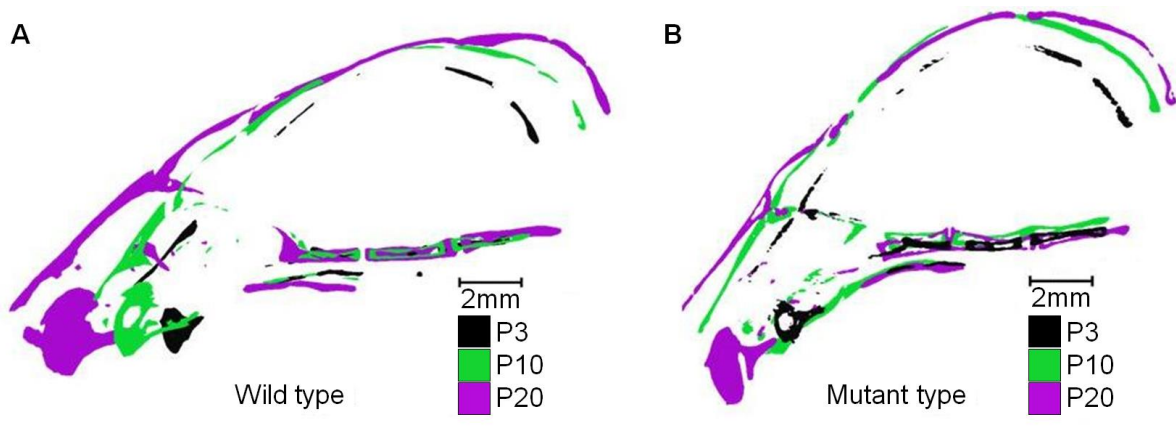
515   Figure 1

516

517

518

519

520

521

522   Figure 2

model development   loading - brain expansion

523

524

525   Figure 3

526

527

528

529

530

531

532

533

534

535

536

537

538

539   Figure 4

540

541   Figure 5

A   B

Wild type   Mutant type

2mm   2mm
■ P3   ■ P3
■ P10   ■ P10
■ P20   ■ P20

542

543

544   Figure 6

7.16 6.63   10.31
    13.14   10.28
   12.59

WT ■ MT ■

(under estimation) -0.75 mm   0   0.75 mm (over estimation)
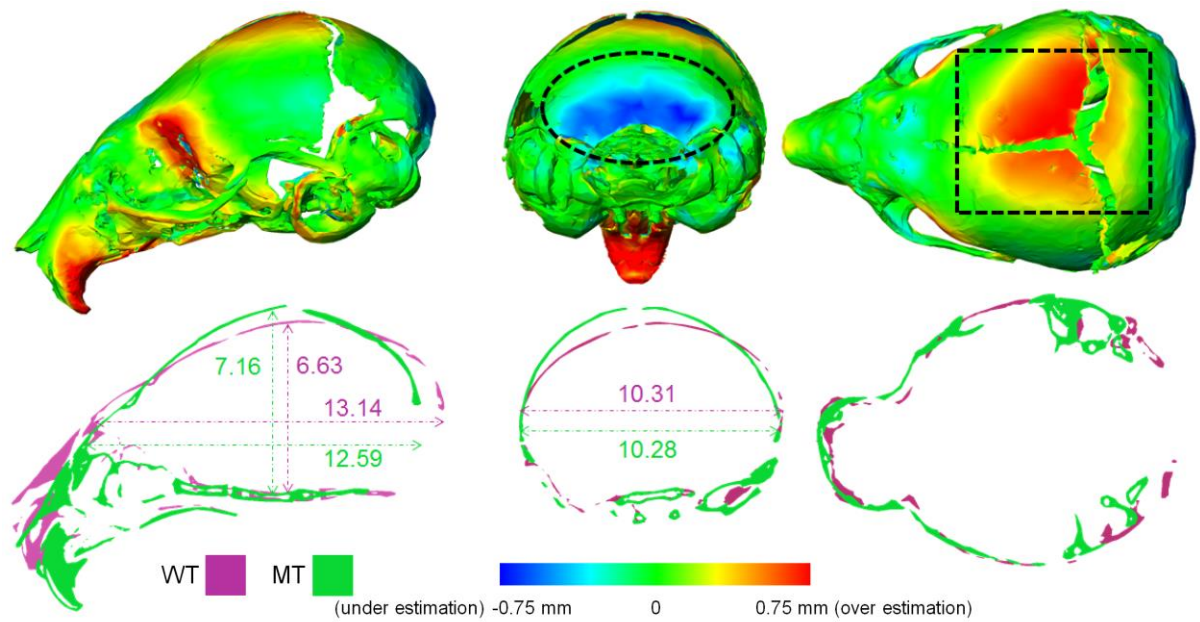
545

546

547

548

549

550

551

552

553   Figure 7
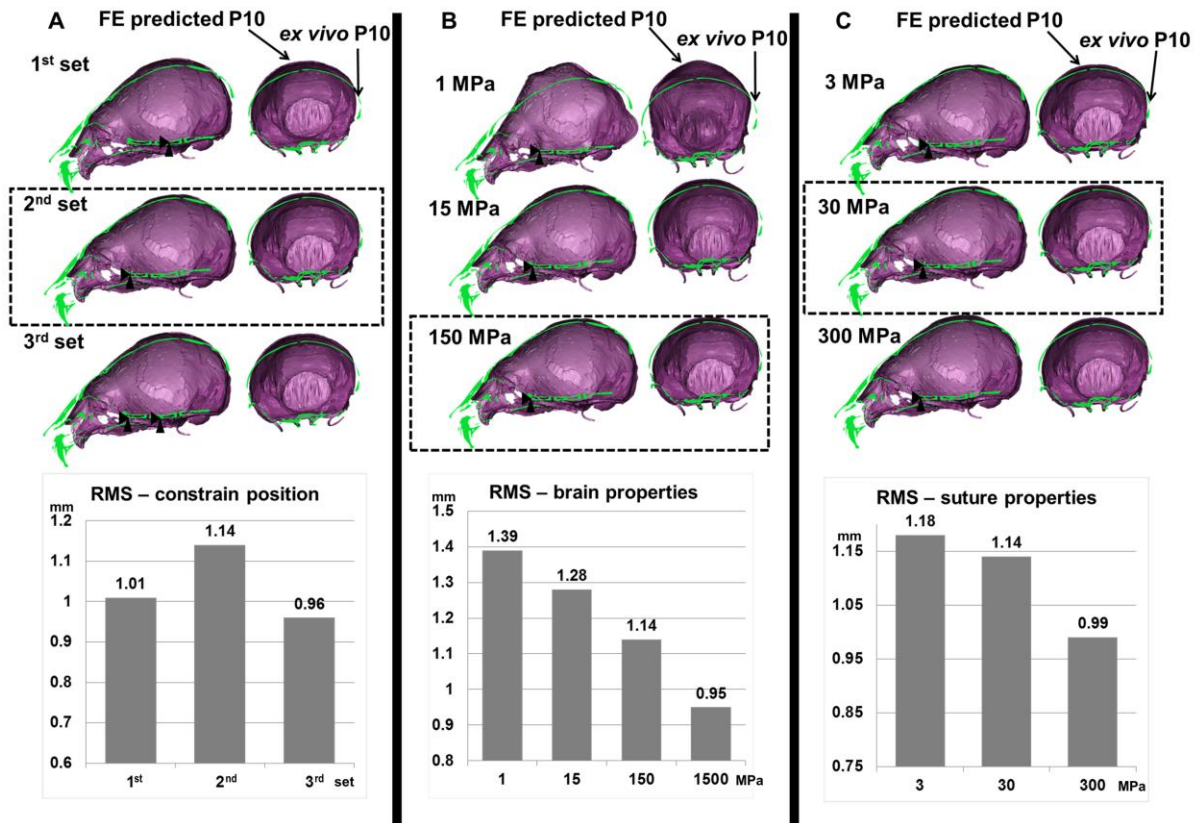
554

555   Figure 8

556

557

558

559

560   Figure 9

ex-vivo ▇   FE ▇

(under estimation) -0.75 mm   0   0.75 mm (over estimation)
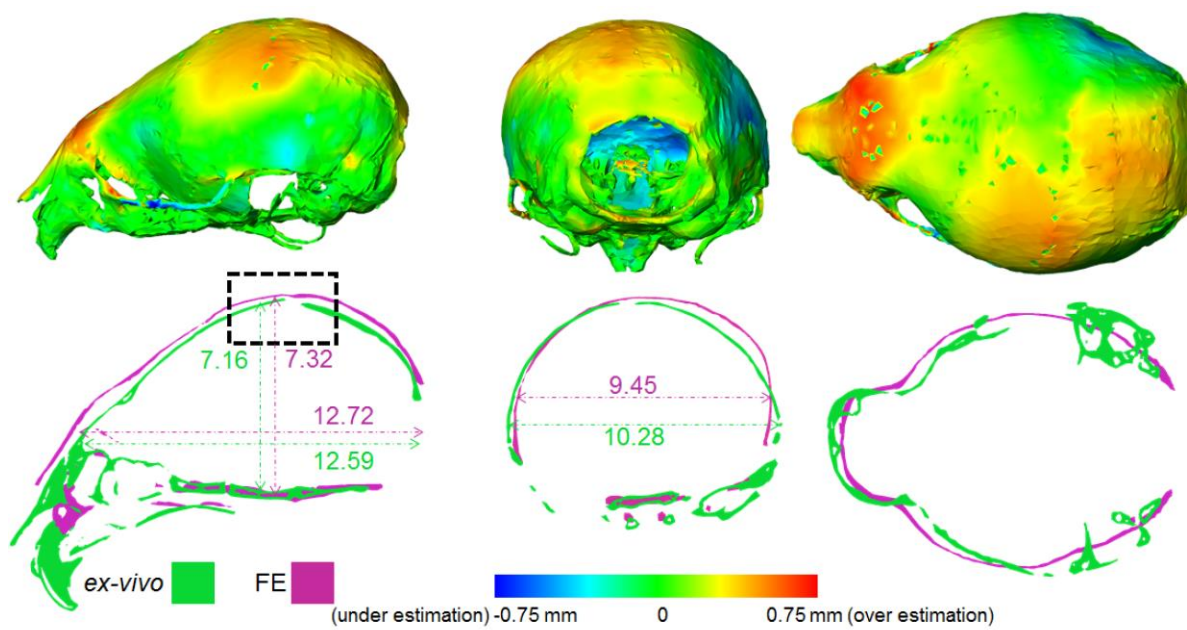
561
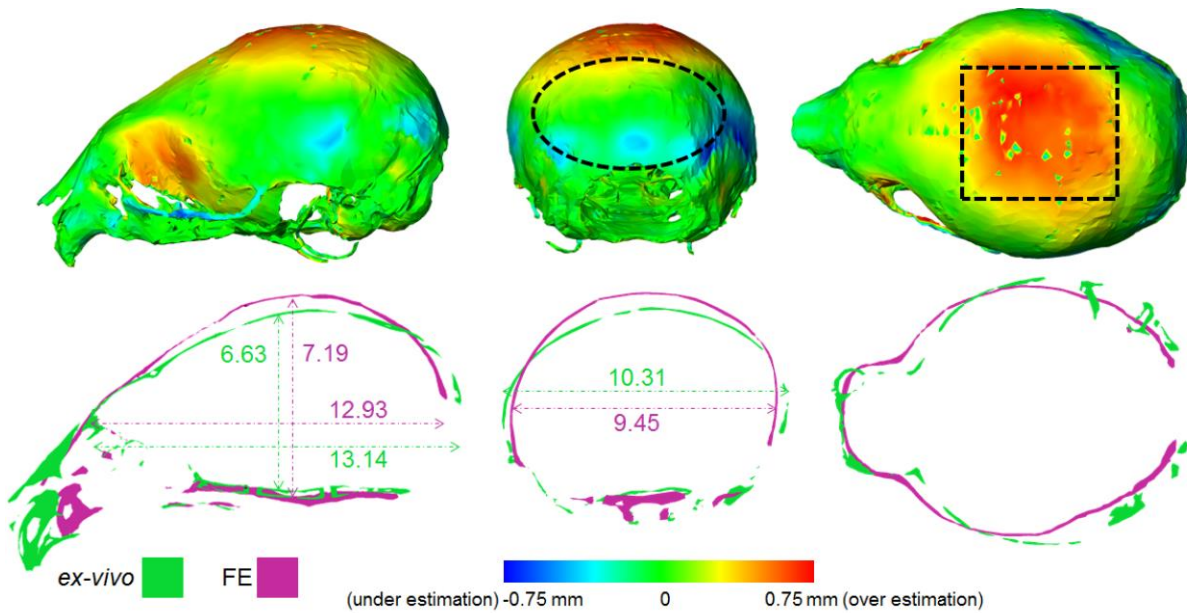
1 **Characterizing and modeling bone formation during mouse**
2 **calvarial development**

3 **Arsalan Marghoub[1], Joseph Libby[2], Christian Babbs[3], Yiannis Ventikos[1],**
4 **Michael J Fagan[2], Mehran Moazen[1]**

5

6 [1]Department of Mechanical Engineering, University College London, Torrington Place,
7 London, WC1E 7JE, UK

8 [2]Medical and Biological Engineering, School of Engineering and Computer Science, University
9 of Hull, Hull, HU6 7RX, UK

10 [3]Weatherall Institute of Molecular Medicine, University of Oxford, Oxford, OX3 9DS, UK

11

12 *Corresponding author:*

13 *Mehran Moazen; Department of Mechanical Engineering, University College London, Torrington Place,*
14 *London, WC1E 7JE, UK; T: +44 (0) 207 679 3862; E: M.Moazen@ucl.ac.uk*

15

16

17 **Abstract**

18 The newborn mammalian cranial vault consists of five flat bones that are joined together along
19 their edges by soft fibrous tissues called sutures. Early fusion of these sutures leads to a
20 medical condition known as craniosynostosis. The mechanobiology of normal and
21 craniosynostotic skull growth is not well understood. In a series of previous studies, we
22 characterised and modelled radial expansion of normal and a craniosynostotic (Crouzon)
23 mice. Here we describe a new modelling algorithm to simulate bone formation at the sutures
24 in normal and craniosynostotic mice. Our results demonstrate our modelling approach is
25 capable of predicting the observed *ex vivo* pattern of bone formation at the sutures in the
26 aforementioned mice. The same approach can be used to model different calvarial
27 reconstruction in children with craniosynostosis to assist in the management of this complex
28 condition.

29

32

33

34

The newborn mammalian cranial vault consists of five flat bones that are joined together along their edges by soft fibrous tissues called sutures [1-4]. The sutures give flexibility for birth and allow the skull to expand and grow as the brain enlarges [3]. Sutures are composites of osteoprogenitor cells of mesenchymal origin that differentiate into osteoblasts during development. These deposit extracellular matrix consisting primarily of type I and other collagens as well as various bone-related proteins and proteoglycans [1].

During the early stages of postnatal development, hand in hand with the radial expansion of the skull, intracranial pressure (ICP) increases and calvarial bones thicken [5-8]. By the time the brain has reached its maximum size (in mice around postnatal day twenty, P20, [9]) visible gaps at the sutures have reduced to micro/nanometer gaps where sutures have differentiated to bone [5,10]. The ICP has plateaued [8] while bone mineralization (i.e. both thickening of the bone and increase in its inherent mechanical properties) continues during adulthood, perhaps in response to muscle forces and mastication that started in the juvenile stages (in mouse P10-20) and continues during life [11,12].

Our understanding of the mechanobiology of the cranial sutures and the level of mechanical stimulus that sutures experience during the natural calvarial growth is still limited [13-18]. This knowledge however is crucial for the development of novel technologies and new approaches to the treatment of pathological conditions associated with (for example) their early fusion, i.e. craniosynostosis [19,20]. In this respect laboratory mouse models are invaluable because of their genetic and morphological similarities to human calvaria [1-3]. Further there are a number mouse models of craniosynostosis. For example, Crouzon type *Fgfr2*[C342Y] shows early bi-coronal suture fusion causing a predictable brachycephalic head shape and bulging across the parietal region [21-24], enabling us to compare the mechanobiology of natural vs. pathological bone formation at the sutures.

In a series of studies, we have previously characterised and modelled expansion of calvaria in wild type (WT) and Crouzon mutant type (MT) mouse [8,11,25]. These have enabled us to estimate the level of mechanical strain that sutures experience during the early postnatal development. In this current work, we first characterised the changes in the calvarial sutures sizes across the skull in a series of *ex vivo* WT and MT mice. Then, we developed a new modelling algorithm, using finite element method, to predict bone formation at the sutures during cranial expansion. Finally, we validated our predictions through comparison with our *ex vivo* measurements. To the best of our knowledge, modelling the bone formation at the gross morphological level in the craniofacial system has not been carried out before. This is the novelty and main contribution of this study.

Ex vivo characterisation of sutures: We obtained microCT images of WT and MT mice at P3 (n=1 for WT and MT), P7 (n=5 for WT and MT), and P10 (n=5 for WT and MT), using an X-Tek HMX160 microCT scanner (XTek Systems Ltd, Hertfordshire, UK). Note the mice were obtained from the same littermates. The images had a voxel size of 0.02 mm in all directions. We used Avizo image processing software (FEI Visualization Sciences Group, Merignac Cedex, France) to reconstruct these data into three dimensional models. The 3D models were positioned so that in the mid-sagittal and transverse planes the basisphenoid and presphenoid bones were aligned with the horizontal axis. Following this alignment, we measured the suture width at 14 locations in the cranial vault (Fig. 1). At each age, we then identified the individual that was the closest average specimen for suture sizes. These specimens were then used for comparison to the computational predictions. At the same time this characterisation highlighted that the average rate of bone formation at the sutures in the WT and MT were 0.14 mm per day from P3 to P10.

Finite element model development: We used micro-CT images of the WT P3 mouse to develop, a three dimensional model of the initial skull (Figs. 2a and b). The geometry was firstly developed in Avizo, and consisted of bone and sutures, with an intracranial volume (ICV)

89   that broadly represented the brain. The whole model was then transformed into a 3D solid
90   meshed model and imported to a finite element solver, ANSYS v.18 (ANSYS Inc.,
91   Canonsburg, PA, USA). Isotropic (linear and elastic) material properties were assigned to all
92   regions with a thermal coefficient defined only for the ICV. Bone and suture were assumed to
93   have an elastic modulus of 3500 MPa and 30 MPa respectively at age P3 [10,11]. The elastic
94   modulus of the ICV was assumed to be 150 MPa from a previous study [25]. The bone and
95   suture materials were assumed to have a Poisson's ratio of 0.3. The ICV value was 0.48.
96
97   *Boundary, interface conditions and simulations*: The bone-suture interfaces and bone-
98   suture-intracranial volume interfaces were assumed to be perfectly connected. Three nodes
99   were selected on the presphenoid bone and all their degrees of freedom were constrained.
100 The presphenoid bone was constrained because previous examination of the growth of the
101 WT mouse skull revealed that this bone grows centrically during development and can be
102 considered to effectively remain at the same position during the skull development (see
103 Supplement Materials Fig. S1 [26]). Also, we carried out several sensitivity analyses of
104 different boundary conditions and summarised their effect on the radial expansion of the skull
105 in a previous study [25]. Brain growth was modelled by including daily expansion of the
106 intracranial volume, i.e. from P3 to P10, using a simple thermal expansion approach, as
107 described previously [25,27].
108
109 *Modelling bone formation:* We first developed and tested our algorithm in the wild type
110 mouse. Here, to test for bone formation at the sutures at each step, we selected only the
111 suture elements within a 0.1 mm radius of the adjacent bone [28], then if the hydrostatic strain
112 within any element was smaller than 5% [29,30] its modulus of elasticity was increased by 250
113 MPa (from 30 MPa). The choice of 250 MPa was based on our previous study on quantifying
114 bone properties on same mouse model [11]; briefly, this was estimated based on a linear
115 extrapolation between the calvarial properties at P10 and P20. Then, the skull shape i.e. the
116 geometry, was updated and the elastic modulus of the bone was increased by 250 MPa in
117 preparation for the next step (or age or day of development). No adaptive re-meshing
118 algorithm was used here as the geometry was updated day by day to the new deformed shape.
119 This approach avoided element distortions that would have otherwise occurred due to the
120 large deformation.
121
122 The same remodelling process was then repeated, i.e. new suture elements (with
123 E=30 MPa) were selected at the edges of the remodelled tissue at the end of the previous
124 step. The model was loaded and pending the level of hydrostatic strain within the selected
125 suture elements their elastic modulus was altered (i.e. increased from E=30 MPa to E=280
126 MPa). Here, before increasing the modulus of elasticity the sutures, the modulus of the
127 previously remodelled layer (with E=280 MPa), was increased by a further 250 MPa to 530
128 MPa. Then, similar to the previous step the skull shape was updated and the same process
129 was repeated up to P10 (see Fig. 2). Note the interfaces between the different layers of
130 materials that formed throughout the tissue differentiation process (i.e. as age increased day
131 by day) were fixed. In other word these elements shared the same nodes and only their
132 modulus of elasticity was altered.
133
134 We carried out a series of detailed sensitivity analyses to test the choice of strain, i.e.
135 comparing hydrostatic strain, von Mises strain and first principal strain, the strain range, and
136 selection radius. The results of these sensitivity analyses are included in the Supplement
137 Materials Fig. S2 [26].
138
139 *Predicting bone formation in the mutant Fgfr2^{C342Y/+} mouse at P10:* Using the baseline
140 WT model, and initially fusing some of the sutures based on the study of Liu et al. [23] and our
141 own observation, the bone formation in the mutant skull at P10 was predicted. During the
142 analysis, the elastic modulus of frontal, coronal, lambdoid, and presphenoid-basisphenoid

140 synchondrosis (PBS) sutures were changed from 30 MPa to 3500 MPa (i.e. the same as bone)
141 to model the premature fusion of these sutures in the mutant model. The expansion rate was
142 kept similar to the WT model and the results were compared to the values from the microCT
143 data of the MT mice at P10.

144 *Measurements and comparisons*: Fig. 3 shows a comparison of our predictions of
145 suture closure at P7 and P10 with the *ex vivo* suture measurements for both WT and MT mice.
146 Our simulation captures the overall pattern of bone formation across the skull. For example, it
147 predicts the fusion of the posterior frontal suture by day 10 while the sagittal suture and
148 posterior fontanel remain open. Similarly, in the mutant mice, anterior-posterior closure of the
149 sagittal suture was comparable to our *ex vivo* findings. See also Supplement Materials Fig S3
150 [26] for the WT results at P7 and P10 with different scale bar i.e. highlighting predicted
151 mineralized tissue with the elastic modulus above 1000 MPa.

152 In Fig. 4 we compare sample suture sizes from our simulations at five regions out of
153 the fourteen regions identified in Fig 1. A full comparison between the *ex vivo* results and our
154 prediction is provided in Table 1. In this analysis, it is assumed that tissues with an elastic
155 modulus equal to or less than 780 MPa (based on our predictions) are still suture, while tissues
156 with elastic modulus greater than 780 MPa are bone/hard tissue (see Supplement Materials
157 Fig. S3 [26]). Our model predicts a gradual reduction in suture sizes across all the sutures
158 from P3 to P10. It should be noted that, in the mutant model at regions 2 and 13, the sutures
159 were assumed to be fused at P3 to mimic the early fusion of these sutures in the Crouzon
160 mouse. Hence, our predictions at P7 and P10 were also a fused suture, whereas our *ex vivo*
161 measurements shows that these regions are not fully fused at the aforementioned ages.

162 *Discussion:* There is no doubt that there is a complex mix of chemical and biological
163 signalling that regulates bone formation at the sutures. Several previous studies have
164 suggested that mechanical strain must also be a key factor [e.g.14,16]. Here we developed a
165 new algorithm to model this phenomenon based on mechanical strain experienced by the
166 sutures during the skull growth.

167 A number of assumptions and approximations had to be made in the simulations, but
168 still there is good agreement in the pattern of bone formation across the sutures and with the
169 *ex vivo* results. Perhaps the most significant were that: (1) the sutures were modelled as a
170 linear elastic material while they are known to be nonlinear and viscoelastic. Given the
171 timescale that our simulations were performed here, i.e. growth over 10 days, we think that
172 perhaps a linear model could be acceptable; (2) uniform bone deposition was assumed at all
173 sutures. It is possible that different sutures may have different bone deposition rate. Including
174 such rate dependent bone deposition might indeed address some of the discrepancies that
175 we observed (Fig. 3); (3) bone formation is a complex mix of various biological and non-
176 biological factors, however our approach is to model the bone formation purely based on the
177 level of hydrostatic strain. While this is indeed a huge simplification, the radius of bone
178 formation that was specified in our approach (i.e. 0.1 mm bone formation rate) implicitly takes
179 into account these complex factors through a combined macroscopic effect. Nonetheless,
180 further work possibly should be undertaken to explicitly incorporate the various signalling
181 events into the approach developed here, and to address the other limitations of this work.

182 We were not able to validate the tissue differentiation that our model predicted at the
183 sutures which will require further experimental measurements [see e.g. 31]. Nonetheless, our
184 previous nanoindentation of bone in mouse models with the same genetic background showed
185 a lower elastic modulus in bone adjacent to the sutures [11]. This is similar to our current
186 predictions but in a qualitative fashion rather than a more quantitative analysis. See also our
187 previous study for a detailed quantitative morphological comparison between the FE prediction
188 of skull shape at P10 with an "average" *ex vivo* wild type and Crouzon mouse at P10 [25].

189　　　　In summary, we think the modelling approach presented here has potential in the
190　modelling of calvarial growth. This could provide significant advancement in terms of
191　comparing different reconstruction methods for the treatment of craniosynostosis and
192　understanding the optimum management of various forms of this condition using finite element
193　method [32], which in the long-term could reduce the complications currently associated with
194　the treatment of craniosynostosis.

References:

1. L.A. Opperman, Dev. Dyn, **219**, 472 (2000).
2. G. Morriss-Kay, and A. O. M. Wilkie, J. Anat. **207**, 637 (2005).
3. J. T. Richtsmeier, and K. Flaherty, Acta Neuropathol. **125**, 469 (2013).
4. S.W. Jin, K.B. Sim, and S.D. Kim, J. Kor. Neur. Soc. **59**,192 (2016).
5. M.L. Moss, Am. J. Anat. **94**, 333 (1954).
6. A.S. Dekaban, Ann. Neurol. **2**, 485 (1977).
7. S.S. Margulies, and K.L. Thibault, J Biomech Eng. **122**, 364 (2000).
8. M. Moazen, A. Alazmani, K. Rafferty, Z.J. Liu, J. Gustafson, M.L. Cunningham, M.J. Fagan, and S.W. Herring, J. Biomech. **49**, 123 (2016).
9. M. Aggarwal , J. Zhang , M.I. Miller, R.L. Sidman, S. Mori, Neuroscience. **162**,1339 (2009).
10. J.H. Henderson, L.Y. Chang, H.M. Song, M.T. Longaker and D.R. Carter, J. Biomech. **38**, 2294 (2005).
11. M. Moazen, E. Peskett, C. Babbs, E. Pauws, M.J. Fagan, PLoS One. **12**, e0125757 (2015).
12. K.L. Rafferty and S.W. Herring, J. Morphol. **242**,167 (1999).
13. J.J. Mao, J. Den Res, **81**, 810 (2002),
14. D. R. Carter and G. S. Beaupre, Skeletal Function and Form: Mechanobiology of Skeletal Development, Aging, and Regeneration (Cambridge University Press, Cambridge, 2007).
15. S.W. Herring, Front. Oral Biol. **12**, 41. (2008).
16. J. Weickenmeier, C. Fischer , D. Carter, E. Kuhl , A. Goriety, Phys. Rev. Lett. **118**, 1 (2017).
17. C. Lee, J.T. Richtsmeier, R.H. Kraft, J. Mech. Behav. Biomed. Mater. **29**, 529 (2017).
18. R.H. Khonsari , J. Olivier , P. Vigneaux , S. Sanchez , P. Tafforeau , P.E. Ahlberg , F. Di Rocco , D. Bresch , P. Corre , A. Ohazama , P.T. Sharpe , V. Calvez, Proc R Soc B **280**, 20122670 (2013).
19. K. Flaherty, N. Singh, and J.T. Richtsmeier, Wiley Interdiscip. Rev. Dev. Biol. **5**, 429 (2016).
20. Z. Al-Rekabi, M.L. Cunningham, and N.J. Sniadecki, ACS Biomat Sci Eng. **3**, 2733 (2017).
21. M. Grova, D.D. Lo, D. Montoro, J.S. Hyun, M.T. Chung, D.C. Wan, and M.T. Longaker, J. Craniofac. Surg. **23**,1954 (2012).
22. V.P. Eswarakumar, M.C. Horowitz, R. Locklin, G.M. Morriss-Kay, and P. Lonai. Proc. Natl. Acad. Sci. USA. **101**,12555 (2004).
23. J. Liu, H.K. Nam, E. Wang, and N.E. Hatch, Cal. Tisu. Int. **92**, 451 (2013).
24. E. Peskett, S. Kumar, W. Baird, J. Jaiswal, M. Li, P. Patel, J.A. Britto, and E. Pauws, Biol. Open. **6**, 223 (2017).
25. A. Marghoub, J. Libby, C. Babbs, E. Pauws, M.J. Fagan, and M. Moazen, J. Anat. **232**, 440 (2018).
26. See Supplement Materials, for further details and several sensitivity analysis.
27. J. Libby, A. Marghoub, D. Johnson, R. Khonsari, M.J. Fagan, and M. Moazen, J. Roy. Soc. Int. **14**, 20170202 (2017).
28. J. H. Henderson, M. T. Longaker, and D. R. Carter, Bone. **34**, 271 (2004).
29. L.E. Claes, and C.A. Heigele, J. Biomech. **32**, 255 (1999).
30. M. Doblaré and J. M. García-Aznar, Arch. Comput. Methods Eng. **13**, 471 (2006).
31. P. L. Leong, and E.F. Morgan, Acta Biomater. **4**,1569 (2008).
32. O. Malde, J. Libby and M. Moazen, Mol Synd. (in press).
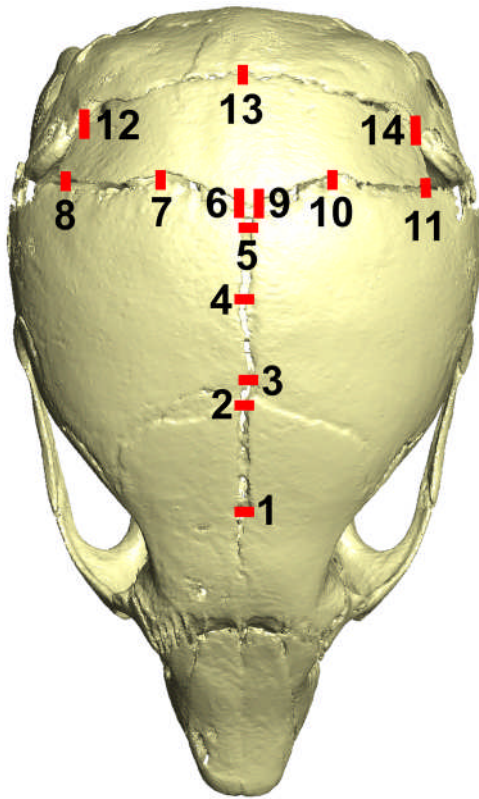
Figures:
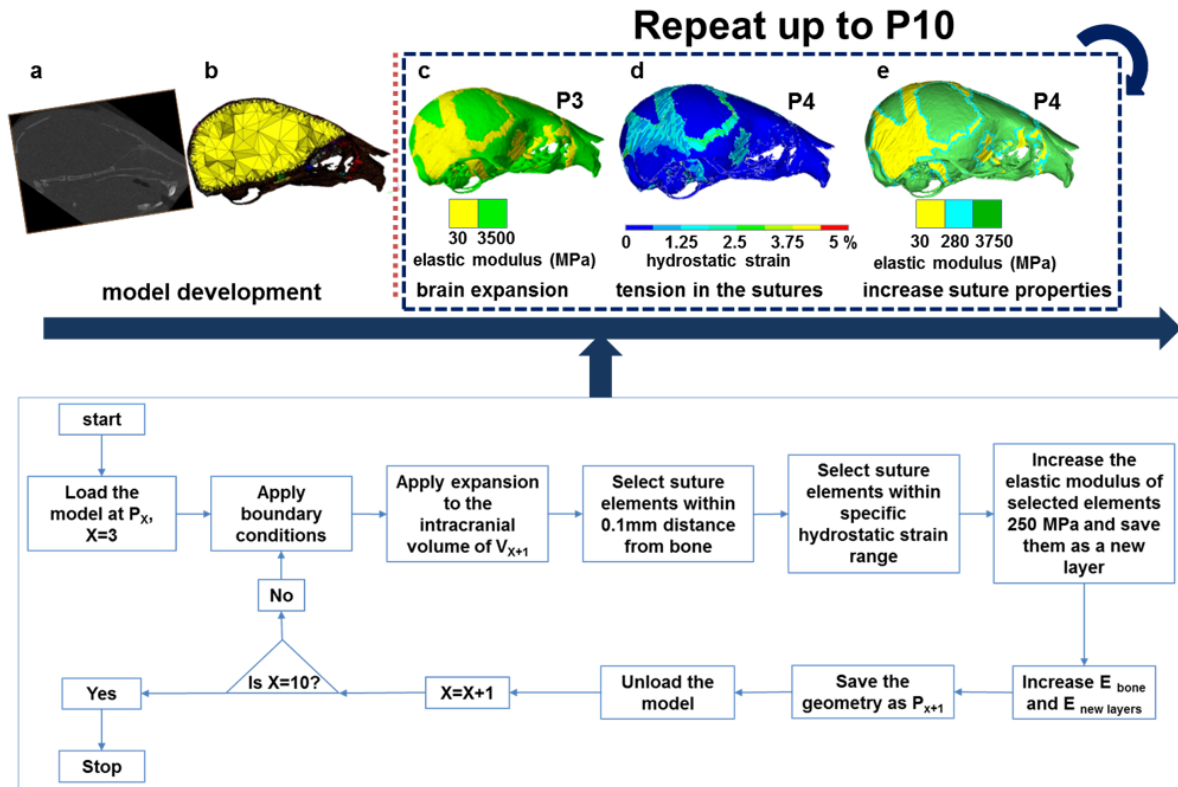
Figure 1: *Ex vivo* and *in silico* suture sizes were measured at 14 locations: 1- Frontal suture, medial point; 2- Frontal suture, posterior point; 3- Sagittal suture, anterior point; 4- Sagittal suture, medial point; 5- Sagittal suture, posterior point; 6- Right Interparietal suture, closest point to the midsagittal plane; 7- Right Interparietal suture, medial point; 8- Right Interparietal suture, most lateral point; 9- Left Interparietal suture, closest point to the midsagittal plane; 10- Left Interparietal suture, medial point; 11- Left Interparietal suture, most lateral point; 12- Most lateral point of the Lambdoid suture- right; 13- Lambdoid suture, medial point; 14- Most lateral point of the Lambdoid suture- left

262

Figure 2: Using microCT images of a WT mouse skull at P3 (a) a 3D finite element model was developed (b). After assigning the material properties and applying boundary conditions (c) the intracranial volume was expanded to the volume of the next age i.e. at P4 (d). Material properties of the bone and the suture elements within the specified hydrostatic strain range and distance from the bone were updated (e). This process was repeated until P10. The flow diagram shows the overall process.

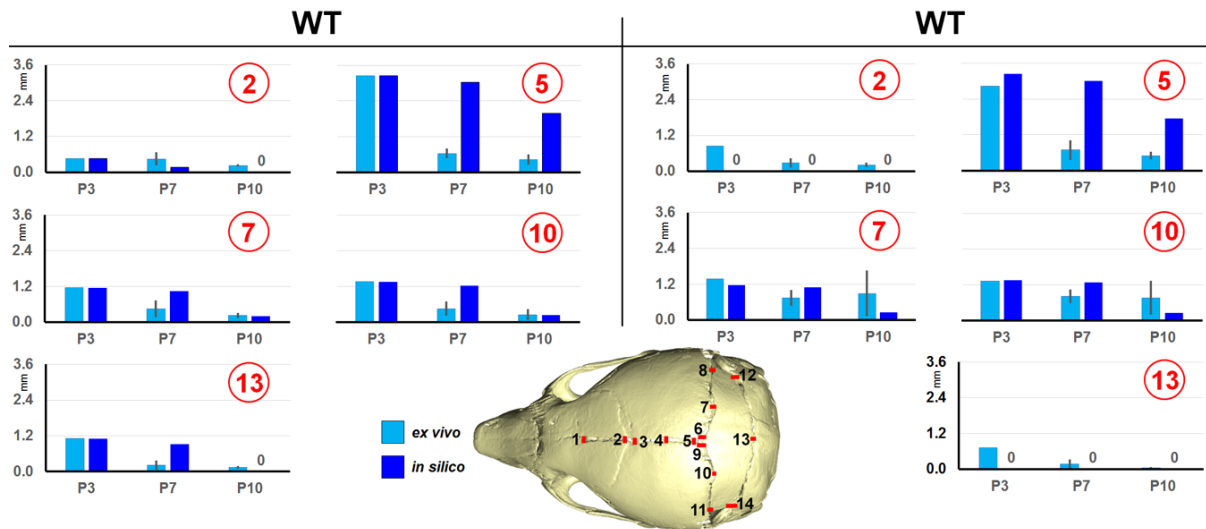268

269

270
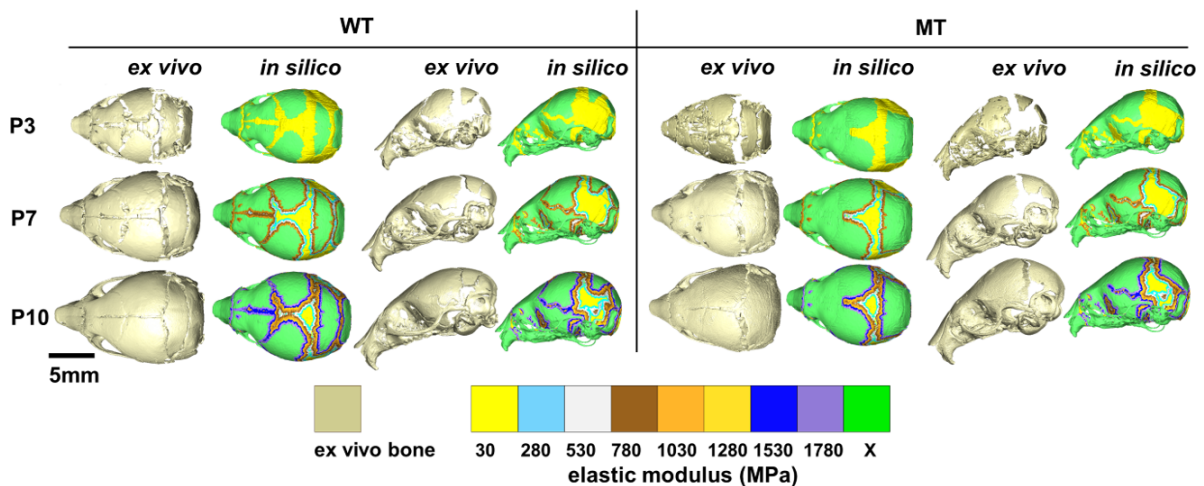
Figure 3: WT and MT *ex vivo* and *in silico* skull and suture size changes from P3 to P10. *In silico* images show the tissue differentiation as skull grows. Note, that the elastic modulus of the bone tissue i.e. green areas (X) is increased by 250 MPa at the end of each age, from 3500 MPa at P3 to 5250 MPa at P10.

Figure 4: Bone formation comparison between *ex vivo* and *in silico* models at 5 measuring points. Note that in MT *in silico* model points 2 and 13 suture sizes are 0 at all ages because they have been considered to be fused prematurely.

Table 1: Suture size changes (mm) measured at 14 locations. SD at P3 for both WT and MT is zero due to having only one sample of each. Since frontal, coronal, lambdoid, and PBS sutures were fused prematurely at P3 for the MT FE model, the suture sizes at points 1, 2, 12, 13 and 14 are 0 from P3 to P10.

| | | P3 | | | | | P7 | | | | | P10 | | | | |
| | WT | | | MT | | | WT | | | MT | | | WT | | | MT | | |
	Av ex vivo	SD*	FE	Av ex vivo	SD*	FE	Av ex vivo	SD	FE	Av ex vivo	SD	FE	Av ex vivo	SD	FE	Av ex vivo	SD	FE
1	0.63	0.00	0.63	1.03	0.00	0.00	0.53	0.17	0.56	0.38	0.18	0.00	0.39	0.13	0.00	0.36	0.22	0.00
2	0.46	0.00	0.46	0.84	0.00	0.00	0.45	0.21	0.17	0.28	0.16	0.00	0.23	0.03	0.00	0.21	0.07	0.00
3	1.20	0.00	1.20	1.88	0.00	1.20	0.61	0.07	1.03	0.36	0.17	0.57	0.31	0.09	0.66	0.27	0.05	0.00
4	1.46	0.00	1.46	1.41	0.00	1.46	0.42	0.11	1.22	0.40	0.29	1.12	0.32	0.15	0.25	0.32	0.13	0.14
5	3.24	0.00	3.24	2.84	0.00	3.24	0.64	0.17	3.03	0.69	0.33	3.00	0.43	0.18	1.99	0.50	0.13	1.74
6	1.11	0.00	1.11	1.86	0.00	1.11	0.73	0.30	1.07	1.13	0.24	1.16	0.33	0.13	0.66	0.64	0.48	0.69
7	1.16	0.00	1.16	1.37	0.00	1.16	0.44	0.28	1.05	0.74	0.27	1.10	0.22	0.10	0.21	0.88	0.77	0.24
8	1.24	0.00	1.24	1.40	0.00	1.24	0.69	0.21	1.10	0.67	0.16	1.15	0.31	0.14	0.25	0.49	0.30	0.28
9	1.10	0.00	1.10	1.58	0.00	1.10	0.80	0.24	1.06	0.89	0.17	1.11	0.45	0.25	0.71	0.60	0.27	0.77
10	1.36	0.00	1.36	1.33	0.00	1.36	0.46	0.24	1.23	0.83	0.23	1.28	0.26	0.19	0.24	0.77	0.56	0.26
11	1.41	0.00	1.41	1.24	0.00	1.41	0.71	0.30	1.34	0.56	0.32	1.45	0.49	0.27	1.04	0.52	0.26	1.09
12	1.53	0.00	1.53	1.16	0.00	0.00	0.51	0.24	1.36	0.36	0.13	0.00	0.37	0.22	1.03	0.33	0.13	0.00
13	1.11	0.00	1.11	0.73	0.00	0.00	0.22	0.15	0.93	0.17	0.13	0.00	0.14	0.04	0.00	0.04	0.06	0.00
14	1.30	0.00	1.30	0.91	0.00	0.00	0.55	0.16	0.95	0.46	0.17	0.00	0.48	0.24	0.58	0.19	0.07	0.00

289

290

Characterizing and modeling bone formation during mouse calvarial development

Arsalan Marghoub[1], Joseph Libby[2], Christian Babbs[3], Yiannis Ventikos[1], Michael J Fagan[2], Mehran Moazen[1]

[1]Department of Mechanical Engineering, University College London, Torrington Place, London, WC1E 7JE, UK

[2]Medical and Biological Engineering, School of Engineering and Computer Science, University of Hull, Hull, HU6 7RX, UK

[3]Weatherall Institute of Molecular Medicine, University of Oxford, Oxford, OX3 9DS, UK

Supplement materials:

Figure S1 highlights that the presphenoid bone in the WT mouse grows centrically during the development and can be considered to effectively remain at the same position. Figure S2 summarises the sensitivity analyses to test the choice of strain, i.e. comparing hydrostatic strain, von Mises strain and first principal strain, the strain range, and selection radius. Figure S3 summarises the pattern of the bone formation for the WT mouse at P7 and P10 with different scale bar comparing to the Figure 3 of the main text i.e. highlighting predicted mineralized tissue with the elastic modulus above 1000 MPa.
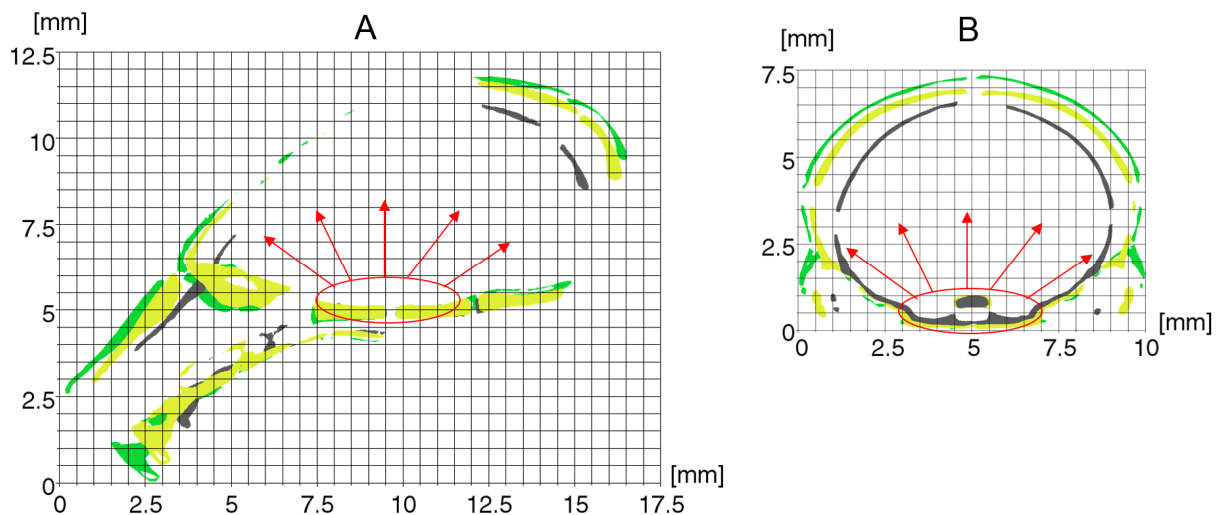

Figure S1: Lateral (A) and anteroposterior (B) cross sections of P3, P7 and P10 skulls. Arrows show how skull grows almost spherically from the base of the skull and around the skull base bones (basisphenoid and presphenoid).
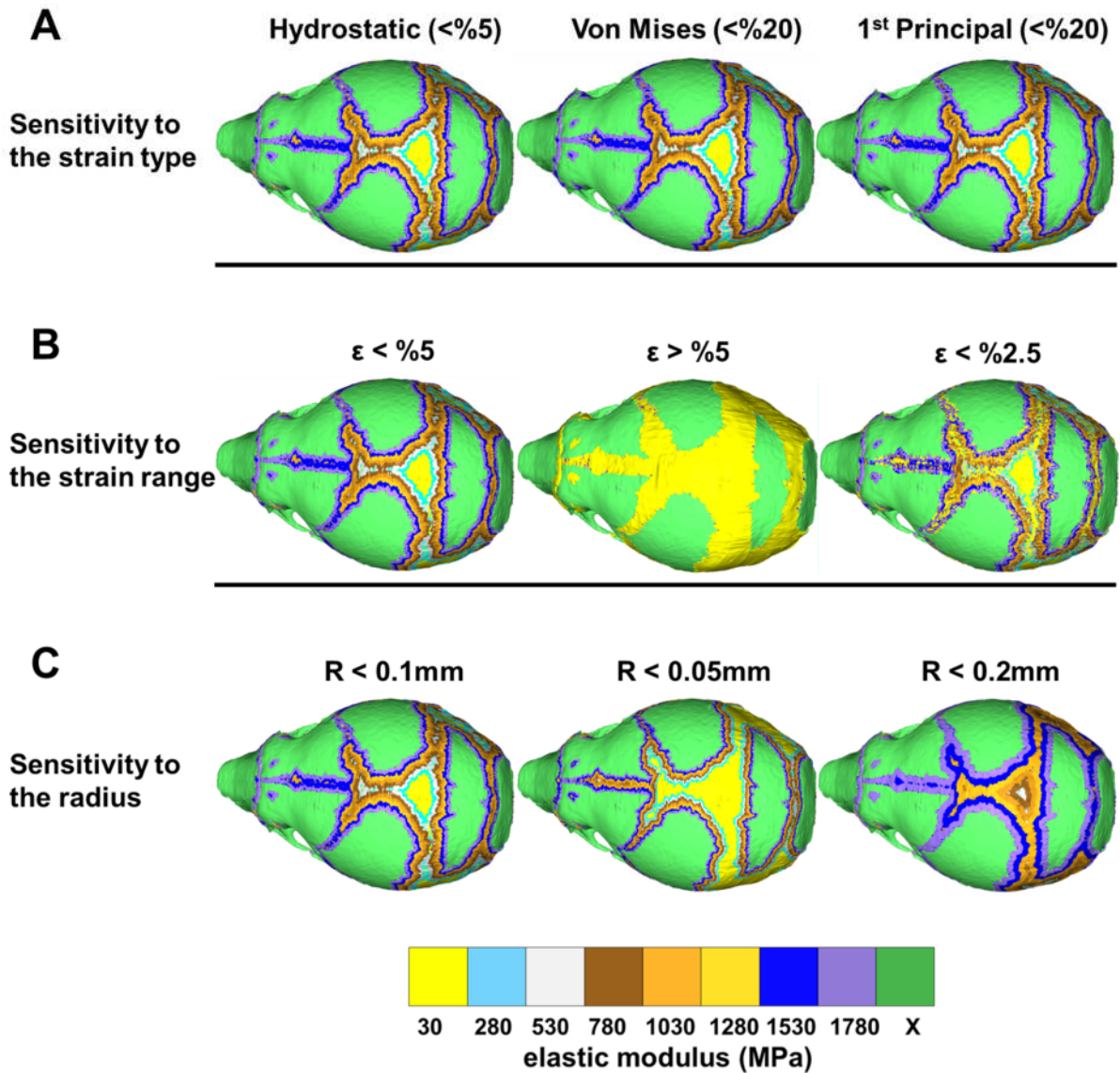
Figure S2: Sensitivity test results for strain (A) type: selecting suture elements with hydrostatic strain less than 5% as the baseline compared with von Mises strain and 1st principal strain less than 20%; strain range (B): selecting suture elements having hydrostatic strain less than %5 as the baseline compared with selecting elements with strain values higher than 5% and less than 2.5%; and tissue differentiation radius (C): 0.1mm as the baseline compared with 0.05mm and 0.2mm. Note that the elastic modulus of the bone tissue (X) is increased by 250 MPa at the end of each age, from 3500 MPa at P3 to 5250 MPa at P10.

P7

P10

ex vivo bone

5mm

1030 1280 1530 1780 X
elastic modulus of bone (MPa)
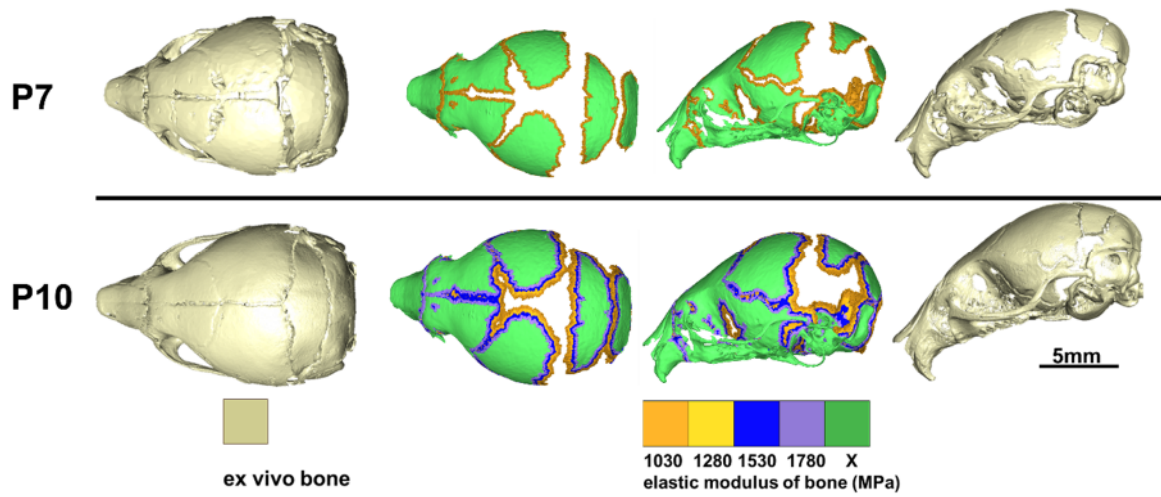
Figure S3: *Ex vivo* and *in silico* bone in WT at P7 and P10. Note that the elastic modulus of the bone tissue (X) is increased by 250 MPa at the end of each age, from 3500 MPa at P3 to 5250 MPa at P10.